

# Quantifying Transport Into the Lowermost Stratosphere



Dissertation  
zur Erlangung des Doktorgrades  
der Naturwissenschaften

vorgelegt beim  
Fachbereich Geowissenschaften/Geographie  
der Johann Wolfgang Goethe-Universität  
in Frankfurt am Main

von

Dipl. Met. Anja Sabine Werner  
aus Gelnhausen

Frankfurt am Main, 2006  
(D30)

Vom Fachbereich Geowissenschaften / Geographie der Johann Wolfgang  
Goethe-Universität als Dissertation angenommen.

Dekan: Prof. Dr. Heinrich Thiemeyer  
Gutachter: Prof. Dr. Ulrich Schmidt, Universität Frankfurt  
Prof. Dr. Thomas Röckmann, Universität Utrecht,  
Niederlande  
Datum der Disputation: 05. März 2007

Für  
Fritz Georg Karl Hartmann  
\* 10.05.1922 † 29.06.2004

„Wir haben ganz einfach das Universum bekommen, das wir verdient  
haben.“

Mikael Niemi (from “Svålhålet”, German edition, 2006)



# Contents

<b>Abstract</b>	<b>1</b>
<b>1 Introduction</b>	<b>3</b>
1.1 The lowermost stratosphere . . . . .	3
1.2 The role of the LMS in the climate system . . . . .	4
1.3 Transport into the LMS . . . . .	5
1.3.1 Mean meridional circulation and stratospheric transport . . . . .	5
1.3.2 Stratosphere-troposphere exchange (STE) . . . . .	7
1.3.3 Seasonal changes in transport . . . . .	11
1.4 Studying transport into the LMS . . . . .	12
1.4.1 Using tracer measurements to study transport processes in the atmosphere . . . . .	13
1.4.2 Tracer measurements in the LMS region . . . . .	13
1.5 Quantifying transport into the LMS — Outline of this thesis . . . . .	15
<b>2 Measurements</b>	<b>17</b>
2.1 The High Altitude Gas Analyser: A general description . . . . .	17
2.1.1 The GC-ECD-System . . . . .	19
2.1.2 CO <sub>2</sub> measurements with the LI-COR-6251 . . . . .	26
2.2 Development of a CH <sub>4</sub> channel for HAGAR . . . . .	28
2.2.1 Theory of doping . . . . .	28
2.2.2 Implementing the doping technique for the HAGAR instrument	29
2.2.3 Necessary changes in channel II due to use of pure N <sub>2</sub> as carrier gas: . . . . .	36
2.3 Campaigns . . . . .	37
2.3.1 The M55 Geophysica . . . . .	37
2.3.2 ENVISAT mid-latitude test and validation campaign . . . . .	38
2.3.3 ENVISAT mid-latitude validation campaign . . . . .	41
2.3.4 Vintersol EuPLEX . . . . .	45
2.3.5 APE ENVISAT Arctic Validation Campaign (AVC) . . . . .	49
<b>3 Quantifying transport into the Arctic lowermost stratosphere</b>	<b>51</b>
3.1 A simple mass balance for the high-latitude LMS . . . . .	51

3.2	Setting up a mass balance linear equation system . . . . .	52
3.3	Suitable tracers . . . . .	53
3.4	Determining the boundary conditions . . . . .	58
3.4.1	Separating data: Vortex, mid-latitude stratosphere, troposphere	59
3.4.2	Tropospheric boundary condition . . . . .	63
3.4.3	The vortex boundary condition . . . . .	64
3.4.4	The stratospheric boundary condition . . . . .	68
3.4.5	Boundary conditions for H <sub>2</sub> O . . . . .	70
3.5	Normalization of the tracer data . . . . .	72
3.6	Sensitivity of the calculation to errors in the boundary conditions . .	74
3.7	Results of the mass balance calculation . . . . .	79
3.7.1	EuPLEx . . . . .	80
3.7.2	AVC . . . . .	86
3.7.3	Comparison with CLaMS results . . . . .	91
3.8	Conclusions . . . . .	92
<b>4</b>	<b>A cut-off low over Europe</b>	<b>95</b>
4.1	Meteorological situation over Italy in July and October 2002 . . . . .	95
4.2	Tracer measurements during July and October 2002 . . . . .	101
4.3	Trajectory analysis . . . . .	105
4.3.1	Flight of July 13, 2002 . . . . .	105
4.3.2	Flight of July 15, 2002 . . . . .	108
4.3.3	Flight of July 18, 2002 . . . . .	109
4.3.4	Flight of July 22, 2002 . . . . .	115
4.3.5	Summary of all July flights . . . . .	118
4.3.6	The October flights . . . . .	118
4.4	Assessment of mixing . . . . .	121
4.4.1	Spring time initial conditions in the LMS . . . . .	121
4.4.2	Results . . . . .	124
4.5	Conclusions . . . . .	130
<b>5</b>	<b>Summary</b>	<b>133</b>
<b>A</b>	<b>Mathematical basics</b>	<b>137</b>
A.1	Mean, standard deviation and deviation from the mean . . . . .	137
A.2	Progression of errors . . . . .	137
A.3	Median filter . . . . .	138
A.4	Savitzky-Golay filter . . . . .	138
A.5	Newton's method . . . . .	138
<b>B</b>	<b>Definitions</b>	<b>141</b>
B.1	Ertels potential vorticity - PV . . . . .	141
B.2	The tropopause . . . . .	141
B.3	Equivalent latitude . . . . .	142

---

B.4	Nash criterium . . . . .	142
B.5	Delta theta . . . . .	142
B.6	Delta $N_2O$ . . . . .	143
B.7	Delta $N_2O_{extra}$ . . . . .	143
B.8	The CLaMS model . . . . .	143
B.9	Trajectories . . . . .	145
<b>C</b>	<b>HAGAR instrumental issues</b>	<b>147</b>
C.1	Calculation of doping gas flow and mixing ratio . . . . .	147
C.2	$N_2O$ contamination problem . . . . .	147
C.3	CAL gas drift correction . . . . .	149
C.4	HAGAR standard gases . . . . .	150
C.5	Calculating the precision of GC of measurements . . . . .	153
C.6	Calculating the precision of $CO_2$ measurements . . . . .	155
C.7	Precision of the HAGAR measurements . . . . .	155
<b>D</b>	<b>HAGAR data</b>	<b>159</b>
D.1	Test and Mid Latitude Validation Campaigns . . . . .	159
D.2	Vintersol EuPLEx . . . . .	163
D.3	APE ENVISAT Arctic Validation Campaign . . . . .	166
<b>E</b>	<b>Meteorological Analysis</b>	<b>169</b>
E.1	July 2002 . . . . .	169
E.2	October 2002 . . . . .	172
	<b>List of figures</b>	<b>175</b>
	<b>List of tables</b>	<b>179</b>
	<b>Bibliography</b>	<b>181</b>
	<b>Zusammenfassung</b>	<b>191</b>
	<b>Acknowledgements</b>	<b>199</b>
	<b>Curriculum Vitae</b>	<b>203</b>





# Abstract

Since the discovery of the ozone hole [Farman *et al.*, 1985], the dynamics of the stratosphere and the transport of anthropogenic trace gases from the surface to the higher atmosphere has come into the focus of interest. In the tropics, air rises high into the stratosphere and is transported poleward. Trace gases like the CFCs<sup>1</sup>, photochemically stable in the troposphere, are thus transported into regions where they are photolyzed. The products of the photolysis reactions (eg. Cl, Br) interact in the catalytic ozone cycles and lead to enhanced ozone depletion.

Regarding the transport of trace gases, the so-called lowermost stratosphere (LMS) is a very interesting region, where the troposphere and the stratosphere directly interact and air masses out of both regions are mixed. It is the lowest part of the stratosphere between the tropopause and the 380 K isentrope. Tropospheric air can enter this region directly via isentropic transport across the extra-tropical tropopause whereas stratospheric air descends across the 380 K isentrope via the mean meridional circulation. Stratosphere-troposphere exchange (STE) controls the chemical composition of the LMS as well as of the tropopause region and thus has an important effect on the radiative and chemical balance of these regions and the climate system. STE exhibits a strong seasonality [Holton *et al.*, 1995]. While downwelling of stratospheric air across the 380 K isentrope is the dominant process in winter, troposphere-to-stratosphere transport (TST) gains importance in summer, when the downwelling from the stratosphere is only weak. Isentropic transport across the extra-tropical tropopause occurs in regions where the tropopause is strongly disturbed and is connected to tropopause folds, streamer events, frontal zones, polar and subtropical jets, warm conveyor belts and cut-off low systems. A short introduction into STE, the LMS region, and methods to study atmospheric transport is given in Chapter 1.

One useful tool to analyse the motions of air and transport processes are long-lived trace gases. Since the lifetimes of these tracers are longer than the time scale of the transport processes they are involved in, the distribution of tracers in the atmosphere is mostly determined by dynamics.

In the context of this thesis, measurements of such long-lived tracers were performed and used to study transport into the LMS region in the northern hemisphere. During the Vintersol/EuPLEX and ENVISAT validation campaigns in win-

---

<sup>1</sup>Chlorofluorocarbons

ter 2003, long-lived tracers such as  $\text{N}_2\text{O}$ ,  $\text{CH}_4$ , CFC-12, CFC-11, H-1211,  $\text{H}_2$ ,  $\text{SF}_6$  and  $\text{CO}_2$  were measured with the High Altitude Gas Analyser (HAGAR), a two channel in-situ gas chromatograph combined with a  $\text{CO}_2$  instrument, based on non-dispersive infrared absorption. Combined with measurements taken during campaigns in Forli/Italy (ENVISAT validation) in July and October 2002, tracer data were gathered from the tropopause up to altitudes around 20 km during 25 flights on board the Russian high-altitude aircraft M55 Geophysica. Thus, a substantial set of high quality tracer data has been obtained covering the polar vortex region as well as the mid latitudes of the northern hemisphere. Chapter 2 gives an overview of the HAGAR instrument and necessary improvements of the instrumental set up (implementing a  $\text{CH}_4$  channel) that were performed in the context of this thesis, and review data processing, the measurement campaigns.

In order to study transport into the LMS it is assumed that air basically enters the LMS via three different pathways: a) quasi-isentropic transport from the troposphere, b) downward advection from the middle stratosphere through the 380 K surface and c) in the polar vortex region subsidence of air from of the polar vortex. Fractions of air originating in each of these source regions are determined with a simple mass balance calculation by using observations of a subset of the above species with distinct lifetimes ( $\text{N}_2\text{O}$ ,  $\text{CH}_4$ , CFC-11, H-1211,  $\text{H}_2$  and  $\text{O}_3$ ) yielding complementary constraints on transport from each region. Details of the mass balance calculation and the results are presented in Chapter 3.

During the mid-latitude measurement campaigns in Forlí the passing of a cut-off low system associated with an elongated streamer over Europe was observed. The impacts of this event on the trace gas mixing ratios in the LMS are examined in Chapter 4.

Finally, a summary is given in Chapter 5.

# Chapter 1

## Introduction

### 1.1 The lowermost stratosphere

The lowest part of our atmosphere is the troposphere. It reaches from the Earth's surface to the tropopause — the upper boundary of the troposphere (see also Appendix B.2). The height of the tropopause varies from about 17 km in the tropics to 8 km in the polar regions. Since the vertical temperature gradient in the troposphere is negative, it represents a highly unstable region of the atmosphere. Transport processes happen on timescales shorter than a few days and the troposphere can be considered as a well mixed region concerning the distribution of long-lived trace gases. Tropospheric air masses are characterized by high water vapour and low ozone values. The characteristics of the stratosphere, the layer above the tropopause to a height of about 50 km, differ from the characteristics of the troposphere. Due to a vertical temperature gradient close to zero in the lower part and even a positive temperature gradient elsewhere, the stratosphere is highly stable regarding vertical transport. The reason for the temperature inversion is the absorption of solar UV radiation by O<sub>3</sub>, which has a maximum mixing ratio in the middle stratosphere at a height around 25 km. Stratospheric air can be characterized by high O<sub>3</sub> values and low water vapour.

The lower stratosphere can be divided into three regions: the so-called over, middle and underworld [*Hoskins, 1991*]. The latter is situated in the troposphere and transport from the underworld into the stratosphere can only happen by diabatic heating across the isentropes. In the middleworld, the isentropes intersect the tropopause allowing bidirectional adiabatic transport of stratospheric and tropospheric air masses across the tropopause [*Chen, 1995*]. A very special part of the stratosphere is stratospheric part of the middle world, the so-called lowermost stratosphere (LMS), the region between the extra-tropical tropopause and the 380 K isentrope (see Figure 1.1). Though the LMS has stratospheric characteristics, it is distinct from the higher stratosphere above 380 K — the overworld — since it is influenced by in-mixing of tropospheric air masses. However, this concept is being refined since satellite water vapour measurements indicated that relatively young air

— air that recently crossed the tropical tropopause — can be found up to heights of about 450 K [Rosenlof *et al.*, 1997]. According to these results, the overworld can be further separated into a “tropically controlled transition region” between 380 K and 450 K where these relatively young air masses occur, and the region above 450 K, where transport barriers inhibit the fast meridional mixing of air masses.

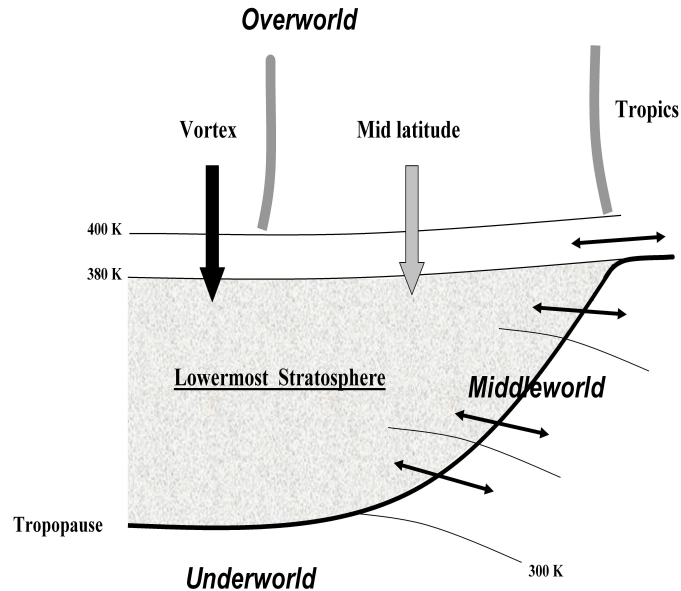


Figure 1.1: Scheme of the lowermost stratosphere. Air enters the LMS from the stratospheric overworld in the mid-latitude (thick grey arrow) and the vortex region (thick black arrow). Transport between the troposphere and the LMS is indicated by thin black arrows.

## 1.2 The role of the LMS in the climate system

Stratosphere-troposphere-exchange (STE) significantly determines the chemical composition [Pan *et al.*, 1997] and radiative balance of the LMS and tropopause region [Holton *et al.*, 1995], which is highly relevant to climate processes [Haynes & Shepard, 2001].

The ozone budget of the UT/LS (upper troposphere/lower stratosphere) region is highly sensitive to transport processes across the tropopause. Since  $O_3$  is a strong greenhouse gas in the troposphere, its transport into the upper troposphere has a high climate impact by influencing the radiative balance of this region [Lacis *et al.*, 1990; Ramaswamy *et al.*, 1992]. Further, it influences the oxidizing capacity of the troposphere being a source for OH radicals [Esler *et al.*, 2001]. OH reacts with other trace gases like  $CH_4$ , CO, or  $NO_x$  which exhibit rising levels due to anthropogenic production. This in turn is relevant for the budgets of greenhouse

gases, gases responsible for stratospheric ozone depletion and the O<sub>3</sub> budget in the UT/LS itself.

Changes in the radiative balance of the tropopause region due to greenhouse gases have a climatic impact. The rising amount of greenhouse gases results in cooling of the stratosphere and warming of the troposphere [Pawson *et al.*, 1998]. Lower temperatures in the middle and upper stratosphere might lead to a decrease in the stratospheric stability [Stohl *et al.*, 2003a] and thus to changes in the mean meridional circulation, which are thought to cause changes of the water vapour content of the stratosphere [Rosenlof, 2002].

In summary it can be said that understanding STE and transport processes in the LMS is elementary for understanding climate change as well as the global ozone budget.

## 1.3 Transport into the LMS

The focus of this thesis is on transport into the LMS via different pathways. The LMS is influenced both by tropospheric and stratospheric air masses. There are several pathways along which transport into the LMS can occur. An overview on the transport mechanisms will be given in the following sections 1.3.1 and 1.3.2. For more details see the works of Holton *et al.* [1995], Plumb [2002], Haynes & Shepard [2001] and Stohl *et al.* [2003a,b].

### 1.3.1 Mean meridional circulation and stratospheric transport

The stratospheric mean meridional circulation determines the global distribution of stratospheric trace gases [Plumb, 2002]. The first to describe this global circulation were Dobson *et al.* [1929] and Brewer [1949].

The mean meridional circulation — thus called the Brewer-Dobson circulation — describes the large-scale transport of tropospheric air masses through the cold tropical tropopause into the stratosphere, the following upwelling in the tropics and a mean meridional flow of the air masses in the stratosphere to the middle and high latitudes, where the air masses descend. In the course of the circulation process the air descends into the LMS and finally re-enters the troposphere. The mean turnover time of air in the stratosphere is about 2 years [Holton *et al.*, 1995]. In connection with the Brewer-Dobson-circulation there is an all year long advection of stratospheric air through the 380 K isentrope into the LMS and further into the troposphere across the extra-tropical tropopause. This transport is intensified in winter time. The downward mass flow across the 380 K isentrope was estimated by Rosenlof & Holton [1993] to be about  $1.7 \times 10^{17}$  kg a<sup>-1</sup> in the northern hemisphere and  $1 \times 10^{17}$  kg a<sup>-1</sup> in the southern hemisphere. In Figure 1.2 this large scale motion is indicated by thick white arrows.

The stratospheric circulation is driven by the breaking of Rossby waves, which propagate upward from the troposphere mostly in winter and spring. The wave

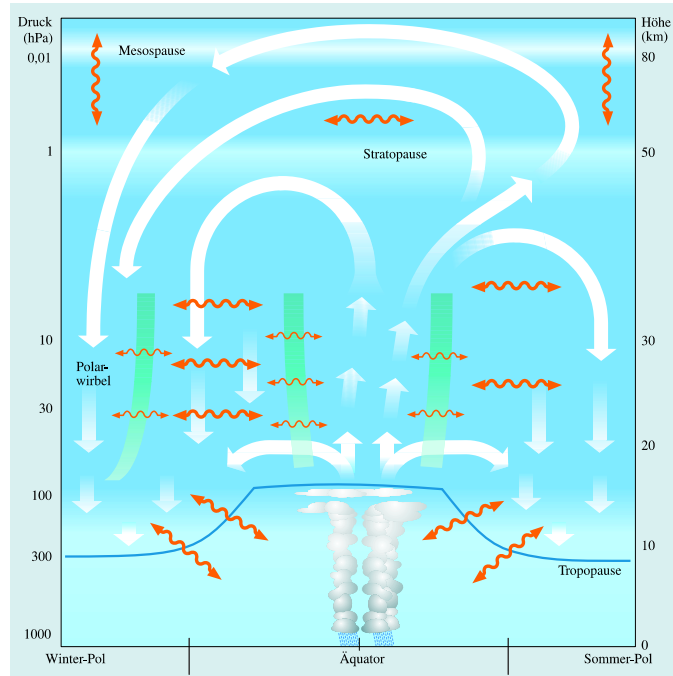


*Figure 1.2:* The global stratospheric transport. Thick arrows mark the diabatic circulation, mixing along isentropes follows the wavy arrows. Grey areas are transport barriers, the troposphere is marked by the thick black line. Source *Schmidt et al.* [2001] based on *WMO* [1999].

breaking provides a westward directed force slowing down the zonal flow in the wintertime stratosphere (where westerlies are predominating). To conserve the angular momentum, a meridional circulation is induced which balances the wave-induced force by the Coriolis force acting on the poleward moving air masses. This non-local wave drag mechanism driving a poleward flow in the middle and upper stratosphere is called the “Rossby-” or “extratropical wave pump” [*Haynes et al.*, 1991; *Holton et al.*, 1995]. The mesospheric branch of the circulation is assumed to be generated by the “gravity wave pump”, with upward propagating inertia-gravity waves driving a summer pole to winter pole circulation [*Plumb*, 2002].

Due to conservation of mass, the poleward flow in the stratosphere and the mesosphere induces upwelling of air in the tropics and diabatic descent at mid to high latitudes and the winter pole. The downward extra-tropical mass flow (in both hemispheres) equals the upward directed mass flow in the tropics.

The region where Rossby wave breaking occurs is called the “surf zone” [*McIntyre & Palmer*, 1983]. Associated with the breaking of Rossby waves is the stirring of air isentropically across the winter stratosphere. As a result the surf zone is a well-mixed region where tracer distributions exhibit a horizontal gradient close

to zero and long-lived tracers exhibit compact relationships [Plumb & Ko, 1992]. The surf zone is indicated in Figure 1.2 by bold wavy red arrows. It is bounded by the dynamical transport barriers of the polar vortex edge and the edge of the inner tropics (shaded in green in Figure 1.2). These transport or mixing barriers are regions of high horizontal shear and maximum PV gradients along isentropes, prohibiting fast isentropic mixing.

Due to their separation by mixing barriers, the tropical stratosphere, mid-latitude stratosphere and the polar vortex region contain different air masses concerning e.g. the stratospheric age [Kida, 1983] (see also section 1.4.1) or the chemical processing. Different tracer-tracer relationships develop during the winter: except for its lowest part where isentropic mixing<sup>1</sup> with the extra-tropics is possible [Volk *et al.*, 1996], the tropical stratosphere is more or less isolated from the extra-tropical stratosphere. Thus, the tropical stratosphere is a unique region (“tropical pipe”; [Plumb, 1996]) dominated by young air masses which recently entered the stratosphere. Inside the tropics, these air masses are transported into the higher stratosphere where the air is photochemically processed. It is therefore photochemically aged air that descends in the mid to high latitudes. In the winter hemisphere this descent is most pronounced in the polar vortex, a strong cyclone over the winter pole, where diabatic cooling due to missing sunlight intensifies the descent. Very low temperatures inside the vortex region promote the formation of polar stratospheric clouds (PSCs). The heterogeneous chemical reactions on the surfaces of the cloud particles enable the release of reactive halogen compounds (e.g.  $Cl_2$ ,  $HOCl$ ). When the vortex is exposed to sunlight these halogen compounds are photolyzed to radicals (e.g. reactive  $Cl$ ,  $Br$  atoms) that lead to the massive depletion of ozone in late winter by catalytic ozone destruction. Thus, the late winter vortex region is characterized not only by very low mixing ratios of aged long-lived tracers, but also by very low ozone mixing ratios.

In the LMS, the mixing barriers that separate the tropics, mid- to high-latitude and the polar stratosphere are not evident. Thus, once the air masses descended from the higher regions into the LMS, fast meridional mixing is possible.

### 1.3.2 Stratosphere-troposphere exchange (STE)

STE occurs in both directions and includes stratosphere-to-troposphere transport (STT) as well as troposphere-to-stratosphere transport (TST). A distinction must be made between STE processes in the tropics and extra-tropics. In the tropics, air is transported to the upper troposphere via the Hadley circulation and ascends further into the stratosphere by transport processes connected to the Brewer-Dobson circulation (section 1.3.1). The main direction of this transport is from the troposphere to the stratosphere. Nevertheless, transport from the stratosphere to the troposphere can happen episodically by breaking Kelvin waves [Fujiwara *et al.*, 1998], in tropical

---

<sup>1</sup>mixing along isentropic surfaces

cyclones [Baray *et al.*, 1999] or in the vicinity of the subtropical jet [Zachariasse *et al.*, 2001].

Of great importance for this work is the transport of air masses across the extra-tropical tropopause, which directly influences the composition of the LMS. Isentropic exchange across the extra-tropical tropopause is of similar magnitude as the flow induced by the Brewer-Dobson circulation there [Stohl *et al.*, 2003b]. Additionally, STE can occur through vertical transport in convective systems. Even though this direct exchange of tropospheric and stratospheric air masses across the extra-tropical tropopause does not influence the composition of the overworld, it is important especially for the chemistry of the upper troposphere and lower stratosphere (UT/LS).

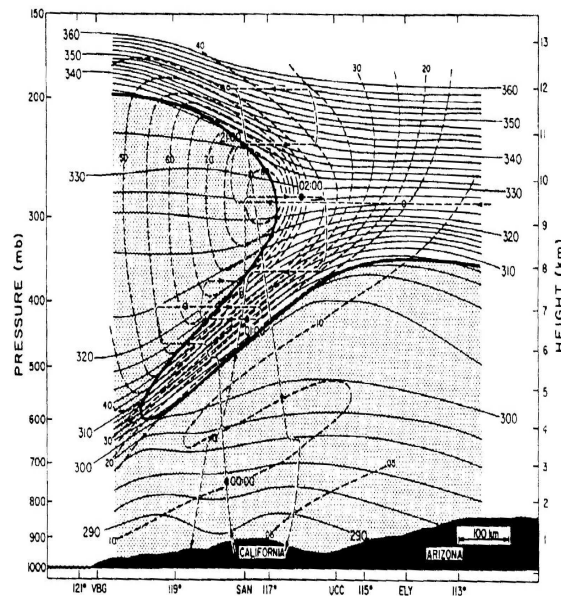


Figure 1.3: Cross section through a tropopause fold; taken from Shapiro [1980].

## Tropopause folds

Since the high PV gradient at the tropopause usually hinders transport across the tropopause, isentropic exchange mainly happens in regions where the tropopause is distorted or interrupted. A very extensive vertical deformation of the tropopause deep into the troposphere is called a tropopause fold [Shapiro, 1980]. A cross section through such a fold is displayed in Figure 1.3. When tropopause folds stretch to finer scales and finally dissolve in the troposphere, stratospheric air is mixed irreversibly into the troposphere. Tropopause folding in the mid latitudes is considered to be the most important process to transport stratospheric ozone to the upper troposphere. Tropopause folds occur in regions of high baroclinic instability.



## Frontal zones

Frontal zones like the polar front or the subtropical front are characterized by high baroclinic instability. Connected with these frontal zones are the jets — regions of wind speed maximum — where the tropopause is bent or broken. STE has been observed in connection with tropopause breaks and even across the jets. *Dethof et al.* [2000] described transport of tropospheric air into the stratosphere close to the subtropical jet even up to potential temperatures of about 360 K in summertime.

## Cyclogenesis, Cut-off lows and streamers

Baroclinic instability also leads to cyclogenesis. In the development of a cyclone, the tropopause is deformed [*Hoerling et al.*, 1991] and intensified [*Wirth*, 2003] allowing irreversible adiabatic mixing of stratospheric and tropospheric air.

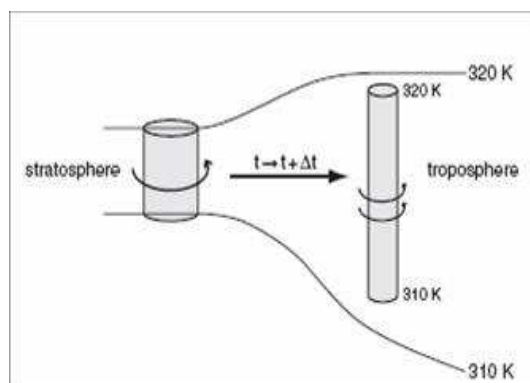


*Figure 1.4:* Scheme of the formation of a cut-off low: stretching of air column and increase of its vorticity in an area of low static stability; taken from *Delden & Neggers* [2003].

Along the region of the polar jet stream, wave processes in the vicinity of the tropopause cause latitudinal displacements of the tropopause, characterized by equatorward anomalies of high PV (and poleward anomalies of low PV). This is connected with transport of cold polar air masses to lower latitudes and warm rising air from the subtropics and tropics to higher latitudes. These displacements can be stretched into long filaments — streamers — or they can roll up to form cut-off cyclones (or cut-off lows). Cut-off lows form in an area of vertically diverging isentropes as depicted in Figure 1.4. The lower static stability of the environment (smaller vertical isentropic gradient) is balanced by the stretching of the air column and an increase of vorticity [*Delden & Neggers*, 2003]. When cut-off lows or streamers finally dissolve, tropospheric and stratospheric air masses are mixed [*Appenzeller & Davies*, 1996; *Gouget et al.*, 2000]. *Vaughan & Timmis* [1998] concluded that, associated with a streamer formation, tropospheric air was transported quasi-isentropically into the LMS between 360K and 390 K. During the development of a cut-off low tropopause folding can be observed as well.

The development of such a cut-off low system was observed over Europe in July 2002. The meteorological situation is displayed in Figures E.1 to E.3 in the attachment. The state of mixing in the LMS region during that event is assessed in Chapter 4.

### Warm conveyor belts

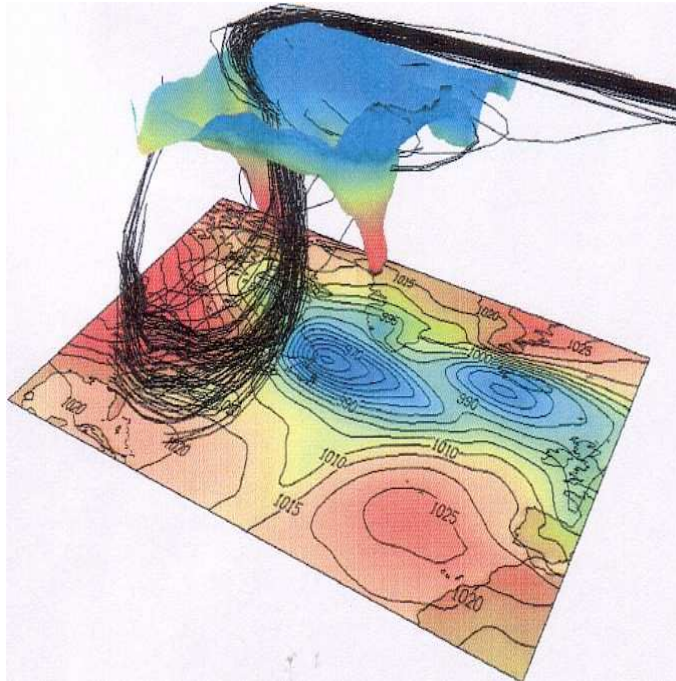


Figure 1.5: Illustration of a deep exchange event in a warm conveyor belt; taken from *Stohl et al. [2003b]*.

A highly important process to provide strong STE in the mid latitudes is assumed to be connected to warm conveyor belts [*Stohl, 2001; Wernli & Bourqui, 2002*], i.e. moist airstreams ahead of the cold fronts of extra-tropical cyclones. Diabatic heating by latent heat release [*Wernli & Davies, 1997*] leads to rising of air masses and a fast transfer (few days) of low tropospheric air masses into the stratosphere (illustrated in Figure 1.5). This deep TST [*Wernli & Bourqui, 2002*] is confined to the mid-latitude regions of baroclinic wave activity. The main source regions correspond to the storm track entry regions close to the Asian and North American east coasts, where warm conveyor belts frequently occur.

### Convective STE

Mesoscale convective systems and thunderstorms diabatically transport air masses from the surface to the tropopause region. In case of intensive convection, the

tropopause is deformed. Even tropopause breaks can occur above convective systems. In diabatic processes, mixing into the stratosphere is possible [Poulida *et al.*, 1996; Jost *et al.*, 2004]. Since STE in thunderstorms happens very locally in the mid to high latitudes and only influences the lowest region of the LMS, it is negligible compared to other STE processes. In any case, it provides very fast transport of tracers from the ground to the stratosphere. Thus, it is important for the transport of short-lived tropospheric trace gases like  $NO_x$  into the stratosphere [Lange, 2001].

### 1.3.3 Seasonal changes in transport

The chemical composition of the LMS depends on the strength and variability of the transport processes introduced above. STE processes are periodically occurring events, associated with synoptic and mesoscale processes, and do not have a constant influence on the LMS. The diabatic descent of stratospheric air from the overworld into the LMS is present all year long but is strongest during winter to spring time, when planetary wave activity is strongest (section 1.3.1). Ray *et al.* [1999] found 80% of the air masses in the mid-latitude LMS to be of stratospheric origin in late spring (see Figure 1.6). Little quasi-isentropic transport across the tropopause above 340 K was detected by Chen [1995] during wintertime when the subtropical jet is strong. Nevertheless, Vaughan & Timmis [1998] found tropospheric air masses in the wintertime LMS even up to 390 K associated with breaking Rossby waves. According to Wernli & Bourqui [2002] deep exchange events associated with the storm track regions are strongest during winter.

During late summer and fall, when the downwelling from the middle stratosphere is weak (see Figure 1.6), STE can be the dominant process to determine the composition of the LMS [Ray *et al.*, 1999; Dethof *et al.*, 2000]; significant tropospheric influence in the mid-latitude LMS has been observed by Kritz *et al.* [1991], Dessler *et al.* [1995] and Hintsa *et al.* [1998].

However, no matter how strong the STE processes are, due to the vertical stability of the stratosphere, the tropospheric influence cannot penetrate deeper into the stratosphere and is mixed with the downwelling air from the overworld. Thus, tropospheric influence can mainly be detected in the so called mixing zone, a layer above the local tropopause with a thickness up to 20-30 K [Fischer *et al.*, 2001; Hoor *et al.*, 2004]. The vertical extent of this mixing layer depends on the strength of the transport processes between the troposphere and stratosphere and varies with the seasonal change of dynamics. In the high-latitude winter, the formation of the polar vortex is an additional factor which has to be considered when examining transport into the LMS, since it is a region of strong descent.

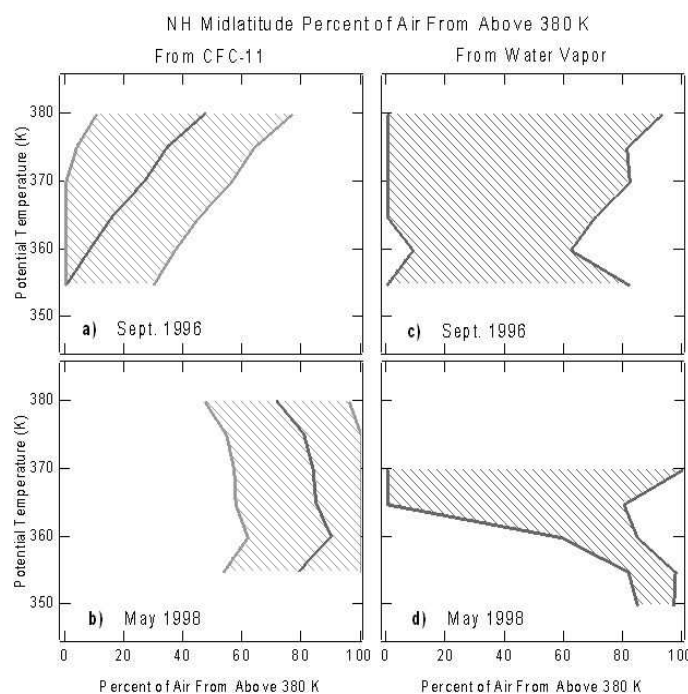


*Figure 1.6:* The percentage of air coming from the stratosphere above 380 K plotted against the potential temperature. The results were derived from northern mid-latitude CFC-11 (a, b) and water vapour (c, d) measurements and are given for September and May 1996. Solid lines in a and b mark the average values and dashed lines the range of uncertainty; taken from *Ray et al.* [1999].

## 1.4 Studying transport into the LMS

Considering the importance of the chemical and dynamical condition of the LMS and tropopause region for the Earth's climate, it is of high interest to study and understand transport processes into the LMS. To achieve this, different methods are applied reaching from modelling to in-situ and remote sensing measurements.

Eulerian general circulation models (GCMs) based on the hydrodynamic equations of motion allow to study the physics and dynamics of transport processes in the remote region of the stratosphere. The trajectories of single air parcels can be studied when Lagrangian transport models are applied. This allows e.g. the simulation of exchange processes across boundary layers (like the tropopause). Chemical transport models (CTMs) are based on Eulerian or Lagrangian Transport Models. Here, chemical reactions, transport and mixing processes are included and it is possible to study the chemical composition of the atmosphere. The application of global models is usually limited to synoptic scale; models at mesoscale resolution exist for limited regions of the atmosphere. For the validation and initialization of models, measurements of meteorological and chemical parameters are an elementary requirement.

For the investigation of dynamics and transport processes even down to small scales, the measurement of chemical constituents is indispensable. In the past, measurements of long-lived trace gases have proven to be a useful tool for studying the transport and dynamics of the atmosphere. In the next sections, some general aspects of the use of trace gases and their measurements are given.

### 1.4.1 Using tracer measurements to study transport processes in the atmosphere

If the lifetime of a gas is longer than the time scale of the transport processes acting on it, its distribution is mainly determined by dynamics. Such gases are called long-lived trace gases or tracers. In the stratosphere, the correlation between two long-lived tracers (“tracer-tracer correlation”) turns out to be very compact [Plumb & Ko, 1992]. The form and curvature of the correlation depends on the lifetimes and transport processes. Different regions may exhibit different correlation curves between tracers. Variations from these correlations are caused by mixing between the regions or by chemical processes (Figure 1.7).

Another concept useful for the study of stratospheric transport is the “age” of a tracer [Kida, 1983]. The “age”-concept assumes that an observed air mass is composed of infinitesimally small single air parcels which travelled on unique pathways from the entry point — the tropical tropopause — to the point of observation. Therefore, the observed air mass exhibits a spectrum of small air parcels with different ages depending on the individual transit times.

Tracer-tracer correlations (e.g. Boering *et al.* [1994]; Volk *et al.* [1997, 1996]; Plumb *et al.* [2000]; Plumb [2002]; Hoor *et al.* [2002]) as well as the age concept (e.g. Hall & Plumb [1994]; Schmidt & Khedim [1991]; Volk *et al.* [1997]; Harnisch *et al.* [1999]; Strunk [1999]) have been successfully used to study stratospheric dynamics.

A further approach for studying stratospheric transport is the use of mass balance calculations. In order to estimate transport into the northern mid-latitude LMS, Ray *et al.* [1999] used a simple mass-balance calculation. They derived fractions of air coming from above 380 K and across the tropopause from balloon profiles as displayed in Figure 1.6.

### 1.4.2 Tracer measurements in the LMS region

Due to the remote location of the LMS above the tropopause, it is difficult to gather data on its physical and chemical condition. Different methods have been developed to gather data either by in-situ or remote sensing instruments.

A well-established method is the whole air sampling (e.g. by a cryo-sampler [Schmidt *et al.*, 1987]); the sampled air is analysed subsequently in the laboratory. With fully automated instruments it is also possible to analyse the air in-situ during the flight (e.g. LACE, ACATS, GhOST, HAGAR which all apply gas chromatography). But in-situ measurements on board of high flying stratospheric balloons

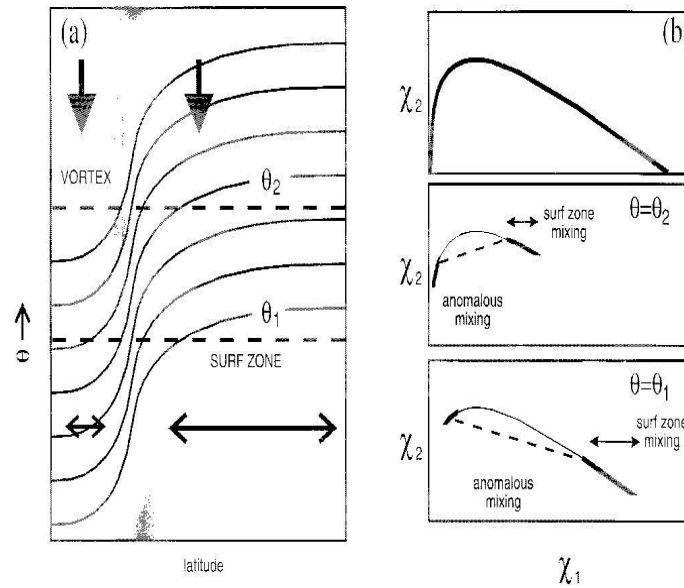


*Figure 1.7:* a) Tracer isopleths in the wintertime stratosphere. Due to the more pronounced descent in the vortex, strong tracer gradients develop at the vortex edge (shaded in grey). b) Tracer-tracer correlations for two long-lived tracers for different mixing characteristics. Tracer 1 is assumed to be a tropospheric source gas, tracer 2 a stratospheric source gas. As long as no mixing between the two regions occurs, the correlation between the two tracers  $\chi_1$  and  $\chi_2$  follows the one in the top panel. The lower plates show anomalous mixing across the vortex edge at the potential temperatures  $\theta_1$  and  $\theta_2$ . This mixing causes the formation of mixing lines in the tracer-tracer correlation; taken from *Plumb et al.* [2000].

(reaching up to 35 km) or high-altitude aircraft (up to 21 km) are limited in space and time. The full extent and the seasonal and spatial variability of the LMS can hardly be captured considering the variety of transport processes which influence the LMS spanning several scales in space and time.

The coverage can be much improved when using satellite measurements, which cover the Earth's atmosphere in a short period of time. Remote sensing techniques are based on the ability of the atmosphere to absorb or emit radiation (either short- or long-wave). This absorption or emission depends on the type and abundance of chemical constituents in the atmosphere. Unfortunately, the uncertainty of satellite measurements is still too high<sup>2</sup> and the spatial resolution is too low to observe all of the transport processes introduced above.

Thus, although only available in limited regions and times, high-precision in-

<sup>2</sup>larger than several per cent especially in the lower part of the atmosphere

situ measurements are generally preferred when studying the LMS and tropopause region.

## 1.5 Quantifying transport into the LMS — Outline of this thesis

This thesis is based on the measurements of the high-precision in-situ instrument HAGAR (High Altitude Gas Analyser) which measures several long-lived trace gases and which will be introduced in detail in Chapter 2. The measurements were performed during four measurement campaigns on board of the high altitude aircraft M55 Geophysica (see Figure 2.12). Two of the campaigns (see section 2.3) took place in the mid-latitude region in July and October 2002 and the other two were performed in the northern high latitudes from January to March 2003.

Since one of the main objectives during these campaigns was the validation of tracer measurements provided by instruments on board the ENVISAT satellite, it was necessary to upgrade HAGAR to measure  $\text{CH}_4$ , which is one of the molecules measured from the satellite. Thus, it was the main experimental part of this thesis to implement a new gas chromatographic channel measuring  $\text{CH}_4$ , which is described in detail in section 2.2. During the course of this thesis,  $\text{CH}_4$  developed to be of high value for the quantification of tracer transport into the LMS.

In order to estimate transport into the Arctic LMS, a simple mass balance calculation is presented using the in-situ Geophysica data from the campaigns mentioned above (Chapter 2). The approach is similar to the one used by *Ray et al.* [1999] who focussed on the northern mid-latitude LMS and inferred the fractions of air coming from above 380 K and across the tropopause from balloon profiles as displayed in Figure 1.6. In the analysis presented in Chapter 3 an additional, separate pathway into the lowermost stratosphere is considered: the transport through the bottom of the polar vortex (around 400 K), which exhibits mixing ratios distinctly different from extra-vortex stratospheric air. Thus, the fractions of air originating from each of the three regions (vortex, high-latitude stratosphere, and troposphere/subtropics) are derived for the high-latitude LMS from in situ observations of  $\text{N}_2\text{O}$ , CFC-11, H-1211,  $\text{CH}_4$ ,  $\text{O}_3$  and  $\text{H}_2\text{O}$ .

Beside the mass balance study, the available data allow the analysis of the phenomenology of single transport processes. Thus, in Chapter 4 mid-latitude data are used to study transport and mixing linked to a cut-off low system that was observed during July 2002.

Finally, a summary will be given in Chapter 5.





# Chapter 2

## Measurements

The measurements in this chapter were performed with the **High Altitude Gas Analyser** (HAGAR) on board the high-altitude aircraft M55 Geophysica during four field campaigns in the northern mid and high latitudes. In the following sections an overview will be given concerning the instrument, the data processing and the specific extensions to HAGAR made during the course of this thesis. Thereafter, the measurement campaigns will be described.

### 2.1 The High Altitude Gas Analyser: A general description

HAGAR is a two-channel in-situ gas chromatograph (GC) combined with a CO<sub>2</sub> sensor (LI-COR 6251). The instrument was built at the Institute for Meteorology and Geophysics (now Institute for Atmosphere and Environment) at the University of Frankfurt (*Riediger* [2000]; *Strunk* [1999]). In the two GC-channels with electron capture detectors (ECD) N<sub>2</sub>O, CFC-12 (CCl<sub>2</sub>F<sub>2</sub>), CFC-11 (CCl<sub>3</sub>F), H-1211 (CBrClF<sub>2</sub>), CH<sub>4</sub>, SF<sub>6</sub>, and H<sub>2</sub> are measured with a temporal resolution of 90 s. CO<sub>2</sub> is measured with a LI-COR 6251 CO<sub>2</sub>-analyser achieving a resolution of 10 s using non-dispersive infrared absorption (NDIR).

Both instruments (GC and LI-COR 6251) are mounted in a pressurized and temperature controlled vessel. Air is pumped through a stream selection valve (SSV) inside the vessel via two parallel running membrane pumps. The SSV is also connected to two calibration gases (CAL and SPAN) and the GC-carrier gas (used as a “blank” probe). For system checks the calibration gas (CAL) and the carrier gas can also be flushed through the pump (“CAL to pump” and “blank to pump”) before entering the SSV. Depending on the valve position one of the three gases or the sample air is flushed into the LI-COR 6251 and the GC, where it is measured. The whole system is controlled by an onboard computer (industrial PC; AT69 ) and can be configured and run fully automatically by a specially developed control software written in C [*Riediger*, 2000]. GC and LI-COR 6251 signals are read out by inte-

grating analogue-digital conversion cards (ADC3, EXXACT) with 16 bit resolution. Data are stored on a PCMCIA flash card and downloaded via ethernet or serial connection (RS232) to a remote computer after a flight. The whole device is about 55 cm x 45 cm diameter and weighs 55 kg (75 kg including a mounting skid and three gas bottles). In Figure 2.1, the schematics are shown. HAGAR can be integrated both on research balloons and high altitude aircraft. The M55 Geophysica, a Russian high altitude aircraft (2.3.1), served as the platform for the stratospheric measurements shown here.

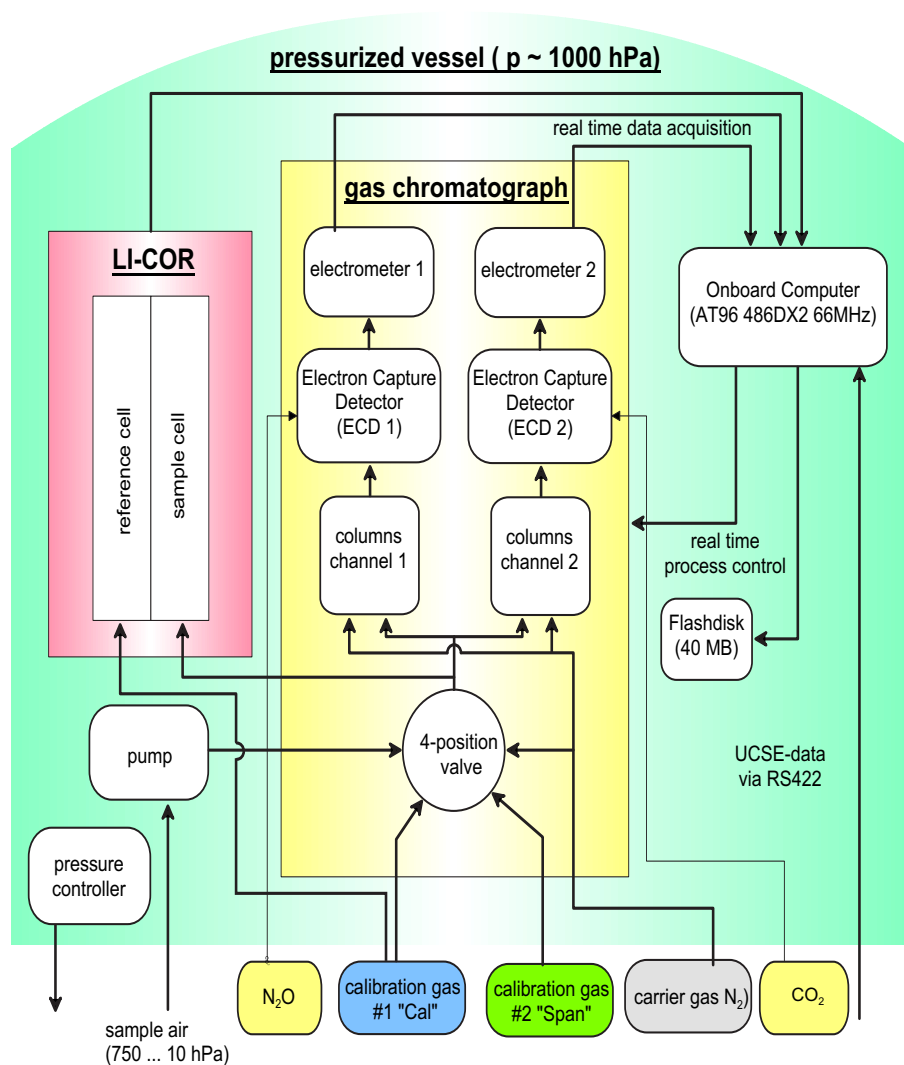


Figure 2.1: Principle scheme of the HAGAR instrument.

### 2.1.1 The GC-ECD-System

Chromatography uses the different absorption, adsorption and desorption characteristics of molecules to separate them from each other. In gas chromatography, a sample gas is injected into a carrier gas stream, the mobile phase. Carried by the mobile phase, the sample flows through a stationary phase — the separation column. There the sample gas is separated into its components depending on the strength of absorption and adsorption of each component on the stationary phase and the desorption to the mobile phase. The retention times of the components are controlled by the choice of the carrier gas, the length, diameter and material of the columns, the carrier gas flow through the columns and the column temperature. After the separation, the components are flushed into the detector unit, in this case an electron capture detector (ECD). An ECD records the effect of electronegative molecules on the concentration of electrons in the carrier gas. Inside the detector, the carrier gas is ionized by beta radiation<sup>1</sup>. The generated electrons are collected by the detector anode when a voltage pulse is applied to the electrodes. These electrons can be captured by electronegative molecules. In the presence of such electronegative molecules (e.g. halogens) in the carrier gas, the detector anode will record a decrease of electron current. This decrease is a measure of the amount of the electronegative molecules, hence of their concentration or mixing ratio in the analysed air sample. An electronic control device of the ECD, the electrometer, keeps the mean current (reference current  $I_{ref}$ ) constant by varying the frequency of the voltage pulses as the charge collected per pulse changes. This pulse frequency (converted to a voltage) is used as detector signal. The detector signal as a function of time following an injection is called a chromatogram. The passing of a component is recognized as a peak in the chromatogram. The area below the peak or the peak height is proportional to the mixing ratio of a molecule (see 2.1.1).

In laboratory conditions the time resolution of a gas chromatograph is of minor interest. The retention times can vary from seconds to several minutes. But carrying out these measurements in situ on board an aircraft travelling at high speed, the temporal resolution of these high-precision measurements comes into the focus of interest. The design of HAGAR was based on the experience with existing in-situ GCs like ACATS [Elkins *et al.*, 1996], GHOST [Bujok *et al.*, 1996] and LACE [Moore *et al.*, 1997]. The following section gives a brief overview of the HAGAR gas chromatograph. For further details see Riediger [2000] or Strunk [1999].

#### The HAGAR-GC

In Figure 2.2, the plumbing diagram of HAGAR is shown. The GC unit has two parallel channels. The first channel originally measured only SF<sub>6</sub> [Strunk, 1999] and was upgraded in the course of this thesis to also measure CH<sub>4</sub> and H<sub>2</sub> (see 2.2). The second channel measures N<sub>2</sub>O, CFC-12, CFC-11 and H-1211.

---

<sup>1</sup>radiation source is a Ni63 foil

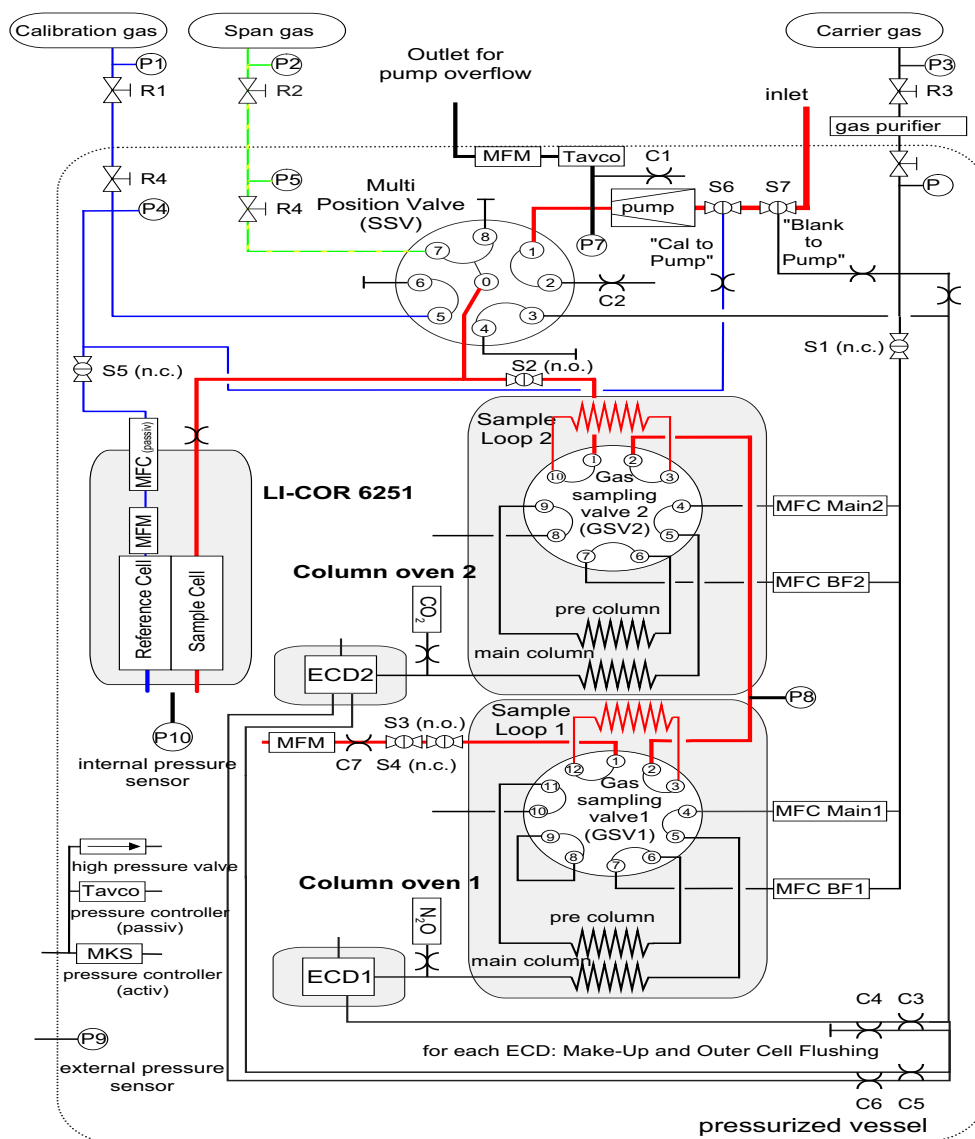


Figure 2.2: The plumbing diagram of HAGAR. The carrier gas line is marked in black, CAL gas line in blue, SPAN gas lines in green/yellow and the sample line in red. The pressurized vessel is marked by a dotted out line.

Each channel consists of a column oven including a sample loop, a pre- and a main column connected to a gas sampling valve (GSV) and an ECD. The columns are 1/8" stainless steel tubings packed with different column materials and heated at different temperatures as given in Table 2.1. They are constantly flushed with the carrier gas (nitrogen 5.0<sup>2</sup>) controlled by mass flow controllers for each column. Any contamination of the carrier gas would lead to increased noise levels and decreased sensitivity of the ECD signals. Therefore, before entering the HAGAR system, the

<sup>2</sup>N<sub>2</sub> with high purity of  $\geq 99,999\%$

Parameter	Channel I	Channel II
Species and retention times	SF <sub>6</sub> ; $t_{ret} = 16$ s H <sub>2</sub> ; $t_{ret} = 19$ s CH <sub>4</sub> ; $t_{ret} = 61$ s	N <sub>2</sub> O; $t_{ret} = 48$ s CFC-12; $t_{ret} = 60$ s Halon-1211; $t_{ret} = 78$ s CFC-11; $t_{ret} = 109$ s
Temperature	82°C <sup>5</sup>	91°C
sample loop	2ml <sup>6</sup>	2ml
<b>Pre column:</b>		
Material	Molecular Sieve 5Å <sup>7</sup> , 60/80 mesh	Porasil C, n-octane, 80/100 mesh
Length	0.7 m	0.8 m
Inner diameter	2.38 mm	2.38 mm
<b>Main column:</b>		
Material	Molecular Sieve 5Å 60/80 mesh	Porasil C, n-octane, 80/100 mesh
Length	1.50 m <sup>8</sup>	1.80 m
Inner diameter	2.38 mm	2.38 mm
ECD	Shimadzu	Siemens
ECD temperature	350°C	350°C
Dop. gas mixing ratio	~ 50 ppm N <sub>2</sub> O	~ 200 ppm CO <sub>2</sub>

Table 2.1: Characteristics of the HAGAR GC.

nitrogen is purified by molecular sieve<sup>3</sup>13Å, activated carbon, a moisture/oxygen trap (OT3-2) and a trap for the removal of CO and H<sub>2</sub> (sofnocat<sup>4</sup>).

The GSVs can be switched between two positions [*Strunk*, 1999]: In the load position, the sample loop is flushed with gas coming from the SSV. The delay time between the inlet to the sample loop is less than 15 s at the lowest pump flows [*Volk & Baehr*, 2004]. In the inject position, the sample loop is injected into the carrier gas flow and the air sample thus flushed through the pre- and main columns. This sample is an average of 2-3 s sampling time.

Switching between these two positions and active control of the carrier gas flow through the columns allows a fast gas chromatography in 90 s [*Moore et al.*, 2003]. The carrier gas transports the separated components of the sample to the ECD

<sup>3</sup>aluminium silicon oxide

<sup>4</sup>trade name for a combination of platinum, palladium and tin oxide

<sup>5</sup>after the flight on October 14, 2002; before 50°C

<sup>6</sup>July 2002: 1ml

<sup>7</sup>July 2002: 2 m Unibeads 1S 80/100 mesh

<sup>8</sup>July 2002: 0.7 m

where the components are detected. The detection signal — the chromatogram — is stored on the onboard computer at the end of every chromatographic cycle [Riediger, 2000].

In Figures 2.3 and 2.4 typical chromatograms of both channels are shown. The GSV was switched to the inject position at 50 s in the chromatogram cycle. The retention times listed in Table 2.1 are given relative to the time of injection.

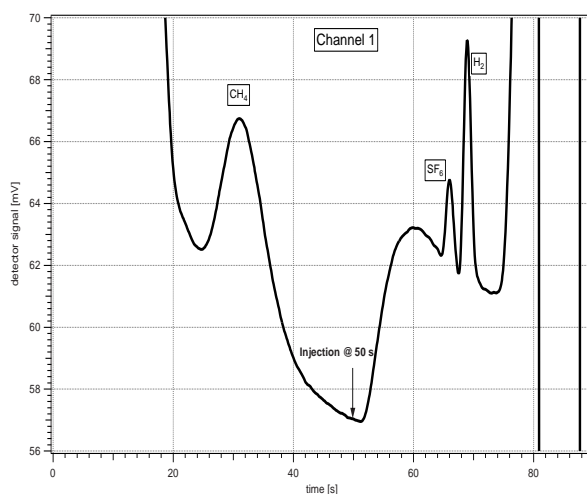


Figure 2.3: Channel I chromatogram with SF<sub>6</sub> (retention time after injection: 16 s), H<sub>2</sub> (19 s) and CH<sub>4</sub> (61 s).

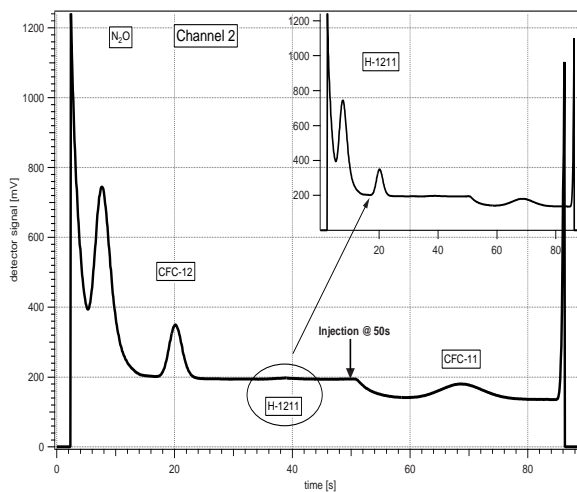


Figure 2.4: Channel II chromatogram with N<sub>2</sub>O (retention time after injection: 48 s), CFC-12 (60 s), Halon-1211 (78 s) and CFC-11 (109 s).

## GC: data processing

The processing and post processing of the raw data is performed with the IGOR PRO graphing and analysis software<sup>9</sup> including the NAOHChrom analysis package developed by NOAA<sup>10</sup>, USA, which was extended and adapted to the HAGAR concept.

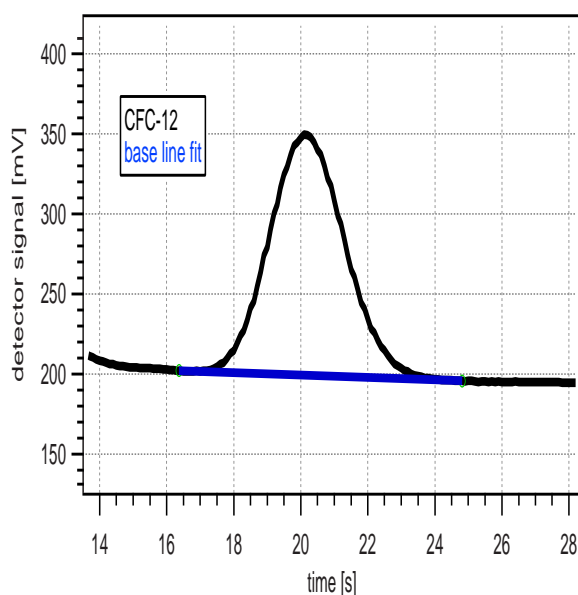


Figure 2.5: A tangent is fitted to the smoothed chromatogram. Shown is the CFC-12 peak of HAGAR channel II.

In Figure 2.5, a peak (CFC-12) is shown with a tangent baseline fitted below the peak. To minimize errors in the determination of peak height or area and the baseline fitting, the chromatograms are smoothed with a Savitzky-Golay filter (A.4). Methods for data processing are described by Volk [1996]. The tangent baseline fit was used to analyse the peaks of  $N_2O$ , CFC-12, CFC-11,  $H_2$  and  $SF_6$ .

If a peak is very small, noise and curvature of the chromatogram can lead to large errors in the peak height determination, when a smoothing filter and a simple tangent baseline fit is applied to the chromatogram. In this case the following procedure was found to provide better precision: No smoothing filter is applied and the original chromatogram is used and a Gaussian curve is fitted to the peak based on a baseline that is described by a polynomial of degree 3. In Fig. 2.6, the channel II H-1211 peak is shown with Gaussian peak fit. Mixing ratios are calculated from the peak height or area of the Gaussian peak. The Gaussian peak fitting algorithm is briefly described in Riediger [2000]. In case of the HAGAR measurements H-1211 and  $CH_4$  were analysed with the Gaussian peak fit method.

<sup>9</sup>WaveMetrics Inc.

<sup>10</sup>National Oceanic Atmospheric Administration

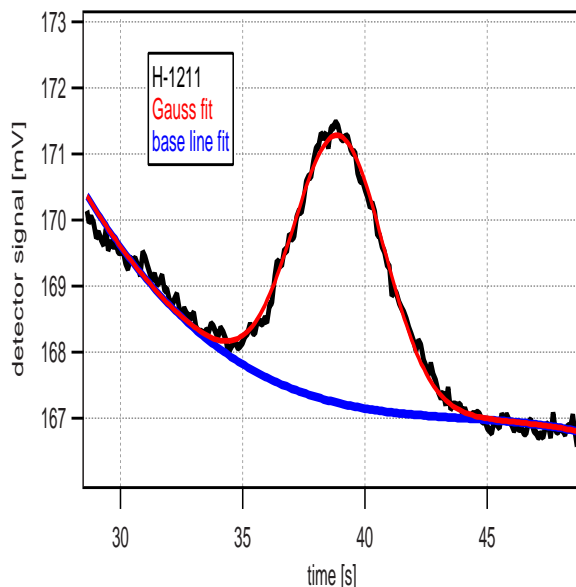


Figure 2.6: H-1211 peak in a non smoothed chromatogram. A Gaussian curve is fitted to the peak.

Independent of the method used for the peak detection, the peak area above the baseline or the peak height is normalized by the pressure of the sample at the time of injection. This pressure correction has to be carried out to take into account any changes of the amount of air in the sample loop. Since the temperature of the sample loop is kept constant (within  $0.1^{\circ}\text{C}$ ), a similar temperature correction is not necessary. The resulting normalized peak height or area  $R$  is called the response of the detector.

The mixing ratio of a substance is a function of the detector response. This detector response function  $f(R)$  is not necessarily linear for all substances and has to be described by a polynomial of at least second order. In Figure 2.7 the detector response curves for  $\text{CH}_4$  are plotted. In this specific case the detector response diverts only slightly from a linear function (red curve) The real detector response curve (blue) is determined in laboratory Calibration experiments by measuring a series of standard gases covering the whole range of mixing ratios from the tropospheric background to zero. The procedure for such a calibration experiment is described in *Riediger* [2000].

Although the laboratory calibrations are performed using the same chromatographic parameters as in flight, differences between the detector response during the flight and the calibration experiment can occur due to small changes in the GC-System affecting the shape of the peaks or the baseline (e.g. temperature, pressure, carrier gas purity; see also section 2.2). To better constrain  $f(R)$  for measurements made during flights, two calibration gases are measured alternating every 5 injections. The response function determined in the laboratory calibration is adjusted to



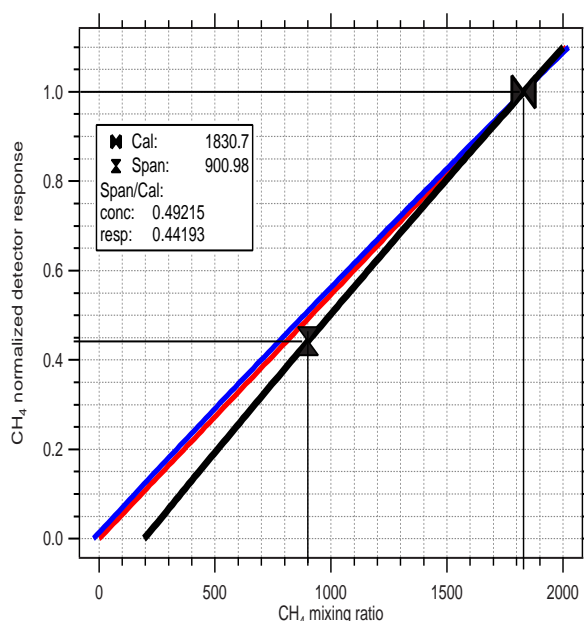


*Figure 2.7:* The detector response (relative to the CAL response) as a function of the mixing ratio for  $\text{CH}_4$ . The red line marks the hypothetical linear detector response, the detector response determined by the lab calibration is marked in blue and the response function used during the flight is marked in black. The CAL and SPAN gas measurements during the flight are highlighted by black markers.

the in flight measurements of both calibration gases (see Figure 2.7, black curve) so that any changes or drifts of the detector response are corrected.

In case of the HAGAR measurements, the two calibration gases are the CAL gas with tropospheric background values and the SPAN gas with typically mixing ratios of 50-60% of tropospheric background values. In case of air samples reaching values much below those of the SPAN (this can happen for e.g. CFC-11, H-1211 in the polar stratosphere) the response curve is forced through zero ( $f(0) = 0$ ).

Consequently, the responses of both calibration gases are used to calculate the air mixing ratios. Thus mixing ratio  $\chi$  is a function of the responses of the CAL and SPAN measurements and the response of the measurement itself.

$$\chi = f(R_{CAL}, R_{SPAN}, R) \quad (2.1)$$

In equation 2.1  $R_{CAL}$  ( $R_{SPAN}$ ) is an interpolation of the closest two CAL (SPAN) measurements to the current air injection.

### Error of the GC measurements

A continuous control of the instrument performance is achieved using the measurements of the two calibration gases (see Appendix C.4) at regular intervals during

the flights. The mean precision is in general better than 1% of the respective tropospheric background level for N<sub>2</sub>O, CFC-12, CFC-11, CH<sub>4</sub> and normally better than 2% for H<sub>2</sub> and SF<sub>6</sub> and better than 3% for H-1211 .

Appendix C.5 describes how the precision of a single measurement is calculated using the local error of the CAL and SPAN measurements. The mean precision for each flight is shown in Tables C.3 and C.4 in the appendix.

The precision only describes the statistical error of the measurement due to random fluctuations of the instrument. For the total error of the measurements the error of the calibration gases has to be regarded in addition. The values of the calibration gases (see Appendix C.4) are based on the CMDL<sup>11</sup>ALM standard (CMDL scale). The error of this standard gas is given as 1% for all molecules measured by the GC.

### 2.1.2 CO<sub>2</sub> measurements with the LI-COR-6251

The method used to measure CO<sub>2</sub> is non-dispersive infrared absorption (NDIR). Infrared (IR) radiation passing through a gas is absorbed by IR absorbing molecules like CO<sub>2</sub>. When looking only at the 4.26 micron absorption band of CO<sub>2</sub> (using a bandpass optical filter at 150 nm) the absorption is a measure of only the CO<sub>2</sub> and the H<sub>2</sub>O mixing ratios in the gas. Absorption by other molecules is negligible. The LI-COR 6251 instrument measures the difference in absorption between a cell flushed with a gas with known CO<sub>2</sub> mixing ratio (reference cell) and a cell flushed with gas of unknown mixing ratio (sample cell). The absorption by water molecules can be neglected for stratospheric conditions (mixing ratio < 100 ppm).

In absolute mode, the reference cell of the LI-COR 6251 is flushed with a zero gas (CO<sub>2</sub> mixing ratio equals zero). For a small range of CO<sub>2</sub> mixing ratios (as occurring in the atmosphere) higher accuracy is achieved in differential mode, where the reference gas has a CO<sub>2</sub> concentration close to the one in the measured air. This increases the analyser sensitivity by increasing its gain [*LI-COR*, 1992] and makes the measurements less sensitive to pressure variations.

#### The HAGAR LI-COR

A simple scheme of the LI-COR 6251 is shown in the plumbing diagram (Figure 2.2). Operated parallel to the GC, the sample cell of the LI-COR 6251 is supplied by sample gas coming from the SSV. For the LI-COR 6251, the delay time between inlet and sample cell is about 10 s at the lowest occurring pump flows (during Forli campaigns about 15 s due to less sample flow, see also sections 2.3.2 and 2.3.3). The reference cell is continuously flushed with CAL gas at a constant flow rate of 30 ml/min controlled by a passive mass flow controller. The flow through the sample cell is normally controlled with an active mass flow controller (MFC). Due

---

<sup>11</sup>Climate Monitoring Diagnostics Laboratory

to problems (described in section 2.3.2) it was only roughly controlled by a restrictor from July 2002 to March 2003 and the flow varied in a range of 100 - 400 ml/min.

The continuously provided LI-COR 6251 raw signal has a time resolution of 5 Hz (*Riediger* [2000], *Exact* [1998]). The final data are a 10 s average, corresponding to the actual time resolution determined by the flushing time of the sample cell at a typical sample flow of 140 ml/min [*Riediger*, 2000]. Like the chromatograms, the LI-COR 6251 signal is stored at the end of every chromatographic cycle.

### CO<sub>2</sub>: data processing

The calculation of the CO<sub>2</sub> concentration from the LI-COR 6251 voltage signal is performed using self-written macros in the IGOR PRO software [*Riediger*, 2000]. The analysis is based on the following basic equations:

The relation between the CO<sub>2</sub> mixing ratio  $\chi$  in the sample cell and the voltage output  $V$  is given by a third order polynomial function  $F(V) = a_1 + a_2V^2 + a_3V^3$  [*LI-COR*, 1992]. The coefficients  $a_i$  are determined in a factory calibration at the temperature  $T_o$  and the pressure  $p_o$ . This relationship has to be corrected for temperature  $t$  and pressure  $p$  changes relative to  $T_o$  and  $p_o$ . The equation to determine the CO<sub>2</sub> mixing ratio in the differential mode is

$$\chi = F[(V_\chi G) + V_r] \frac{p_o}{p} \frac{T}{T_o}. \quad (2.2)$$

At non-zero CO<sub>2</sub> concentration in the reference cell, the gain of the detector changes with the factor  $G = (1 - V_r/K)$  with the constant  $K$ , given by the factory calibration.  $V_r$  is the voltage signal of the reference gas if measured in absolute mode. It can be calculated by Newton iteration [*Bronstein et al.*, 1993] from

$$V_r = F^{-1}[\chi_r \frac{T_o}{T}] \frac{p}{p_o}. \quad (2.3)$$

Changes in temperature lead to a zero drift of the instrument and pressure changes influence the gain of the detector [*LI-COR*, 1992]. Neither temperature nor pressure are actually measured in the cell. Rather, the zero drift is directly corrected from the CAL gas measurements (as a zero reference) and the gain change is directly corrected from the SPAN and CAL gas measurements [*Riediger*, 2000].

### Error of the CO<sub>2</sub> measurements

The mean precision for the CO<sub>2</sub> measurements is better than 0.1 % of its tropospheric background level (371 ppm, value of the CAL gas). Mean precisions for each flight are listed in section C.7. Two main factors influence the precision of the CO<sub>2</sub> measurements: the high frequency noise of the instrument and a low frequency variation due to pressure changes (that can be derived from the SPAN measurements). A more detailed description of the precision calculation is given in Appendix C.6.

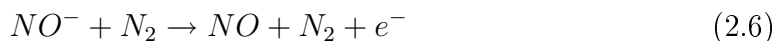
The CO<sub>2</sub> values of the HAGAR calibration gases were derived from an intercalibration with CO<sub>2</sub> standard gases from the Umweltbundesamt (UBA). These standards are based on the Scripps Institution for Oceanography (SIO) scale (Scripps scale) which is shifted by 0.2 ppm to the CMDL scale (*Andrews et al.* [1999]). This has to be considered when comparing the HAGAR CO<sub>2</sub> measurements to those of other instruments. The error of the UBA standard gases is 0.015 ppm [*Riediger, 2000*], well below 0.1% of the corresponding tropospheric background.

## 2.2 Development of a CH<sub>4</sub> channel for HAGAR

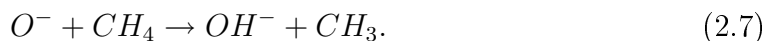
The main experimental part of this thesis was the implementation of a gas chromatographic channel measuring CH<sub>4</sub> (methane). Because of the limited space inside the instrument, no additional channel could be inserted and it was necessary to change the first gas chromatographic channel in order to measure CH<sub>4</sub>. A principal problem was the fact that CH<sub>4</sub> does not capture electrons and can thus not be easily detected by a standard ECD. However, by adding a small quantity of another reacting substance to the carrier gas, the ECD sensitivity to organic compounds can be enhanced such that CH<sub>4</sub> can be measured. This way of enhancing the ECD sensitivity is called doping. In the following sections, the doping technique and necessary changes in the gas chromatographic configuration are described.

### 2.2.1 Theory of doping

When N<sub>2</sub>O is added to the carrier gas, the N<sub>2</sub>O attaches the electrons and the following reactions take place [*Phillips et al., 1979*]:



Any substance that reacts with  $O^-$  or  $NO^-$  and forms a stable ion, interrupts the reaction cycle and reduces the amount of electrons in the detector. Thus, by adding N<sub>2</sub>O the detector is sensitized to measure substances like CH<sub>4</sub> that do not capture electrons directly. For CH<sub>4</sub> the ion reaction is



The enhancement factor of the detector response depends on the concentration of the ions,  $O^-$  and  $NO^-$ . These concentrations are controlled by the rate constants in equations 2.4 to 2.6, the N<sub>2</sub>O concentration in the carrier gas and the temperature of the detector.

## 2.2.2 Implementing the doping technique for the HAGAR instrument

### Mechanical Integration:

The doping gas is added between the column and the ECD (as seen in Figure 2.2) through a restriction (crimp tubing attached to the carrier gas line with branch connection; T-piece). The doping gas concentration or mixing ratio depends on the carrier gas flow and the doping gas flow through the restriction. The latter — too small to be measured — is controlled by the doping gas pressure  $p$  and can be determined from the pressure drop across the crimp tubing (for the calculation see Appendix C.1). The doping gas pressure is controlled by a pressure reducer with an outlet pressure of maximum 7 bar. The doping gas reservoir — a 40 ml stainless steel gas cylinder — is attached to the mounting skid outside the vessel.

### Optimizing the chromatography and ECD sensitivity to measure CH<sub>4</sub>:

In order to optimize the instrument to measure CH<sub>4</sub>, several parameters had to be tested which influence chromatography and ECD sensitivity. The parameters are listed in the following. For all these experiments, the works of *Moore et al.* [2003], *Elkins et al.* [1996] and *Phillips et al.* [1979] have been of high value. The final configuration of the chromatograph can be seen in Table 2.1.

- The ECD temperature is one factor that changes the sensitivity of the ECD. Highest sensitivities to CH<sub>4</sub> are reached when the ECD is operated at the highest possible temperature (laboratory tests). This is due to the dependence of the rate constant of reaction 2.4 on temperature [*Phillips et al.*, 1979]. The maximum operation temperature of an ECD depends on the model and is 350°C for the ECDs used here.
- The doping gas concentration — a measure of carrier gas and doping gas flow (doping gas pressure) — largely determines the sensitivity of the ECD to CH<sub>4</sub>. In the laboratory different N<sub>2</sub>O mixing ratios were tested and the signal to noise ratio was determined for the CH<sub>4</sub> peak. In the tests the doping gas pressure and carrier gas flow were varied and crimp tubings with different restrictions were used.

The amount of N<sub>2</sub>O needed to obtain maximum enhancement factors for the detection of CH<sub>4</sub> is about 10-20 ppm according to *Phillips et al.* [1979]. However, the doping gas mixing ratios finally used during the campaigns were higher and will be given below.

- Along with the doping gas pressure, the reference current  $I_{ref}$  at the electrometer of the ECD has to be optimized.  $I_{ref}$  (see section 2.1.1) also affects the ECD sensitivity, as the optimum reference current depends on the electron

capturing ability of the measured species. Of course, by adding N<sub>2</sub>O the electron capturing ability of the carrier gas is heavily changed and consequently has to be adjusted.

- The carrier gas flow influences the chromatography by changing elution times of the molecules. Since the time resolution of the measurements are supposed to be high, the objective was to achieve a fast chromatography (90 s). The speed is limited by the restriction of the column system (maximum flow rate) and the quality of the chromatogram (peak broadening due to pressure). Also, the coupling with the N<sub>2</sub>O mixing ratio has to be regarded.
- Factors heavily influencing the separation of molecules are the column material, length and temperature. For the columns tested here the optimum column temperature to measure CH<sub>4</sub> was determined to be about 90°C. Since the temperature also influences the retention time, sometimes a temperature different from the optimum was used. This provided the possibility to shift the peak to the desired retention time while keeping the carrier flow (and the doping gas mixing ratio) constant. Between the tested column material this optimum temperature did not change significantly. Changes in column length and material will be described below.
- Finally, the size of the sample loop determines the amount of sample air that is injected into the chromatograph.

All of these parameters have been intensively tested in laboratory experiments. At first, the tests were performed with a special test gas containing a high amount of CH<sub>4</sub> (about 50 ppm CH<sub>4</sub> in N<sub>2</sub>; O<sub>2</sub> < 100 ppm ) to optimize the signal to noise ratio of the CH<sub>4</sub> peak. Subsequent tests were performed with standard air (CH<sub>4</sub> mixing ratio at atmospheric levels, about 1.8 ppm) and the optimized parameters. Every change in the hardware of the instrument (ECD model, columns) was followed by such an intensive test series.

### Chronology of the development

Information on the specification of the columns and the ECDs yielding satisfactory CH<sub>4</sub> sensitivity is available from literature [*Moore et al.*, 2003; *Elkins et al.*, 1996]. Nevertheless, tests were started with the original set-up of the chromatography and detection system of HAGAR in an attempt to change the instrument as little as possible.

#### 1. Set-up until December 2001:

Tests with the special test gas successfully demonstrated that it is possible to measure CH<sub>4</sub> with HAGAR (see Figure 2.8). However, the system was not sensitive enough to detect CH<sub>4</sub> at tropospheric mixing ratios ( $\sim 1.8$  ppm).

ECD	Siemens
Pre Column	0.7 m molecular sieve 5Å 80/100
Main Column	1.2 m molecular sieve 5Å 80/100
Crimp	1 sccm @ 130 bar
Sample loop	1 ml

Table 2.2: Set-up December 2001

The maximum signal to noise ratio of the CH<sub>4</sub> peak was about 300 at a CH<sub>4</sub> mixing ratio of 50 ppm in the test gas. When measuring CH<sub>4</sub> at tropospheric mixing ratios, the signal to noise ratio decreased to  $\sim 10$ . A standard air chromatogram is given in Figure 2.8. When measuring atmospheric standard air the detector signal reached saturation during the passing of the O<sub>2</sub> peak. The CH<sub>4</sub> peak was too small and therefore not detectable on the steep O<sub>2</sub> tail.

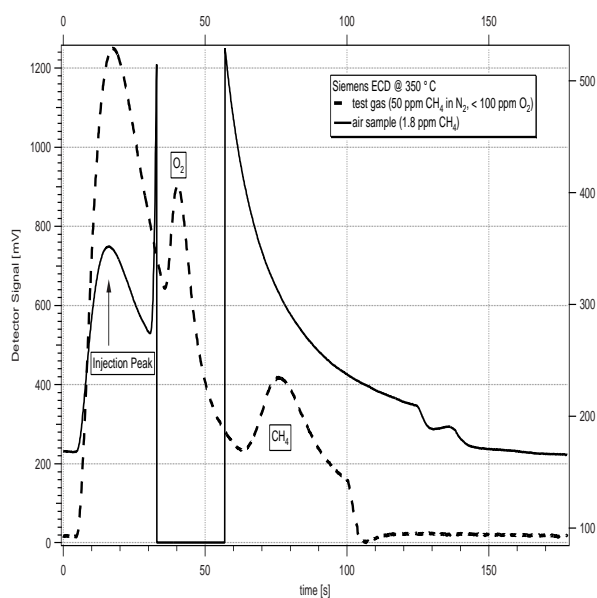


Figure 2.8: Channel I chromatogram measured with a Siemens ECD. The chromatogram of the test gas is displayed with a dashed line, the air sample chromatogram with a solid line. O<sub>2</sub> elutes at 42s, CH<sub>4</sub> at 77 s. The injection peak is a reaction of the baseline due to pressure changes in the GC - system after switching the gas sampling valve into the inject position.

In an effort to eliminate the overlapping of the O<sub>2</sub> tail with the CH<sub>4</sub> peak, the configuration of the gas sampling valve was changed. This was achieved by applying a special port configuration at the GSV (using 12 ports instead of 10) which allowed to “cut off” the O<sub>2</sub> peak and vent it into the vessel while the following CH<sub>4</sub> was flushed into the ECD. Thus, the O<sub>2</sub> peak was not detected

and the  $\text{CH}_4$  was not situated on a steep baseline. A chromatogram with an application of this so-called “heart cut” technique is displayed in Figure 2.9. But still  $\text{CH}_4$  was not detectable in a tropospheric air sample.

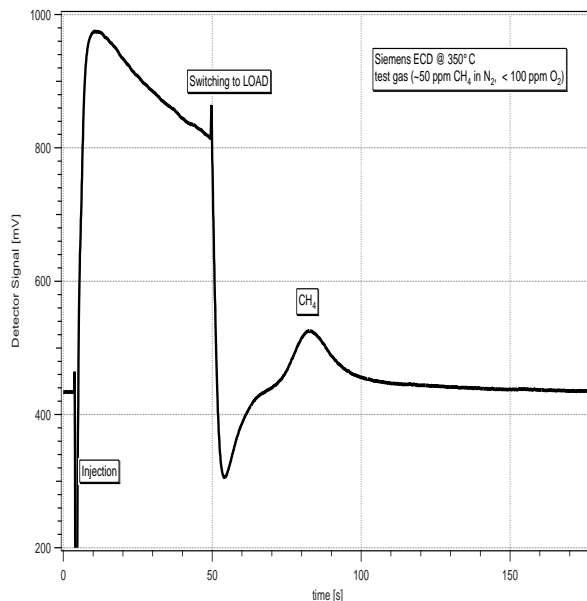


Figure 2.9: Channel I chromatogram of the test gas measured with a Siemens ECD. By using a 12 port GSV, the  $\text{O}_2$  peak is cut off and does not enter the ECD. The GSV was switched into the load position at 50 s; the methane elutes at 83 s.

Similar measurements and tests were performed using a Fisons ECD instead of the Siemens ECD. An important result of this test was the fact that different ECD models exhibit differences in sensitivity. Compared to the Siemens model the sensitivity of the Fisons ECD with respect to  $\text{CH}_4$  turned out to be even smaller and the signal to noise ratio of the  $\text{CH}_4$  peak in the test gas decreased to values of about 100. Since the ECD model apparently also was an important factor, the next step was to test the detector model as used in the LACE and ACATS instruments [Moore et al., 2003; Elkins et al., 1996], namely an ECD by Shimadzu.

## 2. Set-up between January and May 2002

The application of the Shimadzu ECD resulted in significantly higher signal to noise ratios (about 1000) for the  $\text{CH}_4$  peak in the test gas. Hence, for a  $\text{CH}_4$  mixing ratio in the range of the atmospheric background value, a signal to noise ratio of about 30-40 was expected. Still, when measuring tropospheric air,  $\text{CH}_4$  was not detectable. In Figure 2.10, a test gas and an air sample chromatogram are illustrated. Both chromatograms were measured with the Shimadzu ECD. While the  $\text{CH}_4$  peak was clearly visible in the test gas and the separation between  $\text{O}_2$  and  $\text{CH}_4$  was sufficient, no  $\text{CH}_4$  peak could be



ECD	Shimadzu
Pre column	0.7 m molecular sieve 5Å 80/100
Main column	1.2 m molecular sieve 5Å 80/100
Crimp	1 sccm @ 130 bar
Sample loop	1 ml

Table 2.3: Set-up January and May 2002

identified in the air sample. In the presence of atmospheric O<sub>2</sub> levels (20%) the separation between the two species was insufficient and CH<sub>4</sub> was “buried” in the O<sub>2</sub> tail.

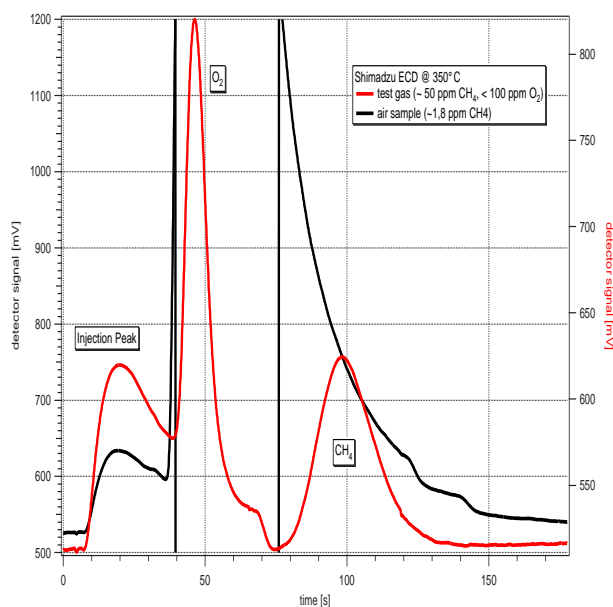


Figure 2.10: Channel I chromatogram measured with a Shimadzu ECD. The test gas chromatogram is displayed in red. The methane elutes at 98 s. The chromatogram of an air sample is displayed in black.

### 3. Set-up in May and early June 2002

In order to improve the separation between O<sub>2</sub> and CH<sub>4</sub>, the columns were modified. First the pre column was changed from 0.7 m mol sieve to a 2 m Unibeads 1S. This column type and length is also used by *Elkins et al.* [1996] in the ACATS instrument. The Unibeads material consists of spherical porous silica beads and is able to separate hydrocarbons (manufacturer description).

However, the separation between O<sub>2</sub> and CH<sub>4</sub> was not improved. In air samples CH<sub>4</sub> was still not detectable.

ECD	Shimadzu
Pre column	2 m Unibeads 1S
Main column	1.2 m molecular sieve 5Å 80/100
Crimp	1 sccm @ 130 bar
Sample loop	1 ml

Table 2.4: Set-up May and early June 2002

4. Set-up in late June and July 2002 (APE-ENVISAT mid-latitude test and validation campaign in Forlí)

ECD	Shimadzu
Pre column	2 m Unibeads 1S
Main column	0.7 m molecular sieve 5Å 60/80
Crimp	2 sccm @ 140 bar
Sample loop	1 ml

Table 2.5: Set-up July 2002

By using molecular sieve 5Å 60/80 mesh instead of 80/100 mesh it was finally possible to detect CH<sub>4</sub> in an air sample. In Figure 2.11, the CH<sub>4</sub> peak can be seen at a retention time of about 32 s. This chromatogram of a CAL gas measurement was recorded in July 2002 during the Forlí measurement campaign (see section 2.3.2). In this configuration CH<sub>4</sub> was measured with an average precision of about 2-3%.

For these measurements a new crimp tubing was used to control the N<sub>2</sub>O flow. This crimp had a flow rate of 2.2 ml @ 140 bar and the N<sub>2</sub>O pressure was adjusted at a pressure between 2.5 bar and 3.5 bar resulting in calculated N<sub>2</sub>O mixing ratio between 260 ppm and 780 ppm in the carrier gas. The doping gas mixing ratio is not constant due to changes of the doping gas pressure that occur during the flight. The doping gas pressure regulator controls the doping gas pressure relative to the ambient pressure. In this special case, the ambient pressure is the pressure inside the HAGAR vessel, which changes rapidly at the beginning of the flight. Besides, temperature changes inside the vessel temporarily effect the doping gas pressure by expansion effects which decay very slowly due to the small flow through the restriction. Thus, the doping gas pressure drifts with time. The resulting slow changes in the chromatography are corrected by the CAL and SPAN measurements as described in section 2.1.1 and do not significantly affect the precision of the measurements.

5. Set-up between September and December 2002 (APE-ENVISAT mid-latitude validation campaign in Forlí)

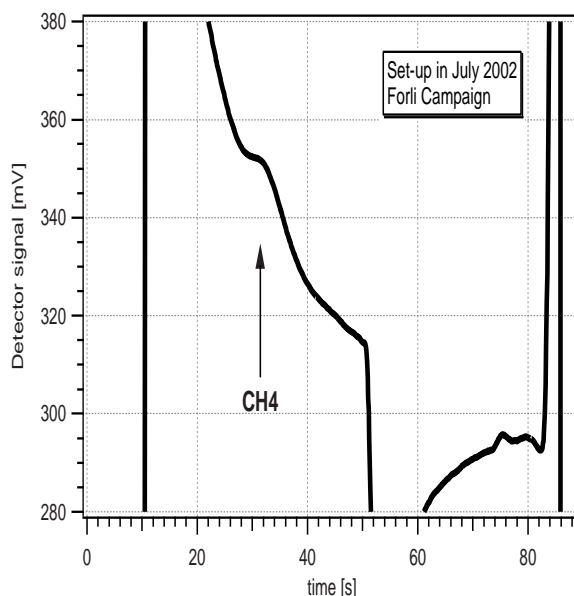


Figure 2.11: Channel I chromatogram of a CAL gas sample measured in July 2002 during the mid-latitude ENVISAT test and validation campaign in Forlì. The methane elutes at 32 s.

ECD	Shimadzu
Pre column	0.7 m molecular sieve 5Å 60/80
Main column	1.5 m molecular sieve 5Å 60/80
Crimp	2 sccm @ 140 bar
Sample loop	2 ml

Table 2.6: Set-up September to December 2002

In order to further improve the separation, molecular sieve 5Å 60/80 was used for both the pre (0.7 m) and the main column (1.5 m). Second, the sample loop was enlarged to 2 ml.

As a result the mean precision of CH<sub>4</sub> was improved to 1%. This column configuration was kept until March 2003.

- Set-up from January to March 2003 (EuPLEx and the APE-ENVISAT arctic validation campaign)

Due to problems with N<sub>2</sub>O-contamination in the HAGAR vessel (see Appendix C.2), it was necessary to change the doping gas from pure N<sub>2</sub>O to 1% N<sub>2</sub>O in N<sub>2</sub>. In order to maintain the doping gas mixing ratio in the carrier gas, a new restriction allowing higher flow rates had to be installed. The new crimp tubing had a flow rate of 13 ml/min at 40 bar resulting in doping gas mixing ratios between 60 ppm and 80 ppm N<sub>2</sub>O in the detector.

ECD	Shimadzu
Pre column	0.7 m molecular sieve 5Å 60/80
Main column	1.5 m molecular sieve 5Å 60/80
Crimp	13 sccm @ 40 bar
Sample loop	2 ml

Table 2.7: Set-up January to March, 2003

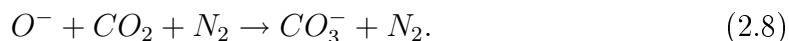
Additionally, a new, more robust flow regulation was installed in both channels (see also 2.3.4) providing a more stable baseline.

In this final set-up of channel I the CH<sub>4</sub> precision improved to values well below 1%. A chromatogram recorded in this configuration is displayed in Figure 2.3.

### 2.2.3 Necessary changes in channel II due to use of pure N<sub>2</sub> as carrier gas:

The changes in channel I, described in the previous section, also required changes in channel II, as will be explained in the following.

N<sub>2</sub>O not only captures an electron but also releases it, thus it cannot be directly detected by an ECD. Making use of the doping reaction of N<sub>2</sub>O and CH<sub>4</sub> as described in section 2.2.1, it is possible to increase the detector sensibility to N<sub>2</sub>O. Therefore, 1% CH<sub>4</sub> in N<sub>2</sub> was used as a carrier gas before the modification of channel I. Applying pure N<sub>2</sub> as a carrier gas, a different dopant has now to be added to channel II. In this case, CO<sub>2</sub> is used as a doping gas. CO<sub>2</sub> reacts in the detector cell with N<sub>2</sub> and O<sup>-</sup> to form the stable ion CO<sub>3</sub><sup>-</sup>.



O<sup>-</sup> is formed in the reactions 2.4, 2.5, 2.6 when N<sub>2</sub>O reaches the detector.

Mechanically, the addition of CO<sub>2</sub> to the carrier gas is accomplished analogue to the N<sub>2</sub>O doping setup. In this case, the CO<sub>2</sub> mixing ratio in the carrier gas has not to be calculated but is measured directly with the HAGAR LI-COR. The crimp was tuned so that at a CO<sub>2</sub> pressure of 5 bar and a carrier gas flow through the ECD of about 50 ml/min — corresponding to the carrier gas flow at the time of the N<sub>2</sub>O peak elution — the LI-COR measured a CO<sub>2</sub> mixing ratio of about 270 ppm. In all flights starting from October 14th 2002 (see the following section) the CO<sub>2</sub> doping was set in this configuration.

During the first two October flights and all the July flights a different crimp was used (see section 2.3.3), allowing a flow rate of 20 ml/min at 140 bar. The CO<sub>2</sub> pressure was set to values between 1.5 bar and 2.1 bar resulting in CO<sub>2</sub> mixing ratios in the carrier gas between 0.3-0.5%<sup>12</sup>. Operating the pressure regulator at

<sup>12</sup>Lace uses a CO<sub>2</sub> mixing ratio of 0.2%

the lower range of its outlet pressure range (1-7 bar) led to pressure fluctuations in the doping gas line and thus to fluctuations of CO<sub>2</sub> mixing ratio during the flight. Furthermore, the consumption of CO<sub>2</sub> doping gas was very high.

To minimize the mixing ratio, eliminate the pressure fluctuation problem and saving gas, this crimp tubing was exchanged with the one described above — providing a lower doping gas concentration at a higher doping gas pressure.

## 2.3 Campaigns

### 2.3.1 The M55 Geophysica



*Figure 2.12:* The M55 Geophysica.

The M55 Geophysica is a Russian high-altitude aircraft operated by Myasishchev Design Bureau (MDB), Russia. It is the only stratospheric aircraft platform in Europe (the only other existing stratospheric research aircrafts are the NASA-ER2<sup>13</sup> and the WB-57). It reaches cruise altitudes up to 21 km and travels at a cruise speed of about 750 km/h for about 5-6 hours. For scientific measurements instruments can be installed in the various bays (max. payload 1500 kg). The Geophysica is also equipped with meteorological sensors and the UCSE<sup>14</sup>, an electronic device to provide flight parameters and a uniform time base for all instruments on board. Due to relatively high maneuverability and little sensitivity to ground conditions, the aircraft is an excellent platform for measurements and can be deployed flexibly

---

<sup>13</sup>former espionage aircraft U2

<sup>14</sup>Unit for Connection with Scientific Equipment

according to scientific objectives even in difficult weather conditions and locations. Center of the APE (Airborne Polar Experiment aka Airborne Platform for Earth observation) project, the aircraft has been deployed successfully during several campaigns since 1996:

- 1996, January: APE-POLECAT (Polar stratospheric clouds, lee waves , chemistry, aerosols and transport), Rovaniemi, Finland, 7 Flights.
- 1999, February to March: APE-THESEO, Mahe, Seychelles, 7 flights.
- 1999, September to October: APE-GAIA (Geophysica aircraft in Antarctica), Ushuaia, Argentina, 5 flights and 8 transfer flights.
- 2002, July: APE ENVISAT mid-latitude test and validation campaign, Forl , Italy, 4 flights.
- 2002, October: APE ENVISAT mid-latitude validation Campaign, Forl , Italy, 7 flights.
- 2003, January to February: EuPLEx (European polar stratospheric cloud and lee wave experiment), Kiruna, Sweden, 10 flights.
- 2003, February to March: APE ENVISAT AVC (Arctic validation campaign), Kiruna, Sweden, 5 flights.
- 2005, January to March: TroCCiNOx (Tropical convection, cirrus and nitrogen oxides experiment), Ara atuba, Brazil, 8 flights, 8 transfer flights plus an additional polar flight (Oberpfaffenhofen, Germany).
- 2005, November to December: SCOUT-O3 (Stratospheric-climate links with emphasis on the UTLS), Darwin, Australia, 8 flights, 12 transfer flights, 1 test flight (Oberpfaffenhofen, Germany).

The data presented in this work were obtained during the APE ENVISAT and the EuPLEx campaigns. The payload of the Geophysica for these campaign is given in Table 2.8. Depending on the focus of a mission or flight — on measurements of aerosols or chemical constituents — the payload was modified and concentrated either on chemical or aerosol sensors. Nevertheless, HAGAR was always part of the payload. Further information will be given in the following.

### 2.3.2 ENVISAT mid-latitude test and validation campaign

From July 1 to July 25, 2002, a Geophysica test and validation campaign was performed from Forl , Italy (44°1' N, 12°04' E). The major objectives of this campaign were the test of new instruments on board the Geophysica and the validation of the ESA Satellite ENVISAT<sup>15</sup>. Four flights were performed between 36° N and 46° N

<sup>15</sup>ENVIRONMENT SATellite launched in March 2002 by the European Space Agency ESA. A polar orbiter for earth observation.

Instrument	Measured Parameter	Technique	Institute	Campaigns
FOZAN	O <sub>3</sub>	Dye chemiluminescence	CAO, Russia and ISAC-CNR, Italia	all
FOX	O <sub>3</sub>	UV absorption	DLR	3,4
FISH	H <sub>2</sub> O(total)	Lyman- $\alpha$ photo-fragment fluorescence	FZJ	all
FLASH	H <sub>2</sub> O(gas phase)	Lyman- $\alpha$	CAO	all
SIoux	NO, NO <sub>2</sub> , particle NO <sub>y</sub>	Chemiluminescence; AU converter; subsokinetic conversion, resonance fluorescence, therm. dissociation	DLR	all
HALOX	ClO, BrO, ClONO <sub>2</sub>	GC/ECD and IR absorption	FZJ	all
HAGAR	N <sub>2</sub> O, CH <sub>4</sub> , CFC-11, H-1211, SF <sub>6</sub> , H <sub>2</sub> , CO <sub>2</sub>	TDL	JWG	all
ALTO	N <sub>2</sub> O, CH <sub>4</sub> , CO	UV visible spectrometer	INOA	1,2,3
GASCOD	Vertical column O <sub>3</sub> , N <sub>2</sub> O <sub>2</sub> , O <sub>2</sub> , O <sub>2</sub> , O <sub>2</sub> , BrO	Mid infrared Fourier transform spectrometer	CNR	1,4
MIPAS-STR	Vertical profiles of T, O <sub>3</sub> , HNO <sub>3</sub> , N <sub>2</sub> O, CH <sub>4</sub> , H <sub>2</sub> O	Far infrared Fourier transform spectrometer	IMK-FZK	1,2,4
SAPHIRE	Vertical profiles of O <sub>3</sub> , HNO <sub>3</sub> , N <sub>2</sub> O, H <sub>2</sub> O	2 channel CN counter, one inlet heated	IFAC-CNR	1,2,4
COPAS	Condensation nuclei (total, non-volatile)	Laser particle spectrometer	Uni Mainz	all
FSSP3000	Aerosols (0.4-40 $\mu$ m)	Multi wavelength scattering	Uni Mainz	all
MAS	Aerosol optical properties	Microjoule lidar	CNR	all
MAL 1/2	Remote aerosol profile	Backscattering lidar	Obs., Neuchatel	all
ABLE	Remote aerosol profile	Microwave radiometer	Uni Roma	all
MTP	Temperature profile (+/- 3km from aircraft altitude)	Whole air sampler	JPL	3
WAS	Trace gas isotopes	PT100, 5 hole probe	MPI Heidelberg	3
Rosemount probe	Temperature, wind	Thermodynamic complex	CAO	all
TDC	Temperature, pressure		CAO	all

Table 2.8: Payload of the Geophysica. The campaigns are labelled with 1 = ENVISAT mid-latitude test and validation campaign in Forlì (July), 2= ENVISAT mid-latitude validation campaign in Forlì (October), 3= EuPLEx and 4=AVC.

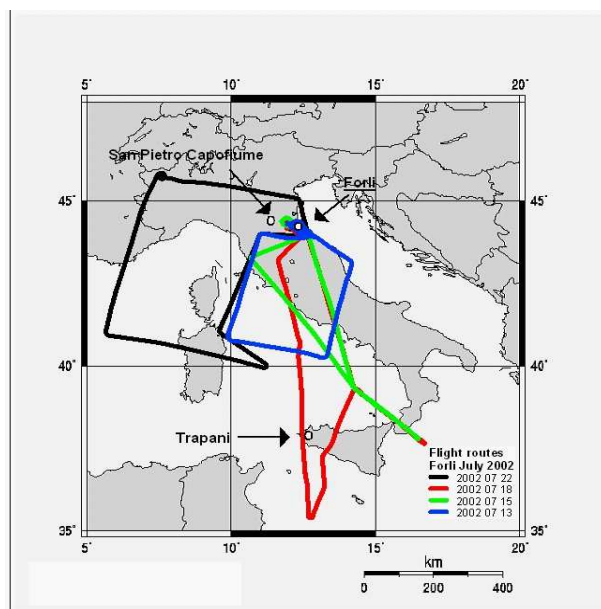


Figure 2.13: Flight paths of the Geophysica aircraft during the ENVISAT mid-latitude test campaign in Forlì, July 2002.

and  $6^{\circ}$  E and  $17^{\circ}$  E. The first two flights were test flights and the latter validation flights.

### HAGAR performance and data status

The main action item of this campaign was the test of the new implemented  $\text{CH}_4$  channel. The performance of this channel was improved during the campaign (see section 2.2). It was the first time ever that HAGAR measured  $\text{CH}_4$  during a campaign. Furthermore, a new HAGAR software that provided easier handling and more flexibility in the configuration of the instrument was tested and successfully used.

Data was measured on all four flights. The measurements and their precisions (Table C.3) for this campaign are given in the appendix. During the campaign, several instrumental problems occurred. These are listed in the following:

- The vessel temperature was very noisy because of problems with the temperature registration, which showed high noise and sudden jumps. Normally, the vessel temperature can be controlled to within  $3^{\circ}\text{C}$ . Here the temperature varied about  $\pm 10^{\circ}\text{C}$  resulting in a lower precision (see Table C.3 in the appendix) for all molecules. The temperature is measured with PT 100 sensors and the signal is recorded via a special signal conversion card that was built at the institute.
- Due to problems with a defect mass flow controller in the sample cell of the



LI-COR 6251 instrument, reference and sample cell were changed at the beginning of the campaign, i.e. the reference cell was used as sample cell and vice versa. This led to strong drifts in the CO<sub>2</sub> measurements, hence to a worse precision (see Tables C.3, C.4 in the appendix). This was the case, because the analyser operates in a way to keep the transmission through the reference cell — then used as the sample cell — constant. A change in the reference gas CO<sub>2</sub> concentration leads to a change in the gain of the detector (*LI-COR* [1992]). When flushing ambient air through the reference cell the mixing ratio in this cell varied continuously. Another factor that potentially increased the noise level of the LI-COR 6251 signal was the use of a crimp instead of a mass flow controller to control the sample flow. The flow thus varied during a flight due to a decrease in pump power with decreasing ambient pressure. This configuration was kept during all the following campaigns.

- In the last flight, the N<sub>2</sub>O exhibits a small contamination of about 5% in the beginning of the flight (see C.2). This was not detected during the campaign.
- Only one of the two parallel running vacuum pumps was working, leading to relatively low sample flows at high altitudes. This was not noticed during the campaign.
- The flight bottle containing the CAL gas showed mixing ratio drifts for the species N<sub>2</sub>O, CCl<sub>3</sub>F, CCl<sub>2</sub>F<sub>2</sub> and CO<sub>2</sub> of magnitudes up to 1%. This effect was not noticed during the campaign. For the correction of the CAL gas drift see section C.3 in the appendix.

### 2.3.3 ENVISAT mid-latitude validation campaign

The major objective of this second mid-latitude campaign in Forlí was the validation of the ESA Satellite ENVISAT. Seven flights were carried out between October 1 and 29, 2002 in a region between 37° N and 48° N and 6° E and 19° E. The Geophysica flights were planned according to the orbits of the satellite and footprints of selected satellite instruments (mostly MIPAS-E) in order to measure as close as possible in space and time to the air masses measured by the satellite instruments. Ideally, the Geophysica- and ENVISAT instruments measure the same air mass at the same time.

#### HAGAR performance and data status

Before the campaign, the temperature registration was changed and the formerly used conversion card (section 2.3.2) was replaced by a conventional ADC4 conversion card. This finally improved the temperature regulation to nominal values and the precision of all measurements (see Table C.3 in the appendix). Due to further

Flight	Data	Problems
2002 07 13 07:18 UTC 3:30 h Chemistry/Test	no H <sub>2</sub> and SF <sub>6</sub> no CH <sub>4</sub> (2. half)	not measured bad separation from O <sub>2</sub> $T_{vessel}$ highly variable
2002 07 15 17:50 UTC 3:25 h Aerosol	no H <sub>2</sub> and SF <sub>6</sub>	not measured $T_{vessel}$ highly variable
2002 07 18 16:38 UTC 5:10 h Aerosol	no H <sub>2</sub> and SF <sub>6</sub>	not measured $T_{vessel}$ highly variable
2002 07 22 6:01 UTC 4:10 h Chemistry	no H <sub>2</sub> and SF <sub>6</sub> N <sub>2</sub> O contaminated	not analysed contamination $\sim$ 5% $T_{vessel}$ highly variable

Table 2.9: Status of the HAGAR data during the ENVISAT mid-latitude test and validation campaign in Forlì, July 2002.

improvements of channel I (see section 2.2) the precision of CH<sub>4</sub> was increased to about 1%.

With SF<sub>6</sub> and H<sub>2</sub> two more molecules were now analysed from channel I. Since this channel was optimized for measuring CH<sub>4</sub>, these two peaks exhibit a rather low precision, especially the SF<sub>6</sub>, which is negatively influenced by the N<sub>2</sub>O doping (decreasing peak height with increasing doping gas concentration).

HAGAR gathered data on all seven flights. Unfortunately, a power failure occurred during the first flight and HAGAR only measured in the first hour of the flight. The reason for the failure is still unknown. Further new and old problems, that occurred during the campaign are listed below:

- During the first two flights, channel II exhibited rather strong pressure fluctuations in the CO<sub>2</sub> doping gas line. Therefore, a new crimp tubing was installed in the CO<sub>2</sub> doping line. This improved the stability of the CO<sub>2</sub> pressure in the doping line (see also section 2.2.3) and thus the performance of channel II.
- The N<sub>2</sub>O measurements show a severe contamination up to 30% during the first three flights. After the third flight, the contamination was detected and several actions were taken to eliminate or at least decrease the contamination (see Appendix C.2). Although the problem was not completely eliminated during the campaign, all flights that took place from October 17 on exhibit only a slight N<sub>2</sub>O contamination between 1-2%.
- Only one of the two parallel running vacuum pumps was working. This was again not noticed during the campaign.

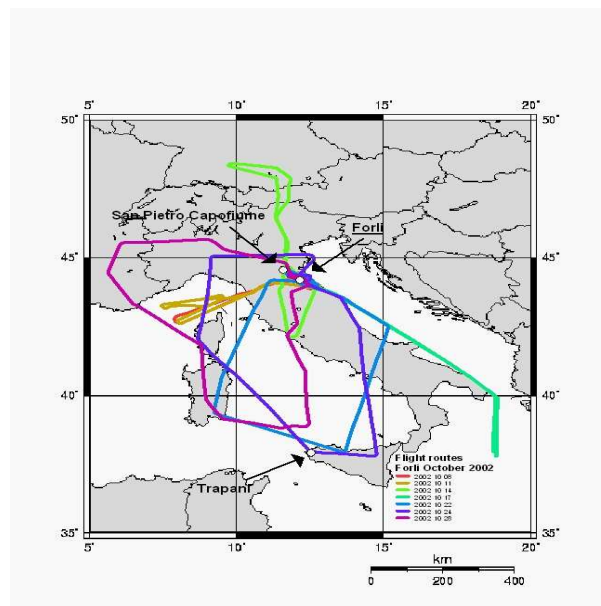


Figure 2.14: Flight paths of the Geophysica aircraft during the ENVISAT mid-latitude validation campaign in Forlì, October 2002.

- Drift of CAL gas in the flight bottle (see previous section 2.3.2). This effect was not detected during the campaign.

<sup>16</sup>This flight was funded by the Natural environment research council (NERC) to examine effects of aircraft plumes to the upper troposphere region

Flight	Data	Problems
2002 10 08 8:58 UTC 2 h Chemistry/Test	N <sub>2</sub> O contaminated 1 h measurements	contamination ~ 20% power failure after 1h vessel pressure 850 hPa
2002 10 11 08:29 UTC 3:05 h Aerosol	N <sub>2</sub> O contaminated	contamination ~ 10%
2002 10 14 08:41 UTC 3:55 h Aerosol	N <sub>2</sub> O contaminated	contamination ~ 30%
2002 10 17 08:30 UTC 4:25 h NERC <sup>15</sup>	N <sub>2</sub> O corrected	N <sub>2</sub> O contamination 1-2%
2002 10 22 07:19 UTC 4:00 h Chemistry	N <sub>2</sub> O corrected	N <sub>2</sub> O contamination 1-2%
2002 10 24 18:41 UTC 3:55 h Chemistry	N <sub>2</sub> O corrected	N <sub>2</sub> O contamination 1-2%
2002 10 28 06:59 UTC 4:00 h Chemistry	N <sub>2</sub> O corrected	contamination 1-2%

Table 2.10: Status of the HAGAR data during the ENVISAT mid-latitude validation campaign in Forl , October 2002.

### 2.3.4 Vintersol EuPLEx



Figure 2.15: Logo of the EuPLEx campaign in Kiruna, January to February 2003.

The EuPLEx campaign — European Polar Stratospheric Cloud and Lee Wave experiment — took place from January 10 to February 12, 2003. Based in Kiruna (67°49' N, 20°30' E), northern Sweden, the Geophysica made 10 flights in the Arctic vortex region. Main objectives of EuPLEx were [EuPLEx, 2001]

- Formation of polar stratospheric clouds (PSCs). Observations of PSC growth rates and properties, and the comparison to the theoretical understanding of PSC microphysics.
- The effects of PSCs on denitrification and dehydration.
- Observation of halogen activation rates and their consistency with the current theory of heterogeneous activation on PSC particles.
- The importance of PSCs on chlorine activation and ozone loss in the Arctic.
- Validation of the known ozone loss cycles by considering observed ClO, BrO and NO/NO<sub>y</sub> mixing ratios and simultaneously observed ozone loss.

Tracer relationships, correlations, subsidence and dynamics of the vortex are of basic interest when studying these objectives. The objectives of the tracer measurements were the following:

- Effect of transport on the development of the constituent distributions, particularly of ozone and reactive nitrogen and water vapour.
- Quantification of the cumulative chemical ozone loss, denitrification and dehydration from simultaneous aircraft observations.

- Determination of the total amount of inorganic chlorine, bromine, and available nitrogen along the flight track.
- Mixing between vortex and extra-vortex air and its effect on tracer relationships.

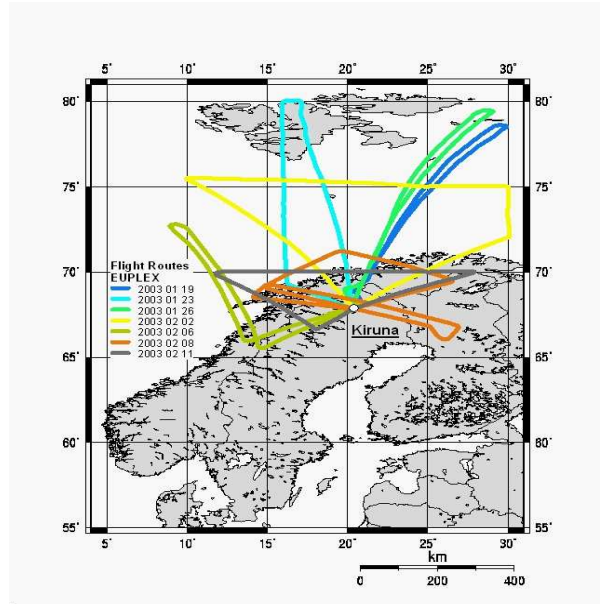


*Figure 2.16:* Flight Paths of the Geophysica aircraft during the EuPLEx campaign in Kiruna, January to February 2003. Only those flights are plotted where HAGAR was fully operational.

In order to address these objectives, the Geophysica was equipped with 16 instruments measuring gas-phase composition of the stratosphere, aerosol and particle properties and physical/meteorological parameters. The payload of the Geophysica is listed in Table 2.8.

In addition to the Geophysica the DLR<sup>17</sup> Falcon carried out observations with remote sensing instruments. The objectives of the Falcon were to guide the Geophysica to interesting structures by the lidar measurements (path finder mode) and to make lidar observations of the air masses the Geophysica measured in situ or that were above the altitude range of the Geophysica.

EuPLEx was part of the VINTERSOL-campaign (**V**alidation of **I**nternational **S**atellites and **S**tudy of **O**zone **L**oss) a pan European project and was funded by the European Union through its 5th framework programme.

<sup>17</sup>German Aerospace Center; Deutsches Luft- und Raumfahrtzentrum

### HAGAR performance during the EuPLEx campaigns

In the run-up to the campaign HAGAR was completely disassembled in order to check the instrument for leakages. During these checks, the malfunctioning vacuum pump was detected and repaired. Thus, HAGAR operated with maximum pump power during the campaign. The MFCs controlling the main column flows in both channels were changed. The new controllers provided a more stable flow through the chromatographic system and the ECDs.

In seven of the ten performed flights, HAGAR successfully obtained data. The reasons for the failure during three flights and further instrumental problems are listed in the following:

- The first four flights in January (15 to 26) suffered from a severe N<sub>2</sub>O contamination. The N<sub>2</sub>O data were corrected as described in Appendix C.2 following equation C.4. The contamination problem was finally solved during the campaign (see Appendix C.2) and all flights starting from January 30 exhibit no contamination.
- During 3 of the 10 flights that were performed during the EuPLEx campaign, HAGAR did not obtain a full data set:
  - In the beginning of the first flight, the HAGAR vessel depressurized. Consequently, the Licor signal was out of range and the ECD signal of channel I was saturated. The ECD signal of channel II drifted strongly. However, N<sub>2</sub>O, CFC-12, CFC-11 and H-1211 could be retrieved at a slightly reduced precision.
  - Due to a configuration error, the HAGAR pumps were continuously switched off during the flight on January 30. Consequently, no air was measured. The calibration measurements, however, were perfectly performed and in the CAL to pump measurements no contamination with N<sub>2</sub>O was detected.
  - A total failure of the instrument occurred on February 9. In the warm up phase prior to the flight, the computer shut down and no measurements were performed. No definite reason for this failure could be identified. To avoid potential problems with the storage system, the PCMCIA flash card was replaced before the following flight. In several tests thereafter and during the last flight on February 11 this error did not occur again.
- A drift of the CAL gas in the flight bottle (see also previous sections) was finally detected during the campaign. This problem was addressed by performing calibration measurements after each refilling of the bottle and after each flight. For the correction of the CAL gas drift see section C.3 in the appendix.

Flight date	Data	Problem
2003 01 15 08:15 UTC 4:30 h Lee wave	no Licor data no data from channel 1 N <sub>2</sub> O corrected	pressure drop due to leakage in the vessel: Li-COR out of range ECD signals shifted /out of range contamination due to leakage in N <sub>2</sub> O line
2003 01 19 13:40 UTC 4:30 h Vortex	N <sub>2</sub> O corrected reduced CFC-12 precision	contamination due to leakage in N <sub>2</sub> O line ch.II backflush turned off
2003 01 23 12:55 UTC 4:40 h Vortex intrusion	N <sub>2</sub> O corrected reduced CFC-12 precision	contamination due to leakage in N <sub>2</sub> O line ch.II backflush turned off
2003 01 26 11:09 UTC 4:40 h Vortex	N <sub>2</sub> O corrected reduced CFC-12 precision	contamination due to leakage in N <sub>2</sub> O line ch.II backflush turned off
2003 01 30 08:45 UTC 4:50 h Match	no data	configuration error
2003 02 02 08:35 UTC 4:30 h Envisat/aerosol	ok	
2003 02 06 13:35 UTC 4:35 h Cold pool	ok	
2003 02 08 15:00 UTC 4:30 h Lee wave	ok	
2003 02 09 08:45 UTC 4:50 h Match	no data	computer shutdown
2003 02 11 08:45 UTC 4:50 h Match	ok	no

Table 2.11: Status of the HAGAR data during the EuPLEX measurement campaign.



### 2.3.5 APE ENVISAT Arctic Validation Campaign (AVC)

Between February 24 and March 19, 2003, five flights for the validation of the ENVISAT satellite were carried out. Again, the base for the flights was Kiruna. The main objective was to make comparison measurements with instruments on board the ENVISAT satellite, mainly MIPAS-E, concentrating on polar chemistry. Therefore, the flights were planned according to the ENVISAT orbits and footprints of MIPAS-E in order to perform measurements as close as possible in space and time. Figure 2.17 displays the flight routes during the AVC campaign.

The ENVISAT Validation Campaigns were funded by the European Space Agency (ESA), the European Union (EU), the German Federal Ministry of Education and Research and the Italian Space Agency.

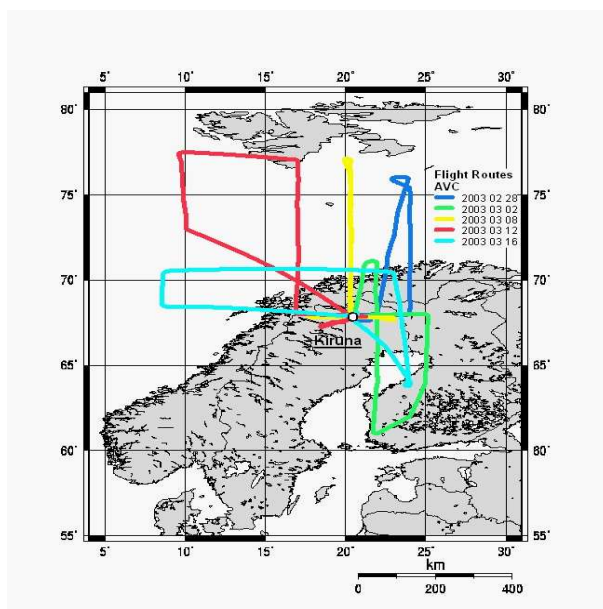


Figure 2.17: Flight paths of the Geophysica aircraft during the AVC campaign in Kiruna, February to March 2003.

#### HAGAR performance during the AVC campaign

In the beginning of the campaign the on board computer, a PC 486DX2 66 MHz, was replaced by an AT96 Fox II Pentium MMX GXM 200 MHz. At the backplane a bus termination was integrated to avoid signal reflection on the bus, as these reflections can produce computer failures [Rossberg, 2003].

The overall performance of HAGAR was very good. No failures and contaminations occurred and the instrument provided reliable, high-precision data during all five scientific flights.

The only persisting problem during this campaign was the drift of CAL gas in the flight bottle (also see previous sections), which could be corrected in the data

Flight date	Data
2003 02 28 07:22 UTC 4:00 h Envisat chemistry/cold pool	ok
2003 03 02 18:41 UTC 4:25 h Envisat chemistry/vortex edge	ok
2003 03 08 06:29 UTC 4:20 h Envisat chemistry/vortex	ok
2003 03 12 07:13 UTC 4:34 h Envisat chemistry/vortex edge	ok
2003 03 16 05:57 UTC 4:29 h Envisat chemistry/cold pool	ok

*Table 2.12:* Status of the HAGAR data during the AVC measurement campaign.

(see Appendix C.3).

# Chapter 3

## Quantifying transport into the Arctic lowermost stratosphere

In this chapter, a simple mass balance is presented with the goal of quantifying transport into the Arctic LMS. After a discussion on the determination of the boundary conditions, the results of the mass balance study are presented for the EuPLEx and the AVC campaigns. The results of both campaigns will be compared and a sensitivity study will be performed on the results. Finally, conclusions and an outlook will be given.

### 3.1 A simple mass balance for the high-latitude LMS

As described in section 1.3 and indicated in Figure 3.1, air in the lowermost stratosphere (here defined as the region between the extra-tropical tropopause and the 400 K isentrope) in middle to high latitudes can be assumed to be a mixture of

1. air descending from the polar vortex ( $> 400$  K): **fraction**  $f_{vortex}$
2. air descending from the extra-vortex/mid-latitude stratosphere ( $> 400$  K) : **fraction**  $f_{strat}$
3. and air transported isentropically from the troposphere or the tropical stratosphere ( $< 400$  K) : **fraction**  $f_{trop}$

Although the LMS is most commonly defined as the region between the tropopause and the 380 K isentrope, the 400 K isentrope was used as the upper boundary to include the transport from the lowest part of the tropical stratosphere, which exhibits a similar chemical composition as the upper troposphere for the tracers considered here.

The mixing ratio  $\chi_\theta$  of a tracer at the potential temperature  $\theta$  in the lowermost stratosphere can thus be expressed by the following linear equation:

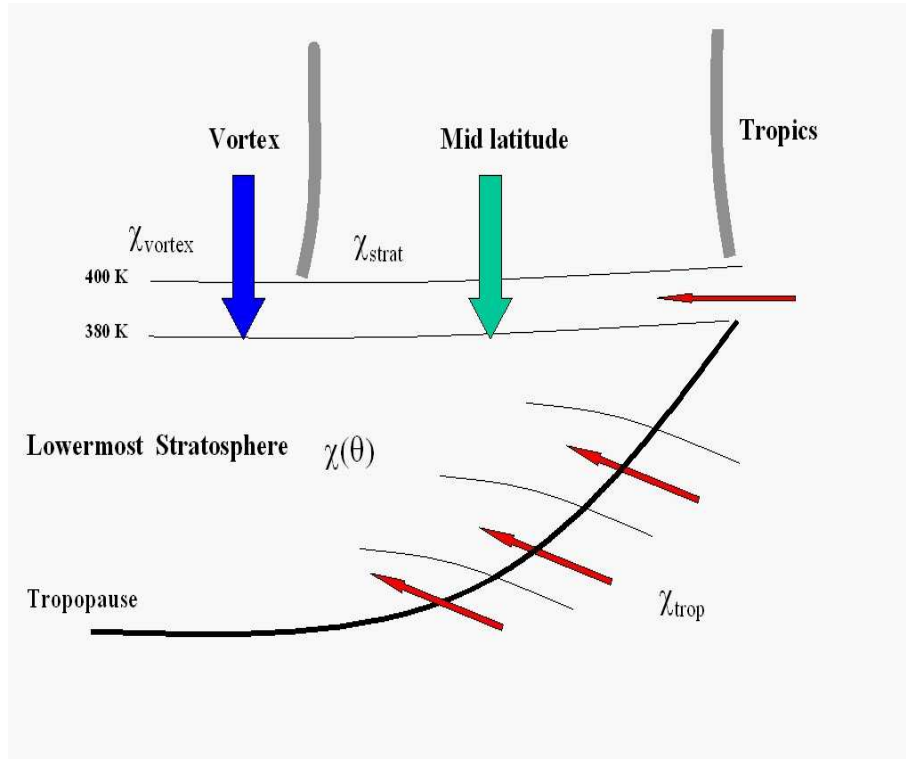


Figure 3.1: Transport into the lowermost stratosphere. Air enters the LMS from the mid-latitude stratosphere (green arrow), from the vortex region (blue arrow) and from the troposphere and the lowest part of the tropical stratosphere (red arrows).

$$\chi_{\theta} = f_{trop}\chi_{trop} + f_{strat}\chi_{strat} + f_{vortex}\chi_{vortex} \quad (3.1)$$

$\chi_{trop}$ ,  $\chi_{strat}$  and  $\chi_{vortex}$  are the average mixing ratios of the tracer in the troposphere, the mid-latitude stratosphere at 400 K and inside the vortex at 400 K. The determination of these boundary conditions will be discussed in section 3.4.

With the constraint  $f_{trop} + f_{strat} + f_{vortex} = 1$  the fractions can be derived from at least two observed tracers which are sufficiently different to provide complementary constraints on transport; e.g. different source and sink regions, non-linear tracer-tracer correlation (see section 3.3).

## 3.2 Setting up a mass balance linear equation system

The mass balance equation 3.1 can be set up for the mixing ratios  $\chi_i$  of tracers  $i = (1, 2, \dots, n)$  and for the air mass:



Species	Lifetime (Years) <sup>1</sup>	trop. abundance	Source
CFC-11 (CCl <sub>3</sub> F)	45	251 ppt <sup>2</sup>	anthrop. emission
CFC-12 (CCl <sub>2</sub> F <sub>2</sub> )	100	533 ppt	anthrop. emission
H-1211 (CBrClF <sub>2</sub> )	11	4.3 ppt	anthrop. emission
Nitrous oxide N <sub>2</sub> O	120	320 ppb <sup>3</sup>	nat. + anthrop. emission
Methane CH <sub>4</sub>	8.4(trop.)/120 (strat.)	1775 ppb	nat. + anthrop. emission
trop. Ozone O <sub>3</sub>	days to weeks	10-100 ppb <sup>4</sup>	photochemical prod.
strat. Ozone O <sub>3</sub>	months to years	100-8000 ppb; max.	photochemical prod.
strat. H <sub>2</sub> O	1-6	3-6 ppmv	troposphere; methane oxidation

Table 3.1: Tracers used in the mass balance analysis. The abundances for CFC-11, CFC-12, N<sub>2</sub>O and CH<sub>4</sub> refer to the year 2006 [NOAA-CMDL, 2006], those for O<sub>3</sub> and H<sub>2</sub>O to the year 1998 [IPCC, 2001].

The photochemical destruction of CFC-11 and -12 in the stratosphere leads to the formation of chlorine radicals while H-1211 is a source for bromine radicals. All three gases, thus, are significant for ozone depletion and are controlled under the Montreal protocol [UNEP, 1987]. The tropospheric abundance of CFC-11 is decreasing and CFC-12 has levelled in the meanwhile; even a slight decrease can be observed [NOAA-CMDL, 2006]. H-1211 is still increasing, however, with a decreasing rate.

N<sub>2</sub>O is emitted both from natural and anthropogenic sources. Its main sources are biogenic emissions from oceans and soils, farming and agricultural soils, industrial sources and biomass burning. N<sub>2</sub>O is destroyed photochemically in the stratosphere. It is one of the important greenhouse gases and its tropospheric abundance is still increasing. Since the correlation between N<sub>2</sub>O and CFC-12 is unique and close to linear, due to their similar lifetimes, only N<sub>2</sub>O is used in the calculation. CFC-12 could be used instead, but the usage of both does not provide additional information to the equation system.

The atmospheric abundance of CH<sub>4</sub> has also increased over the past decades. CH<sub>4</sub> is mainly produced by natural sources, e.g. wetlands, termites and in ocean surface waters. The most important anthropogenic sources are rice agriculture, ruminants, energy production and biomass burning. The dominant sink is the reaction with OH in the troposphere. Once it reaches the stratosphere it is destroyed in reactions with OH, Cl and O(<sup>1</sup>D) resulting in a stratospheric lifetime similar to that of N<sub>2</sub>O (see Table 3.1).

Tropospheric O<sub>3</sub> has a rather short lifetime. Sources of tropospheric O<sub>3</sub> are transport from the stratosphere by STE and the photochemical production related to pollutants like NO<sub>x</sub>. The destruction by catalytic and photochemical reactions, as well as loss to vegetation are balanced by the photochemical production. As already mentioned, O<sub>3</sub> is a strong greenhouse gas. Due to anthropogenic emissions of pollutant precursor gases (e.g. NO<sub>x</sub>, CO) the surface O<sub>3</sub> is increasing. In the middle

<sup>1</sup>Global mean atmospheric lifetime

<sup>2</sup>Parts Per Trillion (10<sup>-9</sup>); molar mixing ratio

<sup>3</sup>Parts Per Billion (10<sup>-12</sup>); molar mixing ratio

<sup>4</sup>10 ppb in remote areas at the surface, 100 ppb in the upper troposphere or polluted areas

stratosphere, where  $O_3$  has its largest source, a maximum  $O_3$  mixing ratio of about 5 ppm occurs. In the lower stratosphere the  $O_3$  lifetime ranges from months to years and sources are small. Here, the anthropogenically produced halogen compounds cause a depletion of  $O_3$  via catalytic chain reactions, which is particularly severe and fast in the wintertime polar vortex (e.g. in the ozone hole [Farman *et al.*, 1985]). Concerning the usability of  $O_3$  as a tracer in the wintertime high-latitude LMS, it is argued here, that once  $O_3$  has descended to the LMS, it can be assumed to be rather conserved and further changes in mixing ratios or in the correlation with other tracers are produced predominantly by transport rather than chemistry. This assumption is supported by the observation, that correlations between  $O_3$  and the other tracers in the LMS do not significantly change throughout a winter.  $O_3$  measurements were provided by the FOZAN and the FOX instrument. In the context of this work, the FOX measurements were used for the mass balance calculation (see Table 2.8 in section 2.3.1).

Water vapour is a very effective greenhouse gas, especially in the lower stratosphere. Its stratospheric mixing ratio is basically controlled by the temperature of the tropical tropopause, where most of the tropospheric  $H_2O$  is frozen out while crossing the tropopause region and entering the tropical stratosphere. This results in a very low  $H_2O$  abundance in the tropical lower stratosphere of about 3 ppm. In the middle stratosphere, the oxidation of  $CH_4$  leads to an increase of the  $H_2O$  mixing ratio to values of about 6 ppm. Recent observations show an increase of stratospheric  $H_2O$  by 1% per year [Rosenlof, 2002]. The reasons for this increase are not understood yet. For this study,  $H_2O$  measurements were taken from the FISH instrument (see Table 2.8 in section 2.3.1).

Vertical distributions of the used tracers from the EuPLEx and the AVC campaigns are plotted in Figures 3.2 and 3.3.

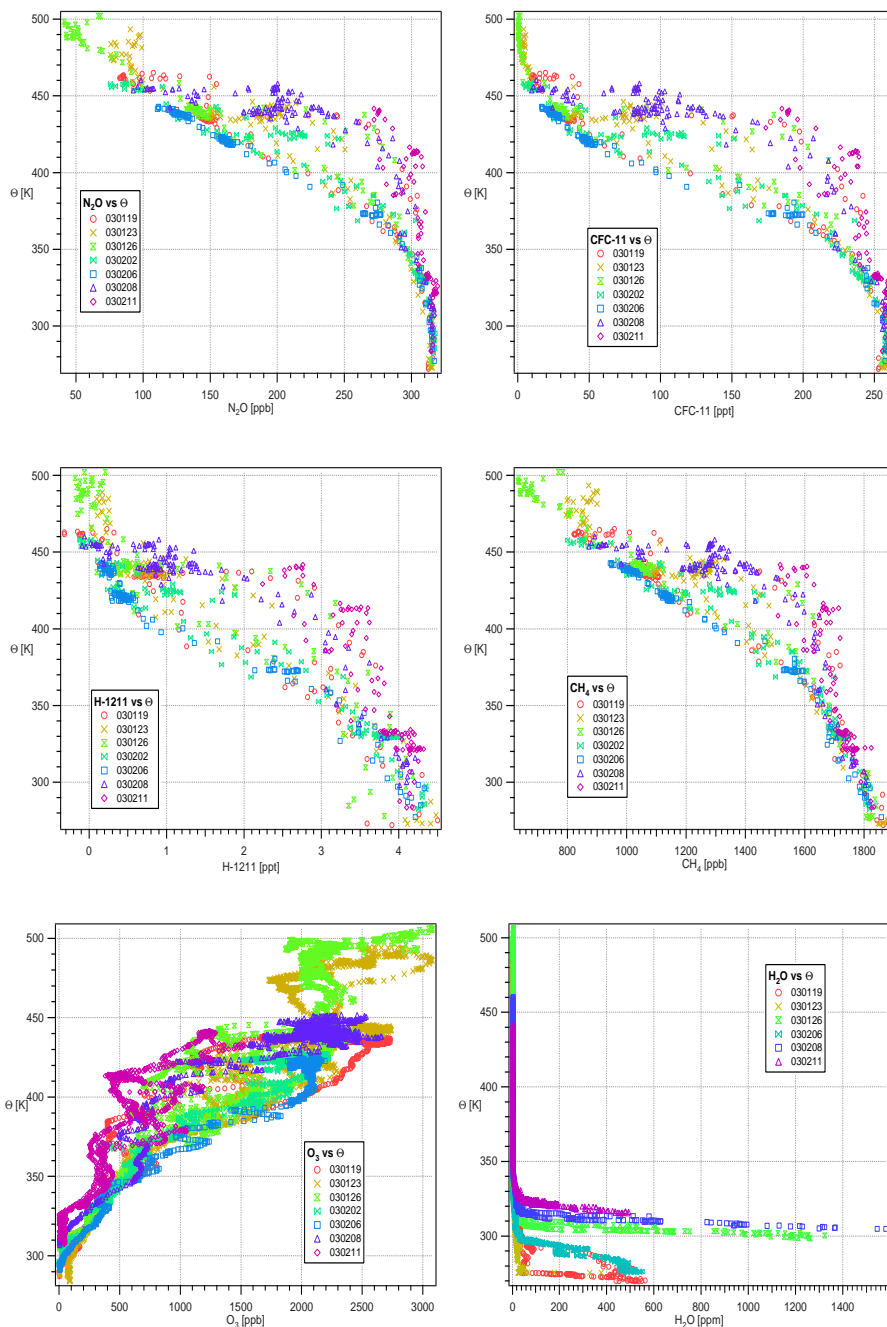


Figure 3.2: EuPLEx tracer mixing ratios plotted versus the potential temperature.



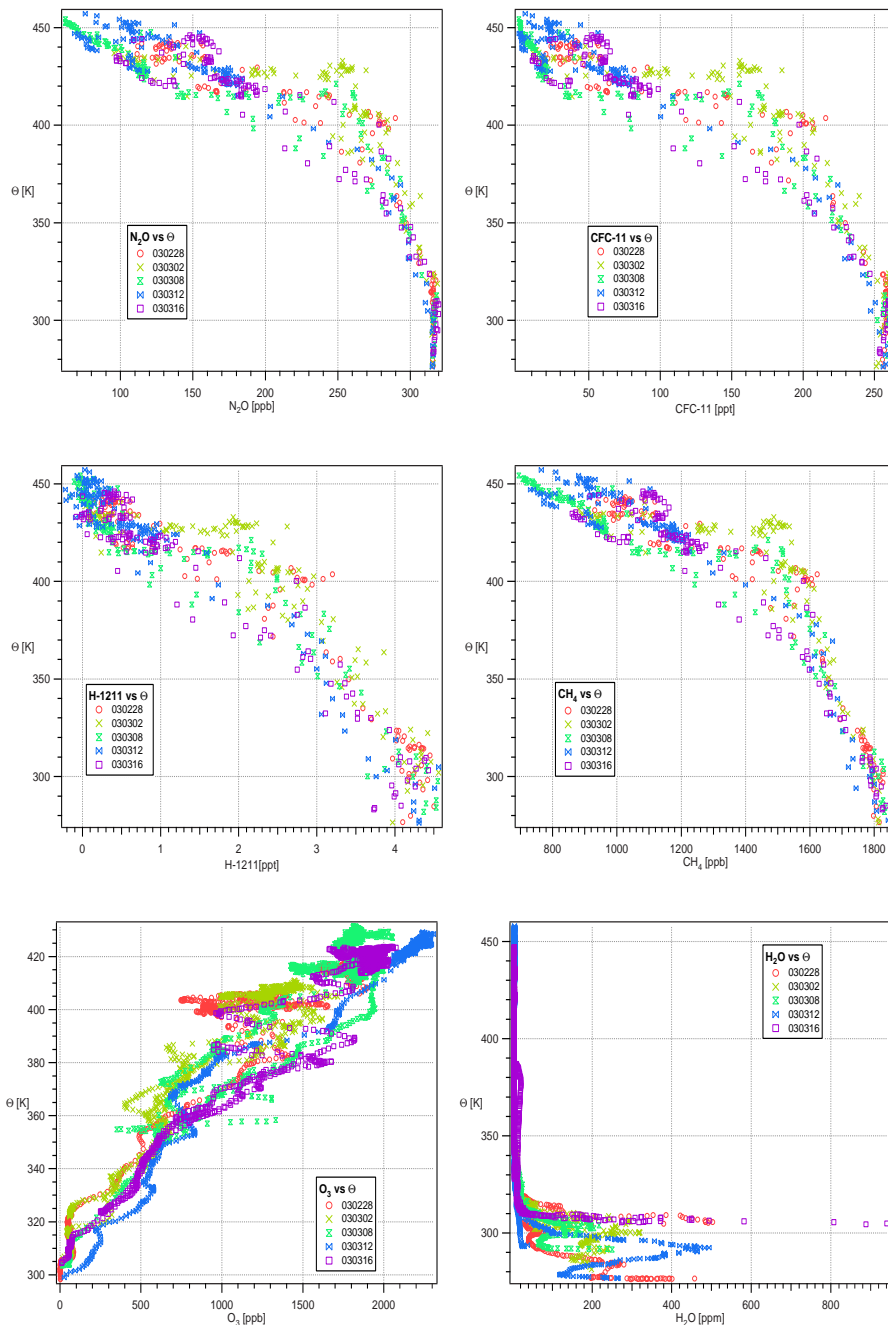


Figure 3.3: AVC tracer mixing ratios plotted versus the potential temperature.

### 3.4 Determining the boundary conditions

This section explains how the boundary conditions for the trace gases mentioned in section 3.3 were determined. Boundary conditions for  $\text{H}_2\text{O}$  represent an exception and will therefore be discussed in a separate section 3.4.5.

All these gases, except  $\text{O}_3$ , are rather long-lived compared to the transport times in the well- and fast-mixed troposphere, and furthermore the tropopause is far away from the source and sink regions of these gases. Thus, spatial and temporal constancy can be assumed for the tropospheric boundary conditions, regarding the transport time scales of less than a few months that are considered in this study. The variability of the tropospheric boundary condition of  $\text{O}_3$ , though being much larger than for the other gases, can still be neglected compared to the differences between the tropospheric and stratospheric mixing ratios.

Since the timescales of transport and mixing in the stratosphere are rather slow compared to the tropospheric ones, tracer measurements at the stratospheric boundary at 400 K at mid latitudes reveal a relatively large variability (see Figure 3.4). However, a comparison of tracer measurements at the 400 K isentrope at mid and high latitudes in autumn and winter (Forlí, 2002; EuPLEx, 2003; and Polaris, 1999) exhibits negligible differences between the seasons. Therefore, the constancy of the stratospheric boundary can also be assumed.

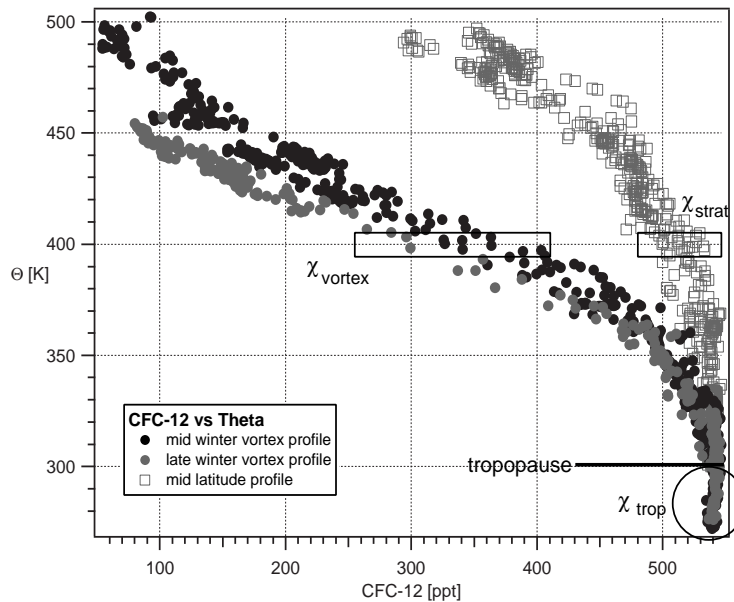


*Figure 3.4:* Vertical profiles of HAGAR CFC-12 (ppt) plotted vs the potential temperature  $\theta$ (K). Black dots indicate a mid winter (EuPLEx) and gray dots a late winter (AVC) profile measured in the vortex region. A mid-latitude profile (October 2002) is displayed as grey squares. The mean tropopause height is indicated at 300 K. The data determining the boundary conditions are highlighted by frames.

The boundary values at the tropopause (for all tracers but H<sub>2</sub>O) and in the stratosphere at 400 K outside the vortex can thus be calculated as the average mixing ratios of the respective tracer data (see sections 3.4.2 and 3.4.4). In Figure 3.4, profiles of CFC-12 versus the potential temperature are shown. The average tropopause height was indicated at 300 K. The data points used to calculate the boundary conditions are enclosed by frames.

In the case of the vortex boundary, tracer mixing ratios are highly variable in time due to the fast subsidence in the vortex region. As seen in Figure 3.4, the vortex profile is changing in time. During winter the profiles steepen and by the end of winter the strongest gradients are reached. This subsidence results in an increase of the O<sub>3</sub> mixing ratio in time, since its mixing ratio is increasing with height. But the fast depletion of O<sub>3</sub>, happening in the polar vortex above 400 K, has to be regarded as well. A variable boundary condition has to be derived that provides distinct values dependent on the time that the descending vortex air has passed the 400 K surface. This will be explained in detail in section 3.4.3.

### 3.4.1 Separating data: Vortex, mid-latitude stratosphere, troposphere

For the determination of the distinct boundary values (section 3.4) and for the interpretation of the data, it is necessary to separate the data into vortex and non-vortex as well as into stratospheric and tropospheric data (section 3.4.1).

In Figure 3.5, the vertical distribution of CFC-11 is plotted versus the potential temperature. The plot includes the data of all flights performed from January to March 2003 during the EuPLEx and AVC campaigns. A wide spread in the data can be seen. This is due to the Geophysica flight path crossing the vortex boundary; measurements were thus performed both inside and outside the vortex. Additionally, changes in mixing ratios are induced during the winter by air subsiding in the polar vortex and by mixing processes; the profiles of the AVC campaign (red) in late winter are therefore generally lower than the EuPLEx profiles (black). A relatively wide spread of nearly 20 ppt is observed in the lowest measurements from 280 K to 330 K. This is the effect of a highly variable tropopause whose height can vary significantly, both within a flight and between the individual flights.

#### Tropospheric measurements

In order to separate tropospheric from stratospheric air, the tropopause height had to be determined. This was achieved with the help of a very useful height coordinate for the tropopause region,  $\Delta\theta$  (see Appendix B.5). This coordinate describes the distance in K (potential temperature) to the local tropopause and was calculated using the tropopause height below the flight path as simulated by the CLaMS model (see Appendix B.8).

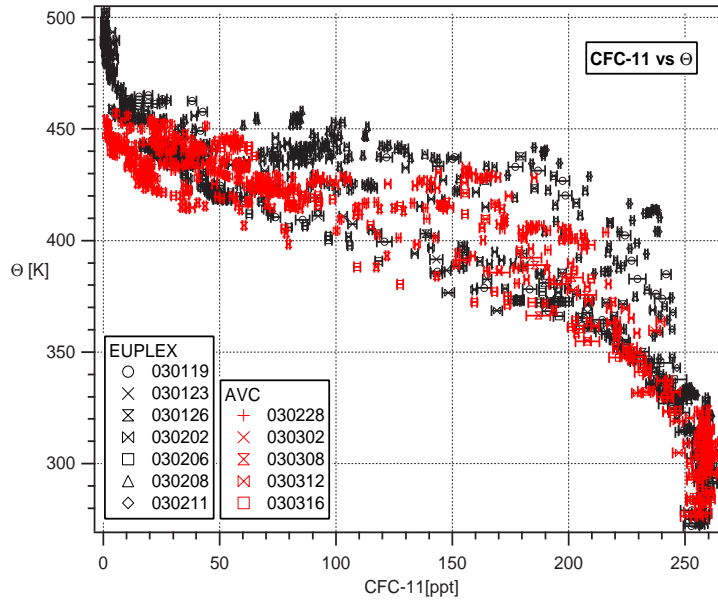


Figure 3.5: HAGAR CFC-11 (ppt) plotted vs the potential temperature  $\theta$  (K). The EuPLEx flights are displayed as black symbols and the AVC flights as red symbols. Error bars represent the precision of the single measurements.

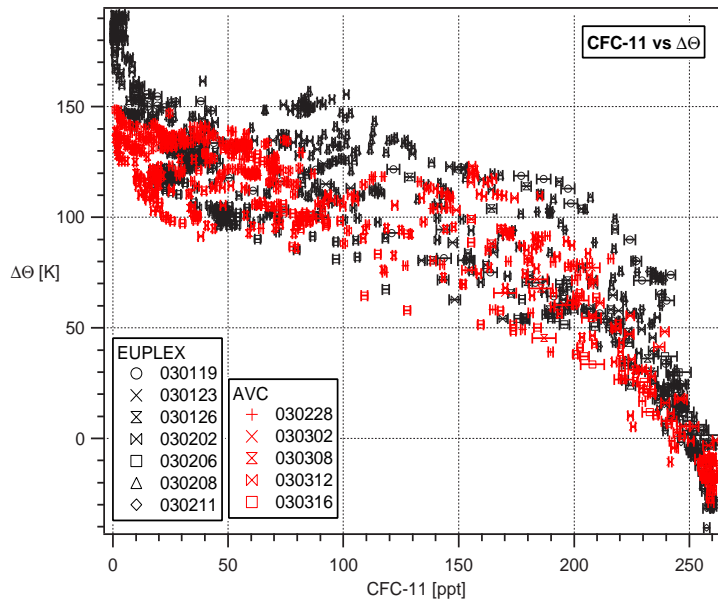


Figure 3.6: HAGAR measurements of CFC-11 plotted vs  $\Delta\theta$ . The EuPLEx flights are displayed as black symbols and the AVC flights as red symbols. Error bars represent the precision of the single measurements.

In Figure 3.6, the CFC-11 distribution from Figure 3.5 is plotted versus  $\Delta\theta$ . All data points below  $\Delta\theta = 0$  K belong to the troposphere.

### Vortex and non-vortex measurements

In the case of the measurements at 400 K, the data have to be separated into vortex and extra-vortex data. Therefore, the equivalent latitude  $\phi_{equiv}$  (see Appendix B.3) of the vortex edge at the  $\theta$  of a given measurement was determined by the Nash criterium [Nash *et al.*, 1996] (see Appendix B.4) from PV data provided by the CLaMS model. In the following, the HAGAR N<sub>2</sub>O data were filtered with respect to the equivalent latitude relative to the vortex edge. In Figure 3.7, N<sub>2</sub>O is plotted versus the potential temperature for all EuPLEx flights. Black circles denote data that are well inside the vortex, i.e. at least 5° equivalent latitude north of the vortex edge as defined by Nash. It can be assumed that this profile represents a vortex profile and that the measured air masses have not experienced any recent mixing with extra vortex air above 400 K. This is consistent with CLaMS calculations, which show a rather isolated polar vortex above 400 K during the EuPLEx campaign, and with findings on vortex mixing and dilution from HAGAR tracer measurements [EuPLEx, 2004].

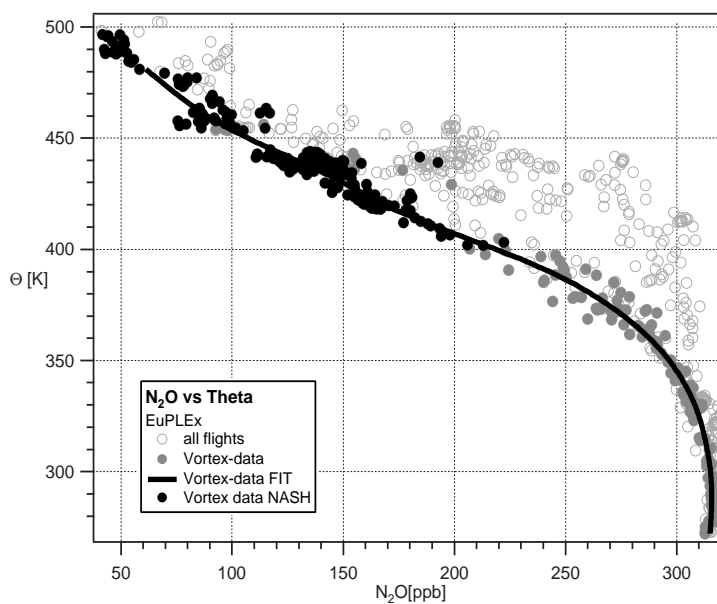


Figure 3.7: HAGAR N<sub>2</sub>O (ppb) measurements during the EuPLEx campaign (grey open circles) plotted versus the potential temperature  $\theta$  (K). Black markers indicate data that were measured well inside the vortex, according to the vortex edge definition by Nash. Grey dots mark vortex or sub-vortex data according to the position of the vortex edge ( $\phi_{equiv} > 67^\circ\text{N}$ ). The fit through these data is displayed as a black line.

The vortex edge according to Nash can only be calculated meaningfully down to

400 K. In order to define a continuous criterium for the whole stratosphere including the LMS, the vortex profile below 400 K was completed with data following the lower envelope of all measurements (marked as grey filled circles in Figure 3.7). These data were measured at an equivalent latitude  $\phi_{equiv} \geq 67^\circ$  N, which was the lowest equivalent latitude at which the vortex edge was located during the EuPLEx campaign. These data were predominantly obtained during the flight of February 6. During this flight, the Geophysica flight path was situated either below or fully inside the polar vortex as can be seen in the PV plot for February 6 at the 450 K level (Figure 3.8). The interpolation of this vortex/sub-vortex data set with a smoothing spline (“vortex-fit”) is plotted as a black line in Figure 3.7.

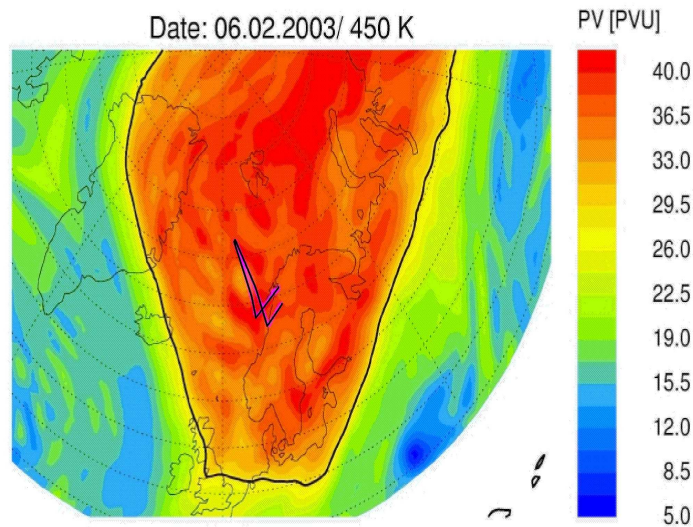


Figure 3.8: PV at 450 K on February 6, 2003. Result of a high-resolution (50 km) CLaMS-2d transport study of PV. The flight path of the Geophysica is plotted in black.

This “vortex-fit” was then used to define a new parameter called  $\Delta N_2O$  (see Appendix B.6), which defines the meridional distance given in  $N_2O$  mixing ratio (ppb) from the  $N_2O$  “vortex-fit” at a given  $\theta$ . Due to the subsidence in the vortex region, distinct vortex profiles had to be determined for each campaign. Thus, similar calculations were performed for the AVC data. The  $\Delta N_2O$  for AVC refers to the AVC vortex profile.

The parameter  $\Delta N_2O$  can be used to divide all tracer data throughout the stratosphere into vortex and non-vortex data [Greenblatt *et al.*, 2002].  $\Delta N_2O$  has two advantages compared to using equivalent latitude to sort the data: (i) it is a quantity directly measured at high resolution rather than a processed low-resolution quantity; (ii) it is directly related to chemical air composition, whereas equivalent latitude is a purely dynamical diagnostic.

In Figure 3.9, the vertical distribution of CFC-11 for all EuPLEx flights is dis-

played. The vertical coordinate is the potential temperature. Data following the “vortex-fit” by  $\pm 20$  ppb are plotted as black filled circles.

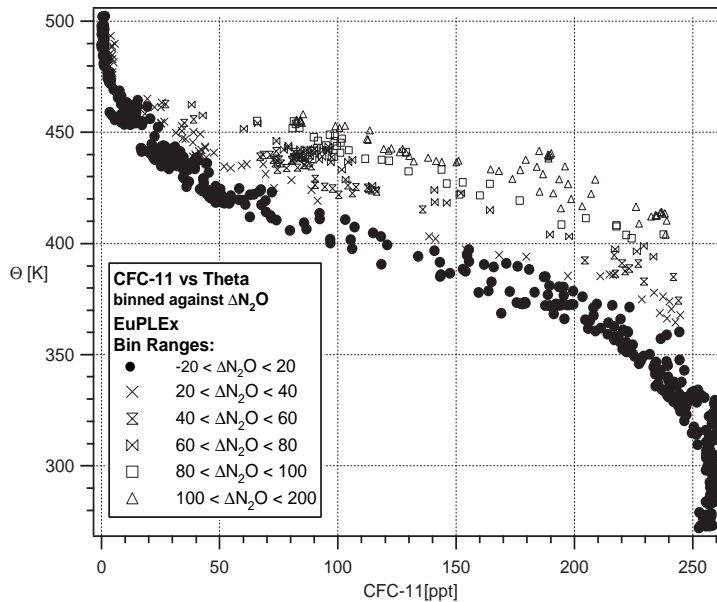


Figure 3.9: HAGAR CFC-11 (ppt) plotted versus the potential temperature for all flights performed during the EuPLEx campaign. The data were binned by  $\Delta N_2O$  as marked by different symbols.

### 3.4.2 Tropospheric boundary condition

The boundary value at the tropopause,  $\chi_{trop}$ , was calculated as the average mixing ratio from tracer measurements with  $\Delta\theta < -10$  K:

$$\chi_{trop} = \overline{\chi(\theta)} \text{ for } \Delta\theta < -10 \text{ K} \quad (3.3)$$

All tropospheric measurements obtained during the mid- (Forlí) and high-latitude measurement campaigns (Kiruna; EuPLEx and AVC) were used for the calculation. In Table 3.2, the resulting tropospheric boundary values are given for all tracers used in the mass balance calculation. Since the troposphere is well mixed, the variability of the tracer measurements inside the troposphere is dominated by the precision of the instrument. The standard deviation of the data, also given in Table 3.2, is thus of the magnitude of the instrumental precisions (about 1% for  $N_2O$ , CFC-11 and  $CH_4$ , and below 4% for H-1211; see Table C.3 in the appendix). This is not the case for  $O_3$  measurements. The vertical gradient of the  $O_3$  mixing ratio in the tropopause region is larger than for the other tracer species. Recent injections of stratospheric air as well as transport of air from polluted areas in the boundary layer can, therefore, lead to strongly elevated  $O_3$  levels compared to the tropospheric background of  $O_3$ .

As a consequence, the standard deviation of the O<sub>3</sub> measurements is about 20% for the FOX measurements (only EuPLEx and AVC data available) and 40% for the FOZAN measurements (instrumental precision 10% [Ulanovsky, 2006]).

Molecule	$\chi_{trop}$	Estimated uncertainty
N <sub>2</sub> O	315.84 ppb	2.16 ppb
CH <sub>4</sub>	1769.01 ppb	26.45 ppb
Halon-1211	4.18 ppt	0.16 ppt
CFC-11	258.3 ppt	2.48 ppt
<i>Ozone<sub>Fox</sub></i>	48.69 ppb	8.3 ppb
<i>Ozone<sub>Fozan</sub></i>	35.4 ppb	14 ppb

Table 3.2: Boundary values at the tropopause for the mass balance tracers N<sub>2</sub>O, CFC-11, Halon-1211, CH<sub>4</sub> and O<sub>3</sub>, and their absolute errors.

### 3.4.3 The vortex boundary condition

During winter, tracer profiles change in the vortex region, where the descent is strongest. In Figure 3.10, all available CFC-11 vortex profiles for the winter 2002/2003 are plotted. In addition to the EuPLEx and AVC campaigns, the measurements of the MKIV<sup>1</sup> instrument from a balloon flight on the 16th of December 2002<sup>2</sup> are available. During this flight, the balloon was well inside the vortex. The MKIV flight was the earliest observation made inside the vortex during that winter and the corresponding tracer profiles describe the initial condition of the early vortex. Figure 3.10 shows that the mixing ratio at the 400 K isentrope  $\chi_{vortex}$  changes significantly during winter season.  $\chi_{vortex}$  for every vortex profile is determined as the average mixing ratio

$$\chi_{vortex} = \overline{\chi(\theta)}, \text{ for } 395 \text{ K} < \theta < 405 \text{ K and } \Delta N_2O < 5 \text{ ppb} \quad (3.4)$$

With several profiles of a tracer inside the vortex during the evolution of the winter, it is possible to determine an average mixing ratio at 400 K as a function of time,  $\chi_{vortex}(t)$ , as plotted for the mass balance tracers in Figure 3.11. In order to synchronize this calculation with the CLaMS simulations, all changes refer to December 1 (see below), when the vortex was already fully developed. The MKIV profiles were used as the corresponding initial tracer profiles on December 1, being the only available vortex measurements in the early vortex. The information on  $\chi_{vortex}(t)$  before December 1 does not explicitly enter the calculation of the vortex boundary values but is important for the form of the fitting function (smoothing

<sup>1</sup>A Fourier Transform InfraRed (FTIR) Interferometer

<sup>2</sup>Launched at Esrangle, Sweden, 67° 53' N, long 21° 04' E



spline). Thus, to complete the set and describe the pre-vortex status in the high-latitude fall, the stratospheric boundary condition (see section 3.4.4 below) was used and regarded as the initial condition at the 400 K isentrope in high latitudes at the end of autumn before the development of the vortex. It was dated the 1st of November, which is an approximate date for the beginning of the descent and the development of the vortex [Müller, 2004].

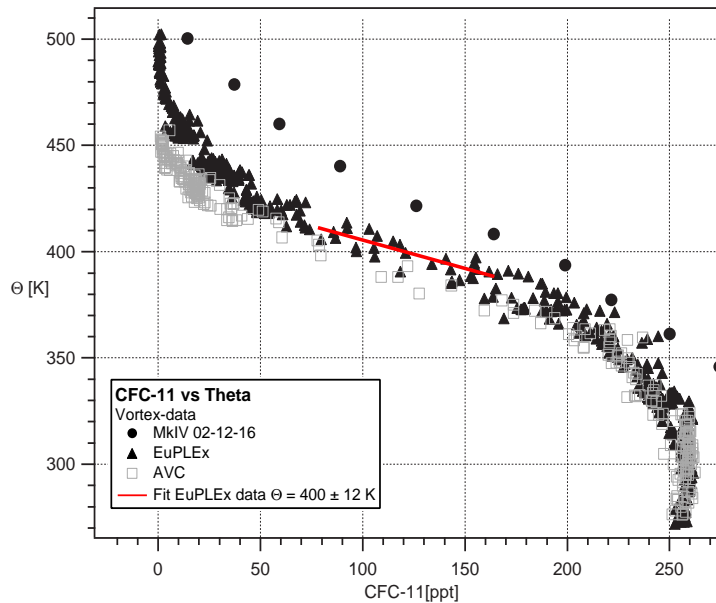


Figure 3.10: HAGAR CFC-11 (ppt) measured inside the vortex plotted versus the potential temperature for the MKIV (black filled circles), the EuPLEx (black triangles) and the AVC (grey open squares) flights.

In order to calculate a corresponding vortex boundary value for every data point in the LMS, the time when the air parcels crossed the 400 K isentrope and thus entered the LMS had to be determined. The necessary information about the descent rates below the vortex were provided by CLaMS calculations initialized on the 1st of December 2002. The trajectories of the descent can be seen in Figure 4.3. Starting from the time and the potential temperature of the measurement, the CLaMS descent rates were used to calculate the time  $t_{400K}$  when an air parcel crossed the 400 K isentrope. With the knowledge of  $\chi_{vortex}(t)$  it is then possible to give the corresponding mixing ratio  $\chi_{vortex}$  at the time  $t_{400K}$  for every data point inside the LMS. In case the air parcel is already found below 400 K on December 1, the corresponding vortex boundary value is set to the mixing ratio at 400 K on December 1. Within its error margins (see below), this mixing ratio is a reasonable proxy for air masses that crossed the 400 K isentrope prior to the 1st of December. Since there were no high-precision measurements in the high-latitude LMS region available prior to December 1, assumptions on the descent and the evolution of the mixing ratios at 400 K in the early, developing vortex would not yield a more accurate estimate.

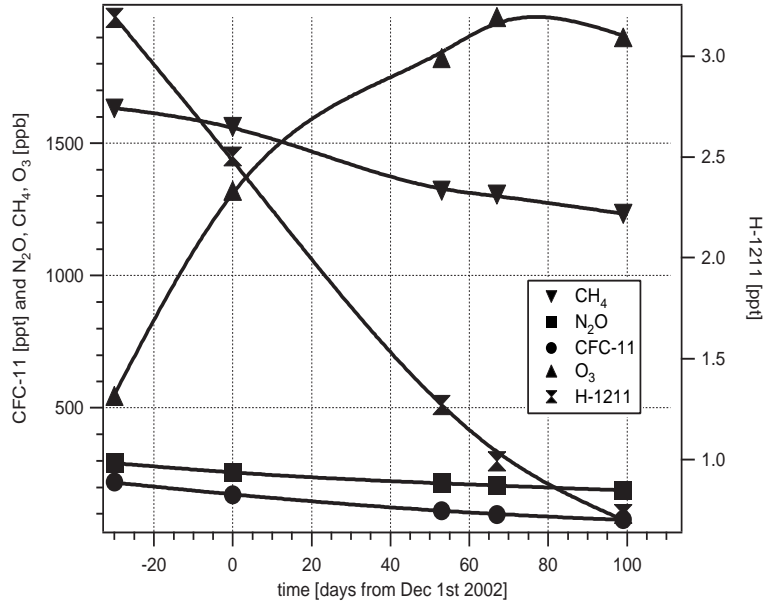


Figure 3.11: Averages of tracers at the 400 K isentrope in the vortex versus the time ( $\chi_{vortex}(t)$ ). The data were fitted with a 4th order Polynomial.

Furthermore, in the early stage of the vortex evolution, the differences between vortex and non-vortex air are small and better captured by the stratospheric boundary condition within its variability (see 3.4.4).

The error of the vortex boundary condition depends on several components:

- errors in the CLaMS descent rates  $\delta\chi_{descent}$ ,
- the atmospheric variability at 400 K  $\delta\chi_{atm}$ ,
- instrumental errors  $\delta\chi_{HAGAR}$  and
- error in the constructed time evolution of  $\chi_{vortex}(t)$ .

The error in the CLaMS descent calculation can be assumed to be about 20 % in the lower stratosphere (conservative estimate). With air parcels descending from the 400 K isentrope by about 60 K during the winter from December 1, 2002 to March 20, 2003, this would lead to an absolute error in the determination of the potential temperature of 12 K. The deduction of descent rates within the isolated vortex from the evolution of tracer mixing ratios yields similar values as the CLaMS simulation. For potential temperature levels between 400 K and 450 K the average descent was found to be about 50-55 K between the MKIV and the AVC profile, resulting in an average deviation from the CLaMS descent of no more than 10 K. (Below 400 K, descent rates cannot be derived in the same way from measurements, because of the influence of mixing processes).

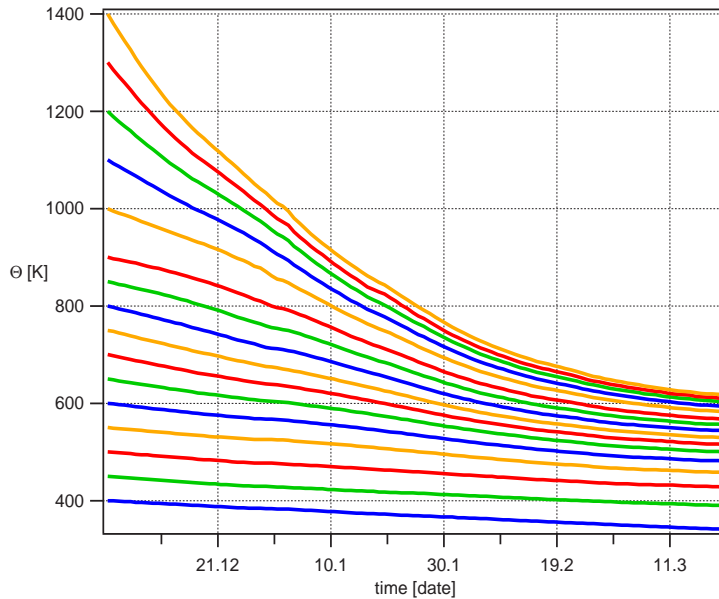


Figure 3.12: Trajectories by the CLaMS model starting on December 1, 2002.

The estimated descent error of 12 K will be most representative for air located at 340 K (having descended from  $400 \pm 12$  K). Air that is closer to 400 K would be affected by a smaller error, whereas the error might increase for air below 340 K. To simplify matters, 12 K was used as the error for the whole range. An error of 12 K in the determination of the average mixing ratio at 400 K translates into an error in mixing ratio at 400 K dependent on the local vertical gradient of a tracer. This local gradient can be described best by a linear fit of the data  $400 \text{ K} \pm 12 \text{ K}$  (red line in Figure 3.10). The error due to errors in the descent calculation is then calculated as

$$\delta\chi_{descent} = \frac{|MAX - MIN|_{fit}}{2} \quad (3.5)$$

The atmospheric variability leads to scatter of the data around the fit. This can be described by subtracting the fit from the data and calculating the standard deviation of the residuals:

$$\delta\chi_{atm} = \sigma(\chi - \chi_{fit}) \quad (3.6)$$

As the measurements are performed, in the worst case, with a precision of 3 % (H-1211), the error in the measurement can be neglected compared to  $\delta\chi_{descent}$  and  $\delta\chi_{atm}$ . The dominant factor is the error in the determination of the descent inside the vortex.

The error in the constructed time evolution of  $\chi_{vortex}$  (Figure 3.11) is hard to assess. Due to the sparsity of the available tracer measurements, the form of the fit function is arbitrary. Thus, the time of a tracer mixing ratio at 400 K is certainly only a rough estimate. However, given the smooth forms of the simulated descent trajectories (Figure 4.3) and of the observed profiles (Figure 3.10), it is clear that

a smooth interpolation between the various measurements (Figure 3.11) will be a reasonable estimate for  $\chi_{vortex}(t)$ . Furthermore note, that an error in  $\chi_{vortex}(t)$  will have a similar effect as an error in  $t_{400}$ , which is accounted for in  $\delta\chi_{descent}$ . Considering that  $\delta\chi_{descent}$  was estimated quite conservatively, the error in  $\chi_{vortex}(t)$  will not be considered explicitly here.

The total error as displayed in Table 3.3 of the vortex boundary condition is thus estimated as

$$\delta\chi_{vortex} = \sqrt{\delta\chi_{descent}^2 + \delta\chi_{atm}^2} \quad (3.7)$$

Molecule	Estimated uncertainty
N <sub>2</sub> O	32 ppb
CH <sub>4</sub>	131 ppb
Halon-1211	0.64 ppt
CFC-11	45 ppt
Ozone <sub>Fox</sub>	452 ppb
Ozone <sub>Fozan</sub>	407 ppb

Table 3.3: Estimated errors in the boundary values at the vortex at 400 K for the mass balance tracers N<sub>2</sub>O, CFC-11, Halon-1211, CH<sub>4</sub> and O<sub>3</sub>.

### 3.4.4 The stratospheric boundary condition

For the calculation of the boundary value at 400 K outside the vortex, data are favoured for which no vortex influence can be detected. This is certainly the case for the tracer data obtained during the mid-latitude campaign in October 2002 in Forlí. Additionally, it is of interest to have extra-vortex data from the high-latitude winter. In Figure 3.13, EuPLEx and AVC CFC-11 data are plotted versus the equivalent latitude between 395 and 405 K potential temperature. During these measurements the southernmost occurrence of the vortex edge, which is indicated by the grey vertical line, was at an equivalent latitude of about 65° N. The CFC-11 data were binned by  $\Delta N_2O$  and it is obvious that EuPLEx data with a  $\Delta N_2O > 60$  ppb and high mixing ratios are found at low equivalent latitudes and thus far from the vortex edge. These tracer data can therefore be considered as high-latitude air that is not influenced by any mixing with vortex air. During the AVC campaign, the same separation cannot be performed with success. Due to ongoing mixing processes and perforation of the vortex edge at the end of the winter [EuPLEx, 2004], relatively low mixing ratios are measured at about  $\chi_{equiv} = 60^\circ$  N, while the high latitudes exhibit rather high mixing ratios. Thus, for the determination of the stratospheric boundary condition, EuPLEx data with a  $\Delta N_2O > 60$  ppb were used together with data from the mid-latitude campaign in Forlí in October. A comparison with high-latitude tracer measurements by the ACATS instrument

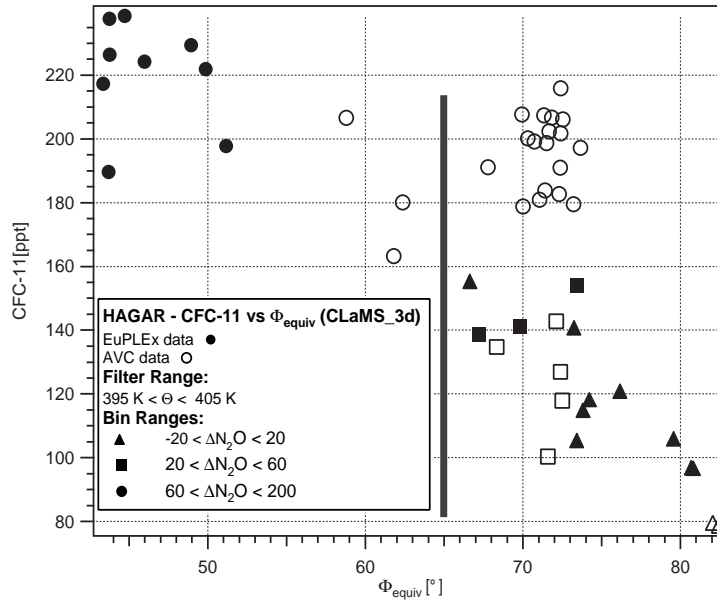


Figure 3.13: HAGAR CFC-11 plotted versus equivalent latitude (from 3D calculations by CLaMS) for data measured at potential temperatures  $395\text{ K} < \Theta < 405\text{ K}$ . The data were binned by  $\Delta N_2O$ . Filled symbols denote EuPLEX and unfilled symbols AVC data. The grey vertical line indicates the lowest latitude at which the vortex edge occurred during the measurements.

[Elkins *et al.*, 1996] in September 1997 during the POLARIS<sup>3</sup> mission shows good agreement with the EuPLEX extra-vortex data and the Forlí data, and differences between the data sets are negligible.

The stratospheric boundary value  $\chi_{strat}$  is calculated as

$$\chi_{strat} = \overline{\chi(\theta)}, \text{ for } 395\text{ K} < \theta < 405\text{ K and } \Delta N_2O > 60\text{ ppb} \quad (3.8)$$

In Table 3.4, the stratospheric boundary values for all mass balance tracers are listed. As the mixing ratio in the stratosphere depends on the transport history of an air parcel (mid- and high-latitude data) and the mixing processes are not as fast as in the troposphere, the tracer measurements show a distinct variability larger than the instrumental precision. Furthermore, there is only a limited number of measurements in this region over high latitudes. The standard deviation of the data would be likely to underestimate the atmospheric variability. The error is therefore more conservatively described by the half of the total span  $\frac{|max-min|}{2}$  of the data points used for the calculation of the mean at 400 K. The resulting uncertainties are specified in the last column of Table 3.4.

<sup>3</sup>Photochemistry of Ozone Loss in the Arctic Region In Summer

Molecule	Average	Estimated uncertainty
N <sub>2</sub> O	299.17 ppb	18.35 ppb
CH <sub>4</sub>	1655.52 ppb	105 ppb
Halon-1211	3.45 ppt	0.78 ppt
CFC-11	230.64 ppt	32.75 ppt
<i>Ozone<sub>Fox</sub></i>	522.65 ppb	347.3 ppb
<i>Ozone<sub>Fozan</sub></i>	516.1 ppb	300 ppb

Table 3.4: Boundary values at the mid- to high-latitude stratosphere for the mass balance tracers N<sub>2</sub>O, CFC-11, Halon-1211, CH<sub>4</sub> and O<sub>3</sub>, and their absolute errors.

### 3.4.5 Boundary conditions for H<sub>2</sub>O

The tropospheric boundary value of H<sub>2</sub>O has to be regarded separately from the other tracers, since H<sub>2</sub>O has a different transport history. The quantity of H<sub>2</sub>O that enters the stratosphere by crossing the tropopause depends on the temperature at the tropopause. Thus, the entry mixing ratio of H<sub>2</sub>O is not a constant but a function of time and potential temperature. The values used in this work were derived from a climatology of H<sub>2</sub>O entry values by *Krebsbach* [2005] based on measurements performed in the UT/LS region during the SPURT [*Engel et al.*, 2006] (see also section 4.4.1) and POLSTAR<sup>4</sup> campaigns. Only autumn and winter data were used (October-February). The derived entry function  $H_2O_{entry}(\theta)$  for the LMS is displayed in Figure 3.14 together with H<sub>2</sub>O measurements obtained during the EuPLEX and AVC campaigns, provided by the FISH instrument (see Table 2.8 in section 2.3.1).

With this entry function, a H<sub>2</sub>O entry value can be given for every potential temperature between 300 K and 380 K. Above 380 K, the entry value of H<sub>2</sub>O is set constant at 3.5 ppm, since transport through the cold tropical tropopause certainly leads to the lowest entry values.

The error of the H<sub>2</sub>O boundary value was estimated separately for three potential temperature regions as the standard deviation of the residuals from the fit within each region:

- $\theta < 340\text{ K}$  : 10 ppm
- $340\text{ K} < \theta < 360\text{ K}$ : 6 ppm
- $\theta > 360\text{ K}$ : 1 ppm

---

<sup>4</sup>Polar Stratospheric Aerosol Experiment; 1997/98

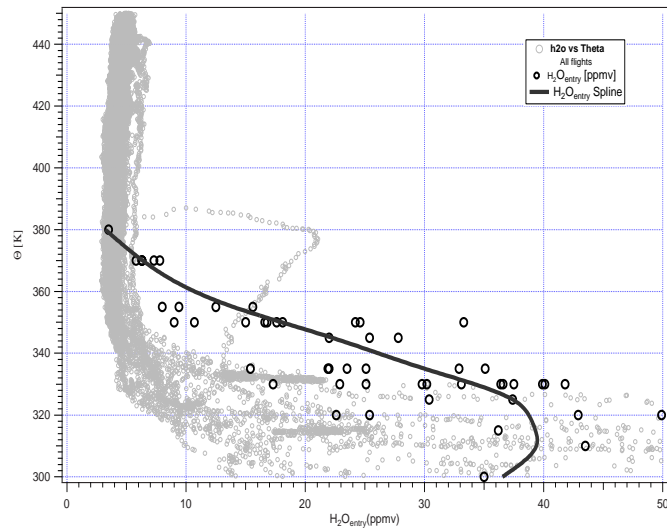


Figure 3.14:  $\text{H}_2\text{O}$  data plotted versus the potential temperature. Small grey circles show FISH data during the EuPLEx/AVC campaigns, large black circles mark the  $\text{H}_2\text{O}$  entry values given by *Krebsbach* [2005] and the black line denotes the  $\text{H}_2\text{O}$  entry fit,  $H_2O_{\text{entry}}(\theta)$ , used to derive tropospheric boundary values.

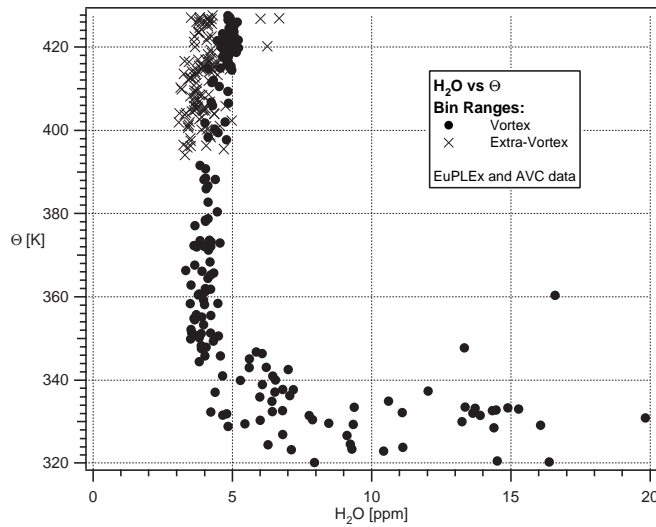


Figure 3.15: FISH  $\text{H}_2\text{O}$ (ppm) data during EuPLEx and AVC plotted versus the potential temperature  $\theta$  (K). Black circles mark data with  $-25 < \Delta N_2O < 5$  ppb and grey crosses mark the data with  $\Delta N_2O > 60$  ppb.

The stratospheric and vortex boundary values of H<sub>2</sub>O are determined more easily as H<sub>2</sub>O is almost constant at values of 3-6 ppm above 400 K. A separation between vortex and stratospheric data, as displayed in Figure 3.15, can again be made based on  $\Delta N_2O$ . The FISH data were split up into vortex data with a  $\Delta N_2O$  between -25 and 5 ppb and non-vortex data with a  $\Delta N_2O$  larger than 60 ppb. The resulting value for the stratosphere at 400 K outside the vortex is 3.8 ppm and the value for the vortex at 400 K is 4.4 ppm. Both values were calculated as the averages between 395 K and 405 K.

The variability of the H<sub>2</sub>O mixing ratio at 400 K — corresponding to the error of the boundary values in this region — is derived from the standard deviation of the measurements. Part of this variability can be explained by the instrumental precision, which is usually 0.15 ppm but can be slightly elevated, when the measurements were noisy [Rohs, 2006]. The rest of the variability can be explained by the atmospheric variability. For the vortex measurements, the standard deviation was calculated between potential temperatures of 388 K and 412 K (see section 3.4.3) as 0.32 ppm. For extra-vortex data, the error was found to be 0.5 ppm between 395 K and 405 K (see section 3.4.4).

### 3.5 Normalization of the tracer data

The mixing ratios of the used tracers span two orders of magnitude (ppt-ppm). In order to remove the influence of the size of absolute values of the different tracer mixing ratios on the numerical solution of the mass balance equation, the data had to be normalized. The data were normalized relative to the span of mixing ratios which are considered in the LMS mass balance study following equation 3.9:

$$\chi_{norm} = \frac{\chi - \widetilde{\chi}_{vortex}}{\chi_{trop} - \widetilde{\chi}_{vortex}} \quad (3.9)$$

with

$\chi_{norm}$  = normalized tracer mixing ratio

$\chi$  = tracer mixing ratio

$\widetilde{\chi}_{vortex}$  = average mixing ratio at the vortex boundary in the middle of the winter 2002/2003, i.e. during EuPLEx

$\chi_{trop}$  = average mixing ratio at the tropopause.

This normalization results in values changing from about zero in the vicinity of the vortex boundary to about 1 at the tropopause. Now, every tracer enters the mass balance equation with the same weight, while the characteristic structure of each tracer in the LMS is preserved. In Figure 3.16, the normalized CFC-11 and O<sub>3</sub> data are displayed versus the potential temperature.

In addition to the above normalization, a weighting of the single tracer equations is of advantage, since not every tracer provides information for the solution of the



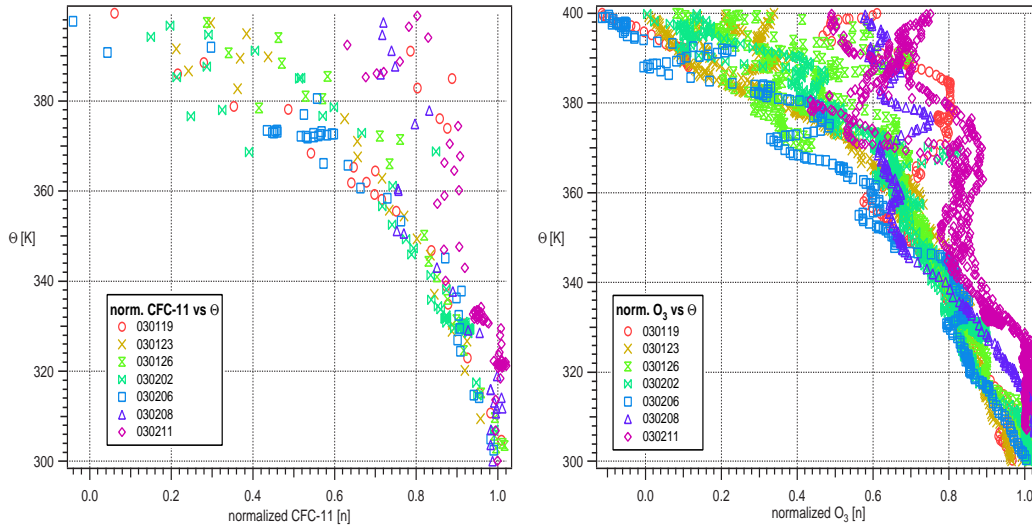


Figure 3.16: Normalized profiles of HAGAR CFC-11 and FOX  $O_3$  versus the potential temperature  $\theta$ (K).

linear equation system with the same quality. As a measure for this quality, the relation of the normalized error at the worst defined boundary ( $\chi_{norm,max}$ ) was used. The mass balance equation of each tracer was thus multiplied with a weighting factor  $W$ :

$$W = \frac{1}{\delta\chi_{norm,max}^2} = \frac{1}{\left[\frac{\chi_{max}}{\chi_{trop} - \chi_{vortex}}\right]^2} \quad (3.10)$$

The resulting weighting factors for all mass balance tracers are given in Table 3.5.

Molecule	W
$N_2O$	11.11
$CH_4$	11.11
H-1211	20.66
CFC-11	11.11
$O_3$	16
$H_2O$	16

Table 3.5: Weighting factors for the mass balance calculation for  $N_2O$ ,  $CH_4$ , H-1211, CFC-11,  $O_3$  and  $H_2O$ .

$H_2O$ , H-1211 and  $O_3$  are the more weighted tracers and will have a slightly stronger influence on the solution of the linear equation system. The strongest influence is given to the mass balance equation  $\Sigma f_i = 1$  (section 3.2), since this constraint has no associated uncertainty, but describes the physical necessity that the sum of all three fractions has to equal one. For the presented results, this

equation was weighted with  $W = 10^8$ ; the results are insensitive to the absolute value of  $W_{mass}$  as long as  $W_{mass} \gg W_{tracers}$ .

### 3.6 Sensitivity of the calculation to errors in the boundary conditions

The solution of the linear equation system is highly sensitive to the values of the boundary conditions. In order to analyse this sensitivity, a Monte Carlo simulation was performed. The linear equation system was solved with simultaneously varying boundary values. Each boundary value was randomly varied according to a Gaussian probability distribution, centered on its nominal value with a standard deviation equal to its estimated uncertainty as given in Tables 3.4, 3.8 and 3.3 in section 3.4. In practice the procedure is as follows:

A random numbers generator (function “*gnoise*”; [*Wave Metric*, 2000]) generates a random value (called “*random*”) according to a Gaussian distribution (centered on 0) such that the standard deviation of an infinite number of such values would be 1, i.e.  $\overline{random} = 0$ ;  $\sigma_{random} = 1$ . This value is then multiplied with the error of the boundary condition ( $\delta\chi_b$ ) of each tracer, and the product is added to the corresponding nominal value of the boundary condition ( $\overline{\chi_b}$ ).

The tropospheric boundary value is varied simultaneously and independently for each tracer:

$$\chi_{trop,i} = \overline{\chi_{trop,i}} + random_i \times \delta\chi_{trop} \quad (3.11)$$

In case of the stratospheric boundary values in- and outside the vortex, the dominant factor for the uncertainty at the boundary  $b$  for most tracers is the atmospheric variability, which causes correlated variations of tracer mixing ratios. Thus, the simultaneous variation of the boundary conditions has to be performed in a way that preserves the correlation between the different tracers. This is achieved by synchronizing the variation of the tracers by using the same random value “*random*” for all of them:

$$\chi_{b,i} = \overline{\chi_{b,i}} + random \times \delta\chi_b \quad (3.12)$$

with  $b = \text{vortex or strat.}$

$O_3$  is an exception as its correlation with the other tracers is negative, thus “*random*” is replaced by “*-random*” in case of  $O_3$ .

Another exception is  $H_2O$  which is varied independently of the other tracers, i.e. an independent random variable “*random<sub>H2O</sub>*” also for the variation of the vortex and stratospheric boundary values.

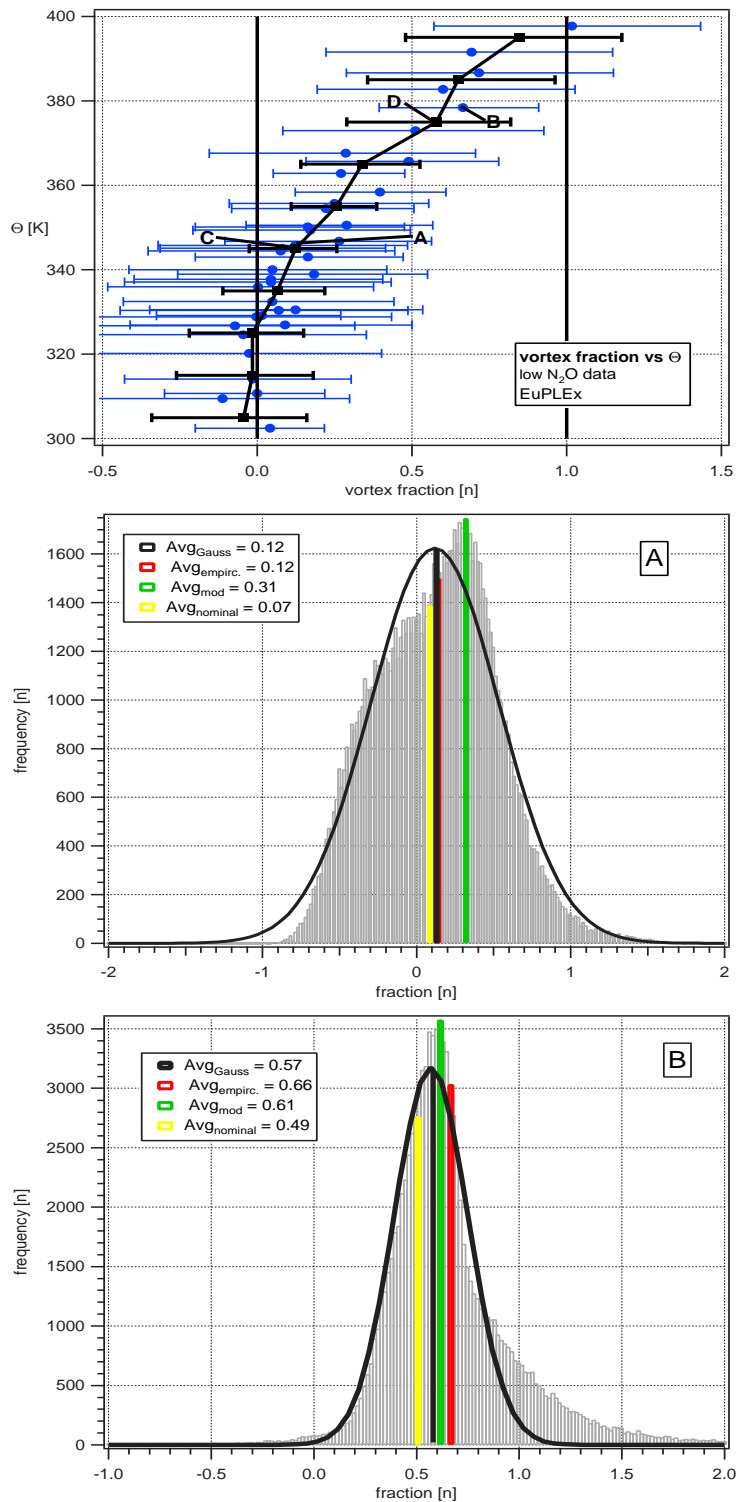


Figure 3.17: Histograms (grey bars in the lower panels) of the Monte Carlo calculation for points (A) and (B), which are shown in an exemplary vertical profile of the vortex fraction (upper panel). Fitted theoretical Gaussian curves are displayed as black lines. Also shown are the average of the Gaussian curve (black bar), empirical average of the distribution (red bar), modulus (green bar) and the result of the calculation using nominal values for the boundary conditions (yellow bar).

All boundary values were varied simultaneously for all tracers according to equations 3.11 and 3.12. The whole procedure was performed  $10^5$  times for each single data point in order to get reliable statistics. An exemplary  $\theta$  profile of the vortex fraction is shown in the upper panel of Figure 3.17. The error bars shown for each data point range from the 16th to the 84th percentiles of the distribution of the results for the  $10^5$  calculations. The histograms of the distributions for two individual data points, A and B, are shown in the lower panels of the figure. The distributions for different data points vary strongly from each other. Furthermore, they vary significantly in shape and spread from the theoretical Gaussian distribution that is plotted for comparison (black curve). The chi-square test of goodness of fit rejected the Gaussian distribution for the histograms shown in Figure 3.17. Since the distribution is not Gaussian, the arithmetic average is not necessarily the expectation value of the distribution. Thus, modus (green), average (red) and the result of the nominal calculation (one time calculation with the nominal boundary conditions given in yellow) differ from each other. Other theoretical distributions, Weibull and Gumbel, were also fitted to the empirical distributions, but both were rejected by statistical testing (Kolmogorof-Smirnoff-test). For the presentation of the results, the average values of the Monte Carlo simulation will be shown in the following section 3.7. The corresponding error bars are defined as the range from the 16th to the 84th percentile of the distribution, where the lowest and highest 16% of the data are cut off (corresponding to  $\pm 1\sigma$  for a Gaussian distribution).

### Calculating a weighted average profile

For the presentation of the results in the following sections, average vertical profiles were calculated in steps of 10 K from 305 K to 395 K potential temperature. For each averaging interval, cumulative histograms were calculated for the results of all data points ( $10^5$  calculations per data point) falling into the interval  $X \pm 5K$ . The average of the cumulative histogram is then taken as the average result within the  $\theta$ -interval. Error bars represent  $1/\sqrt{n}$  ( $n$  = number of points in the averaging interval) of the difference between the average and the 16th (lower error bar), respectively the 84th percentile (upper error bar) of the cumulative histogram. This error was chosen as an approximation to the  $1\sigma$  error of the mean value, as used in Gaussian statistics. The factor  $1/\sqrt{n}$  accounts for the error cancellation between  $n$  independent data points with Gaussian error distribution. Since the errors in the boundary values largely occur due to atmospheric variability and instrumental precision, the errors of the results for the individual data points can be regarded as independent.

By using the information of the Monte Carlo simulation, the error of each data point (spread and shape of its distribution) is automatically included and the resulting average is a weighted average taking into account both the spread between the data points and the errors of the single data points. Again, the arithmetic average is used, although the frequency distributions for the individual data points are not Gaussian. Following the central limit theorem [Bosch, 1995] the sum of  $n$

independent random variables with existing average and variance is a Gaussian variable. However, due to the limited number of measurements,  $n$  is not large enough to fulfill this constraint and the cumulative histogram is not necessarily normally distributed.

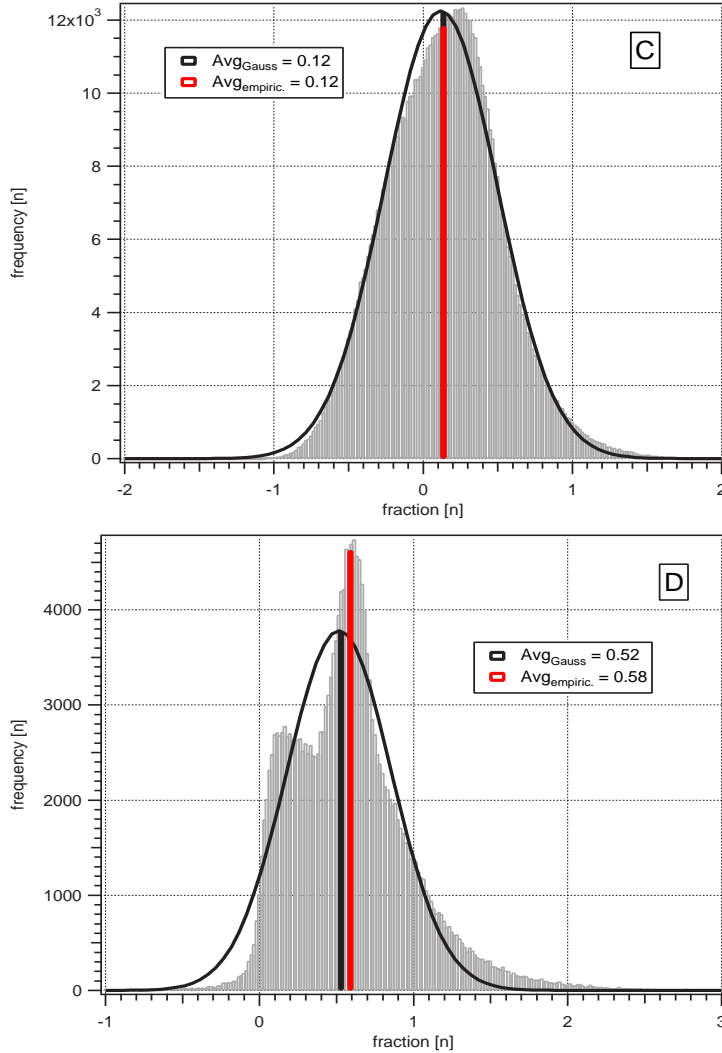


Figure 3.18: Cumulative histograms are shown for points (C) and (D) in the averaged vertical profile of the vortex fraction shown in Figure 3.17. The average of the Gaussian curve (black bar) and the empirical average (red bar) are added.

In Figure 3.17, an exemplary  $\theta$  profile of the vortex fraction is shown. The results were averaged as described and the average profile is added in black. Error bars range from the 16th respectively the 84th percentile scaled by  $1/\sqrt{n}$ . For two of the averages (points C and D), the corresponding cumulative frequency distributions are shown in Figure 3.18. The difference between the average of the cumulative histogram (grey bars) and the theoretical Gaussian distribution (red line) appear

insignificant for point C. For point B, which is based on the sparse statistics of two points, there is a rather large difference between both averages; the  $\chi^2$ -test rejects the Gaussian distribution in both cases. However, for lack of a better parameter and in order to use a consistent method for all points, the arithmetic average is applied.

## 3.7 Results of the mass balance calculation

In this section, the results of the mass balance calculation are presented for each campaign. The linear equation system that was introduced in the preceding sections was solved using the normalized mixing ratios (see section 3.5) of the tracers  $\text{N}_2\text{O}$ ,  $\text{CH}_4$ , CFC-11, Halon-1211,  $\text{O}_3$  and  $\text{H}_2\text{O}$ .

The fractions of air originating from the troposphere and the stratosphere above 400 K inside and outside the vortex region are plotted versus the potential temperature. For each fraction, the individual results of each data point are given as well as an average profile. The average profile was calculated as described in section 3.6. Error bars of the results range from the 16th to the 84th percentile of the Monte Carlo simulation; additionally, the error bars of the average profiles are divided by  $\sqrt{n}$ ,  $n$  giving the number of data points used for averaging (also described in section 3.6).

First, two extreme sub-sets of the data are considered separately:

- i) heavily vortex-influenced data below the vortex and
- ii) LMS data with little vortex influence.

The division of the data into these sub-sets is achieved by establishing an upper envelope and a lower envelope profile. In Figure 3.19, the CFC-11 mixing ratio is plotted versus the potential temperature  $\theta$ . The data of the lower envelope profile (hereafter called “low  $\text{N}_2\text{O}$  data”), which includes all data points with a  $\Delta\text{N}_2\text{O}$  between -25 and +5 ppb, are enclosed by black squares. Data belonging to the upper envelope profile (hereafter called “high  $\text{N}_2\text{O}$  data”), which are determined using the parameter  $\Delta\text{N}_2\text{O}_{extra}$  (see Appendix B.7), are enclosed by black circles.

After a look at the fraction versus  $\theta$  profiles for the two data sub-sets, the fractions for the complete data set in the LMS are displayed in a  $\theta$  versus  $\phi_{equiv}$  plot. This gives a more general overview on the composition of the LMS. All results shown were filtered between 300 K and 400 K potential temperature and only those data with  $\Delta\theta > 0$  K were plotted, thus providing pure LMS data between the tropopause and the 400 K isentrope. In Figure 3.20, such a  $\theta$  versus  $\phi_{equiv}$  plot is shown for the CFC-11 mixing ratio, which is indicated by colour code. Again, the data of the “low  $\text{N}_2\text{O}$ ” (“high  $\text{N}_2\text{O}$ ”) profile are enclosed by squares (circles).

In this illustration, differences between the data of the two campaigns become obvious. During the EuPLEx campaign the observed spread in CFC-11 mixing ratio correlates well with the spread in equivalent latitude. Above 350 K, measurements were taken either at low equivalent latitude between  $35^\circ$  and  $51^\circ$  or at high equivalent latitude between  $63^\circ$  and  $80^\circ$ . In between — below the vortex edge region (roughly  $\phi_{equiv} \approx 65^\circ$  for  $\theta \geq 400$  K) — only few measurements were taken. This is slightly different for the measurements taken during the AVC campaign. The bulk of the measurements are distributed evenly between  $50^\circ$  and  $80^\circ$ , with many data points in the vicinity of the equivalent latitude, where the vortex edge can be found above 400

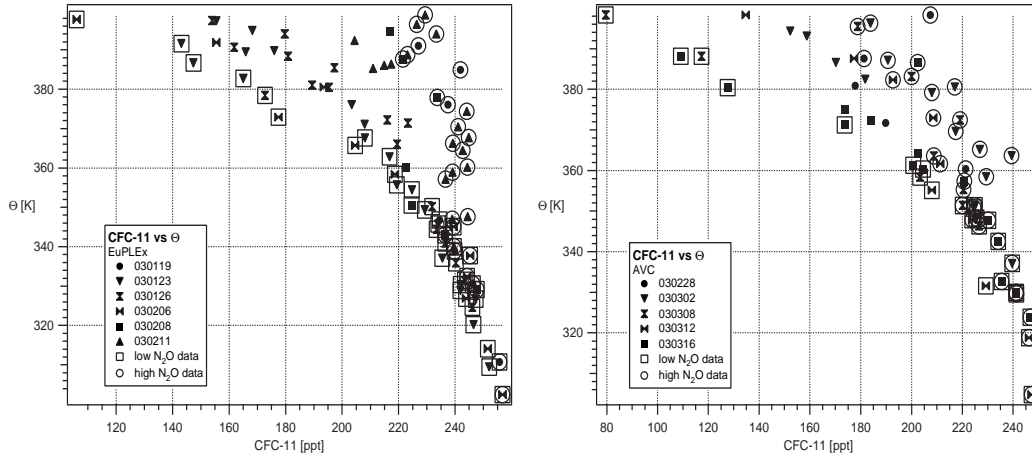


Figure 3.19: CFC-11 (ppt) plotted versus the potential temperature  $\theta$  (K) in the LMS for EuPLEX (left) and AVC (right). The “low  $N_2O$ ” ( $-25 \text{ ppb} < \Delta N_2O < +5 \text{ ppb}$ ) data are highlighted by black squares and the “high  $N_2O$ ” ( $-5 \text{ ppb} < \Delta N_2O_{extra} < +25 \text{ ppb}$ ) data are highlighted by black circles.

K. In contrast to the EuPLEX data, “low  $N_2O$ ” and “high  $N_2O$ ” data are not well separated above 350 K. “High  $N_2O$ ” data points can frequently be found below the vortex. By March, stirring in the LMS has apparently managed to distribute both vortex-influenced and non-influenced air widely from mid to high latitudes. By this time, the vortex had weakened and some in-mixing of extra-vortex air was observed for  $\theta > 400 \text{ K}$  [EuPLEX, 2004].

At this point it should be kept in mind that the mass balance results simply represent the fractions of air that were transported through the tropopause or through the 400 K isentrope in or outside the vortex region. Thus, the vortex fraction is not necessarily the fraction of originally pure vortex air, but the fraction of air that descended through the 400 K isentrope in the vortex region. In case extra-vortex air has mixed into the vortex region above 400 K, the calculated variable vortex boundary condition already includes this effect and it will not be detected as an increase in the stratospheric fraction at the expense of the vortex fraction. However, vortex air mixed into the extra-vortex stratosphere above 400 K which further on descends into the extra-vortex LMS, will be detected as an increase in the vortex fraction because the extra-vortex boundary is kept constant at typical extra-vortex values. This finally means that an increased vortex fraction signifies that vortex air has been transported or mixed into the LMS, but the path it took — directly from the vortex region or via the extra-vortex stratosphere — cannot be determined.

### 3.7.1 EuPLEX

In Figure 3.21, the results of the mass balance calculation are shown for the EuPLEX campaign. The results are given separately for each fraction (tropospheric, strato-



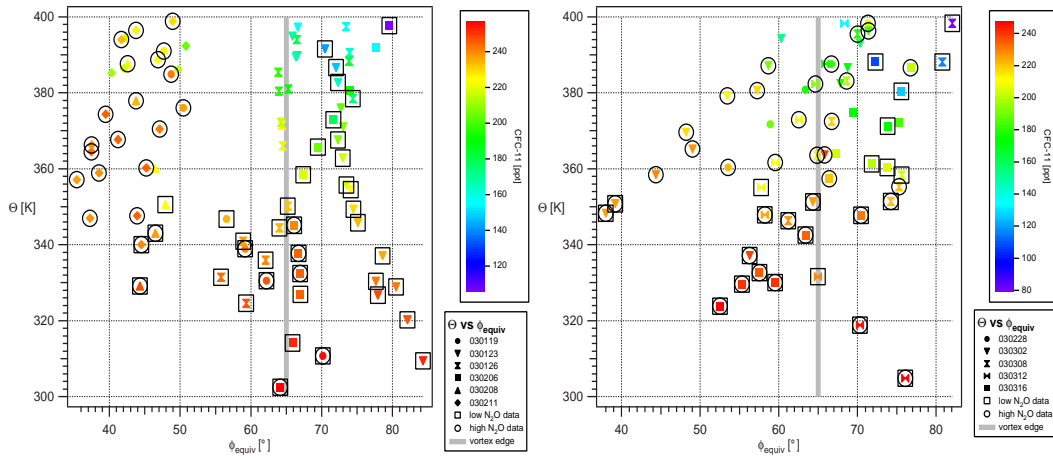


Figure 3.20: Potential temperature  $\theta$  (K) plotted versus the  $\phi_{equiv}$  ( $^{\circ}$ ) in the LMS for EuPLEx (left) and AVC (right). The colour code of the symbols denotes the CFC-11 mixing ratio (ppt). The “low  $N_2O$ ” data ( $-25 \text{ ppb} < \Delta N_2O < +5 \text{ ppb}$ ) are highlighted by black squares and the “high  $N_2O$ ” data ( $-5 \text{ ppb} < \Delta N_2O_{extra} < +25 \text{ ppb}$ ) are highlighted by circles. The line indicates the approximate  $\phi_{equiv}$  of the vortex edge above 400 K.

spheric, vortex) and for the “low  $N_2O$ ” and “high  $N_2O$ ” data. The 10 K average profiles, displayed in black, were calculated as described in section 3.6.

The upper panel of Figure 3.21 shows the vortex fraction, the middle panel the stratospheric fraction and the lower panel the tropospheric fraction. Results for the “low  $N_2O$ ” data are shown on the left side and results for the “high  $N_2O$ ” data on the right side.

Error bars are generally large, indicating a wide spread of the results of the Monte Carlo simulation (see section 3.6). Furthermore, the calculated fractions are not always within the expected physical range of zero to one. However, they always match the physical range within their error bars.

One of the reasons for the large uncertainties is that the used tracers are almost linearly correlated with each other in the LMS (except  $H_2O$ ). Thus, they do not provide sufficiently independent constraints for the solution of the linear equation system. Together with the rather large uncertainties at the boundaries, the information fed into the linear equation system is only providing weak constraints for the solution. An additional problem can be created by the distribution of boundary values. While  $H_2O$  yields good constraints for the definition of the tropospheric fraction, the vortex and the stratospheric boundary values are almost identical, thus not providing constraints on the respective fractions. With increasing  $\theta$  even the constraint on the tropospheric fraction is gradually lost, since the variable boundary value for the tropospheric fraction approaches the other two boundary values at 400 K, such that  $H_2O$  hardly yields any constraints for the solution of the equation system at high  $\theta$  (see section 3.4.5 and Figure 3.23 below).

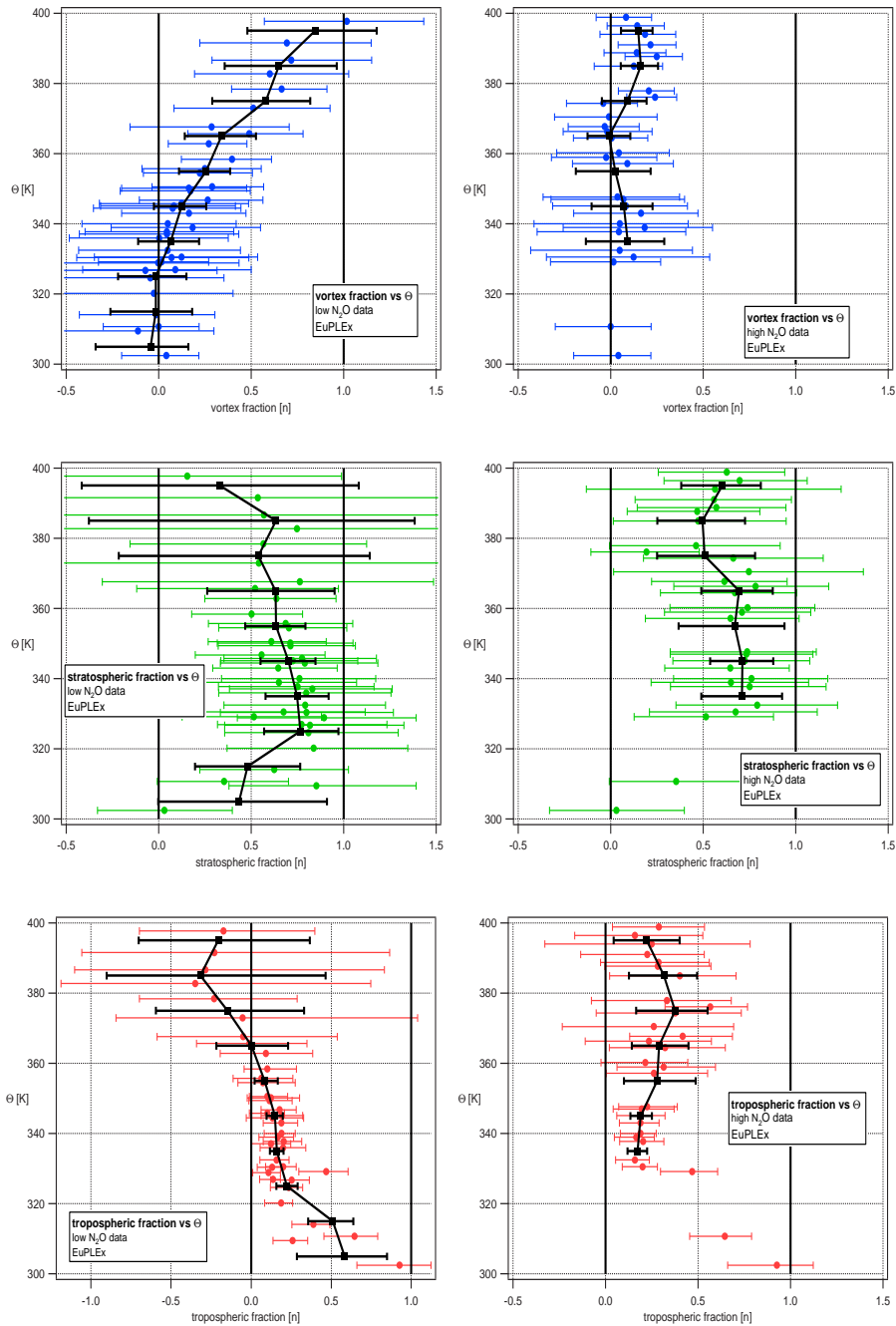


Figure 3.21: EuPLEX fractions of air in the LMS originating in the vortex region ( $> 400$  K)(top), stratosphere ( $> 400$  K)(middle) or the troposphere (bottom). Results for the “low  $N_2O$ ” data are shown on the left, results for “high  $N_2O$ ” data on the right. Error bars range from the 16th to the 84th percentile for the individual data points. The profile averaged over 10 K bins is shown in black. Error bars of the average are divided by  $\sqrt{n}$  where  $n$  is the number of data points used for averaging in each bin.

As a result, the error bars are found to be relatively small for the tropospheric fraction below 360 K and become larger above. In parallel, the stratospheric and vortex fractions exhibit rather large error bars over the whole range of the LMS as a result of large uncertainties of the corresponding boundary conditions and the weak constraints from H<sub>2</sub>O. For all other tracers, the tropospheric and stratospheric boundary values are relatively close together, taking into account the large uncertainty of the stratospheric boundary value (see section 3.4.4), while the vortex boundary value is distinct from the other boundary value.

Hence, in case of measurements close to the vortex boundary value, the system still defines the vortex fraction relatively well, despite large uncertainties, while the determination of the stratospheric and the tropospheric fractions becomes difficult. Considering the variability at the stratospheric boundary, it is even possible that the difference between tropospheric and stratospheric boundary values is 0.

Despite the substantial uncertainties, the results of the calculations show that the LMS region for the “low  $N_2O$ ” data are mostly dominated by air masses that have descended from the stratosphere. For these data, the stratospheric fraction ranges between 0.5 and 0.75 for  $310\text{ K} < \theta < 370\text{ K}$ ; above 370 K it is not constraint by the observations. No significant vortex influence is found in the lower half of the LMS, while the vortex fraction steadily increases in the upper half of the LMS. Around 370 K, the LMS air is found to be a mixture of  $\sim 50\%$  vortex and  $\sim 50\%$  stratospheric air. Even higher, the vortex fraction increases to 100% at 400 K. In parallel to the increasing influence of the vortex, the stratospheric influence must decrease, although, as mentioned above, this decrease cannot be quantitatively assessed due to the large error bars for  $\theta > 360\text{ K}$ . The same is true for the tropospheric fraction above 360 K, which is likely 0. However, below 360 K the findings on the tropospheric influence are more reliable, as indicated by very small error bars. In the lowest 20 K, tropospheric fractions are found to exceed 50%; above that, they rapidly decrease to about 20% at 330K (the tropopause was usually situated at 300 K) and then gradually decrease further toward 0 at 360 K. These results correspond well with findings of *Hoor et al.* [2004], who proposed a mixing layer above the tropopause in the LMS with increased tropospheric influence for the lowest 20-30 K above the tropopause.

For the “high  $N_2O$ ” data, no significant influence of vortex air is found below 380 K. Only the highest levels ( $> 380\text{ K}$ ) exhibit a significant fraction, yet, less than 20%. In comparison to the “low  $N_2O$ ” data smaller error bars are derived for  $\theta > 360\text{ K}$ . Since the mixing ratios in the “high  $N_2O$ ” data are rather large (small for O<sub>3</sub>), the uncertainty of the vortex boundary value is relatively small compared to the difference between the measured data and the boundary value, thus resulting in a smaller uncertainty of the results. The dominant fraction of air comes again from the extra-vortex stratosphere. Between 330 K and 370 K this fraction ranges between 50% and 90%; above 370 K slightly smaller fractions are derived. The large error bars again indicate that the data provide only weak constraints on these results. The tropospheric fraction in the lowest 30 K behaves similarly as for the

“low  $N_2O$ ” data, but cannot be well quantified because of the sparsity of data points. At higher levels, the tropospheric fraction is constantly calculated as significantly above 0.

This result is in accord with a study by *Curtius et al.* [2005], who discuss unexpectedly high particle measurements in the LMS region that occurred during the flight on February 8, 2003. Although definite conclusions on the origin of these high particle concentrations could not be given, transport from the tropopause region was discussed as a possible cause and a trajectory analysis indeed showed evidence of transport from the lower latitude tropopause region.

In Figure 3.22, the results of the mass balance calculation for the complete data set are shown in a potential temperature versus equivalent latitude plot. Equivalent latitude was calculated by the CLaMS model. The colour code denotes the fractions of air in the LMS coming from the vortex above 400 K (upper panel), the extra-vortex mid to high-latitude stratosphere above 400 K (middle panel) and the troposphere (lower panel). Blue symbols denote low fractions and red symbols high fractions.

Substantial evidence of vortex air (with fractions  $> 50\%$ ) is only indicated for measurements above 360 K and at high equivalent latitudes well north of the indicated vortex edge. The dominant fraction of air at the lowest potential temperature levels has its origin in the troposphere. It should be taken into account that for this region only four measurements were available simultaneously for all tracers. At higher levels, the tropospheric fraction — as seen above — is usually less than 25%. Considering the error bars for  $\theta > 360$  K, no quantitative conclusion can be given for high equivalent latitudes. However, the mass balance calculation yields the lowest tropospheric influence for the region directly below the vortex, where descent from the vortex is detected.

The “high  $N_2O$ ” data, which are taken at an equivalent latitude between  $40^\circ$  and  $50^\circ$ , describe a LMS region well equatorward of the vortex edge. Consequently, the mass balance calculation characterizes the region as mostly influenced by air masses which were transported from the extra-vortex stratosphere above 400 K. The vortex and the tropospheric fractions remain small, while the stratospheric fraction varies between 50% and 70%. In the high-latitude region the mostly stratospheric influence is decreasing above a potential temperature of 370 K and a gradually increasing influence of air from the vortex is detected. A tropospheric fraction different from zero is only observed in the lowest 20-30 K of the LMS, and it is quickly decreasing to zero.

As already discussed above (see Figure 3.20) in this presentation of the data the separation between low- and high-latitude data is obvious. The data falling into the space between the “low  $N_2O$ ” and the “high  $N_2O$ ” data meaningfully complete the picture for these extreme data sets presented in Figure 3.21. Only for the stratospheric fraction some data points appear to be out of the physical range, but considering the large uncertainties for this fraction this is not surprising.

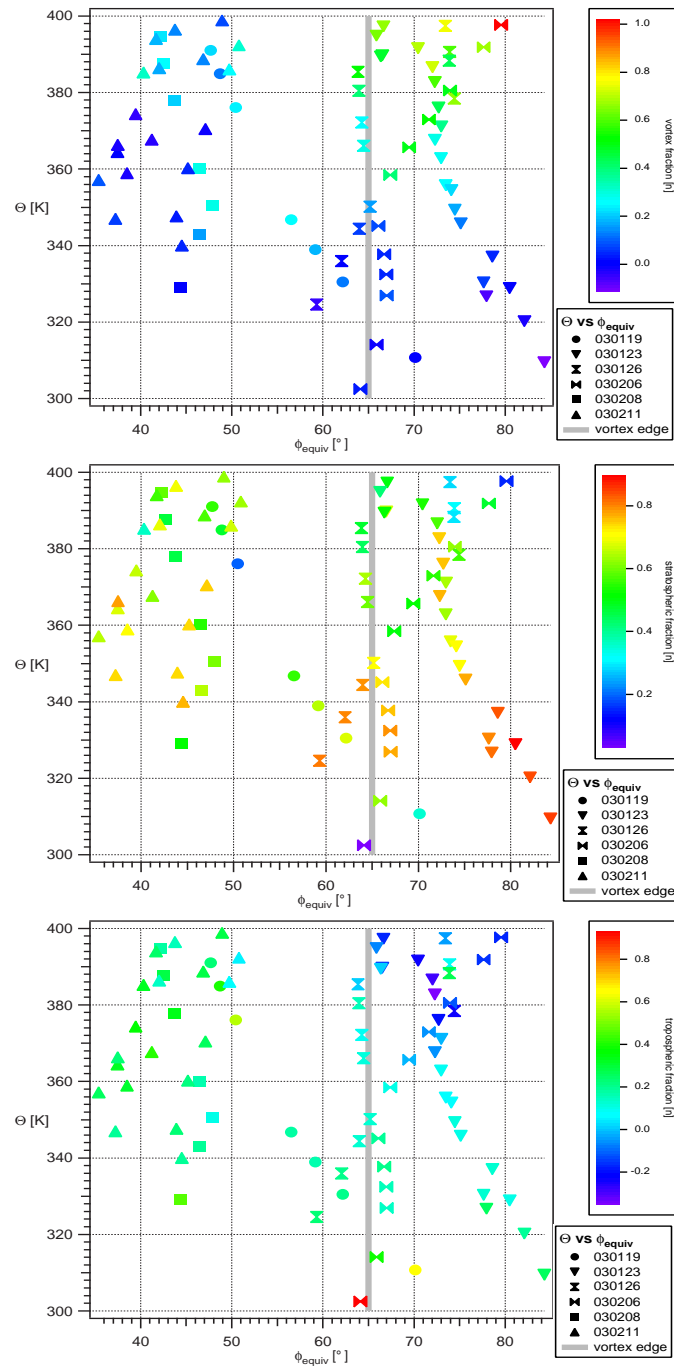


Figure 3.22: Fractions of air in potential temperature - equivalent latitude space. Colour indicates the vortex (top panel), stratospheric (middle panel) or tropospheric fractions (lower panel) and the symbols mark the different flights during the EuPLEX campaign.

However, one data point around 375 K from the flight on January 19 exhibits an exceptionally low stratospheric influence. A closer look at the  $\text{H}_2\text{O}$  for this flight (Figure 3.23) reveals the problem: At this level the vortex (blue line) and the tropospheric (red line) boundary values are almost equal while this data point exhibits a rather high mixing ratio. Thus,  $\text{H}_2\text{O}$  yields the information that the stratospheric (stratospheric boundary value indicated by a green line) influence must be small. Since the other tracers do not give the same information — the data for CFC-11 is shown exemplarily in Figure 3.23 as well — this constellation yields a rather ambiguous information from the different tracers. Since the mass balance system is very sensitive to changes in the boundary conditions and  $\text{H}_2\text{O}$  is one of the more weighted tracers (section 3.5), this might be the reason for the outlier in the results. Furthermore,  $\text{H}_2\text{O}$  is the only tracer which shows a highly non-linear correlation with the other tracers and has thus a very strong influence on the results. A similar case is discussed below for the AVC campaign.

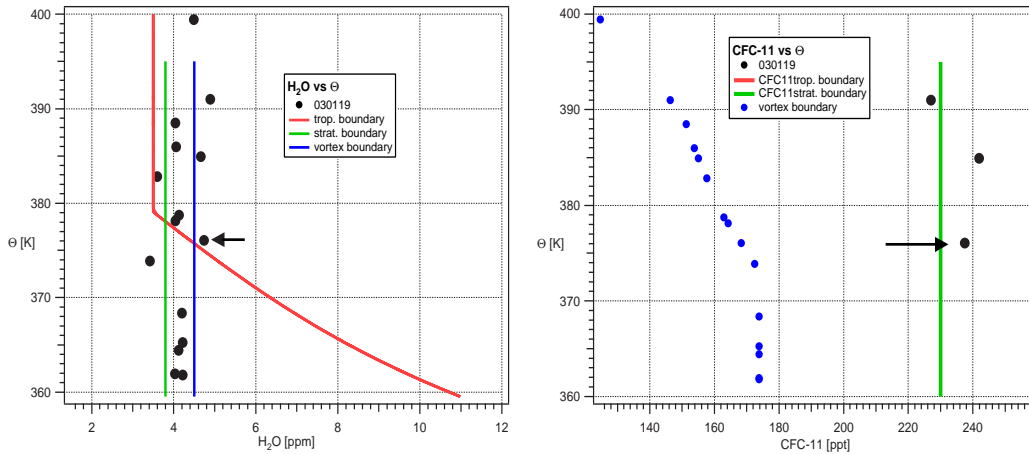


Figure 3.23:  $\text{H}_2\text{O}$  (ppm) and CFC-11 (ppt) plotted versus the potential temperature  $\theta$  (K) in the LMS for January 19, 2003. For comparison the boundary values at the tropopause, the extra-vortex stratosphere at 400 K and the vortex at 400 K are indicated as red, green and blue lines, respectively.

### 3.7.2 AVC

The results of the mass balance calculation for the AVC campaign are displayed in Figure 3.24. The presentation is carried out analogous to the one for the EuPLEx results. For the discussion of error bars and problems of the mass balance calculation, the reader is referred to the discussion of the EuPLEx results in the previous section 3.7.1.

During the course of the winter, more air masses are transported into the LMS through the 400 K isentrope. Thus, in the upper region of the LMS an increased vortex fraction is evident. For the “low  $N_2O$ ” data, the increase in vortex fraction

already starts at 330 K and at 360 K the vortex influence is already around 50%, while the stratospheric fraction decreases and becomes smaller than 50% for  $\theta > 360$  K. For the “high  $N_2O$ ” data this is slightly different. The stratospheric fraction stays above 50% at all  $\theta$ -levels and even increases up to 100% at 390 K. However, as observed before, the error bars are rather large. Compared to the uncertainty of the stratospheric fraction, the vortex fraction is relatively well defined and it increases to values of about 25% to 30% between 340 K and 390 K, indicating a moderate influence of air coming from the vortex region. Nevertheless, compared to the EuPLEX campaign, the influence from the lower stratosphere inside and outside the vortex region has increased slightly. As mentioned earlier (see section 3.7), it is not possible to determine which way the air mass has taken. Further discussion of this problem is given in the following section 3.7.3.

The tropospheric fraction is hardly evident in the upper half of the LMS. However, data below 350 K exhibit fractions significantly above zero, increasing from about 20% at 340 K, to about 50% just above the tropopause. Of course, it has to be considered that this conclusion is based on only two data points below 320 K. Above 370 K, no significant tropospheric influence is detectable.

The presentation of the AVC data in the potential temperature versus equivalent latitude plots (Figure 3.25) shows that the data are relatively compact and do not separate into high and low equivalent latitude data as is characteristic for the EuPLEX campaign (see Figures 3.3 in section 3.3 and Figure 3.20 in this section). As mentioned before, the vortex had already experienced some mixing above 400 K and most of the data in the LMS were obtained below the edge region of the vortex. Although a general structure and dependence on equivalent latitude and  $\theta$  is still observed, the separation is not as pronounced as for the EuPLEX data.

Some data points whose air fractions are outside the physical range, will now be examined more closely. In Figure 3.25, the most pronounced outliers are marked with letters from A to D. All points are from the flight on March 16, 2003. In Figure 3.26,  $H_2O$  and CFC-11 data from this flight are plotted versus  $\theta$ . The corresponding tracer measurements used to calculate the fractions at points A - D exhibit unusually high  $H_2O$  mixing ratios exceeding 10 ppm at potential temperatures above 340 K and thus well inside the LMS. Even though instrumental problems (i.e. contamination) cannot be excluded, they are not expected [Schiller & Spelten, 2006]. An explanation for this  $H_2O$  anomaly cannot be given at this time; work on this feature is in progress.

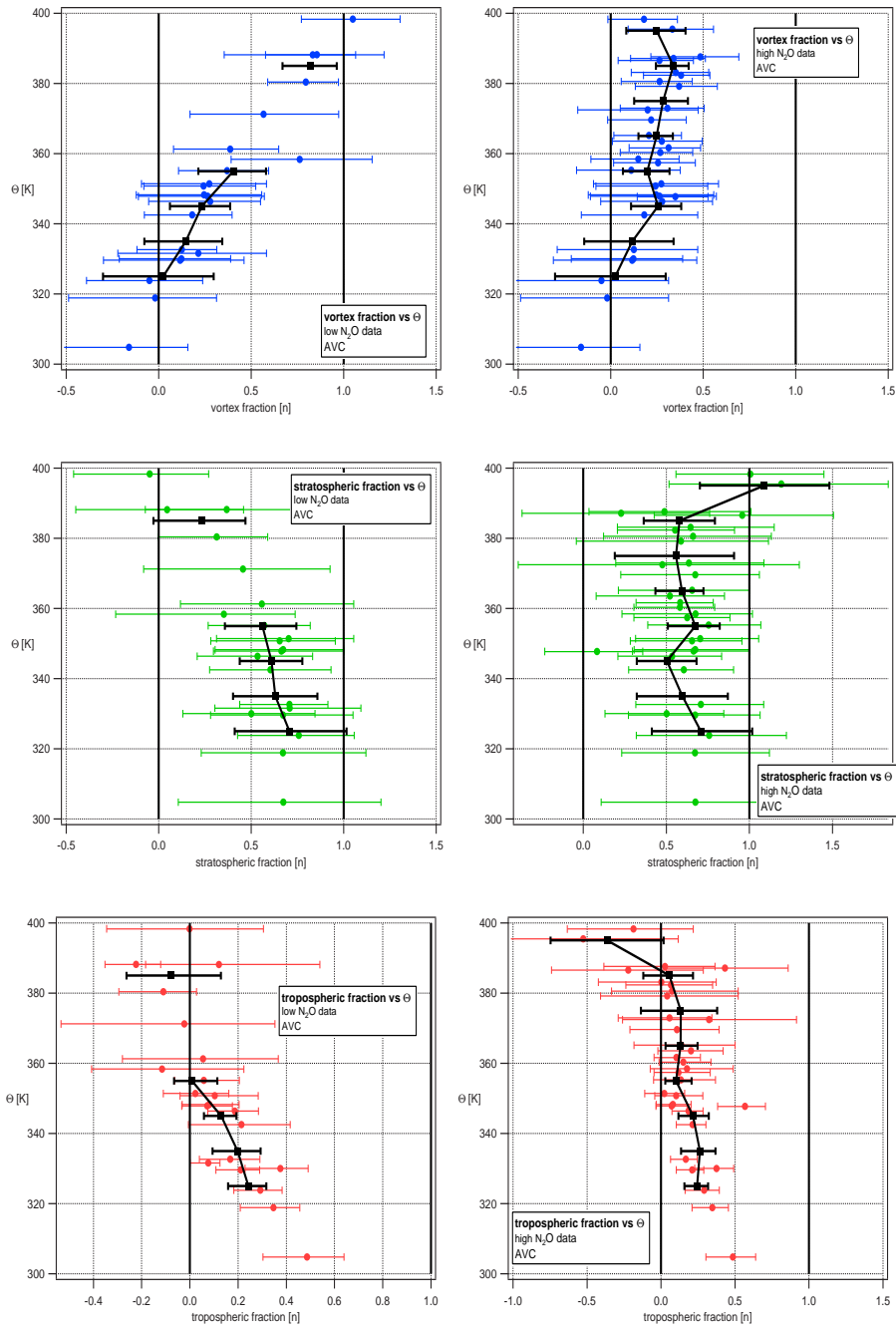


Figure 3.24: AVC fractions of air in the LMS originating in the vortex region ( $> 400$  K)(top), stratosphere ( $> 400$  K)(middle) or the troposphere (bottom). Results for the “low  $N_2O$ ” data are shown on the left, results for “high  $N_2O$ ” data on the right. Error bars range from the 16th to the 84th percentile for the individual data points. The profile averaged over 10 K bins is shown in black. Error bars of the average are divided by  $\sqrt{n}$  where  $n$  is the number of data points used for averaging in each bin.



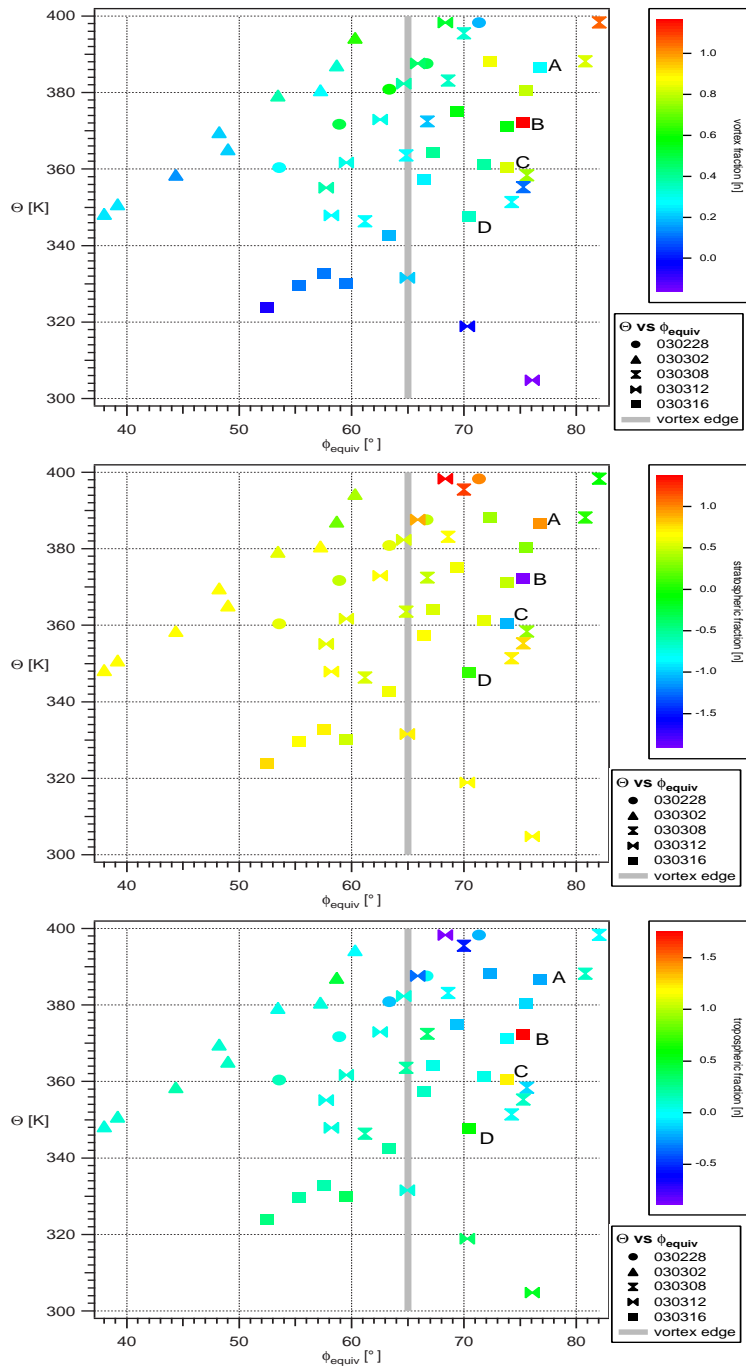


Figure 3.25: Air fractions in potential temperature - equivalent latitude space. Colour indicates the vortex (top panel), stratospheric (middle panel) or tropospheric (lower panel) fractions and the symbols mark the different flights during the AVC campaign.

All other tracers (CFC-11 is shown as an example in Figure 3.26) show mostly low mixing ratios close to the lower envelope of the measurements, mostly indicating influence from the stratosphere above 400 K. However, much of the high  $H_2O$  layer exhibits mixing ratios much higher than the tropospheric boundary value, which cannot arise from a mixture of air with the boundary values assumed here. The solution of the mass balance system must therefore yield unphysical air fractions. Since the cause of the high  $H_2O$  layer is not understood, the respective four data points will be neglected in the further discussion.

Neglecting the mentioned outliers, a general structure can be seen in the LMS. The vortex fraction increases from zero at low potential temperature and low equivalent latitude to almost 1 at high potential temperature and high equivalent latitude. Compared to the EuPLEX campaign, the vortex influence reaches further down into the LMS. For example for  $\theta = 360$  K, at high equivalent latitude ( $\phi_{equiv} \geq 75^\circ$ ), the vortex fraction is now at about 0.4 - 0.8, while during the EuPLEX campaign maximum fractions of 0.4 are found.

The stratospheric fraction shows a similar change with  $\theta$  and  $\phi_{equiv}$ : It generally reveals fractions larger than 50% with a change towards higher  $\theta$  and  $\phi_{equiv}$ . The fraction either decreases to zero or increases to 1 as  $\theta$  approaches 400 K (better seen in Figure 3.24). The first case happens for  $\phi_{equiv} > 70^\circ$ , the latter for  $\phi_{equiv} < 70^\circ$ .

The tropospheric fraction exhibits high values only close to the tropopause; above 350 K the fraction is close to zero.

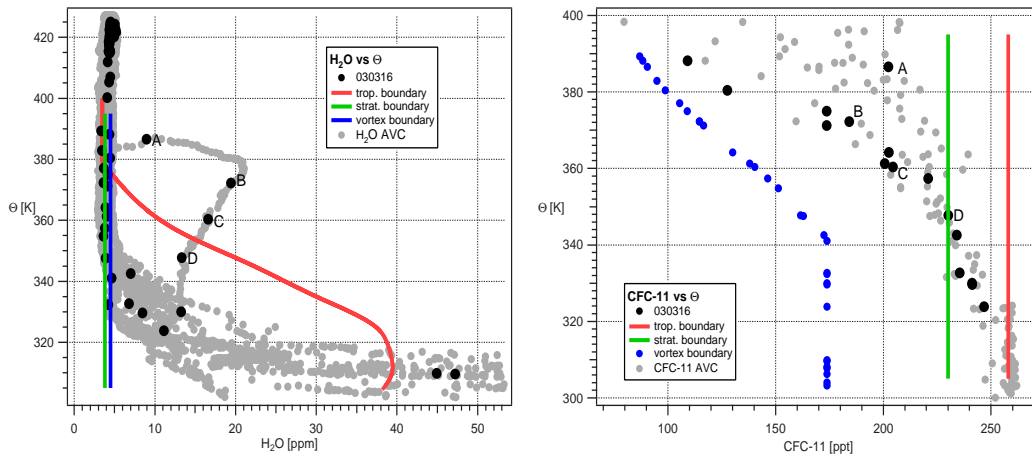


Figure 3.26:  $H_2O$  (ppm) and CFC-11 (ppt) plotted versus the potential temperature  $\theta$  (K) in the LMS for March 16, 2003. For comparison the boundary values at the tropopause, the extra-vortex stratosphere at 400 K and the vortex at 400 K are shown as red, green and blue lines, respectively.

### 3.7.3 Comparison with CLaMS results

The CLaMS model calculates an artificial tracer called vortex tracer. Its value ranges from 0 to 1 and it is initialized at time step  $t = 0$  to be per definition 1 inside and 0 everywhere outside the vortex. During the simulation and ongoing mixing, the value of this tracer changes. The more extra-vortex air is mixed in, the more its value decreases inside the vortex. The CLaMS model, however, does not distinguish between tropospheric and non-vortex stratospheric air. It generally takes into account mixing across the vortex edge (vertical and horizontal).

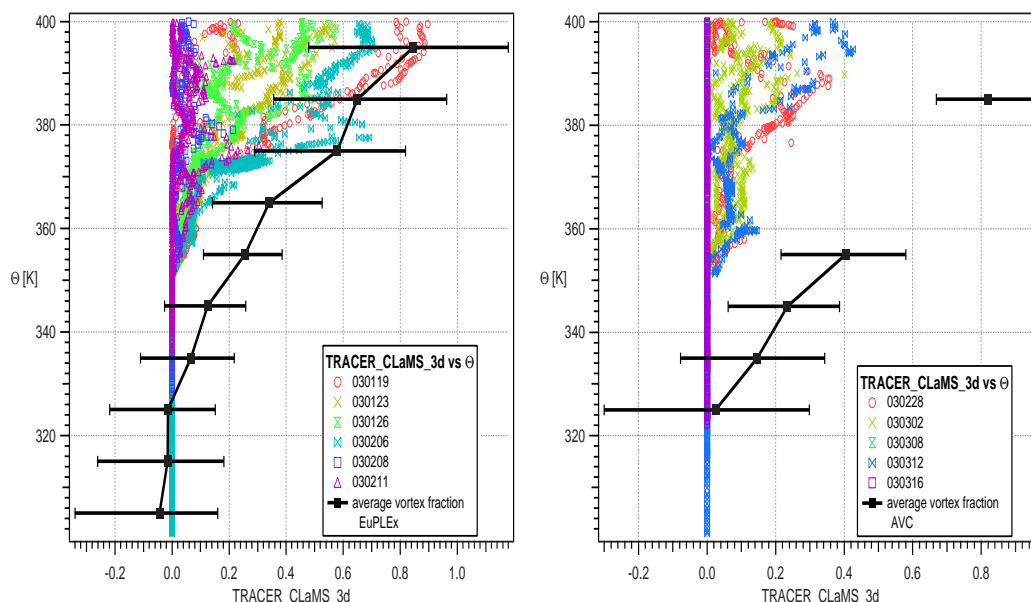


Figure 3.27: CLaMS vortex tracer plotted versus the potential temperature. In the left panel, all EuPLEX flights are displayed except for February 2, 2003. In black the average vortex fraction is given as determined from the mass balance calculation. In the right panel, the same is displayed for the AVC campaign.

In the left panel of Figure 3.27, the vertical profiles of the CLaMS vortex tracer are plotted versus the potential temperature for all EuPLEX flights. Above 370 K, the largest values of this vortex tracer agree well with the average profile of the vortex fraction for “low  $N_2O$ ” data, as calculated from the mass balance calculation. CLaMS finds these largest values of the vortex tracer on January 19 and February 6, 2003. These are the flights that are also found predominantly in the “low  $N_2O$ ” data (see section 3.4.1).

Further down, CLaMS vortex tracer values are smaller than the vortex fractions derived from the mass balance. This is expected as the CLaMS vortex tracer was initialized with 0 on December 1 everywhere below 400 K; it is thus a measure for transport of vortex air to lower levels since December 1, only. The vortex fraction from the mass balance, on the other hand, includes air that has descended through

the 400 K surface before December 1, and the fraction of this air increases with decreasing theta.

Between EuPLEx and AVC, stronger in-mixing of non-vortex air occurred above 400 K [EuPLEx, 2004]. The comparison of the AVC vortex fraction for “low  $N_2O$ ” data with the CLaMS vortex tracer (right panel of Figure 3.27) shows larger deviations; a constant offset is apparent. The likely reason for this offset is that the CLaMS vortex tracer is affected by mixing into the vortex above 400 K; thus, already diluted vortex air (vortex tracer  $< 1$ ) is transported into the LMS. In the mass balance study, only transport through the 400 K isentrope is considered. The vortex fraction at 400 K is per definition 1, no matter if stratospheric air has already been mixed into the vortex above. Any effect of such mixing on tracer mixing ratios is taken into account by the variable boundary condition.

In summary, the two quantities are related, but not the same. The CLaMS vortex tracer is the fraction of air that resided anywhere inside the vortex on December 1; the vortex fraction from the mass balance is the fraction of air that descended through the bottom of the vortex anytime.

## 3.8 Conclusions

In a simple mass balance study, fractions of air coming from the tropopause, the mid-latitude stratosphere above 400 K and the vortex region above 400 K were calculated applying a linear equation system. This linear equation system was solved via least squares adjustment using the HAGAR  $N_2O$ ,  $CH_4$ , CFC-11, H-1211 as well as  $O_3$  (FOX, DLR) and  $H_2O$  (FISH, FZ Jülich) measurements from the EuPLEx and the ENVISAT AVC campaign in January-March 2003.

The results of the mass balance calculation have to be considered with care, since the available tracer data do not always provide sufficient constraints to fully determine the linear equation system. This lack of information in the tracer data results in a high sensitivity of the solution to the large errors in the boundary values of the regarded tracers; especially at the vortex boundary, errors are large due to difficulties in the determination of descent through the vortex. Thus, the results suffer from large error bars in some regions. However, in certain regions the fractions can be determined quite well.

The EuPLEx and AVC results show a shallow layer of about 20 K above the tropopause with an increased tropospheric influence. During EuPLEx, the tropospheric fraction in this layer is larger than 50% and during AVC larger than 20%. This corresponds well to the findings of Hoor *et al.* [2004], who postulate a shallow mixing layer in the lowest 20-30 K of the LMS region where an enhanced tropospheric fraction of air can be found. Above this layer, the tropospheric influence is only minor with values lower than 20%; above 350 K, the tropospheric fraction is mostly not significantly different from zero. An exception occurs for the “high  $N_2O$ ” data during the EuPLEx campaign, where slightly increased tropospheric fractions

(up to 30%) are derived above 350 K. Although error bars in this region are large, this observation of transport from the tropical tropopause region is consistent with trajectory studies presented in *Curtius et al.* [2005].

Above the tropospherically influenced region, the dominant fraction of air (average 75%) descended from the mid- to high-latitude stratosphere outside the vortex. Only for the “low  $N_2O$ ” data and at highest levels the dominant fraction of air originates from the vortex region with values of 50% at 370 K increasing toward 100% at 400 K during EuPLEx. For the AVC campaign, this picture changed only slightly, since the main descent already happened before EuPLEx. Further descent of air masses from the vortex region through the 400 K isentrope manifests itself in slightly larger vortex fractions than those derived for EuPLEx. However, the differences between EuPLEx and AVC are hardly significant for the “low  $N_2O$ ” data. The “high  $N_2O$ ” data also exhibit slightly higher vortex fractions (up to 30%) for AVC than for EuPLEx between 360 K and 400 K. However, this comparison has to be regarded with caution since the “high  $N_2O$ ” data were obtained at higher equivalents during AVC than during EuPLEx and part of the respective AVC samples were even located in the edge region of the vortex (see Figure 3.20). The enhanced vortex fraction during AVC can thus not be regarded as an indication for transport of vortex air to mid latitudes.

Comparisons of the derived vortex fraction with an artificial vortex tracer calculated by the CLaMS model exhibit large deviation for the results of the AVC campaign, due to in-mixing of extra-vortex air into the vortex above 400 K, which is detected by the CLaMS tracer but not by the vortex fraction of the mass balance study. For the EuPLEx campaign, during which the vortex edge above 400 K was still largely impermeable, the results compare quite well.



# Chapter 4

## Results II: A cut off low over Europe — Assessment of mixing in the LMS

During the ENVISAT mid latitude test and validation campaigns in Forlì, during July and October 2002, an overall number of 11 flights were performed in the northern hemisphere mid-latitude region between  $30^\circ$  and  $45^\circ$  N. A passing cut-off low system in July 2002 resulted in highly variable tracer measurements in the LMS region. In October, a similar but less intensive event was observed. After a brief discussion of the meteorological situation, the impact on tracer measurements will be discussed.

### 4.1 Meteorological situation over Italy in July and October 2002

In July 2002, a cut-off low system passed over Italy (for maps of the geopotential height at 500 hPa see Figures E.1 to E.3 in the appendix). Corresponding to this event, an extended streamer of very high PV crossed over Europe. In Figure 4.1 the PV (interpolated from ECMWF fields) at 350 K potential temperature is displayed. Starting from a large field of elevated PV on 13th of July, the streamer intensified until the 15th and passed over Italy in the following days.

A close up look at the region where the Geophysica flights were performed is given in Figure 4.2. The PV on the 350 K and 370 K potential temperature level is shown for the flights on 15th, 18th and 22nd of July at 12 UTC. The flight path of the Geophysica interpolated to 12 UTC is plotted in black. The maps show that the Geophysica flight paths intersected areas of high and low PV. And, of course, due to the temporal variability of the PV field, the LMS over the region of Forlì exhibited changing conditions from flight to flight. This variability can also be seen in the soundings over San Pietro Capofiume ( $44.39^\circ$  N,  $11.37^\circ$  E) shown in Figure 4.3. The temperature profile shows several changes with height in the LMS region between 10 km and 20 km. It was most pronounced on July 15 and 18 when the

passing of the streamer occurred.

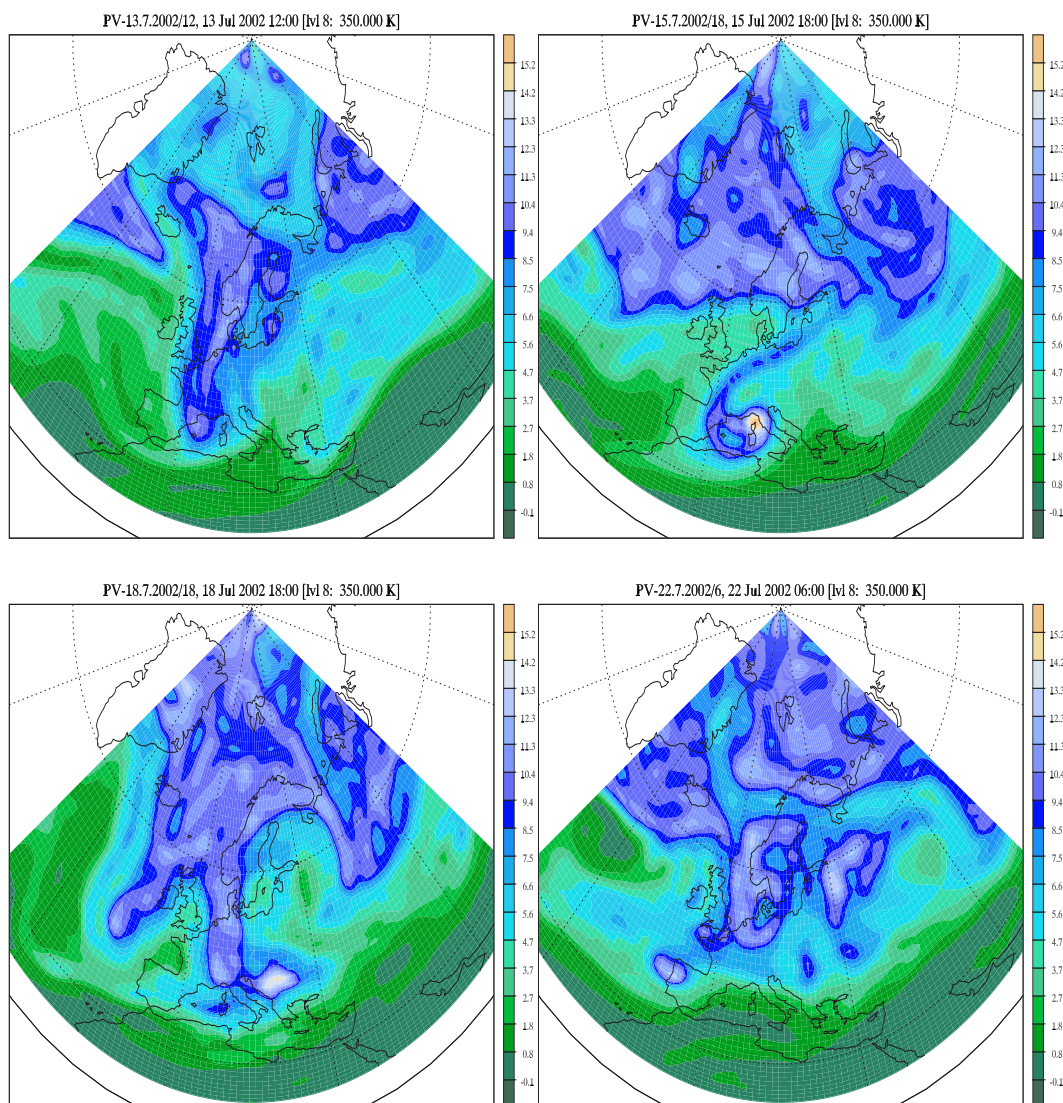


Figure 4.1: PV (ECMWF) maps for the flights on 13th, 15th, 18th and 22nd of July 2002 at 350 K potential temperature.



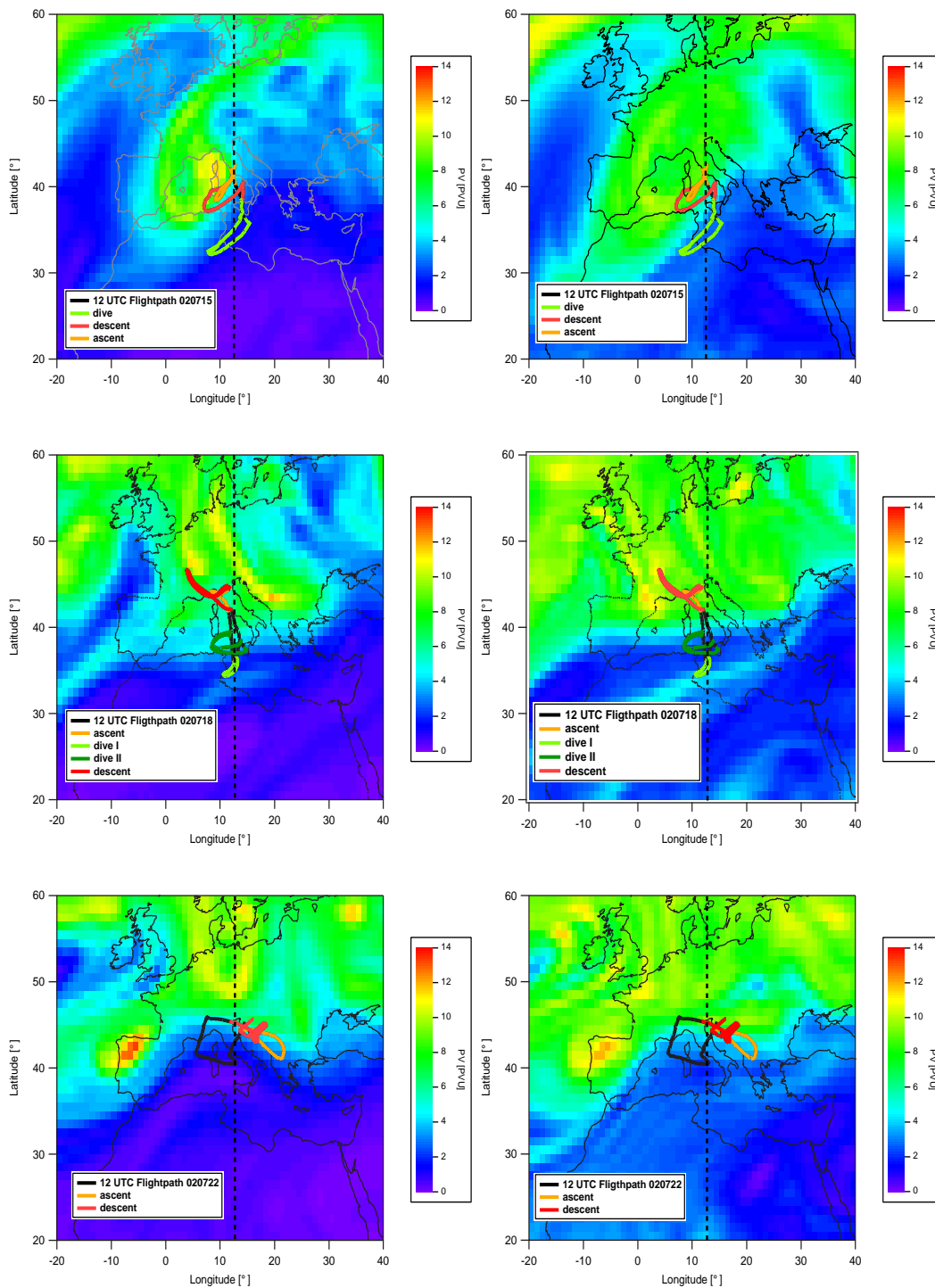


Figure 4.2: PV (ECMWF) maps for the flights on 15th, 18th and 22nd of July 2002 at 350 K (left side) and 370 K (right side) potential temperature. The Geophysica flight path interpolated on 12 UTC is displayed colour coded for the different flight sections. The location of a latitude cross section at 12° E is indicated as a dashed line.

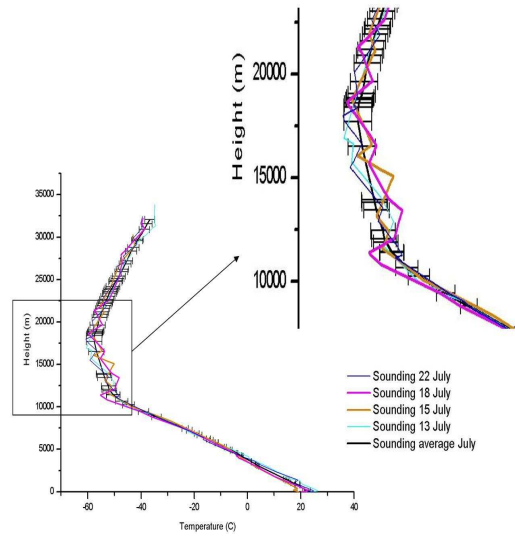


Figure 4.3: Soundings at San Pietro Capofiume/Italy (44.39 N, 11.37 E, elevation 11 m) in July 2002.

With the passing of the streamer, a layering of the UT/LS region occurred. This can be seen by examining PV cross sections along  $12^{\circ}$  E longitude shown in Figure 4.4. The location of the cross section is indicated in the PV maps of July in Figure 4.2 as a dashed line. With the arrival of the streamer on the 13th (see Figure 4.1), the tropopause level decreased over Forlí, leading to a relatively sharp change in tropopause height between  $36^{\circ}$  and  $38^{\circ}$  N (in Figure 4.4 the 2 PVU isoline is highlighted; the 4 PVU isoline runs more or less in parallel). The different layers of lower and higher PV (low - high - low) started to develop. On the 15th, the high PV area had moved further south and the layer of high PV was evident between 340 K and 380 K. This development progressed and distinct layers intensified until July 18. Finally, on July 22 — after the passing of the streamer — the high PV had vanished.

During the October campaign a similar event occurred. The PV at 350 K for the flights on 8th, 11th, 14th, 17th and 22nd of October is shown in Figure 4.5. Also shown are the 12 UTC flight paths of the Geophysica. On 11th of October, a small area of high PV crossed over Italy and the Geophysica flight was performed inside this PV feature. By the 14th this feature had already disappeared and during all other flights no significant PV feature was seen along the flight path. However, the Geophysica was flying in the boundary region between areas of higher and lower PV on October 22. For further illustration of the meteorological situation in the troposphere, the maps of the geopotential at 500 hPa are shown for all Geophysica flights in October in the appendix (Figures E.4 and E.5).

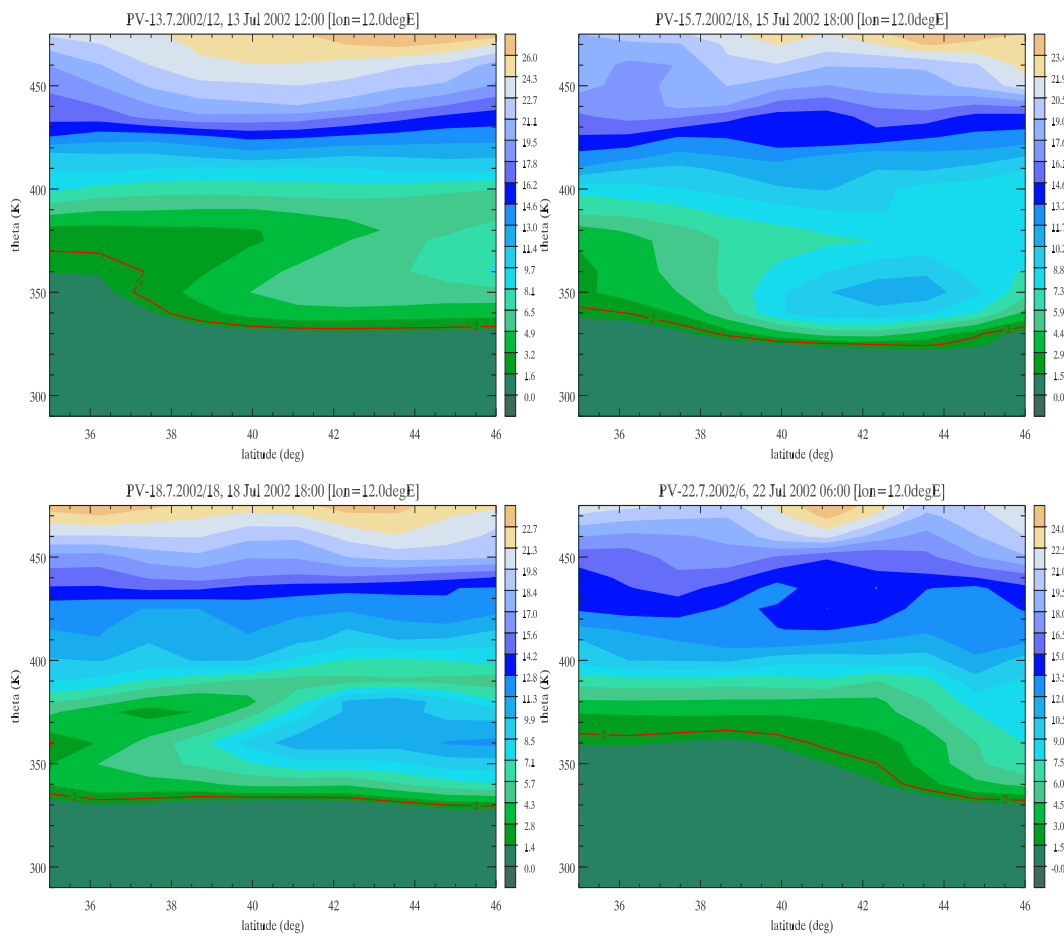


Figure 4.4: PV [PVU] cross sections at  $12^\circ$  E plotted versus latitude at 12 UTC for all July 2002 flights. Marked in red is the 2 PVU isoline. PV was interpolated from ECMWF data.

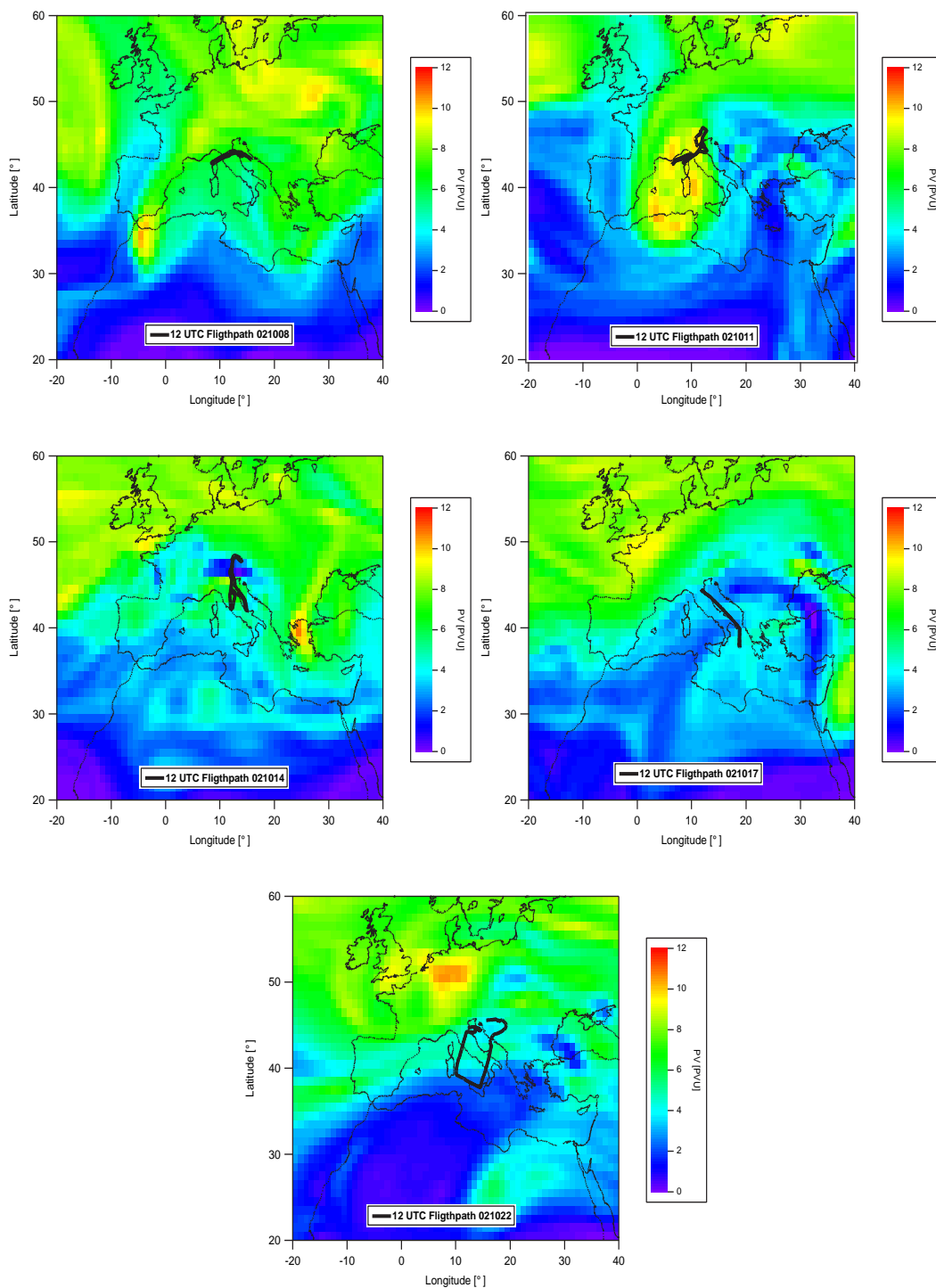


Figure 4.5: PV (ECMWF) maps at 350 K potential temperature for the flights on 8th, 11th, 14th, 17th and 22nd of October 2002. The Geophysica flight paths interpolated on 12 UTC are given in black.

## 4.2 Tracer measurements during July and October 2002

The tracer measurements obtained during flights that were performed in regions of highly variable PV, exhibit highly variable mixing ratios. The vertical profiles for  $O_3$  and CFC-11 for all mid-latitude flights performed from Forlì, are displayed in Figure 4.6. Coloured symbols denote the July flights and the flight of October 11. All other October flights that were performed during the ENVISAT mid-latitude validation campaign are displayed as black filled circles. The high variability in the July measurements is obvious in both species and can also be seen in all other HAGAR species (not shown here). Very low mixing ratios of CFC-11 correspond to very high mixing ratios of  $O_3$  measured by the FOZAN instrument. The only summer flight that does not show this elevated variability is that of July 22, when the flight path of the Geophysica did not cross a high PV region (see Figure 4.2). The October data are in general more compact and tend to higher CFC-11 mixing ratios in the LMS. An exception is the flight of October 11, when the Geophysica crossed an area of high PV and, as in July, rather low mixing ratios of the HAGAR tracers were observed. In the  $O_3$  data, the flight of October 11 also seems to be out of range compared to all other measurements and does not show the expected high mixing ratios above 400 K. To confirm that, the variability in all these flights is directly linked to the passing of the PV streamers, other potential reasons for increased variability must be excluded.

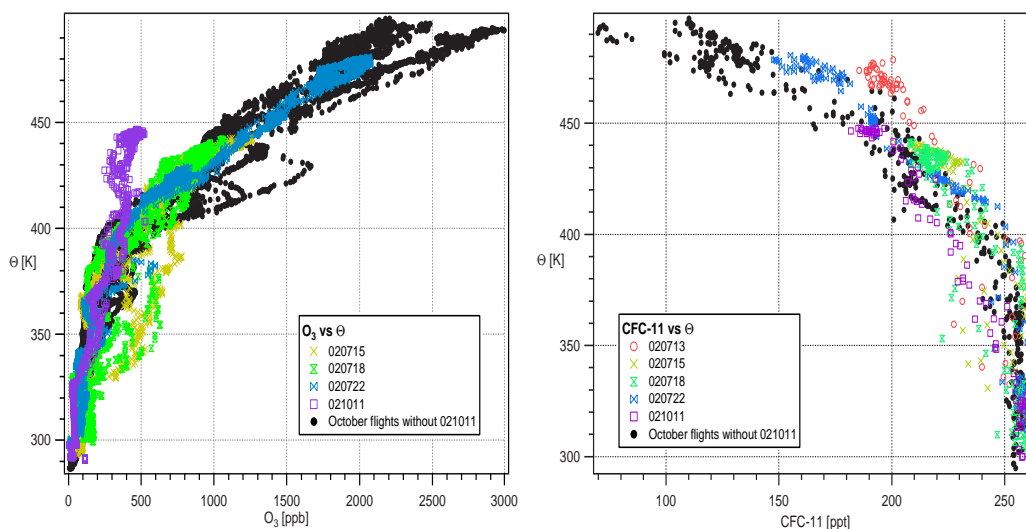


Figure 4.6: Ozone (ppb) (left panel) and CFC-11 (ppt) (right panel) plotted versus the potential temperature (K). Flights on 13th, 15th, 18th and 22nd of July and the 11th of October are marked by coloured symbols. All other flights are displayed as black circles.

Of course there can be several other reasons for the observation of such extreme

mixing ratios. The HAGAR instrument itself operated with a relatively low precision during the summer campaign. The newly implemented  $\text{CH}_4$  channel and several problems with the temperature control of the vessel led to a decreased precision and thus to a higher variability in the data set (section 2.3.2). Therefore, the extremely varying mixing ratios might be an instrumental artifact.

In the worst case, however, the precision was 3% for CFC-11 (Table C.3 in the appendix) which cannot explain the high variability of about 10%. In Figure 4.7, CFC-11 data for the flights with high variability in the LMS are displayed; error bars denoting the precision of the measurements<sup>1</sup>. It is evident that the variability is far larger than the precision of the instrument. This is also the case for CFC-12, H-1211, and in spite of a rather poor precision, for  $\text{N}_2\text{O}$  and  $\text{CH}_4$ .

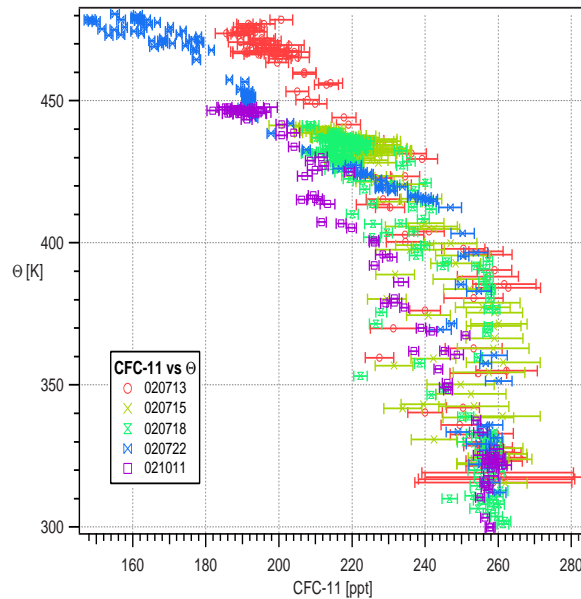


Figure 4.7: CFC-11 (ppt) plotted versus the potential temperature (K) for the flights on 13th, 15th, 18th and 22nd of July and the 11th of October. Error bars denote the precision of the measurement as given in the appendix.

Furthermore, the differences in variability can also be seen in the  $\text{O}_3$  data of the FOZAN instrument (Figure 4.6). This leads to the conclusion that the observed high variability in the tracers mixing ratios in the LMS is not an instrumental artifact. As mentioned before, the data of the flight of October 11 seem to be an exception, since here the FOZAN  $\text{O}_3$  and HAGAR tracers do not show the same high variability and the  $\text{O}_3$  strongly differs from the rest of the measurements. The correlation between CFC-11 and  $\text{O}_3$  (Figure 4.8) confirms this impression. The correlation curve is far from the expected curve, suggesting an artifact in the  $\text{O}_3$  measurement. However, for the July flights, instrumental artifacts can be excluded as the reason for the observed variability.

<sup>1</sup>A brief description of how error bars are estimated, is given in Appendix C.5

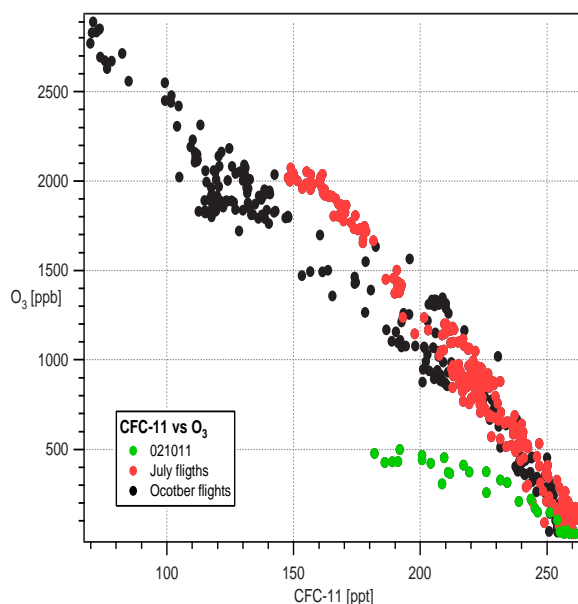


Figure 4.8: O<sub>3</sub> (ppb) plotted versus CFC-11 (ppt). July data is plotted in red, October data in black and the flight on 11th of October 2002 in green.

Since the tropopause height varies in time and space, some of the observed variability might be produced by the variation of the tropopause height which is shown in Figure 4.9A. To eliminate the tropopause variation, the potential temperature difference relative to the tropopause,  $\Delta\theta$ , is used as a vertical coordinate (see Appendix B.5). In Figures 4.9B and C, CFC-11 is plotted versus  $\Delta\theta$ . Only those data are shown that were measured between 300 K and 400 K potential temperature. This includes the upper troposphere (data with  $\Delta\theta < 0$  K) and the LMS region (data with  $\Delta\theta > 0$  K). In Figure 4.9B, the July flights are marked with coloured symbols. To draw a comparison the October data have been added (marked as black circles). Although the variability due to variations in the tropopause height has been eliminated, the broader scatter in the July data is still evident. The July data exhibit a larger range of mixing ratios compared to the October data, which are rather compact. The single flights of the October campaign are presented in Figure 4.9C (coloured symbols). Here, the July data were added to draw a comparison (black circles). The flight of October 11 seems to fit much better with the rest of the October flights when mixing ratios are plotted versus  $\Delta\theta$  rather than the absolute potential temperature. During this flight, a very low tropopause was observed. However, compared to all other October flights, the lowest mixing ratios in the LMS were measured on October 11 and 14 — three days after the passing of the low PV feature.

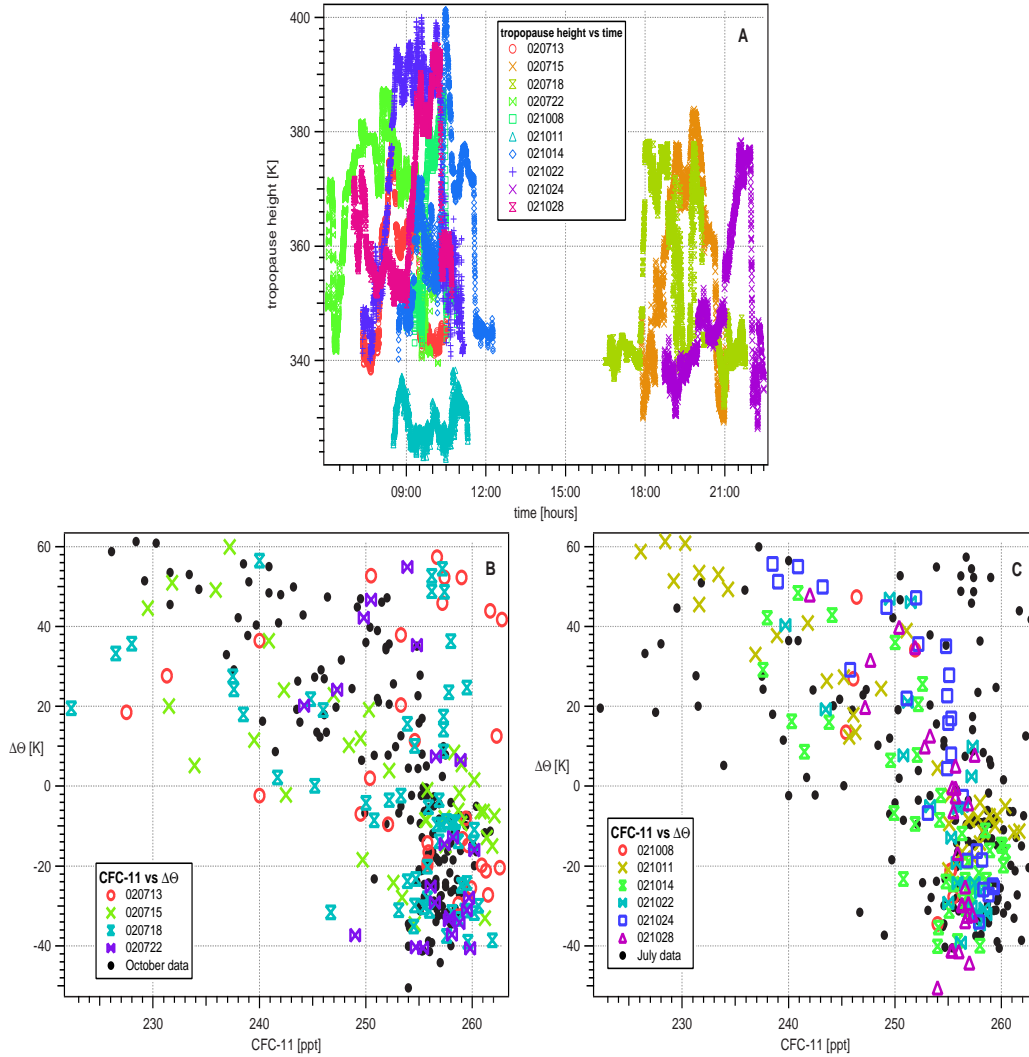


Figure 4.9: (A) Tropopause height (K) below the aircraft's location plotted versus the time of flight (hours of a day). Shown are all flights of the mid-latitude campaigns in Forlí, except for the flight of October 17. (B) CFC-11 (ppt) plotted versus  $\Delta\theta$  (K) between 300 K and 400 K potential temperature. Coloured symbols represent July flights and black points mark the October flights. (C) CFC-11 (ppt) plotted versus  $\Delta\theta$  (K) between 300 K and 400 K potential temperature. Coloured symbols represent October flights and black points mark the July flights.



## 4.3 Transport of air masses — Analysis using backward trajectories

In order to get an insight into processes for transport of air masses that are indicated by the measurements on these “streamer days”, isentropic 5-days backward trajectories have been calculated (see Appendix B.9).

In the following section, the July 2002 flights will be described in detail. For this purpose, the sections of the flights when the Geophysica crossed the region between 300 K and 400 K potential temperature — the upper troposphere and LMS region — have been separated. For each of these sections CFC-11 measurements are plotted versus  $\Delta\theta$  and the data points are colour coded by the potential temperature at which the measurement was taken (upper panels in Figures 4.10 - 4.15 and 4.17-4.20). Additionally, the corresponding isentropic 5-day backward trajectories are plotted, showing the potential temperature  $\theta$  of the trajectories (equal to the potential temperature at the starting point of the trajectory, the point of measurement) in the left panel and the PV along the trajectories in the right panel.

### 4.3.1 Flight of July 13, 2002

During this flight, the Geophysica was probing the LMS region only during the ascent and the descent. These two flight sections will be described in the following. On this day, the feature of high PV was approaching the area over Forlí (see Figure 4.1). It was situated west of the Geophysica flight path.

#### The ascent

The measurements taken during the ascent on July 13, 2002 (see Figure 4.10) show tropospheric mixing ratios of CFC-11 in the uppermost part of the LMS ( $\Delta\theta > 50$  K) and of course below the tropopause. The trajectories corresponding to these measurements originated from the middle Atlantic at 35° N to 43° N. The upper two data points (marked in red and orange) are of special interest. Starting at about 4 PVU, the tropopause region, the air parcels corresponding to these measurements were transported isentropically north-east towards Italy. Thus, resulting in mostly tropospheric mixing ratios in the LMS at roughly 390 K.

The remaining measurements (marked in green and yellow) exhibit mixing ratios below the tropospheric background. The air parcels belonging to the data points between the tropopause and  $\Delta\theta = 40$  K above, were transported rapidly from the eastern pacific region in a wave-like motion to the Mediterranean. The trajectory (A) for the value close to the tropopause stayed constantly in the tropopause region, while the other (B) shows significant stratospheric influence, experiencing high PV. The third data point (C) with low mixing ratio (at  $\Delta\theta = 380$  K) came from the Atlantic region but west of the source region of the measurements characterized by tropospheric mixing ratios.

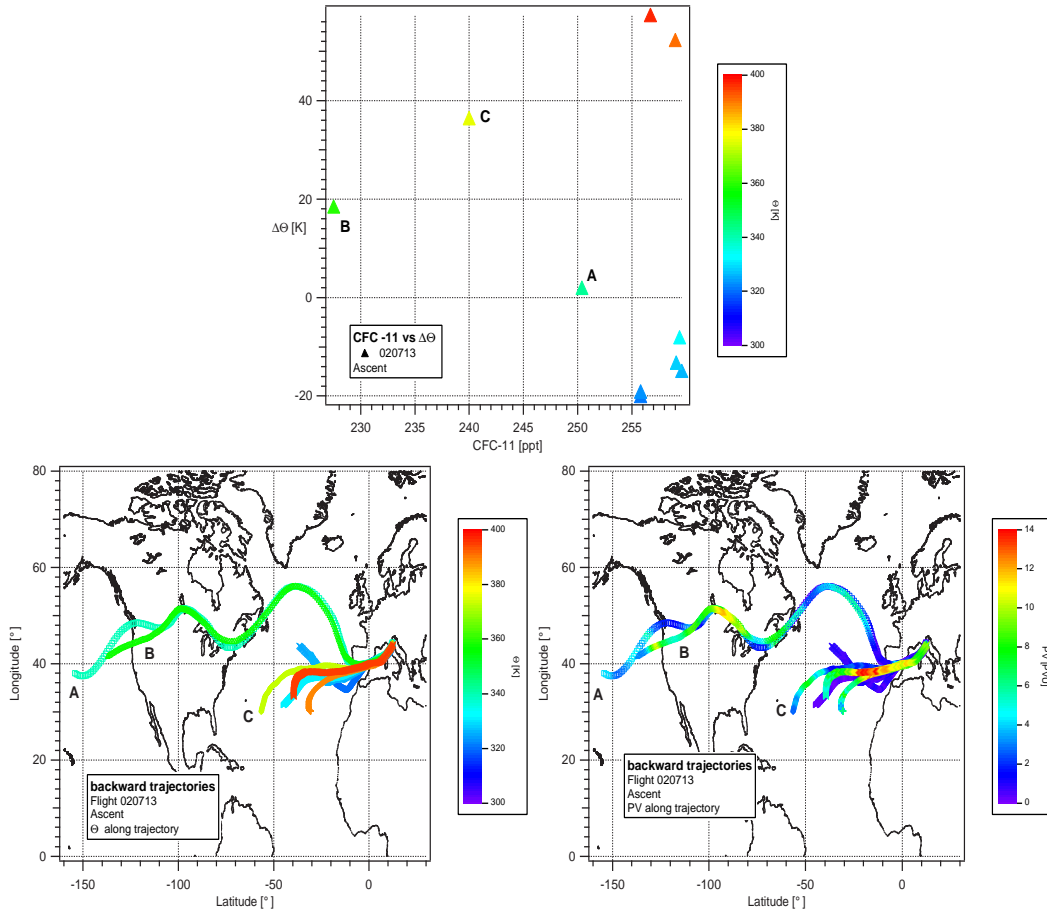


Figure 4.10: (Upper panel) CFC-11 (ppt) on July 13 plotted versus  $\Delta\theta$  (K). Only data that were measured in the LMS and upper troposphere during the ascent are shown. (Lower panel, left side)  $\theta$  along the 5-day backward trajectories for the measurements during the ascent. (Lower panel, right side) PV along the 5-day backward trajectories for the measurements during the ascent.

### The descent

During the descent, the measurements show extremely variable mixing ratios. Except for three outliers with mixing ratios smaller than 250 ppt of CFC-11, the rest of the data points are spread between 250 ppt and 263 ppt. The variability is reflected by the trajectories. The source regions are geographically spread over the north Atlantic and the north American continent north of 40° N. However, a classification similar to the ascent can be given: the highest air parcels (380 K - 400 K, yellow and red  $\theta$ -trajectories) came from the Atlantic between 25° N and 35° N, the lowest air parcels ( $\leq 320$  K, dark blue  $\theta$ -trajectories) from the Atlantic between 40° N and 55° N and the remaining ones from Canada.

The smallest mixing ratios were observed within the last region. For the data

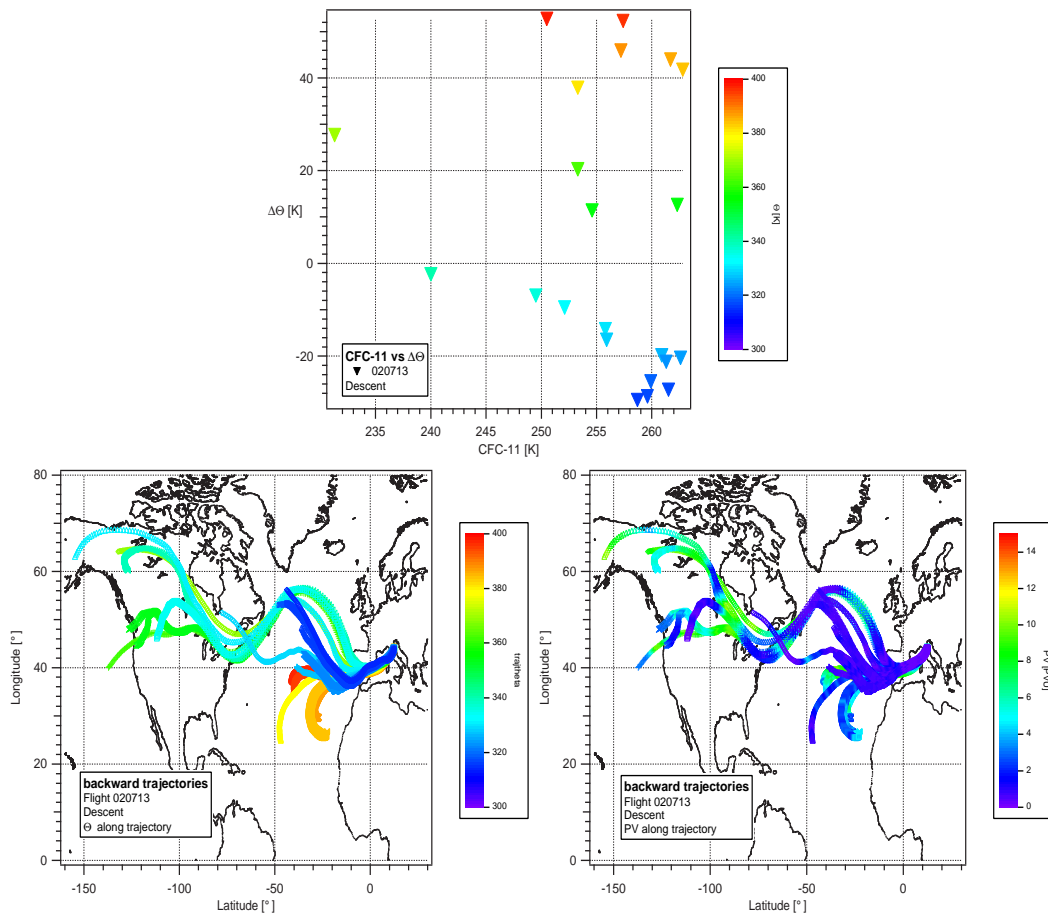


Figure 4.11: (Upper panel) CFC-11 (ppt) on July 13 plotted versus  $\Delta\theta$  (K). Only data that were measured in the LMS and upper troposphere during the descent are shown. (Lower panel, left side)  $\theta$  along the 5-day backward trajectories for the measurements during the descent. (Lower panel, right side) PV along the 5-day backward trajectories for the measurements during the descent.

points with mixing ratios below 250 ppt the air parcels originated from the region of Alaska. The trajectories started at a PV level with more than 4 PVU, thus above the tropopause. The two lower air parcels were then transported into the troposphere, resulting in mixing ratios smaller than 250 ppt even below the tropopause.

All other trajectories started below the tropopause or in the tropopause region ( $\leq 4$  PVU), i.e. the probed air parcels were either transported into the LMS or stayed inside the troposphere.

### 4.3.2 Flight of July 15, 2002

The PV cross section on that day (Figure 4.4) shows the strongly developed PV anomaly over Forlí. The ascent was performed right in the center. For this flight trajectories were available for the ascent only. Consequently, no detailed analysis could be done for the dive and the descent.

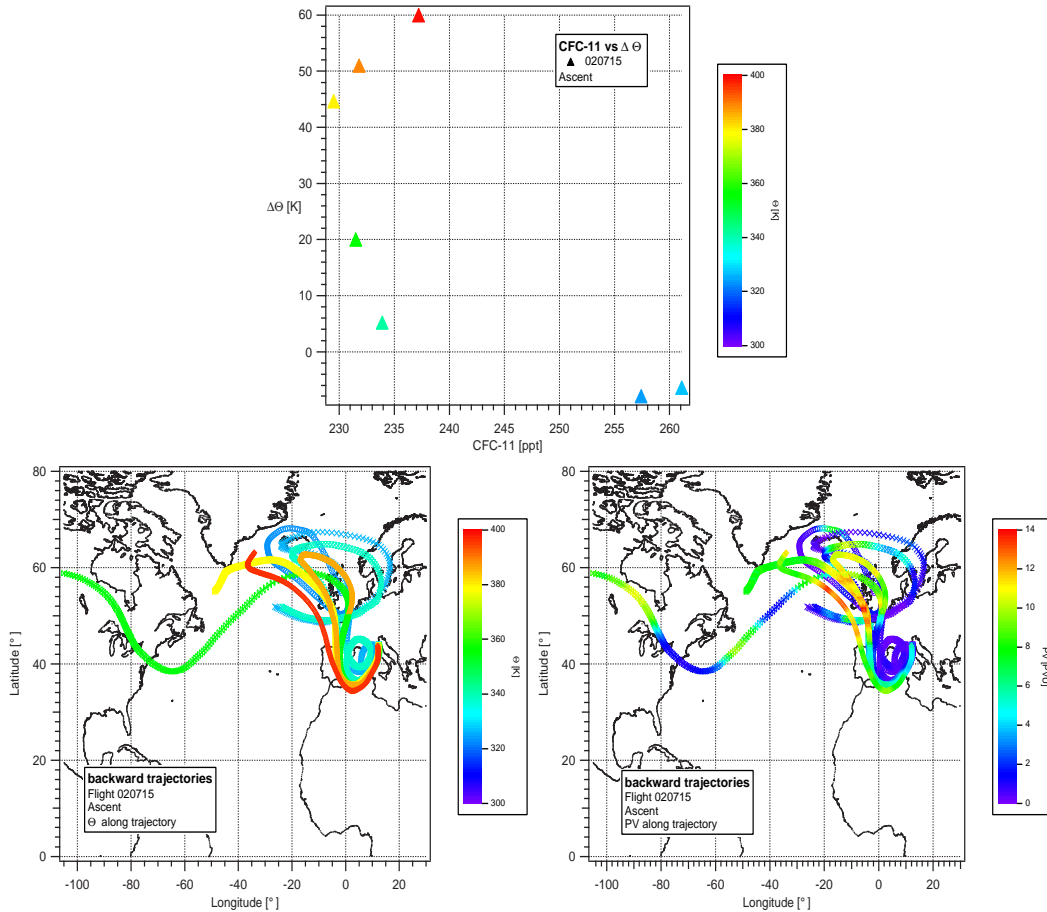


Figure 4.12: (Upper Panel) CFC-11 (ppt) of July 15 plotted versus  $\Delta\theta$  (K). Only data that were measured in the LMS and upper troposphere during the ascent are shown. (Lower panel, left side)  $\theta$  along the 5-day backward trajectories for the measurements during the ascent. (Lower panel, right side) PV along the 5-day backward trajectories for the measurements during the ascent.

The trajectory analysis for the ascent reveals an interesting history of the air parcels. All of them came down in a spiral movement from northern Europe. Although the starting points varied from locations over the Atlantic to Canada, they ran close to each other in the final part. Very high PV values are reached over the British Islands, and generally, at the point of origin the air parcels predominantly

had a stratospheric character ( $PV > 4$  PVU). All measurements taken in the LMS consequently exhibit rather low mixing ratios of CFC-11.

Crossing the LMS from 300 K to 400 K constantly in a high PV region, no pronounced layering in the LMS region is indicated by the mixing ratios as it was the case on the 13th of July; still the trajectories of the air masses show separate source regions, again. At potential temperatures about 360 K there is a layer of air that came from the north American continent, below and above air masses originated over the Atlantic.

The trajectories which correspond to the measurements of tropospheric character started in the troposphere, hardly indicating any in-mixing of stratospheric air.

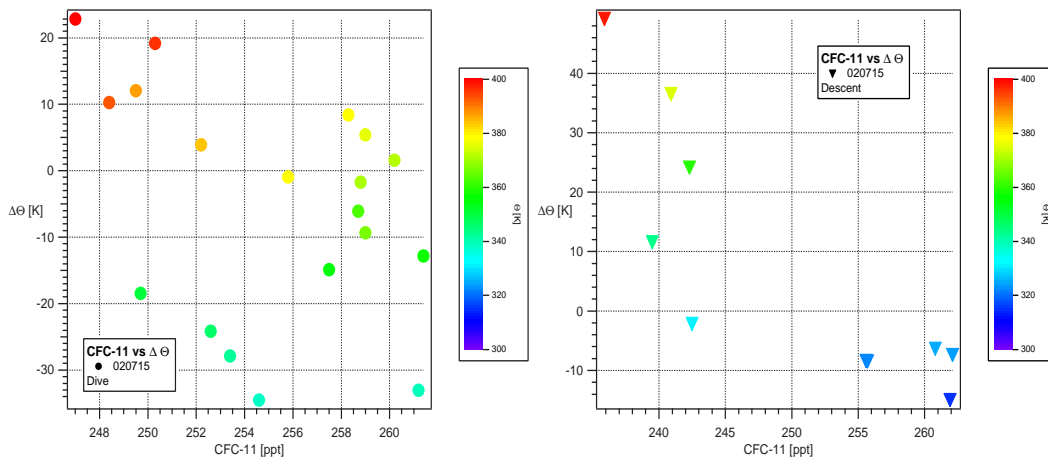


Figure 4.13: CFC-11 (ppt) of July 15 plotted versus  $\Delta\theta$  (K). Only data that were measured in the LMS and upper troposphere during the dive (left panel) and the descent (right panel) are shown.

As mentioned before, no trajectory data were available for the remaining flight, but the tracer data exhibit the same structure during descent as during the ascent. Predominantly, low mixing ratios are observed.

Anyhow, the dive which was carried out south east of Forlí (see Figure 4.1), i.e. at the edge of the PV anomaly, shows a distinct layering with two  $\theta$  - levels with relatively low mixing ratios in CFC-11. One level is  $\Delta\theta = 20$  K below the tropopause and the other 10 K above the tropopause. The PV cross section (Figure 4.4) shows an inversion of the PV gradient between 350 K and 400 K south of the center of the PV anomaly, implying a layering in the PV as well.

### 4.3.3 Flight of July 18, 2002

Between July 15 and July 18, the PV streamer passed Italy, thus, during this special flight the Geophysica probed the backside of the PV feature. The Geophysica flight path crossed the region  $300 < \theta < 400$  K four times: during the ascent, two dives and the descent.

### The ascent

During the ascent (Figure 4.14) only four measurements were taken in the LMS ( $\Delta\theta > 0\text{K}$ ). Air parcels belonging to the upper two measurements (red and orange points) above 380 K were transported eastward from the Atlantic.

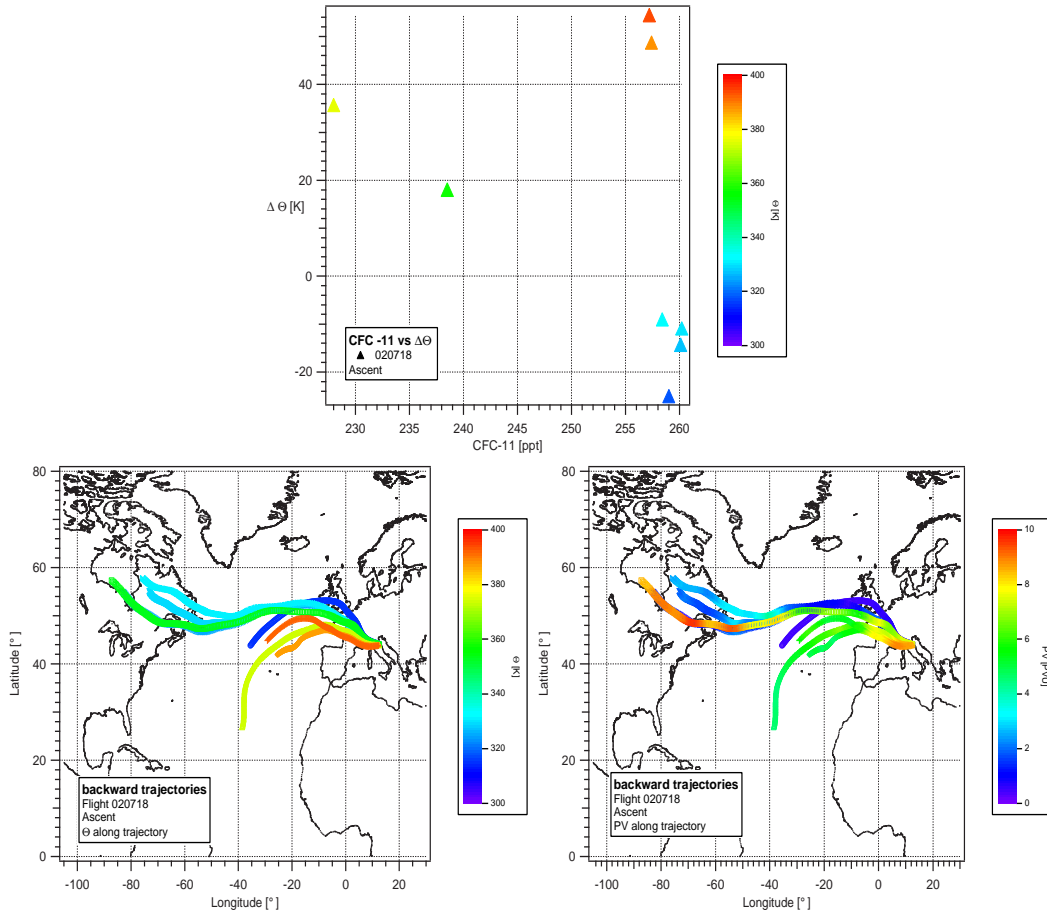


Figure 4.14: (Upper panel) CFC-11 (ppt) on July 18 plotted versus  $\Delta\theta$  (K). Only data that were measured in the LMS and upper troposphere during the ascent are shown. (Lower panel, left side)  $\theta$  along the 5-day backward trajectories for the measurements during the ascent. (Lower panel, right side) PV along the 5-day backward trajectories for the measurements during the ascent.

The PV along the trajectory increased in time; the air parcels, containing almost mixing ratios of CFC-11 ( $> 255$  ppt), were transported isentropically from a region with lower PV into the high PV region. Only few K below, at nearly  $\Delta\theta = 40$  K, the lowest mixing ratio during the ascent was measured. The air mass came from the central Atlantic at about  $30^\circ$  N. The PV along this trajectory increased dramatically towards the point of measurement. Being transported from a lower PV region in the subtropical latitudes, one would rather expect higher than the low mixing ratios of

CFC-11 seen in the measurements above. A similar measurement was taken on the 13th; a rather low mixing ratio obtained in an air mass, that came from the Atlantic about  $30^\circ$  N. The 5-day backward trajectory analysis gives no satisfying explanation for these low mixing ratios.

The air parcels of the following measurements below  $\Delta\theta = 20$  K originated at about  $60^\circ$  N over Western Canada. The trajectory for the one parcel that was measured at  $\Delta\theta = 19$  K (at about 360 K potential temperature, green trajectory) indicates that this air was stratospheric all the time and came down from the high-latitude stratosphere. All other measurements were taken below the tropopause ( $\Delta\theta < 0$  K) at potential temperatures between 300 K and 340 K. Although being of the same geographic origin as the air parcel at  $\Delta\theta = 20$  K, the mixing ratios measured are tropospheric. Consequently, the trajectories corresponding to these measurements were completely tropospheric, staying well below 4 PVU all five days. The air parcel measured at the lowest potential temperature has a similar geographical history as those above 370 K, but was purely tropospheric. Again, the same layering as observed on the previous days can be seen. In the upper and lowest region, the source regions are located over the Atlantic, the air masses in between came from Canada. Corresponding to this layer of low mixing ratio, the PV cross section in Figure 4.4 shows the most pronounced high PV layer on the 18th between 340 K and 380 K. The low mixing ratios above correspond to a layer of low PV in the upper part of the LMS.

### Dive I

During the first dive, four measurements were taken between 390 K and 400 K (Figure 4.15). All measurements exhibit mixing ratios of rather stratospheric character and have the same transport history. Start and endpoint of the trajectories are close to each other, describing a cyclonal movement of air coming down from higher PV levels. However, the upper two measurements were taken at a higher PV and show a stronger stratospheric influence, namely lower mixing ratios. In the PV map at 390 K potential temperature (see Figure 4.16) a slightly increased PV is also visible in the vicinity of the flight path during the first dive. At lower  $\theta$ -levels low PV is observed (see Figure 4.2).

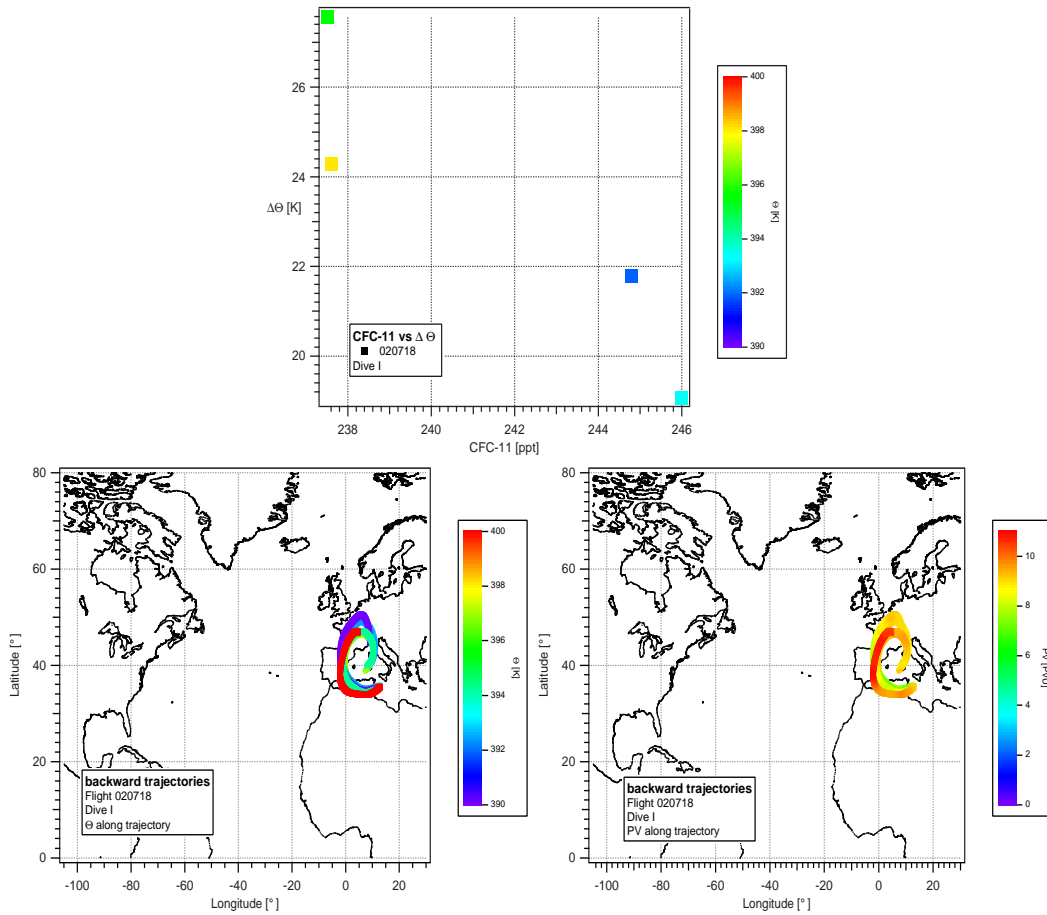


Figure 4.15: (Upper panel) CFC-11 (ppt) on July 18 plotted versus  $\Delta\theta$  (K). Only data that were measured in the LMS and upper troposphere during the first dive are shown. (Lower panel, left side)  $\theta$  along the 5-day backward trajectories for the measurements during the first dive. (Lower panel, right side) PV along the 5-day backward trajectories for the measurements during the first dive.



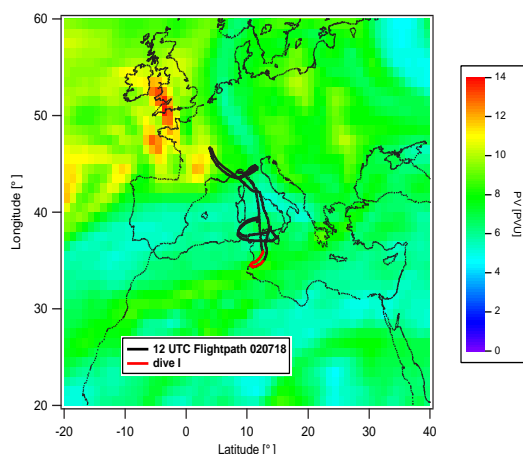


Figure 4.16: PV [PVU] map at 390 K potential temperature on the 18th of July 2002. The Geophysica flight path at 12 UTC is displayed in black. The first dive is highlighted in red. PV was interpolated from ECMWF data.

## Dive II

As during the ascent and the previous flights, the main source regions for the air parcels measured during the second dive, originated either 50-60° N over Western Canada or the Central Atlantic around 30° N (Figure 4.17). Those measurements taken in air masses coming from the latter region show high mixing ratios close to the tropospheric background of 261 ppt, but were all measured well inside the LMS. The PV along the corresponding trajectories increased from values of about 3 PVU to 6 PVU indicating transport from the subtropical tropopause region into the mid-latitude LMS.

Measurements taken in the tropopause region split up into two different groups, one with high mixing ratios above 255 ppt and the other with mixing ratios below 255 ppt (index A-D). The first group was measured in pure tropospheric air; all corresponding trajectories were nearly constantly below 4 PVU. In the second group all trajectories started at a PV level larger than 4 PVU, thus in the LMS and were transported to the tropopause region.

The measurement taken at  $\Delta\theta = 60$  K can be compared with the data from dive I. Again, the air parcel was transported in a cyclonal manner from a high PV level, bringing down air of stratospheric origin into the LMS.

An interesting feature is the fact that the layering seen here in the mixing ratios is contrary to the one observed during the previous flights. Relatively high mixing ratios are found between 360 K and 390 K and low values above and below. The PV cross section along 12° E gives evidence for this behaviour. South of Forlí, where the dive was performed, the layer of low PV is more pronounced in the upper part of the LMS and the high PV layer decreases in height and strength. Thus implying a thin layer of lower mixing ratios in the tropopause region and higher mixing ratio above. Only above 380 K, a sharp increase of PV is seen corresponding to the measurement

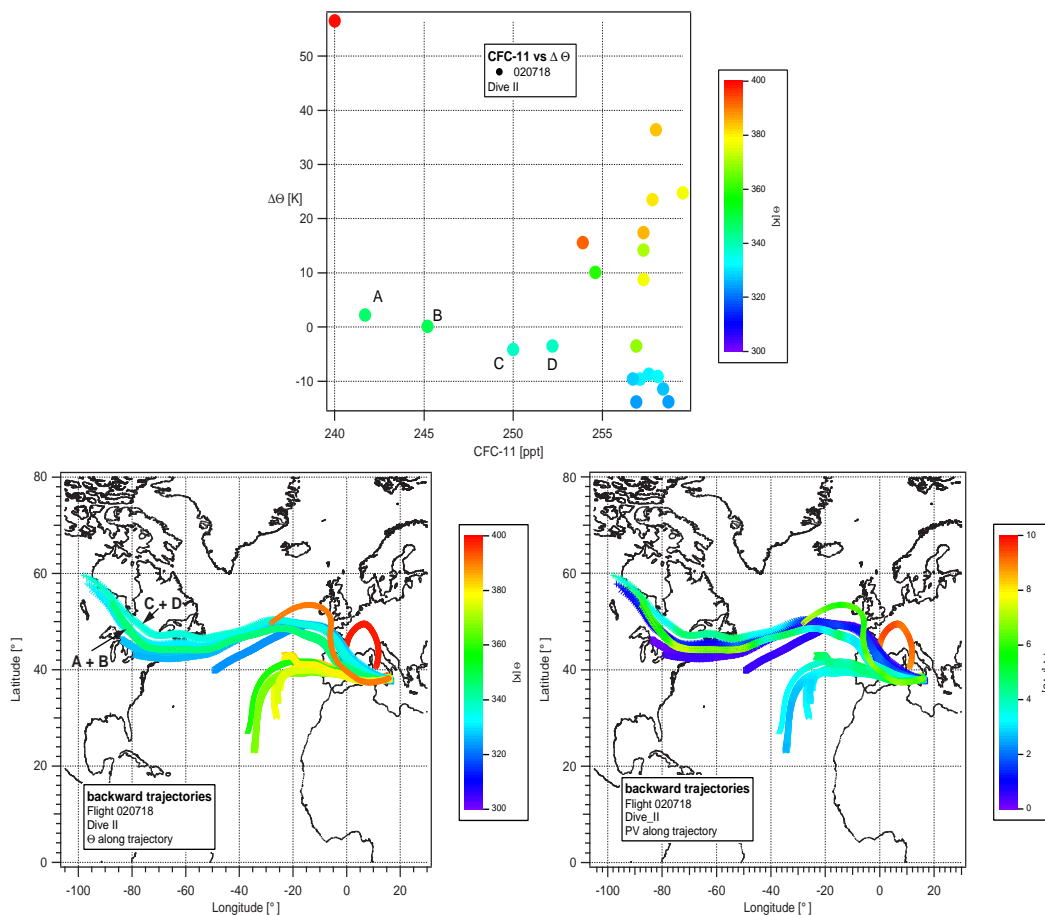


Figure 4.17: (Upper panel) CFC-11 (ppt) on July 18 plotted versus  $\Delta\theta$  (K). Only data that were measured in the LMS and upper troposphere during the second dive are shown. (Lower panel, left side)  $\theta$  along the 5-day backward trajectories for the measurements during the second dive. (Lower panel, right side) PV along the 5-day backward trajectories for the measurements during the second dive.

of again lower mixing ratios in CFC-11.

### The descent

The descent (Figure 4.18) shows the same structure as the ascent (Figure ??). At the highest level, high mixing ratios close to the tropospheric background were measured. Below, a level of high PV is evident and, as for the ascent, the lowest mixing ratios are present. Corresponding trajectories originated as mentioned before in Western Canada, starting at PV levels above 8 PVU (green  $\theta$ -trajectories). The remaining data were obtained in the troposphere, with a PV at the time of measurement about or below 2 PVU. However, for the measurements close to the tropopause with slightly smaller mixing ratios the trajectories show elevated PV along the flight path,

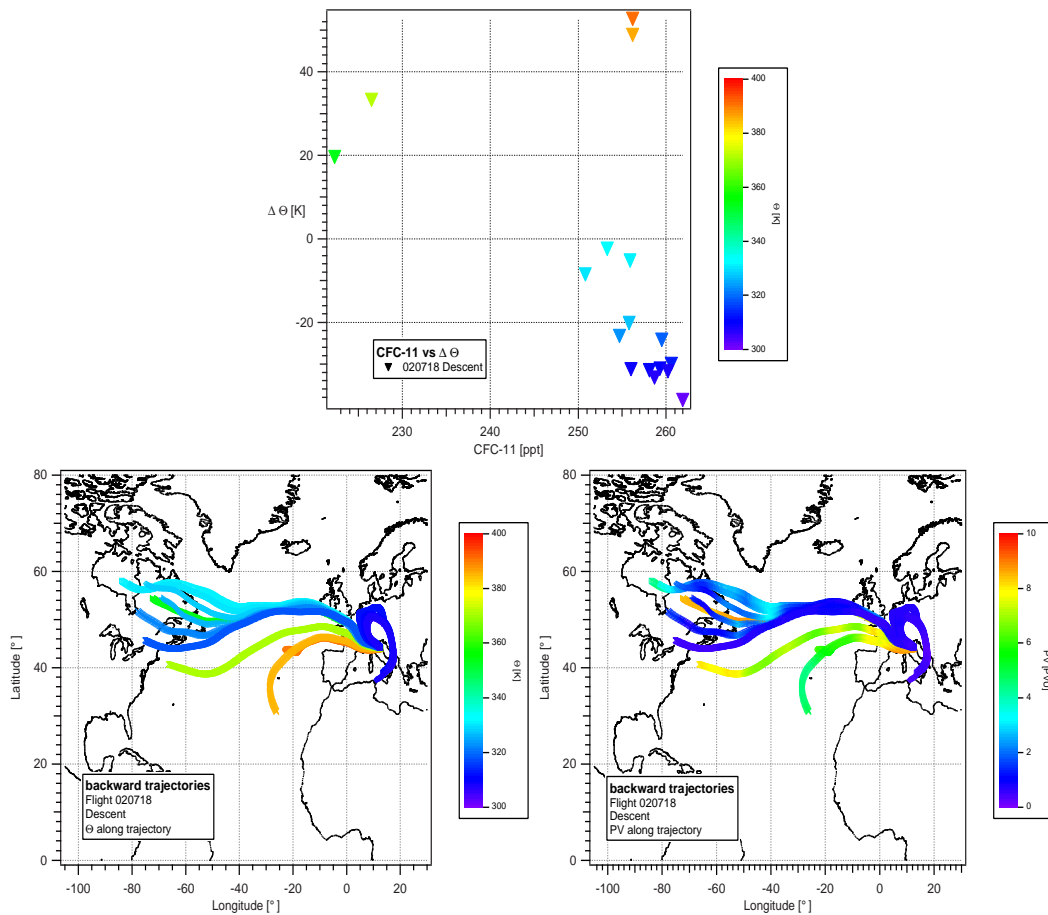


Figure 4.18: (Upper panel) CFC-11 (ppt) on July 18 plotted versus  $\Delta\theta$  (K). Only data that were measured in the LMS and upper troposphere during the descent are shown. (Lower panel, left side)  $\theta$  along the 5-day backward trajectories for the measurements during the descent. (Lower panel, right side) PV along the 5-day backward trajectories for the measurements during the descent.

probably indicating some minor influence from the LMS.

At the lowest potential temperatures cyclonal movement of air can be seen again, this time inside the troposphere. In this last part of the flight, the Geophysica flew through heavy thunderstorm activity.

#### 4.3.4 Flight of July 22, 2002

The flight on the 22nd of July was flown mostly at a high altitude level between 17 km and 19 km. No dive was performed and the LMS region was only crossed during ascent and descent. At roughly  $\theta = 340$  K the tropopause over Forlì was rather high compared to the other July flights. During this last flight of the July campaign, the LMS over Forlì was probed two days after the PV streamer had passed.

## The ascent

During ascent (Figure 4.21) low mixing ratios were measured well inside the troposphere, about 40 K below the tropopause. Towards the tropopause, the mixing ratio increased to tropospheric levels.

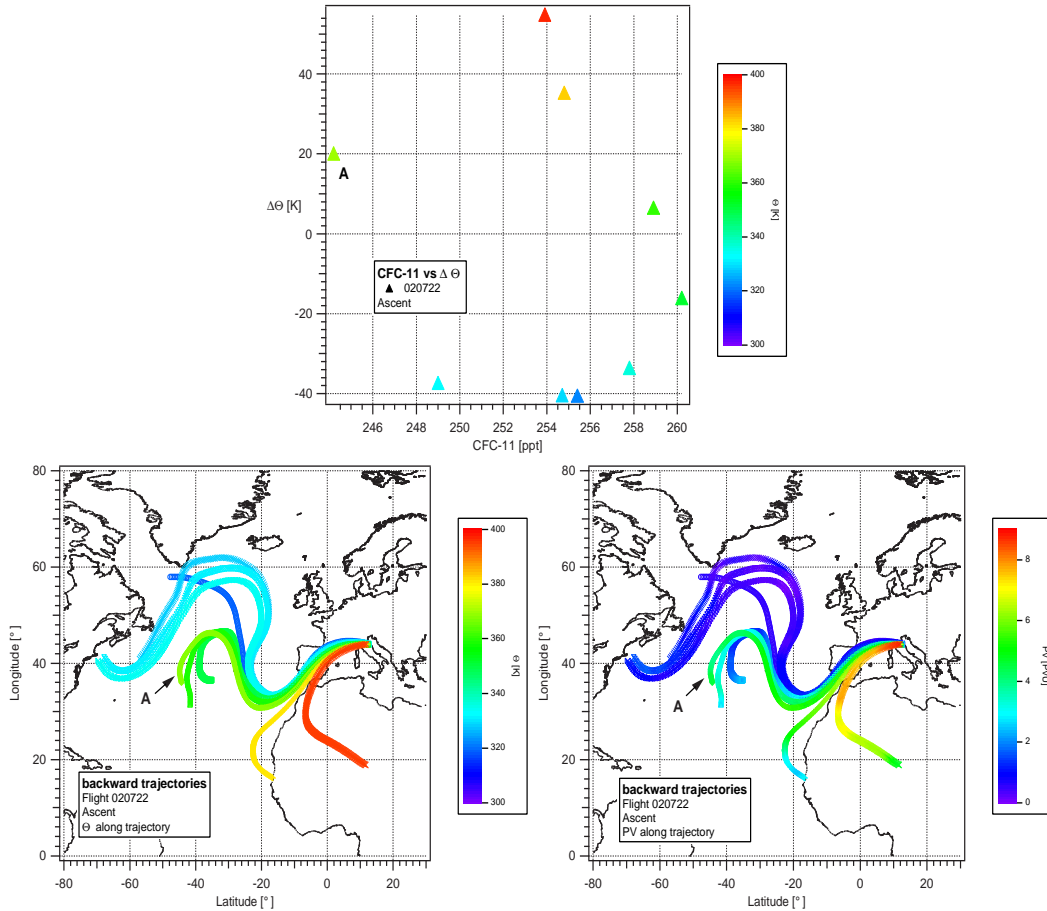


Figure 4.19: (Upper panel) CFC-11 (ppt) on July 22 plotted versus  $\Delta\theta$  (K). Only data that were measured in the LMS and upper troposphere during the ascent are shown. (Lower panel, left side)  $\theta$  along the 5-day backward trajectories for the measurements during the ascent. (Lower panel, right side) PV along the 5-day backward trajectories for the measurements during the ascent.

In the lowest part of the LMS a lower mixing ratio ( $\sim 245$  ppt) was observed, but above, the mixing ratios increased again. Compared to all other July flights, where low mixing ratios occurred, these values are rather high but certainly not merely tropospheric.

Again, the trajectories show an altitude-dependent origin. Below  $\theta = 340$  K, the trajectories came from the American east coast; the lowest one from Greenland. The PV along these trajectories was constantly below 4 PVU indicating no recent

in-mixing of stratospheric air. At the level around 360 K, the air parcels originated over the central Atlantic, the one corresponding to the lowest measured mixing ratio (point A) being the only one that started with a  $PV \geq 4$  PVU. The two uppermost data points derive from air masses coming from the subtropics over the west coast of Africa. Both originated in the tropopause region and were transported to higher PV levels.

### The descent

During the descent (Figure 4.22) the same  $\theta$ -dependent location of the trajectories

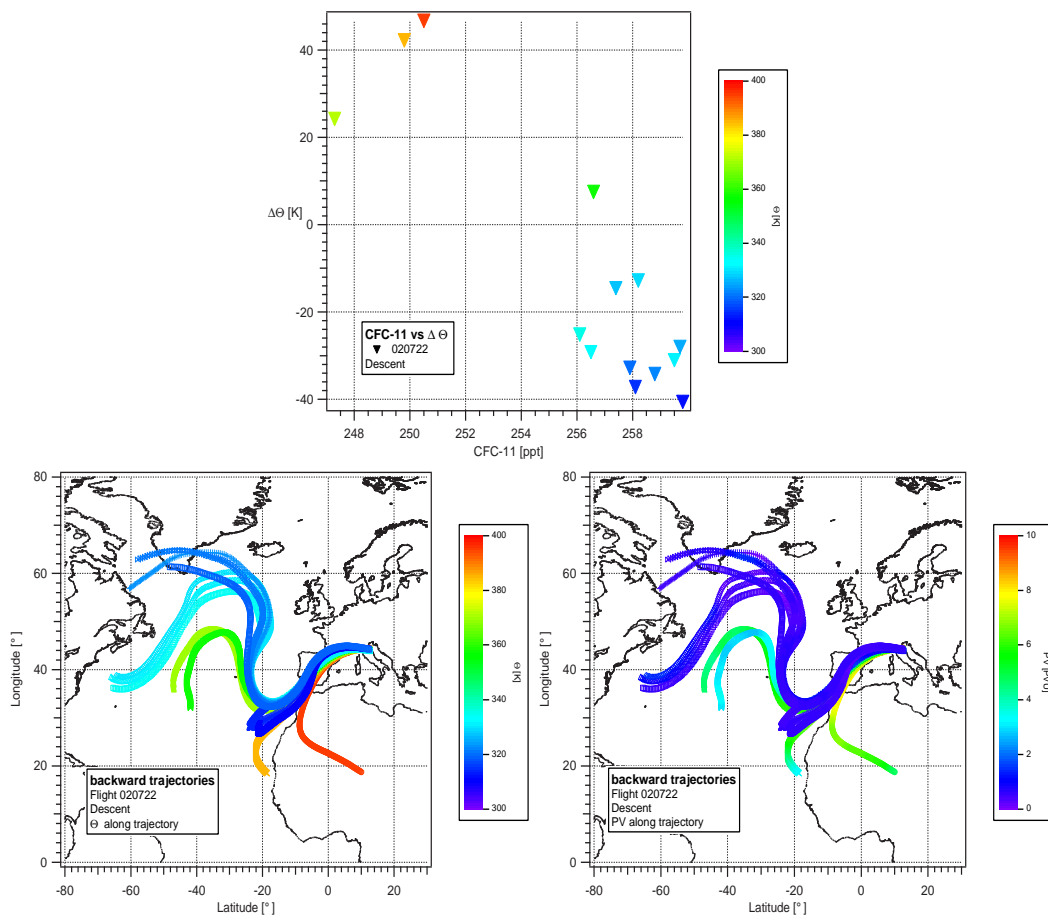


Figure 4.20: (Upper panel) CFC-11 (ppt) on July 22 plotted versus  $\Delta\theta$  (K). Only data that were measured in the LMS and upper troposphere during the descent are shown. (Lower panel, left side)  $\theta$  along the 5-day backward trajectories for the measurements during the descent. (Lower panel, right side) PV along the 5-day backward trajectories for the measurements during the descent.

was observed as during the ascent and the mixing ratios are basically in the same range with the lowest value around 20 K above the tropopause. The upper tropo-

sphere does not show measurements as low as during the ascent but tends to values around the tropospheric background (about 260 ppt).

### 4.3.5 Summary of all July flights

In July 2002, the UT/LS region over Southern Europe was strongly influenced by the crossing of an elongated streamer of high PV.

The trajectory analysis shows that during the passing of the streamer, air masses measured in vertical profiles over Italy originated in different source regions. The main locations were the North American continent, the Central Atlantic, and in a few cases Europe and North Africa. In general, the low mixing ratios were connected to the fast transport of air masses from North America ( $60^{\circ}$  N), whereas the transport from other source regions mostly corresponded to higher mixing ratios, if not tropospheric ones. Except for two cases, an origin in the Atlantic and Africa between  $20\text{-}30^{\circ}$ N was associated with quasi-isentropic transport from the tropopause or even upper troposphere region into the LMS over Italy, resulting in tropospheric mixing ratios at a potential temperature of 400 K. The resulting layering of air masses with different mixing ratios was seen on the 13th on the front side edge and on the 18th on the back side edge of the streamer. This layering was observed again on the 15th during a dive in the edge region of the PV anomaly.

However, during the ascent and the descent over Forlí on the 15th of July — when the fully developed streamer arrived over Italy — different trajectory locations were observed and the trajectories described a spiral-like movement of air masses; just like the motion of the streamer itself. Measuring completely inside the high PV region of the streamer, only low mixing ratios were observed.

After the passing of the streamer, the measurements in the LMS show mixing ratios below the tropospheric background, even though not as low as during the streamer event. Unfortunately, no tracer measurements before July 13 were available in the Forlí area to give evidence, that a mixing event between air masses from high and low latitudes really occurred.

### 4.3.6 The October flights

High variability connected to the fast transport of rather different air masses was seen in the summer data. Compared to this event in the summer season, the observed variability in October is significantly lower. A streamer event similar to the one observed in July 2002 did not show a pronounced effect on tracer mixing ratios. However, compared to all other flights performed in October, the “streamer flight” exhibits the lowest mixing ratios in the LMS, most pronounced at the upper edge of the LMS, 40-60 K above the tropopause (see Figure 4.9). In the region 0-40 K above the tropopause the observed mixing ratios of CFC-11 ( $\text{O}_3$ ) are significantly higher (lower) in October compared to the July campaign. Thus, the LMS generally has a more tropospheric character concerning the mixing ratios of long-lived trace

gases. On the other hand, at 20 K or more above the tropopause, no mixing ratios of purely tropospheric character are observed, indicating far less recent transport from the subtropical tropopause region than in the summertime.

A streamer event has already been described in detail for the July flights. As an example for the October flights, only a description of October 22 will be given. On this day, a weak layering of the LMS was observed (see Figure 4.9), similar to the one in July, even though not as pronounced. As indicated in Figure 4.5, the flight path of the Geophysica was situated in the boundary region between areas of high and lower PV values implying the presence of different regimes of air masses. In Figures 4.21 and 4.22, the trajectories and the corresponding vertical profiles of CFC-11 are plotted for this flight as it was done for the July flights. In order to be able to compare, the July data are plotted in black additionally.

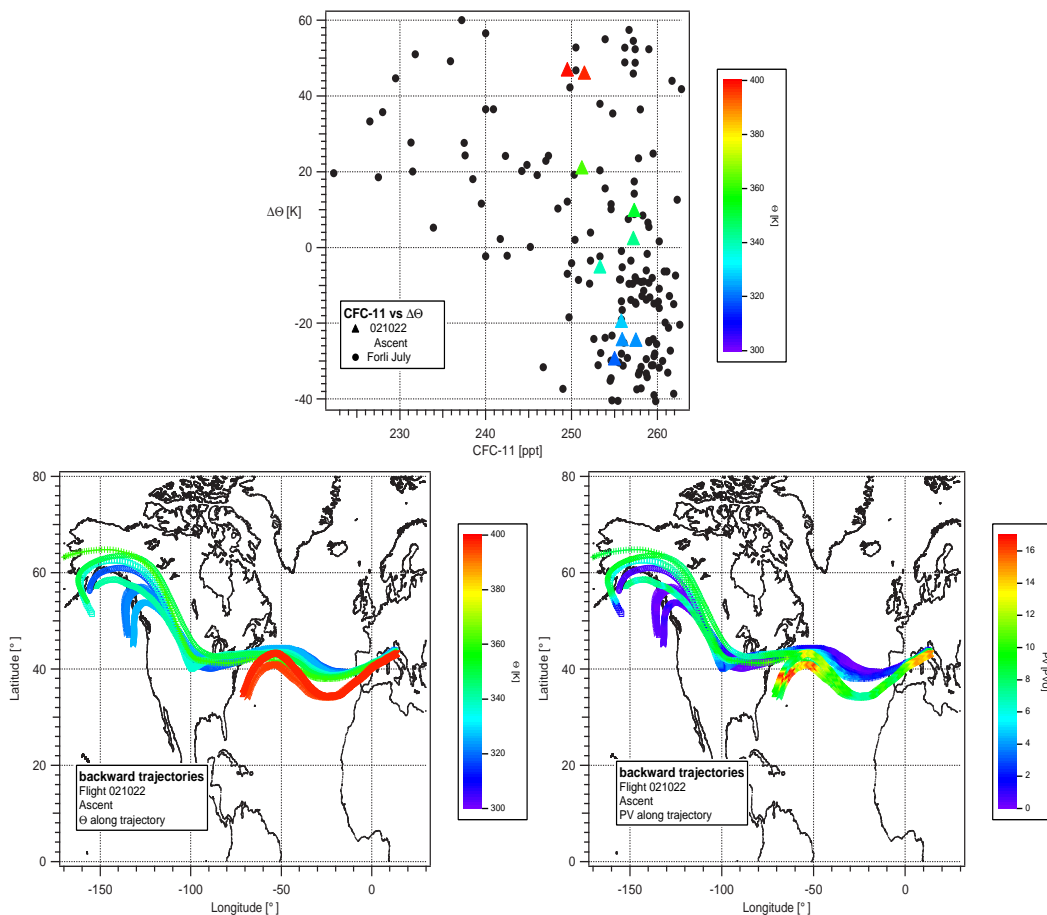


Figure 4.21: (Upper panel) CFC-11 (ppt) on October 22 plotted versus  $\Delta\theta$  (K). Only data that were measured in the LMS and upper troposphere during the ascent are shown. (Lower panel, left side)  $\theta$  along the 5-day backward trajectories for the measurements during the ascent. (Lower panel, right side) PV along the 5-day backward trajectories for the measurements during the descent.

During the ascent (Figure 4.21) we indeed see a split up of the trajectories. The upper measurements were taken in air masses originating from the Atlantic region while all measurements below 360 K were performed in air masses that originated at the west coast of Alaska and Canada. The corresponding CFC-11 measurements exhibit mixing ratios which are only slightly lower than the tropospheric background value. With 250 ppt of CFC-11 the lowest measurements during the ascent were taken at about 390 K. The air masses from the different source regions in the LMS exhibit no significant difference.

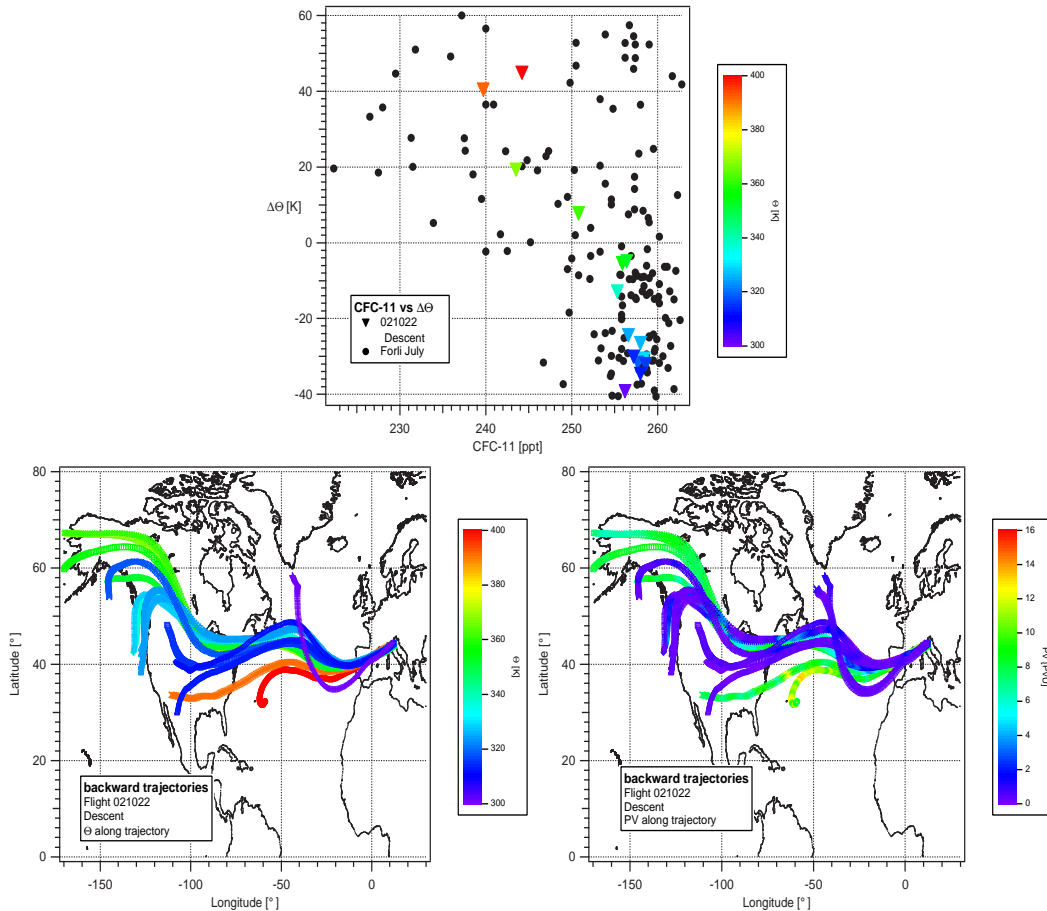


Figure 4.22: (Upper panel) CFC-11 (ppt) on October 22 plotted versus  $\Delta\theta$  (K). Only data that were measured in the LMS and upper troposphere during the descent are shown. (Lower panel, left side)  $\theta$  along the 5-day backward trajectories for the measurements during the descent. (Lower panel, right side) PV along the 5-day backward trajectories for the measurements during the descent.

During the descent (Figure 4.22) a similar, though more spread distribution of trajectories can be observed. While the lowest data points correspond to air masses that were transported from the Greenland region, the air masses between 310 K and 390 K all came from the American continent, though from varying latitudes



(30° N to 70° N). At 400 K the air masses originated over the middle Atlantic. All measurements below 360 K were made still inside the troposphere due to a rather high tropopause on that day. Still all measurements about 350 K and above originated in the stratosphere, having high PV values over large part of the transport history. But only air masses probed well above the tropopause exhibit lower mixing ratios around 240 ppt. Compared to the summer campaign neither the very high, close to tropospheric values, nor the very low mixing ratios about 220 ppt to 230 ppt were obtained, though a similar transport situation was observed with air masses being transported from various regions over the Atlantic to the American continent.

## 4.4 Assessment of mixing in the LMS during summer and fall

The previous section showed that the high variability in the vertical profiles, obtained over Forlí in July 2002, was connected to fast transport of air masses from the high latitudes and the subtropical tropopause region in the vicinity of a streamer of high PV. The corresponding measurements of long-lived tracers exhibit large differences in mixing ratio between those air masses, implying that mixing between them has not happened, yet. In order to assess the state of mixing of the LMS during the summer and fall more systematically, the measurements will now be compared to the conditions of the LMS in spring time.

### 4.4.1 Spring time initial conditions in the LMS

Trace gas measurements in the LMS in different seasons were performed during the SPURT<sup>2</sup> campaign between autumn 2001 and summer 2003 [Engel *et al.*, 2006]. Among other tracers, O<sub>3</sub> (ECO<sup>3</sup>), CFC-12 (GhOST II<sup>4</sup>), N<sub>2</sub>O (GhOST II and Tristar<sup>5</sup>) and CH<sub>4</sub> (TDL) were measured on board a Learjet 35a. In Figure 4.23, the flight paths of the Learjet during the spring, summer and autumn measurement campaigns are plotted. The spring time LMS was probed in May 2002 and April 2003. During the campaigns, north- and southbound flights were performed from Northern Germany. The measurements cover a latitude range from 35° N to 75° N. CFC-12 data obtained during these spring campaigns with the GhOST II instrument are displayed in Figure 4.24 together with the HAGAR CFC-12 measurements from the AVC campaign in Kiruna, March 2003. The colour code of the GhOST II data denotes the PV given in PVU.

All spring measurements are in good agreement with each other. Mid- and high-latitude data are very similar exhibiting mixing ratios below 500 ppt above 360 K.

---

<sup>2</sup>SPURenstofftransport in der Tropopausenregion

<sup>3</sup>chemiluminescence detection, ETH Zürich

<sup>4</sup>Gas Chromatograph for Stratospheric Tracers II, Uni Frankfurt

<sup>5</sup>TDL,MPI Mainz

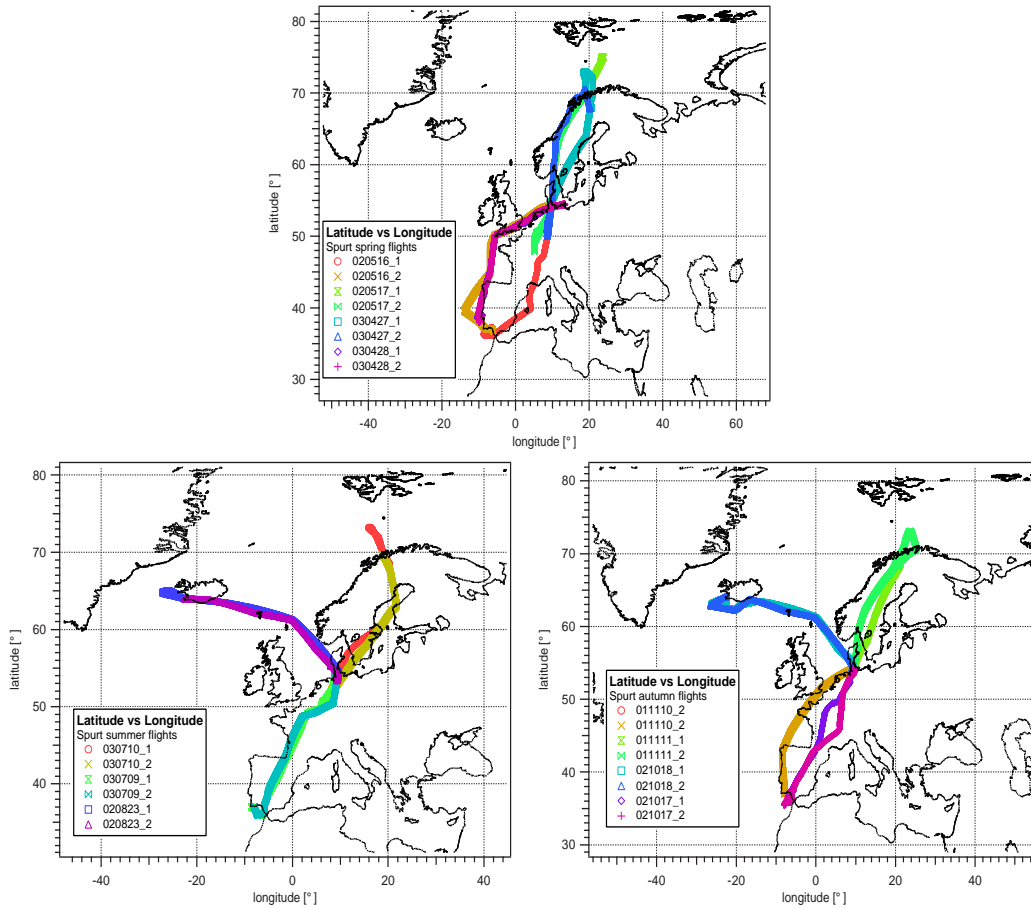


Figure 4.23: Flight paths during the SPURT campaigns [Engel *et al.*, 2006] in spring (upper panel), summer (lower left panel) and fall (lower right panel) 2001, 2002 and 2003.

Outliers are mostly measurements with low PV values, indicating that tropospheric air was probed. On the 27th of April much lower mixing ratios were observed. These correspond well to the lowest mixing ratios measured by HAGAR during the AVC campaign one month earlier. Here, air masses were probed that were influenced by vortex air (also see section 3.7.2). These data imply that the LMS exhibits very similar conditions from mid to high latitudes in the spring season, in accord with the expectation of a well-mixed surf zone after the winter.

The data are now used to set up initial conditions for the mid- to high-latitude LMS in spring, when hardly any tropospheric influence is observed [Ray *et al.*, 1999]. Initial profiles for the spring time are set up using HAGAR data from the AVC campaign obtained in March 2003 and SPURT data from the spring time flights in 2002 and 2003. Only data are used that were sampled well inside the stratosphere between 300 K and 400 K ( $\Delta\theta > 0$  K and  $PV > 4$  PVU). As an example, such stratospheric data are plotted for CFC-12 versus the potential temperature in

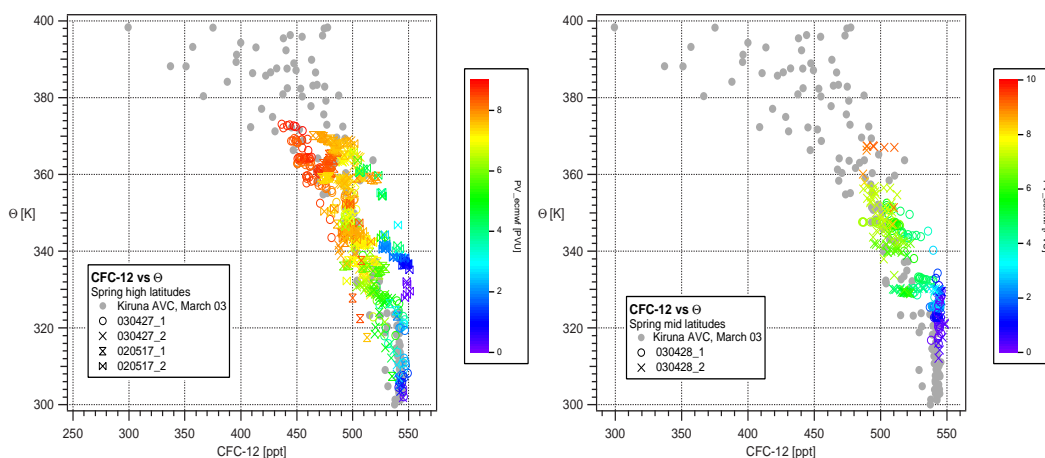


Figure 4.24: CFC-12 (ppt) measured by Ghost II plotted versus  $\theta$  (K) (coloured symbols) at high latitudes (left side) and mid latitudes (right side). Symbols denote the flight date and colour denotes the PV (PVU). For comparison HAGAR CFC-12 measurements obtained in Kiruna, March 2003 (AVC campaign; grey points) are shown. The flight on May 16 is missing; no CFC-12 measurements were performed during that flight.

Figure 4.25. The initial spring time profile for CFC-12 in the LMS was determined by calculating the average mixing ratio every 5 K. Error bars denote the standard deviation ( $1\sigma$ ). The average profile gives a good measure for the initial conditions in the LMS region, though not all variations are captured.

In the following section, these initial profiles will be plotted in tracer- $\theta$  space together with the tropospheric boundary as indicated in Figure 4.25, and compared to all measurements. Data falling into the space within  $1\sigma$  of the tropospheric mixing ratio will be regarded as purely tropospheric, whereas data falling within  $1\sigma$  of the initial profile can be regarded as “originally” stratospheric air, i.e. LMS air that has hardly ever or never seen mixing with tropospheric air since the spring time. With on-going isentropic transport over the summer season, more and more tropospheric influence is found in the LMS and the tracer measurements will exhibit mixing ratios closer to the tropospheric background value. Data points corresponding to air masses that have seen mixing between both initial conditions, will lie in the space between both regions.

Tropopause values were calculated as the average of data with a PV  $< 2$  PVU and  $\Delta\theta < -10$  K. Data from the SPURT campaigns mentioned above and from the Geophysica campaigns in 2002 and 2003 were used. The resulting average tropospheric mixing ratios for CFC-12, N<sub>2</sub>O, CH<sub>4</sub> and O<sub>3</sub> are given in Table 4.1. Initial conditions have been calculated for CFC-12, N<sub>2</sub>O, CH<sub>4</sub> and O<sub>3</sub>. These trace gases were used because they were measured on both aircrafts.

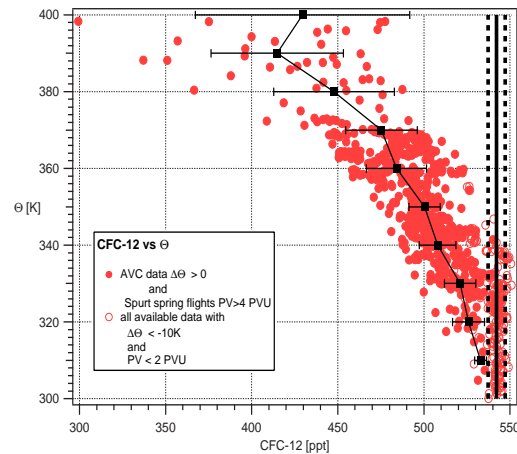


Figure 4.25: Spring time CFC-12 (ppt) measurements by GhOST II and HAGAR plotted versus  $\theta$  (K). LMS data ( $\Delta\theta > 0$  and  $PV > 4$  PVU) are plotted as grey points, grey circles denote tropospheric data ( $\Delta\theta < -10$  K and  $PV < 2$  PVU). The average tropospheric mixing ratio is indicated as a black line and  $\pm 1 \sigma$  as dashed lines.

Molecule	Tropospheric avg	$sdev_{trop}$
$N_2O$	314.4 ppb	4 ppb
$CH_4$	1770.54 ppb	53.42 ppb
CFC-12	538.82 ppt	5.6 ppt
$O_3$	538.82 ppt	5.6 ppt

Table 4.1: Average tropospheric mixing ratios and standard deviations for the tracers  $N_2O$ ,  $CH_4$ , CFC-12 and  $O_3$  from SPURT and Geophysica campaigns in 2002 and 2003.

## 4.4.2 Results

The measurements ( $300 \text{ K} < \theta < 400 \text{ K}$ ) taken with HAGAR during the Forlí campaigns are now compared to the spring initial conditions to give a qualitative view of the “state of mixing” of the LMS at the time of measurement. In Figures 4.26 and 4.29, the Forlí tracer data are shown versus the potential temperature  $\theta$  (K). The data are colour coded by  $\Delta\theta$  given in (K). Additionally, this comparison was made for data from the SPURT campaign for the summer (Figure 4.28) and autumn (Figure 4.31) flights. The SPURT data are colour coded by equivalent latitude  $\phi_{equiv}$  (see section B.3 in the appendix) rather than  $\Delta\theta$  since the measurements were taken at a wide latitude range covering mid to high latitudes, thus probing a variety of air masses. The equivalent latitude thus provides the information on the air mass origin.

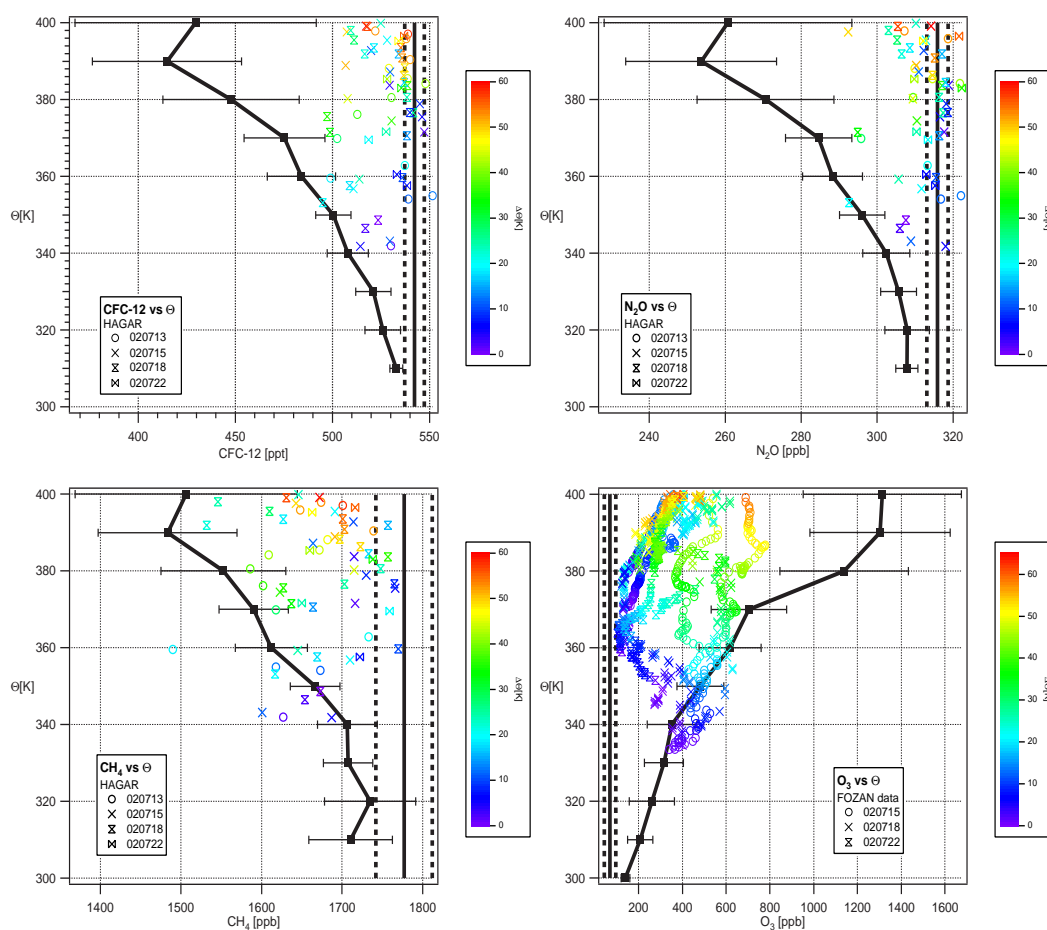


Figure 4.26: Comparison of the measurements made during July 2002 from Forlì with the initial tracer profiles in the LMS in spring and the tropospheric boundary condition. The HAGAR tracers CFC-12,  $N_2O$ ,  $CH_4$  and FOZAN  $O_3$  are shown. The colour code denotes  $\Delta\theta$ , the distance from the local tropopause in K.

## Summer data

The summer data fall between the spring time profile and the tropospheric background value. Below 380 K the lowest mixing ratios (highest for  $O_3$ ) fall within or only slightly above (below) the initial profile in spring, implying that those measurements have hardly seen any in-mixing of tropospheric air. At the same time tropospheric mixing ratios are found even up to 400 K. Thus, during the summer campaign, we find air masses below 380 K in the LMS that have not experienced intensive mixing and fall either within the range of initial spring time conditions or are of pure tropospheric character. As shown in the trajectory analysis (section 4.3), the latter air masses were connected to transport from the subtropical tropopause region while the low mixing ratios were connected to transport from the high-latitude LMS. Most of the data from the flight on 22nd of July — after the

passing of the streamer — are found slightly below tropospheric values. A closer look at  $\Delta\theta$  reveals that only data with  $\Delta\theta \leq 25$  K exhibit tropospheric values in the LMS below 380 K. However, there are also measurements at  $\Delta\theta \leq 20$  K with mixing ratios well below tropospheric values.

Above 380 K, most data points fall within the “mixing range”, indicating the existence of already mixed air. Rather unmixed tropospheric air is found as well, indicating fresh injections from the tropical stratosphere. Only  $O_3$  does not exhibit tropospheric mixing ratios at the highest levels but shows a sudden increase above 380 K. When assuming isentropic transport from the tropical stratosphere above 380 K this is explainable. The long-lived tracers are still at tropospheric levels since little depletion could occur in the short time since the air has been transported from the troposphere.  $O_3$ , however, has a significant source in the lower tropical stratosphere, therefore mixing ratios start increasing at the tropopause. In a correlation plot of  $O_3$  versus a long-lived tracer, such tropically influenced data should be distinguishable from the rest of the data. In Figure 4.27, the CFC-12– $O_3$  correlation is plotted. In the LMS it is difficult to separate the tropical data (grey markers) obtained during the APE THESEO<sup>6</sup> campaign from the mid-latitude measurements in Forlí. The latter are displayed as coloured symbols; the colour denotes the potential temperature at which the measurements were taken. However, the observations taken between 380 K and 400 K (highlighted by black circles) include data points falling in the more tropical part of the correlation curve.

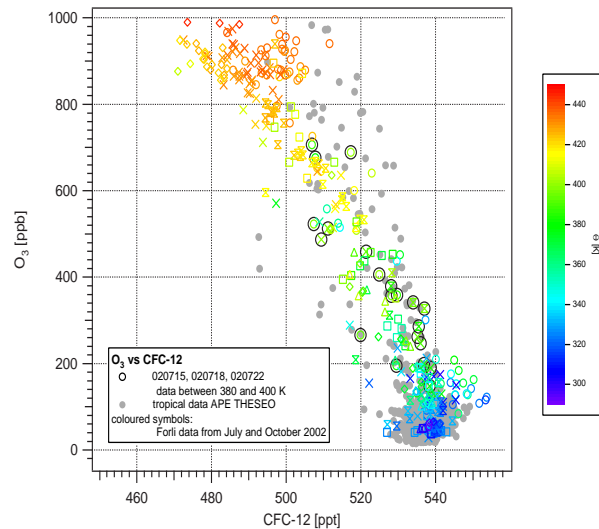


Figure 4.27: Correlation between  $O_3$  (ppb) and CFC-12 (ppt) observed during the tropical APE-THESEO campaign in 1999 (grey markers) and the Forlí campaign (colour coded by potential temperature). Data between 380 K and 400 K are highlighted with black circles.

<sup>6</sup> Airborne Platform for Earth Observation - Contribution to THESEO - Third European Stratospheric Experiment on Ozone; Seychelles 1999

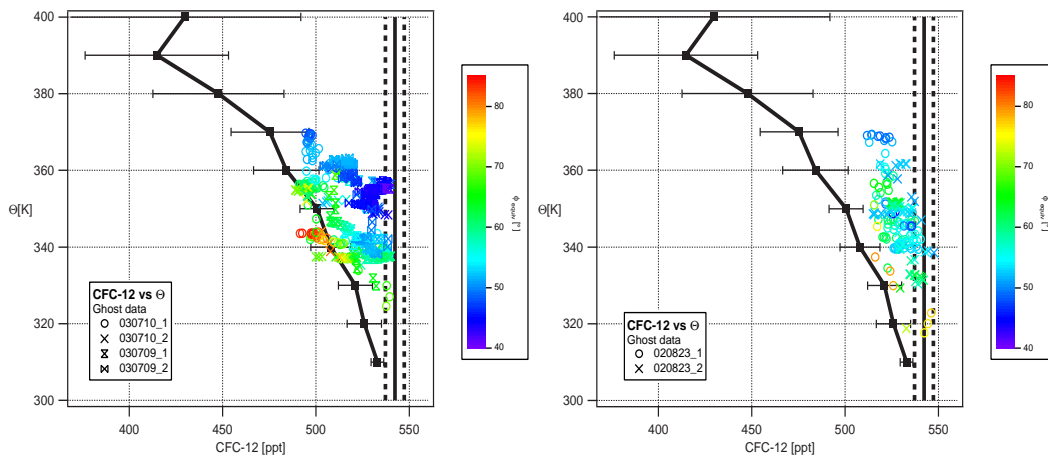


Figure 4.28: Comparison of measurements made during the SPURT campaigns in July 2002 (left panel) and August 2002 (right panel). Results are shown for CFC-12, which was measured with the GhOST II instrument.

In Figure 4.28, the CFC-12 measurements obtained with the GhOST II instrument during the SPURT campaigns performed in July 2002 and August 2003, are compared with the spring initial conditions. The data are colour coded by equivalent latitude. In July 2003 a high variability is again observed: Data at low equivalent latitude exhibit almost tropospheric mixing ratios while the data at high equivalent latitude follow the reference profile for the spring time LMS. In August 2002 a different distribution is observed. Only few data points follow the spring profile; most data are spread between tropospheric and the spring time mixing ratios. The tropospheric influence is increased and generally higher mixing ratios are observed. The separation into two classes of data — high equivalent latitude, low mixing ratio and low equivalent latitude, high mixing ratio — can not be done anymore. The same is found for the other tracers (not shown here).

### Autumn data

In autumn (see Figure 4.29), all data points fall into the space between the boundaries conditions - the spring profile and the tropospheric background value. The whole LMS is now dominated by tropospheric influence. Due to mixing, the variability has decreased and the differences between air masses from higher and lower latitudes (see trajectory analysis) are not pronounced anymore. Data with mostly tropospheric character can now be found up to 30 K above the tropopause. As already seen in Figure 4.9, the flight of October 11 exhibits rather low mixing ratios but most of the variability is produced by a very low tropopause (about 10 K lower than for all other autumn flights).

In the potential temperature range between 380 K and 400 K only mixing ratios below the tropospheric value can be found, although this is not as pronounced for

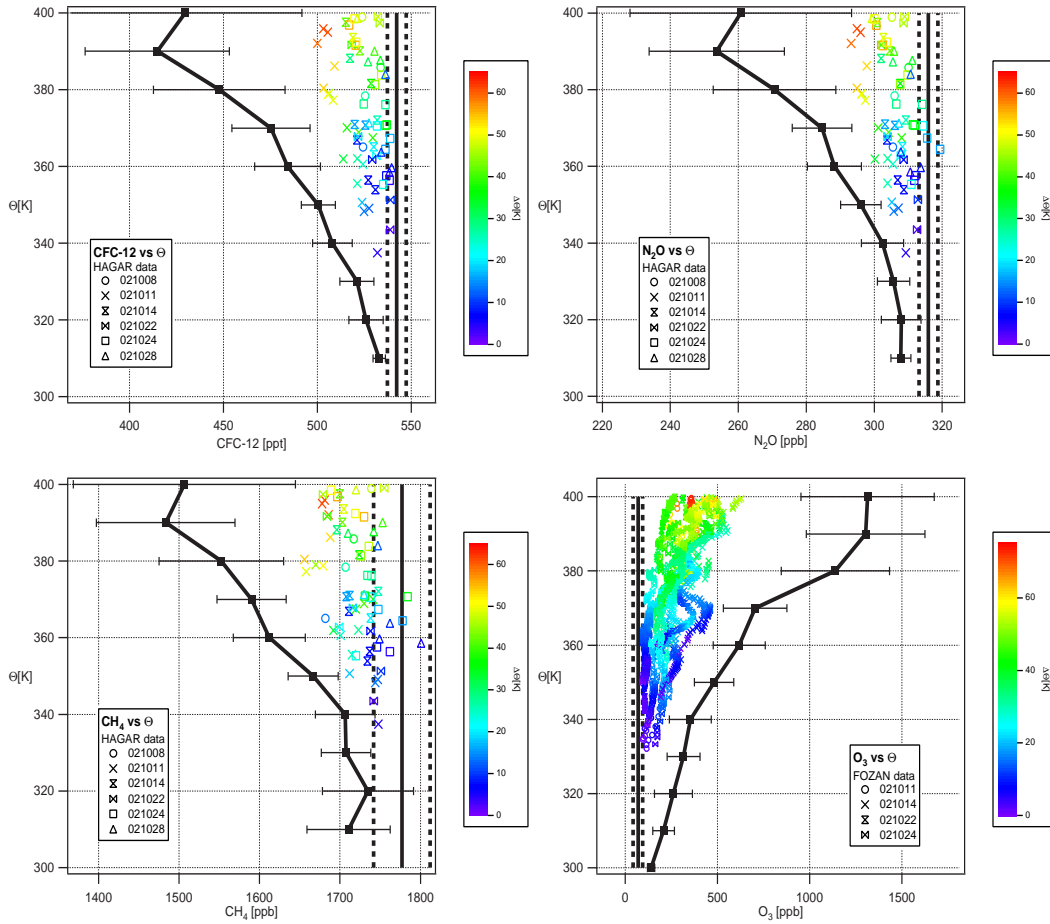


Figure 4.29: Comparison of the measurements made in October 2002 from Forlí with the initial tracer profiles in the LMS in spring and the tropospheric boundary condition. The HAGAR tracers CFC-12, N<sub>2</sub>O, CH<sub>4</sub> and FOZAN O<sub>3</sub> are shown. The colour code denotes  $\Delta\theta$ , the distance from the local tropopause in K.

the HAGAR tracers as for O<sub>3</sub>, indicating that tropical influence is still present. The CFC-12–O<sub>3</sub> correlation (Figure 4.30) of the autumn data exhibits an interesting split in the data (grey markers). Some of the data (mostly data from the 14th of October) fall onto a correlation curve between the tropical (black markers) and the mid-latitude correlation, indicating that there might have been some in-mixing of tropical air into the mid latitudes. In the LMS region (coloured data), however, this effect is not as obvious, since the correlation curves are difficult to separate and differences are marginal.

At the same time as the Forlí campaign, a SPURT campaign took place on the 17th and 18th of October 2002. The CFC-12 measurements obtained during the flights on these days are shown in Figure 4.31. Predominantly, data influenced by the troposphere are observed and differences in mixing ratio between air masses of



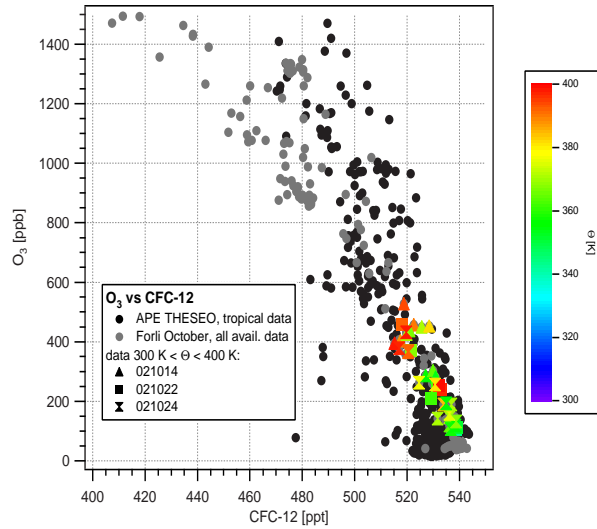


Figure 4.30: Correlation between O<sub>3</sub>(ppb) and CFC-12 (ppt) observed during the tropical APE-THESEO campaign 1999 (black markers) and the Forlì campaign (grey markers). Forlì data observed between 300 K and 400 K potential temperature are displayed as coloured markers with colour code denoting potential temperature.

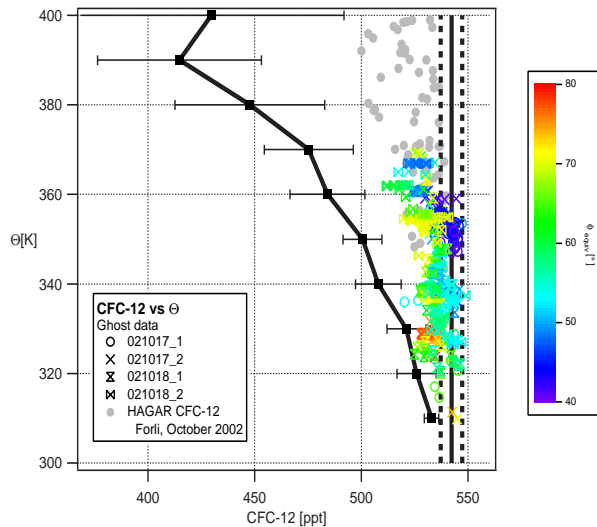


Figure 4.31: Comparison of the measurements made during the October 2002 SPURT campaign with the initial tracer profile in the LMS in spring and the tropospheric boundary condition.

high and low equivalent latitude are reduced as seen in the Forlí data, which is added in Figure 4.31 for comparison. Both the Forlí and the SPURT data fit well to each other, though each data set covers a different  $\theta$ -range.

## 4.5 Conclusions

A passing of a PV streamer in the LMS connected to a cut-off low system was observed in July 2002. During this event, air masses of different origin were transported to the mid latitudes. High-latitude air masses were transported southward, while air masses with mostly tropospheric character were transported northward into the LMS. Different mixing ratios were observed in these air masses, leading to highly variable measurements of tracer mixing ratios and a layering of the LMS. Low mixing ratios (high mixing ratios in  $O_3$ ) were associated with transport from the northern high-latitude LMS and mixing ratios of tropospheric character were found in air masses that have been transported from the tropopause region in the subtropics. In October 2002, a similar event was observed, but in contrast to the July event, the impact on tracer mixing ratios was minimal.

By comparing the measurements to the initial conditions in the spring-time LMS and the tropospheric mixing ratio, it was possible to examine the extent of mixing in the LMS. The initial condition for the LMS was generated from measurements performed in the LMS in the spring of 2002 and 2003 during the AVC and SPURT campaigns in mid to high latitudes.

The tracer observations show that the variability of the summer data matches the full span of the initial conditions. The air masses with high-latitude character and low mixing ratios fall well into the range of mixing ratios obtained in spring-time LMS; this was observed in both the APE ENVISAT and SPURT data set. On the other hand, the air masses that were transported from the subtropical tropopause region fall into the range of purely tropospheric mixing ratios thus implying recent injection of tropospheric air into the stratosphere. Due to strong isentropic transport in the vicinity of the streamer, both air masses were transported to the region over Forlí. Since the transported air masses still show the characteristics of the spring initial conditions, it can be assumed that the LMS region below 370 K has not yet experienced strong mixing events reaching the high-latitude region and that the high-latitude LMS reveals almost no tropospheric influence. Furthermore, tropospheric mixing ratios were found only in the LMS in a range of  $0 \text{ K} < \Delta\theta < 25 \text{ K}$  above the tropopause. Data gathered higher above the tropopause or coming from the high latitudes revealed less tropospheric influence.

This layer of recent tropospheric in-mixing corresponds well to results obtained from the SPURT measurements. *Hoor et al.* [2004] identified a mixing layer where mixing of tropospheric and stratospheric air occurs (see also [*Hoor et al.*, 2002]). This layer extends up to 30 K into the LMS in the summertime. Above, the tropospheric influence was found to decrease significantly.

The situation is slightly different in the range between 380 K and 400 K. Here, predominantly air masses of tropical origin are observed. This level slightly above the LMS is part of the “tropically controlled transition region” [Rosenlof *et al.*, 1997]. O<sub>3</sub> mixing ratios show a stratospheric signature with mixing ratios above 100 ppb, while the other tracers reveal close to tropospheric mixing ratios. This indicates strong transport from the tropical stratosphere as well as from the stratosphere above 400 K. Further descent of these air masses leads to transport of tropically influenced air into the LMS. Evidence for this pathway was found during SPURT [Bönisch, 2006; Hegglin *et al.*, 2006; Hoor *et al.*, 2004], with the indication that, depending on the season, up to 30-50% of the LMS air originated at the tropical tropopause.

In autumn a different situation is observed. Although, like in summer, air masses of different origin are observed, ongoing mixing since the summer has decreased the strong differences between high- and low-latitude air. The variability of the mixing ratios decreases and all measurements show an increased tropospheric influence. This is also observed during the SPURT campaign in October 2002 [Engel *et al.*, 2006]. Although the flight path covered several latitudes, the data are found to be rather compact. The now well-mixed LMS region exhibits no significant differences between the different latitude bands. Measurements taken in August 2002 during the SPURT campaign already show the trend towards a more compact distribution of data, implying that there a already better mixed LMS was probed compared to July 2002.

Generally, the tracer measurements during SPURT and the APE ENVISAT campaign can be compared very well and lead to the same conclusions. Below 380 K, fresh injections of young tropospheric air are found in a layer up 25 K above the local tropopause. There was no extended in-mixing of tropospheric air into the high-latitude ( $> 60^\circ$  N) LMS detected between spring and summer; thus mid- and high-latitude air reveal different tracer mixing ratios. In the course of the late summer the mixing sets in and a rather well-mixed LMS is observed in autumn, highly influenced by tropospheric air masses up to 380 K. This is in agreement with the findings of Hoor *et al.* [2004], who identified a mixing layer 20-30 K above the tropopause, where young tropospheric and stratospheric air masses are mixed within short time scales. Transport and mixing into the higher latitude region and higher levels above the local tropopause happens on longer time scales with a lag time of about 2.5 months.

Concerning mixing in connection with the streamer event no conclusions can be given, since an “undisturbed” mid-latitude LMS over the Mediterranean was not probed before the streamer event. However, measurements obtained after the passing of the streamer fall into the range of the autumn data, LMS data with high tropospheric influence. Though no statement can be made whether this was a local effect of the observed streamer event, it is certain, that this streamer event lead to injections of young tropospheric air into the LMS and the transport of air with mostly stratospheric character to the tropopause region. Thus, the strong and fast

isentropic transport connected to the streamer event is the precondition for further extensive mixing in the lower levels of the LMS.

# Chapter 5

## Summary

An extended data set for long-lived trace gases was obtained with the High Altitude Gas Analyser (HAGAR), an in-situ two-channel gas chromatograph combined with a CO<sub>2</sub> sensor, developed at the Institute for Meteorology and Geophysics at the University of Frankfurt [Strunk, 1999; Riediger, 2000]. Data sampled on board the Russian high altitude aircraft M55 Geophysica with this and with other instruments during four measurement campaigns in Italy and Sweden from July 2002 to March 2003 were used to study transport into and within the northern mid- to high-latitude lowermost stratosphere (LMS).

The experimental part of this thesis was the development of a new gas chromatographic channel for HAGAR. In order to measure CH<sub>4</sub>, the instrument had to be improved and mechanical and electronic changes were necessary (Chapter 2). After the successful improvement of the instrument, all in all eight tracer species could be measured: N<sub>2</sub>O, CFC-12, CFC-11, H-1211, CH<sub>4</sub>, H<sub>2</sub>, SF<sub>6</sub> and CO<sub>2</sub>. Except for H-1211, H<sub>2</sub> and SF<sub>6</sub> (precision of  $\sim 2\%$ ), the tracers were measured with a precision of smaller than 1%.

The data set gathered in the northern high latitudes during the EuPLEX and ENVISAT AVC measurement campaigns based in Kiruna/Sweden in January to March 2003 was used to quantify transport into the LMS (Chapter 3). Inspired by a mass balance study introduced by Ray *et al.* [1999], transport into the high-latitude LMS was examined assuming that air enters the LMS region via three different pathways: (I) quasi-isentropic transport from the troposphere and the lowest part of the tropical stratosphere, (II) descent of air from above 400 K in the mid- to high-latitude stratosphere outside the polar vortex and (III) descent of air from above 400 K inside the polar vortex. The fractions of air originating from these assumed source regions were determined by solving an overdetermined linear equation system using the HAGAR tracers N<sub>2</sub>O, CFC-11, CH<sub>4</sub>, H-1211 as well as O<sub>3</sub> (measured by FOX) and H<sub>2</sub>O (measured by FISH).

In order to solve the mass balance equations, boundary conditions for all three source regions (tropopause, stratosphere outside the vortex at  $\theta > 400$  K and the vortex at  $\theta > 400$  K) had to be determined for all tracers (section 3.4). For the

tropospheric as well as for the stratospheric boundary, constant tracer mixing ratios were assumed. At the vortex boundary, a time dependent boundary condition was determined, considering the strong trend of tracer mixing ratios due to strong subsidence of air in the vortex region during the winter.

Two separate data sub-sets were examined with the mass balance calculation (section 3.4.1): (i) data with relatively high vortex influence exhibiting low  $N_2O$  mixing ratios and (ii) data with high  $N_2O$  mixing ratios, implying only little influence from the vortex region.

The results suffer from relatively large errors due to large uncertainties in the boundary values of the tracers and the fact that the available tracer data do not everywhere provide sufficient constraints to fully determine the equation system. Nevertheless, the mass balance study reveals several aspects and quantitative information on transport into the LMS region between 300 K and 400 K:

An enhanced tropospheric fraction is found in the lowest 20 K of the LMS in both data sets. During the EuPLEx campaign, the tropospheric fraction in this layer is larger than 50% and during AVC larger than 30%. These findings correspond well with those of *Hoor et al.* [2004], who describe a shallow mixing layer with enhanced tropospheric influence in the lowest 20 to 30 K of the LMS.

Above this layer of enhanced tropospheric influence, the dominant fraction of air (on the average 75%) descended from the mid- to high-latitude stratosphere outside the vortex; this is found for both the “high  $N_2O$ ” and “low  $N_2O$ ” data sets.

A substantial ( $> 30\%$ ) influence from the vortex region is found only in the upper half of the LMS and for the “low  $N_2O$ ” data set; the fraction increases from 50% at 370 K to values of about 100% at 400 K during EuPLEx. Since the main descent in the winter 2002/2003 had already occurred prior to the EuPLEx campaign, further descent of air masses from the vortex region through the 400 K isentrope after the EuPLEx campaign is indicated by only a weak increase of the vortex fraction for the AVC campaign. For the “high  $N_2O$ ” data, an appreciable influence from the vortex region ( $f_{vortex} \approx 30\%$ ) is only detected during the AVC campaign for the highest  $\theta$  - levels in the LMS, implying some mixing of vortex and extra-vortex air masses. A comparison of the derived vortex fractions during EuPLEx and AVC with an artificial vortex tracer (CLaMS) also suggests that in-mixing of extra-vortex air into the vortex region has occurred above 400 K.

In order to improve the results, it would be of great interest to solve the mass balance equation with tracers providing more constraints for the solution (e.g. trace gases with rather short lifetimes compared to HAGAR tracers). Further improvements could be achieved by including more tracer measurements (satellite data, other campaigns) in order to improve the description of the boundary conditions. Generally, a comparison of the EuPLEx/AVC data set with other measurements in the Arctic and Antarctic could reveal valuable information on regional as well as temporal differences in the LMS. The presented results refer only to the Arctic region over northern Europe in the winter 2003.

In a second study, using data from the mid-latitude campaigns in Forlí in July and

---

October 2002, the state of mixing of the LMS region was assessed in connection with the passing of a cut-off low system (Chapter 4). A trajectory analysis revealed that during this event, air masses of different origin were transported to the mid latitudes. High-latitude air masses characterized by low tracer mixing ratios (high  $O_3$ ) were transported southward, while air masses with mostly tropospheric character were transported northward into the LMS, leading to highly variable measurements of tracer mixing ratios and a layering of the LMS. In October 2002, a similar event was observed, but in contrast to the July event, the impact on tracer mixing ratios was minimal.

By comparing the measurements to initial conditions in the spring-time LMS — generated from measurements performed in the LMS in the spring of 2002 and 2003 during the AVC and SPURT campaigns — and to the tropospheric mixing ratio, it was possible to examine the extent of mixing in the LMS.

Generally, the tracer measurements during SPURT and during the APE-ENVISAT campaigns compare very well and lead to the same conclusions. The variability of the summer data matches the full span of the initial conditions; this was observed in both the APE-ENVISAT and SPURT data sets. It can be assumed that the LMS region below 370 K has not yet experienced strong mixing events reaching the high-latitude region. The high-latitude LMS reveals almost no tropospheric influence.

Furthermore, tropospheric mixing ratios were found only in the LMS within 25 K above the tropopause, in accord with results obtained from the SPURT measurements identifying a mixing layer, extending up to 30 K into the LMS in the summertime, where mixing of tropospheric and stratospheric air occurs [Hoor *et al.*, 2002, 2004].

Between 380 K and 400 K — part of the “tropically controlled transition region” [Rosenlof *et al.*, 1997] — predominantly air masses of tropical origin were observed.  $O_3$  mixing ratios showed a stratospheric signature with values above 100 ppb, while the other tracers revealed close to tropospheric mixing ratios, indicating strong transport from the tropical stratosphere as well as from the stratosphere above 400 K. Further descent of these air masses leads to transport of tropically influenced air into the LMS. Evidence for this pathway was also found during SPURT [Bönisch, 2006; Hegglin *et al.*, 2006; Hoor *et al.*, 2004].

In autumn, a different situation was observed, as ongoing mixing since the summer had diminished the strong differences between high- and low-latitude air. The variability of the mixing ratios decreased and all measurements showed an increased tropospheric influence. This was also observed during the SPURT campaign in October 2002 [Engel *et al.*, 2006].

Since an “undisturbed” mid-latitude LMS over the Mediterranean was not sampled before the passing of the cut-off low, no conclusions can be given regarding mixing in connection with the associated streamer event. Nevertheless, the strong and large-scale isentropic transport associated with the streamer event can be regarded as the precondition for extensive mixing at smaller scales in the lower levels

of the LMS.

The results of this thesis demonstrate that valuable information on dynamics and transport in the LMS region can be gained from high-precision in-situ measurements of long-lived trace gases. Transport during winter into the high-latitude LMS from three source regions with differing chemical composition has been quantified. Large-scale transport during summer has been observed in a cut-off low juxtaposing photochemically aged high-latitude air and air of recent tropospheric origin. The subsequent mixing of these air masses in the LMS has been qualitatively assessed by the observation of diminished tracer gradients in the following autumn. In agreement with results of the SPURT campaign, influence of recently entrained tropospheric air has only been found in the lowest 20 K to 30 K of the LMS. At higher levels, the in-mixing of air from the troposphere happens on longer time scales; however, significant influence from the lowermost tropical stratosphere is observed at the highest levels.

The HAGAR data set of long-lived trace gases has been recently extended by new tropical and subtropical measurements (TroCCiNOx, Brazil, January/February 2005; SCOUT-O3, Australia, November/December 2005; and, soon to start, AMMA, Burkina Faso, August 2006). The data set now covers the Antarctic during spring, the tropics and the subtropics of both hemispheres at different longitudes and seasons, the northern mid latitudes during summer, fall and winter, and the Arctic during winter. This extensive data set thus holds great potential for further studies of UT/LS transport utilizing in-situ tracer data along the lines of the work of this thesis.

In 2009, a new scientific aircraft, HALO<sup>1</sup> [*HALO*, 2006], will be available as platform for remote sensing and in-situ instruments (including HAGAR). The ceiling height of 16 km and the superior payload capacity and range of HALO promise the possibility of an unprecedented improvement in the temporal and spatial coverage of the UT/LS. There is thus the perspective that significant progress in our understanding of chemical, microphysical, radiative and, last not least, dynamical processes in the UT/LS will be made in the foreseeable future, thus contributing to improved predictions of the composition and climate of our atmosphere.

---

<sup>1</sup>High Altitude and Long Range Aircraft



# Appendix A

## Mathematical basics

### A.1 Mean, standard deviation and deviation from the mean

The mean  $\bar{x}$  of a data set of  $n$  values  $x_i$  is calculated as [Schönwiese, 1992; Bronstein et al., 1993]

$$\bar{x} = \frac{1}{n} \sum_i x_i. \quad (\text{A.1})$$

The standard deviation  $\sigma$  of a data set of  $n$  values is given by the square root of the variance  $\sigma^2$  and is a measure for the scatter of the data.

$$\sigma = \sqrt{\frac{1}{n-1} \sum_{i=1}^n (\bar{x} - x_i)^2} \quad (\text{A.2})$$

If the uncertainties of the single data points are all equal, the estimated error in the mean  $\sigma_{\bar{x}}$  is calculated following

$$\sigma_{\bar{x}} = \frac{\sigma}{\sqrt{n}}. \quad (\text{A.3})$$

### A.2 Progression of errors

If  $Y$  is a function of  $n$  variables  $Y = f(x_1, x_2, \dots, x_n)$  the standard deviation of  $Y$  due to errors of the variables  $\sigma_{x_i}$  is calculated from the error progression equation [Bevington & Robinson, 1992; Schönwiese, 1992] as

$$\sigma_Y = \sqrt{\sum_{i=1}^n \left(\frac{\partial f}{\partial x_i}\right)^2 \sigma_{x_i}^2} \quad (\text{A.4})$$

Special cases of the error progression equation:

$$1. Y = C + \sum_{i=0}^n x_i:$$

$$\sigma_Y = \sqrt{\sum_{i=0}^n \sigma_{x_i}^2} \quad (\text{A.5})$$

$$2. Y = C \prod_{i=0}^n x_i:$$

$$\sigma_{Yrel} = \sqrt{\sum_{i=0}^n \sigma_{x_i,rel}^2} \quad (\text{A.6})$$

with the relative errors  $\sigma_{Yrel} = \frac{\sigma_Y}{Y}$  and  $\sigma_{x_i,rel} = \frac{\sigma_{x_i}}{x_i}$ .

### A.3 Median filter

The median is the middle of a distribution function of a set of data. Half the data points are below the median and half are above. In a data set sorted due to the ranking of values the median is the value in the middle of the set. For an odd number of data points  $n$  the median is the value at the point  $i = \frac{n+1}{2}$  [Schönwiese, 1992].

The median filter is often used for smoothing time series and eliminating outliers. It works by running a “window” ( $i - \frac{n+1}{2} < i < i + \frac{n+1}{2}$ ) over the data set and replacing the data point with number  $i$  by the median of all data points inside the window.

### A.4 Savitzky-Golay filter

The Savitzky-Golay filter is a low-pass filter designed to smooth noisy data while not changing data characteristics like peak height and width [Press et al., 1992]. The principal idea is to fit a Polynom  $P$  of the order  $m$  to the data points  $i - \frac{n-1}{2} < i < i + \frac{n-1}{2}$ :

$$P = \sum_{i=j}^m a_j x^j \quad (\text{A.7})$$

The data point  $i$  is replaced by the value calculated from the fit function.

### A.5 Newton’s method

The numerical solution of the equation  $f(x) = 0$  is given by Newton’s Method [Bronstein et al., 1993] as the convergence value ( $n \rightarrow \infty$ ) of the series

$$x_{n+1} = x_n - \frac{f(x_n)}{f'(x_n)} \quad (\text{A.8})$$

---

The geometric interpretation is the local approximation of a function by a tangent line at the point  $x_n$ . This tangent line is extended until it crosses zero [Press *et al.*, 1992]. That zero crossing provides the next guess  $x_{n+1}$ . This procedure is aborted when the difference  $|x_{n+1} - x_n|$  falls below a given limit.



# Appendix B

## Definitions

### B.1 Ertels potential vorticity - PV

The potential vorticity in isentropic coordinates is given as [*Holton, 1992*]

$$PV = (\zeta_\theta + f)\left(-g\frac{\partial\theta}{\partial p}\right) \quad (\text{B.1})$$

where  $\zeta_\theta$  is the vertical component of the relative vorticity on an isentropic surface,  $f = 2\Omega\sin\phi$  is the Coriolis parameter with the angular speed of the Earth's rotation  $\Omega$  and the latitude  $\phi$ ,  $g$  is the gravitational acceleration,  $\theta$  the potential temperature and  $p$  the pressure. Due to its dependence on the isentropic mass density  $-g\frac{\partial\theta}{\partial p}$ , which is a measure for the stability of an air mass, the PV (units:  $10^{-6}Km^2kg^{-1}s^{-2} = 1PVU$ ) exhibits high values in the stable stratosphere.

In a frictionless adiabatic flow the PV is conserved, which is a powerful constraint to large scale motions in the atmosphere. Neglecting the minimal friction and diabatic processes the PV in the stratosphere can be regarded as constant for a period up to 10 days. Hence, regarding these constraints, PV can be used as a material tracer in the stratosphere.

### B.2 The tropopause

There are several definitions for the tropopause:

- LRT - The laps-rate tropopause is the conventional meteorological definition given by the World Meteorological Organisation [*WMO, 1957*]. It describes the base of a layer above 500 hPa with a minimum thickness of 2 km in which the temperature gradient with height  $dT/dz > -2K/km$ .
- CPT - the cold point tropopause is the level of minimum temperature.

- Following the chemical definition the tropopause separates two layers with different chemical characteristics. The mixing ratios of many trace gases exhibit a strong gradient at the tropopause, which can be used for its identification.
- The dynamical tropopause is defined by a specific value of PV (potential vorticity, see also section B.1) ranging from 1.5 PVU [WMO, 1986] to 4.5 PVU [Haynes & Shuckburgh, 2000a,b].

All these definitions do not necessarily yield the same result. Usually the chemical definition, using O<sub>3</sub> as a tracer, places the chemical tropopause below the LRT. The dynamical tropopause is in general agreement with the LRT concerning large scale structures. But in regions of high synoptic activity the LRT and the dynamical tropopause can vary significantly. Apart from its definition as a boundary surface, the tropopause must be seen as a layer of finite thickness in which all the definitions are valid [Haynes & Shepard, 2001]. In the tropics the tropopause roughly coincides with the 380 K potential temperature surface. Approaching the poles it slopes downward to potential temperatures of about 290 K to 320 K. The tropopause height is controlled by processes like radiation, baroclinic eddies and the mean meridional circulation [Stohl *et al.*, 2003a].

### B.3 Equivalent latitude

The equivalent latitude [McIntyre & Palmer, 1984] is determined by calculating the area enclosed by isolines of PV on a given isentrope and specified as a fraction of the whole hemispheric area. These areas are rearranged concentrically around the pole, reaching from 0 at the pole to 1 at the equator. The latitudes of the transformed PV isolines, surrounding these rearranged areas, are referred to as equivalent latitude.

### B.4 Nash criterium

The Nash criterium is an objective way of locating the Arctic polar vortex boundary. It was developed by Nash *et al.* [1996]:

When plotting the PV on a given isentrope against the equivalent latitude, the vortex edge is defined as the maximum PV gradient  $\frac{\partial PV}{\partial \Phi_{equiv.lat.}}$  in the vicinity of a strong westerly jet. The boundary region of the vortex, which surrounds the vortex edge, is defined by the maxima in concave and convex curvature in the PV curve to the left and right of the maximum PV gradient.

### B.5 Delta theta

$\Delta\theta$  gives the vertical distance in K potential temperature from the local tropopause:

$$\Delta\theta = \theta(x, y) - \theta_{tropopause}(x, y) \quad (\text{B.2})$$

## B.6 Delta N<sub>2</sub>O

$\Delta N_2O$  [Greenblatt *et al.*, 2002] defines the meridional distance (given in N<sub>2</sub>O mixing ratio [ppb]) from the N<sub>2</sub>O “vortex-fit”  $N_2O_{vortex}(\theta)$ .

$$\Delta N_2O(\theta) = N_2O(\theta) - N_2O_{vortex}(\theta) \quad (\text{B.3})$$

## B.7 Delta N<sub>2</sub>O<sub>extra</sub>

Similarly to  $\Delta N_2O$  the parameter  $\Delta N_2O_{extra}(\theta)$  defines the distance from the high latitude “high N<sub>2</sub>O data fit”  $N_2O_{extra}(\theta)$ .

$$\Delta N_2O_{extra}(\theta) = N_2O(\theta) - N_2O_{extra}(\theta) \quad (\text{B.4})$$

In Figure B.1 the N<sub>2</sub>O data of the EuPLEx and the AVC campaigns are plotted versus the potential temperature. The colour code defines the  $\Delta N_2O_{extra}$  bins. Grey circles denote the selected “high N<sub>2</sub>O” data on which the fit  $N_2O_{extra}(\theta)$  is based. They were taken from flights or parts of flights that were performed outside the vortex region ( $\phi_{equiv} < 67^\circ\text{N}$ ), thus including only measurements with high N<sub>2</sub>O mixing ratios, implying little or even no vortex influence. For the EuPLEx campaign these were e.g. the flights on February 8th and 11th. During the AVC campaign data were taken from the flights of the 2nd, 8th and 12th of March. The data of these flights were fitted and the resulting fit was used to calculate the  $\Delta N_2O_{extra}$  parameter for each campaign.

$\Delta N_2O_{extra}$  is used to filter the data in order to set up so-called “high N<sub>2</sub>O” profiles for the EuPLEx and the AVC campaigns. These profiles containing data with  $-5 < \Delta N_2O_{extra} < 25$  form the upper envelope of the measured data in a tracer versus potential temperature distribution.

## B.8 The CLaMS model

The Chemical Lagrangian Model of the Stratosphere (CLaMS) is developed and operated at the Forschungszentrum Jülich, Germany [McKenna *et al.*, 2002b,a]. This model is based on Lagrangian tracer transport. The advantage of this approach is the ability to resolve small scale structures like filaments. Starting from a quasi-uniformly spaced ensemble of air parcels defining a quasi-uniform grid, the air parcels are transported on a time-dependent irregular grid following the motion of the air. For each air parcel the trajectory of the movement can be calculated numerically in time steps of 30 min using assimilated horizontal wind and temperature fields. The

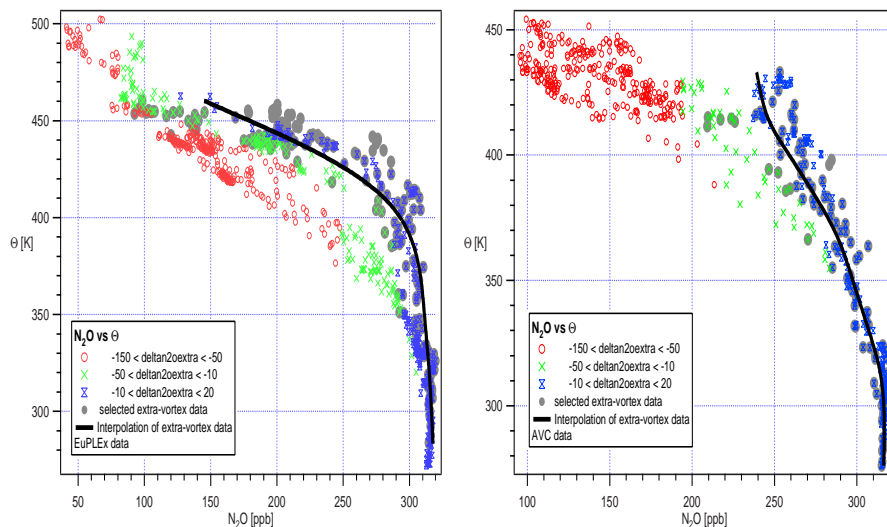


Figure B.1:  $N_2O$  data [ppb] plotted versus the potential temperature [K]. Colour code denotes the  $\Delta N_2O_{extra}$  bins, grey circles “high  $N_2O$ ” data. The fit through the “high  $N_2O$ ” data is displayed in black.

meteorological data are provided by UKMO<sup>1</sup> or the ECMWF<sup>2</sup>. Vertical motion is calculated using a radiation model.

The chemistry module calculating the chemical composition of the air parcels is based on stratospheric gas phase chemistry with 40 species and 112 reactions.

After each time step the new distribution of the air parcels is calculated and after a certain time clustering or dispersion of the air parcels in comparison to the initial grid occurs. When the distance between two air parcels is below a critical distance the corresponding air parcels will be eliminated and a new one is formed, which will carry the mean chemical properties of the former air parcels. In case a critical distance is exceeded a new air parcel will be inserted in between. By this dynamically adaptive grid algorithm the quasi-uniform grid is maintained and mixing processes between the air parcels are modelled. The critical distances are defined by the Lyapunov exponent [Geist *et al.*, 1990] which can be described by Eulerian flow properties like horizontal strain and the shear rate.

For the work presented here, trajectories  $\theta(t)$  of the mean descent in the vortex from 01.12.2002 - 20.03.2003 were simulated with the 3D model version of CLaMS. The trajectories were started at potential temperatures between 400 K and 1400 K and calculated from a mean of 14 vortex trajectories in time steps of days.

Furthermore, the tropopause height in K, defined as the potential temperature of the 4.0 PVU surface below the flight path of the Geophysica, was interpolated between daily ECMWF PV-fields at 12 UTC. The flight path was transposed to this time and the tropopause height was determined by interpolation between the

<sup>1</sup>United Kingdom Meteorological Office

<sup>2</sup>European Center for Medium Range Weather Forecast



closest ECMWF grid points to the transposed coordinates of the flight path.

## B.9 Trajectories

5-day backward trajectories starting from each HAGAR sampling position were calculated from ECMWF data fields. Calculated were latitude, longitude, temperature, pressure and PV at each time step (about 30 min) along the trajectory. These calculations were performed by Gianluca Redaelli. For more information contact:

Dr. Gianluca Redaelli  
Universita' degli studi Dell'Aquila  
Dipartimento di Fisica  
Via Vetoio, 67010 Coppito (AQ), Italy  
Phone : +39-0862-433076  
Fax : +39-0862-433033  
E-mail: [Gianluca.Redaeli@aquila.infn.it](mailto:Gianluca.Redaeli@aquila.infn.it)



# Appendix C

## HAGAR instrumental issues

### C.1 Calculation of doping gas flow and mixing ratio

The doping gas flow through the restriction is too small to be measured and has thus to be calculated.

When a gas with the pressure  $p$  passes a restriction, the pressure drops from  $p$  to the pressure level on the downstream side of the restriction. In the case considered here, the restriction is used to control the doping gas flow and the downstream pressure is about 1 bar; hence, the pressure difference at the restriction is  $\Delta p = p - 1$ . The turbulent flow through the restriction is given as

$$Q \sim \sqrt{p\Delta p}. \quad (\text{C.1})$$

Knowing the (measurable) flow  $Q_{@hp}$  through the restriction when using a gas at high pressure  $p_{@hp}$ , the actual doping gas flow can be determined by

$$Q_{doping} = \frac{Q_{@hp}}{\sqrt{p_{@hp}\Delta p_{@hp}}} \sqrt{p\Delta p}. \quad (\text{C.2})$$

The doping gas mixing ratio in the carrier gas is then calculated as the ratio of the doping gas to the total gas flow:

$$\chi_{doping} = \frac{Q_{doping}}{Q_{carrier} + Q_{makeup}} \quad (\text{C.3})$$

### C.2 N<sub>2</sub>O contamination problem

During all the flights from July 22, 2002 to the 26th of January 2003 a sometimes severe contamination occurred in the N<sub>2</sub>O signal of the second channel. The problem was detected after the flight on October 11. In a process lasting from October 2002 to January 2003 the instrument was checked for several probable causes of the contamination, and measures to minimize it were applied to the HAGAR system:

- Comparing CAL and CAL to pump injections revealed that the contamination occurred in the pump system. Therefore as a first action the pressure controller regulating the pump flow was reset from 1050 mbar to 1000 mbar, in order to maximize the outflow through the pump overflow and minimize the residence time of air in the pumps, when they were not running. Additionally the pumps were continuously flushed with N<sub>2</sub> between the flights to make sure no N<sub>2</sub>O rich air could accumulate in the pumps. These actions did minimize the strong contaminations that were observed in the beginning of the flights from October 8 to 14 (10% to 30%). But still a slight contamination of about 1 to 2% appeared during the following flights.
- In order to quantify the contamination during the flight, CAL to pump injections were performed every 6 cycles.
- It was discovered that the relatively N<sub>2</sub>O rich air from the exhaust of ECD I might be sucked in by the pump via a connection of the blank to pump and the make up gas lines in case of any leakage of the blank to pump solenoid valve. This potential problem was eliminated before the flight on 22nd of October by changing the blank to pump connection. However, this measure did not eliminate the contamination.
- Obviously, N<sub>2</sub>O, coming from the exhaust of ECD I was accumulating in the vessel. The contaminated air inside the vessel could be sucked into the pump through leaking fittings. New fittings were attached after the October 2002 campaign in December 2002. Still the contamination persisted.
- The factory leakage rate through the pump membranes is limited to 10<sup>-3</sup>, therefore
  1. the pump housing surrounding the pump membranes was flushed with N<sub>2</sub>.
  2. it was necessary to minimize the N<sub>2</sub>O concentration inside the vessel. To this goal the exhaust of ECD I, containing N<sub>2</sub>O enriched air, was directly ventilated to the MKS, the pressure controller of the HAGAR vessel controlling the vessel outlet flow (this was done after the flight on January 23 during EuPLEx).

All these measures, however, did not eliminate the contamination problem. In fact, a sample of the gas inside the vessel taken directly after the flight of February 26 yielded a high N<sub>2</sub>O mixing ratio inside the vessel ( $\sim 5$  ppm). The cause for this high amount of N<sub>2</sub>O in the vessel finally turned out to be a small leakage in the high pressure system of the N<sub>2</sub>O doping gas line. This was not detected until late January 2003 during the EuPLEx campaign. Thereafter the leakage was eliminated and the doping gas was changed from pure N<sub>2</sub>O to a mixture of 1% of N<sub>2</sub>O in N<sub>2</sub> (this change was compensated by increasing the N<sub>2</sub>O doping gas flow by a factor of 100).

The last two measures finally eliminated the problem and after January 26 2003 no more contamination was detected.

The correction of contaminated N<sub>2</sub>O data is achieved by using the regularly performed CAL to pump measurements ( $N_2O_{C2P}$  at the flow  $F_{C2P}$ ) and assuming a simple inversely proportional dependence of the contamination from the total pump flow F (i.e. assuming a constant leak rate of vessel air into the pump system).

A corrected N<sub>2</sub>O ( $N_2O_{CORR}$ ) is then given as follows:

$$N_2O_{CORR} = N_2O - \frac{F_{C2P} + \delta}{F + \delta} \times (N_2O_{C2P} - N_2O_{cal}) \quad (C.4)$$

The total pump flow F is determined as an average during the relevant sampling interval prior to the respective injection.  $N_2O_{C2P}$  for the respective air injection is determined by interpolation between the closest two CAL to pump injections. The additional parameter  $\delta$  takes into account a constant error in the flow measurements and is determined empirically as follows. The corrected N<sub>2</sub>O is correlated with other tracers (like CFC-12; here the correlation is close to linear and very compact [Plumb & Ko, 1992]) and compared with the correlations of non contaminated N<sub>2</sub>O data.  $\delta$  is chosen such that the statistical spread of the correlation is minimized.

### C.3 CAL gas drift correction

During the flight of February 2, 2003 strikingly high CO<sub>2</sub> values were measured. Calibrating the flight bottles against the original CAL and SPAN it became obvious that the CO<sub>2</sub> mixing ratio in the CAL flight bottle was about 5 ppm too low. Due to unidentified effects some species in the CAL gas showed a significant decrease in mixing ratio with residence time in the flight bottle. Those species were N<sub>2</sub>O, CFC-12, CFC-11 and CO<sub>2</sub>. The SPAN flight bottle did not show this effect.

The drift in the CAL gas mixing ratio was quantified and corrected in the following way: The mixing ratio of a tracer as a function of time since the last filling was determined for the CAL flight bottle by calibration measurements after each flight bottle refilling and flight (starting from February 2, 2003). In plot C.1 the CO<sub>2</sub> mixing ratio versus the residence time in the flight bottle is displayed. The relation is close to linear (correlation coefficient for CO<sub>2</sub>  $r^2 = 0.97$ ). Corrected values for each of the affected tracers  $\chi_{CALflight}$  were determined for every flight given the linear fit for each species (parameters A and B) and the time t since the filling of the flight bottle:

$$\chi_{CALflight} = At + B \quad (C.5)$$

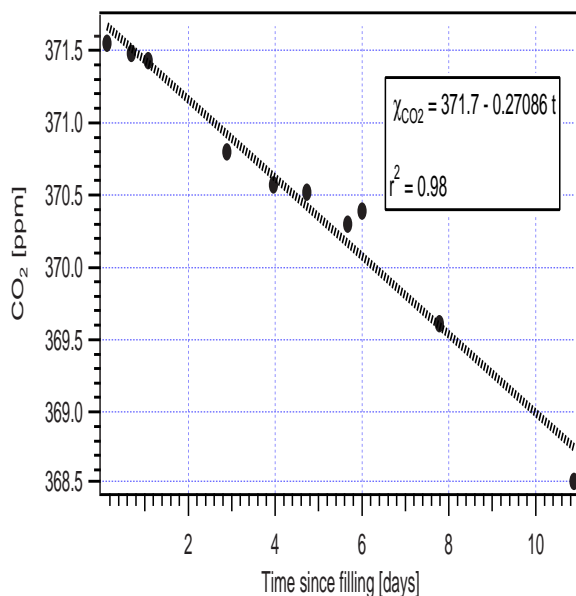


Figure C.1: CO<sub>2</sub> mixing ratio in the CAL flight bottle as a function of days since the last filling. The dotted line represents the linear fit.

## C.4 HAGAR standard gases

The HAGAR working standards CAL and SPAN gas are measured against calibrated gases whose well known mixing ratios vary from zero up to values around the atmospheric background. With these experiments the detector response curves (see section 2.1.1) and the mixing ratios of the measured species in the HAGAR working standards are determined [Riediger, 2000]. Except CO<sub>2</sub> all values are based on the CMDL calibration scale (see section 2.1.1). The error of the CMDL master standard gas (CMDL) used to determine the absolute values is given as 1%. The CO<sub>2</sub> values are based on CO<sub>2</sub> standard gases produced by UBA that were calibrated against the Scripps scale (see section 2.1.2). Tables C.1 and C.2 show the mixing ratios of all HAGAR species for the HAGAR working standards.

Molecule	CMDL	HAGAR CAL 40L					avg.
		prelim.	02-08-07	02-11-04	03-04-02	misc.	
N <sub>2</sub> O[ppb]	311.6	311.5	314.79	316.47	315.98	-	315.75
CFC-12[ppt]	524.20	541.1	544.13	544.9	544.7	-	544.58
H-1211[ppt]	3.2	4.3	4.47	4.43	-	-	4.41
H-1211*[ppt]	4.11	-	5.38	5.25	5.15	-	5.26
CFC-11[ppt]	271.3	265.2	263.42	261.91	263.33	-	262.89
SF <sub>6</sub> [ppt]	3.31	5.3	-	5.38	5.49	-	5.435
CH <sub>4</sub> [ppb]	-	1850	1828.8	1836.6	1826.7	-	1830.69
H <sub>2</sub> [ppb]	579.9	500	526.72	533.76	524.64	529.7	528.37
CO <sub>2</sub> [ppm]	358.20	372.90	-	371.8	371.97	371.86	371.9

Table C.1: Mixing ratios of HAGAR species in the HAGAR working standards. All values are based on the CMDL scale, except for CO<sub>2</sub> (SIO scale). Black figures are HAGAR measurements. In column "avg.", the averaged mixing ratios of the different calibration experiments are given. The mixing ratios of the CMDL master standard printed in blue are given by Elkins (1994); the values printed in cyan are the mean at Niwot Ridge for the year 1994 when the CMDL was filled determined from flask measurements (Butler); dark green: Maiss 1996; light green figures denote measurements by Thomas Wetter with RGA-3 instrument in April 2003; in brown: GC (Si3) measurements at the University of Frankfurt by Sven Brinckmann (July 1st 2002); in orange: GC (Si14) measurements at the University of Frankfurt against CMDL and the LITES standard by Hans-Peter Haase (June 27th 2002); in red: Ghost measurements against the SPURF standard performed by Harald Bönisch on Sept. 16, 2003. All CO<sub>2</sub> measurements were performed by the HAGAR LI-COR except for those figures marked in grey which were performed with the IMGF LI-COR against UBA CO<sub>2</sub> standards on June 26, 2002.

Molecule	CMDL	HAGAR SPAN 10L						
		prelim.	02-08-07	02-11-04	03-04-02	misc.	avg.	
N <sub>2</sub> O[ppb]	311.6	154.8	155.43	155.6	154.03	155.98	155.15	
CF <sub>4</sub> -12[ppb]	524.20	265.6	268.12	268.34	267.22	270.85	267.89	
H-1211[ppb]	3.2	2.14	2.25	2.26	-	-	2.26	
H-1211*[ppb]	4.11	-	2.61	2.54	2.49	-	2.55	
CF <sub>4</sub> -11[ppb]	271.3	131.2	130.86	129.76	129.86	-	130.16	
SF <sub>6</sub> [ppt]	3.31	2.36	-	2.55	2.50	2.375	2.53	
CH <sub>4</sub> [ppb]	-	919.03	907.6	892.5	902.84	-	900.98	
H <sub>2</sub> [ppb]	579.9	248.39	262.58	260.42	254.7	256.7	259.23	
CO <sub>2</sub> [ppm]	358.20	364.3	-	364.01	364.21	364.12	364.1	

*Table C.2:* Mixing ratios of HAGAR species in the HAGAR working standards. All values are based on the CMDL scale, except for CO<sub>2</sub> (SIO scale). Black figures are HAGAR measurements. In column “avg.”, the averaged mixing ratios of the different calibration experiments are given. The mixing ratios of the CMDL master standard printed in blue are given by Elkins (1994); the values printed in cyan are the mean at Niwot Ridge for the year 1994 when the CMDL was filled determined from flask measurements (Butler); dark green: Maiss 1996; light green figures denote measurements by Thomas Wetter with RGA-3 instrument in April 2003; in brown: GC (Si3) measurements at the University of Frankfurt by Sven Brinckmann (July 1st 2002); in orange: GC (Si14) measurements at the University of Frankfurt against CMDL and the LITES standard by Hans-Peter Haase (June 27th 2002); in red: Ghost measurements against the SPURT standard performed by Harald Bönisch on Sept. 16, 2003. All CO<sub>2</sub> measurements were performed by the HAGAR LI-COR except for those figures marked in grey which were performed with the IMGF LI-COR against UBA CO<sub>2</sub> standards on June 26, 2002.



## C.5 Calculating the precision of GC of measurements

As already described in section 2.1.1 (equation 2.1), the mixing ratio of a tracer  $\chi$  is determined as a function of the detector responses of the “local” CAL and SPAN measurements  $R'_{cal}$  and  $R'_{span}$  (derived by interpolation between the closest CAL and SPAN measurements), and the response  $R$  of the measurement itself,  $\chi = f(R'_{cal}, R'_{span}, R)$ .

The precision of a measurement  $\delta\chi_{prec}$  is then calculated as follows:

$$\delta\chi_{prec} = \sqrt{\delta\chi_{Rcal}^2 + \delta\chi_{Rspan}^2 + \delta\chi_R^2} \quad (C.6)$$

where  $\delta\chi_{Rcal}$  and  $\delta\chi_{Rspan}$  are the error contributions due to errors in the responses of the local CAL and SPAN measurements ( $\delta R'_{cal}$  and  $\delta R'_{span}$ ) and  $\delta\chi_R$  is the error contribution due to the error in the response  $R$  of the measurement itself ( $\delta R$ ).

The error contribution  $\delta\chi_{Rcal}$  due to a given error in the local CAL response  $\delta R'_{cal}$  is determined simply by calculating mixing ratios for  $R'_{cal} \pm \delta R'_{cal}$ :

$$\delta\chi_{Rcal}^+ = f(R'_{cal} + \delta R'_{cal}, R'_{span}, R) - \chi \quad (C.7)$$

$$\delta\chi_{Rcal}^- = f(R'_{cal} - \delta R'_{cal}, R'_{span}, R) - \chi \quad (C.8)$$

and

$$\delta\chi_{Rcal} = \frac{1}{2}|\delta\chi_{Rcal}^+| + \frac{1}{2}|\delta\chi_{Rcal}^-| \quad (C.9)$$

$\delta\chi_{Rspan}$  and  $\delta\chi_R$  are determined likewise. The errors in the responses ( $\delta R'_{cal}$ ,  $\delta R'_{span}$ ,  $\delta R$ ) needed for the error determination have to be estimated from the time series of CAL and SPAN measurements. This is done in the following way.

### Determination of $\delta R_{cal}$ and $\delta R_{span}$

The time series of detector responses may show significant drifts over the time interval of several calibrations. Therefore, the local errors  $\delta R'_{cal}$  and  $\delta R'_{span}$  cannot easily be estimated from the variability of  $R_{cal}$  and  $R'_{span}$  over an interval. Instead, “fictive” CAL and SPAN mixing ratios,  $\tilde{\chi}_{cal}$  and  $\tilde{\chi}_{span}$ , are calculated from their neighbouring CAL and SPAN responses just as it is done for the concentration of an unknown air sample. These fictive mixing ratios are largely drift free and therefore more useful for estimating errors from their variability.

As mixing ratio can be considered to be approximately proportional to response over the small variation range, the fictive mixing ratio of the  $i$ -th CAL measurement is:

$$\tilde{\chi}_{cal,i} \approx \frac{R_{cal,i}}{\frac{1}{2}R_{cal,i-1} + \frac{1}{2}R_{cal,i+1}} \times \chi_{cal} \quad (C.10)$$

Considering quadratic error addition and equal errors  $\delta R_{cal}$  and responses  $R_{CAL}$  in the right hand side of C.10, the error of the fictive mixing ratio  $\chi_{cal,i}$  is then

$$\delta \tilde{\chi}_{cal,i} \approx \sqrt{\frac{3}{2}} \times \frac{\delta R_{cal,i}}{R_{cal,i}} \times \chi_{cal} \quad (C.11)$$

Next, the ‘‘local’’ CAL response  $R'_{cal}$  used for calculating the mixing ratio of an arbitrary air sample is an interpolation from the closest neighbouring CAL measurements, thus for an air sample at average relative distances of 1 and 3 from the closest CAL injections it is:

$$R'_{cal} = \frac{1}{4} R_{cal,left} + \frac{3}{4} R_{cal,right} \quad (C.12)$$

Quadratic error addition under the assumption of equal errors  $\delta R_{cal}$  and responses  $R_{cal}$  yields

$$\delta R'_{cal} \approx \sqrt{\frac{1}{4^2} + \frac{3^2}{4^2}} \times \delta R_{cal} = \sqrt{\frac{5}{8}} \times \delta R_{cal} \quad (C.13)$$

substituting equation C.11 finally yields

$$\delta R'_{cal} = \sqrt{\frac{5}{12}} \times \frac{R_{cal}}{\chi_{cal}} \times \delta \tilde{\chi}_{cal} \quad (C.14)$$

$\delta \tilde{\chi}_{cal}$  is here estimated locally as the standard deviation of  $\tilde{\chi}_{cal}$  for the two closest neighbouring CAL measurements, which are the ones used for calculating the mixing ratio of the air sample.  $\delta R'_{span}$  is calculated similarly using the SPAN measurements.

### Determination of $\delta R$

The error of the response  $\delta R$  is dependent on the size of the response  $R$  relative to  $R_{cal}$  and  $R_{span}$  and approximated as:

$$\delta R = \begin{cases} \overline{\delta R_{cal}} & : R > R_{cal} \\ \overline{\delta R_{span}} & : R < R_{span} \\ R \text{ interpolation between } \overline{\delta R_{cal}} \text{ and } \overline{\delta R_{span}} : R_{span} < R < R_{cal} \end{cases} \quad (C.15)$$

where following C.11

$$\overline{\delta R_{cal}} = \sqrt{\frac{2}{3}} \times \frac{\overline{\delta \tilde{\chi}_{cal}}}{\chi_{cal}} \times R_{cal}. \quad (C.16)$$

In this case  $\overline{\delta \tilde{\chi}_{cal}}$  is estimated as the standard deviation of all fictive CAL concentrations in a representative interval of the flight.  $\overline{\delta R_{span}}$  is determined analogously.

## C.6 Calculating the precision of CO<sub>2</sub> measurements

As already mentioned in section 2.1.2 the precision of the CO<sub>2</sub> measurements is influenced by two factors: high frequency noise in the LI-COR 6251 signal and slower variations (periods shorter than the time interval between calibrations) due to changes in the detector gain (SPAN drift), drifts of the cell pressure and other (unknown) sources. Errors from both influences can be derived. The errors are calculated for the median filtered signals. The total error is calculated according to equation A.6. A detailed description is given in *Riediger* [2000].

### Noise of the LI-COR 6251 signal

In order to determine the noise of the LI-COR 6251 signal the standard deviation  $\sigma_V$  in a range of constant CO<sub>2</sub> mixing ratio is calculated. Here the de-trended signal of the CAL measurements was used. Since the LI-COR 6251 signal is a voltage signal [mV] the standard deviation has to be converted to mixing ratio [ppm]  $\sigma_\chi$ . For the conversion linearity between the voltage signal V of the LI-COR 6251 and the CO<sub>2</sub> mixing ratio  $\chi$  is assumed:

$$\sigma_\chi = \sigma_V \frac{\chi_{CAL} - \chi_{SPAN}}{V_{CAL} - V_{SPAN}} \quad (C.17)$$

In figure C.2 the mixing ratio as a function of the LI-COR signal is displayed. The red line shows the factory given calibration function (see section 2.1.2) that is used to calculate CO<sub>2</sub> mixing ratio from the LI-COR voltage signal. In the small range of atmospheric measurements the relation is close to linear (blue line). The error in the conversion when assuming linearity can be neglected.

### Error produced by slower variations (span drift, pressure drifts, etc.)

The error due to slower variations,  $\sigma_{\chi,P}$ , is estimated as described in *LI-COR* [1992] and *Riediger* [2000]:

$$\sigma_{\chi,P} = \frac{\sigma_{\Delta P}}{P + \Delta P} (\chi_{REF} - \chi)_{max} \quad (C.18)$$

$\Delta P$  is the difference between measured pressure P and the pressure calculated from the SPAN measurements  $\tilde{P}$ .  $(\chi_{REF} - \chi)_{max}$  is the maximum difference between the reference gas  $\chi_{REF}$  and air sample mixing ratio  $\chi$ .

## C.7 Precision of the HAGAR measurements

In the following section the mean precisions of the HAGAR measurements for each flight are given in % (error relative to tropospheric background mixing ratio) for the GC - and in ppm (absolute error) for CO<sub>2</sub> data. The mean precision is the average of the precision errors of the single measurements (see section C.5) over the whole

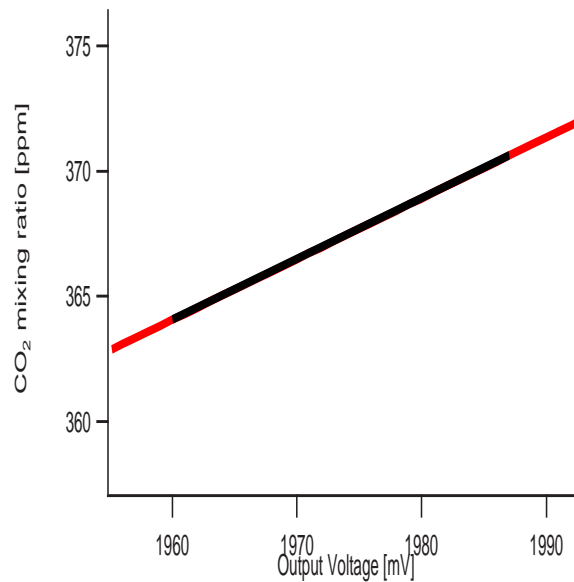


*Figure C.2:* CO<sub>2</sub> mixing ratio as a function of LICOR signal [mV]. The red line represents the factory given Calibration function. In black a linear correlation is shown.

flight. For the mean total error, i.e. the accuracy, about 1% has to be added for the accuracy of the mixing ratios of the standard gases used in flight.

Precision of the HAGAR instrument during the mid latitude campaigns in Forlí

Date	N <sub>2</sub> O	CFC-12	CFC-11	H-1211	SF <sub>6</sub>	CH <sub>4</sub>	H <sub>2</sub>	CO <sub>2</sub> [ppm]
2002 07 13	2.48	1.93	1.44	3.89	-	9.61	-	0.27
2002 07 15	3.7	2.85	2.47	5.93	-	3.79	-	0.65
2002 07 18	0.43	0.44	0.64	2.4	-	1.94	-	0.26
2002 07 22	0.73	0.77	0.41	3.14	-	2.83	-	0.69
2002 10 08	-	2.04	2.01	1.76	8.34	5.44	12.76	0.2
2002 10 11	-	0.29	0.69	2.78	8.67	1.61	1.7	0.18
2002 10 14	-	0.44	0.55	1.42	8.62	0.8	2.51	0.17
2002 10 17	0.25	0.6	0.41	1.58	14.11	1.06	2.5	0.23
2002 10 22	0.22	0.24	0.44	2.33	14.15	0.84	2.86	0.13
2002 10 24	0.17	0.24	0.81	1.6	7.36	0.92	2.59	0.1
2002 10 28	0.3	0.40	0.46	1.36	5.42	0.76	3.18	0.13

Table C.3: Average precision of the HAGAR measurements during the mid latitude measurement campaigns in Forlí, July and October 2002. The precision of the GC measurements is given in percent relative to the tropospheric background mixing ratio, except for the CO<sub>2</sub> precision which is given in ppm.

## Precision of the HAGAR instrument during EUPLEX and ENVISAT-AVC

Date	N <sub>2</sub> O	CFC-12	CFC-11	H-1211	SF <sub>6</sub>	CH <sub>4</sub>	H <sub>2</sub>	CO <sub>2</sub> [ppm]
2003 01 15	1.28	0.99	2.41	10.5	-	-	-	-
2003 01 19	1.18	1.41	0.94	6.50	3.18	1.29	2.83	0.2
2003 01 23	1.04	0.99	0.50	3.60	1.85	0.44	2.22	0.22
2003 01 26	0.97	1.29	0.57	3.38	2.12	0.45	1.27	0.21
2003 01 30	-	-	-	-	-	-	-	-
2003 02 02	0.23	0.26	0.37	2.25	1.47	0.53	1.11	0.3
2003 02 06	0.23	0.39	0.57	2.29	1.09	0.49	1.71	0.22
2003 02 08	0.19	0.27	0.34	1.79	1.00	0.41	1.29	0.14
2003 02 09	-	-	-	-	-	-	-	-
2003 02 11	0.35	0.40	0.31	3.76	1.35	1.08	1.22	0.26
2003 02 28	0.17	0.18	0.42	1.75	1.30	0.41	0.63	0.21
2003 03 02	0.16	0.22	0.51	2.36	1.83	0.87	2.75	0.22
2003 03 08	0.17	0.31	0.37	2.41	1.43	0.41	0.71	0.36
2003 03 12	0.17	0.28	0.29	2.58	1.49	0.55	1.25	0.18
2003 03 16	0.15	0.23	0.50	2.16	1.31	0.31	0.88	0.28

Table C.4: Precision of the HAGAR measurements during the EUPLEX and ENVISAT-AVC measurement campaigns in Kiruna/Sweden, January to March 2003. The precision is given in percent relative to the tropospheric background mixing ratio, except for the CO<sub>2</sub> precision which is given in ppm.

# Appendix D

## HAGAR data

This chapter contains graphs of all HAGAR data obtained during the measurement campaigns in Forlì and Kiruna from July 2002 to March 2003. The mixing ratios of the measured species are plotted versus the time of flight. Error bars representing the precision error are displayed for all species except CO<sub>2</sub>. The pressure data of the Geophysica are included as well.

### D.1 Test and Mid Latitude Validation Campaigns

All data were obtained during the Mid Latitude Test and Validation campaigns in Forlì/Italy in July and October 2002.

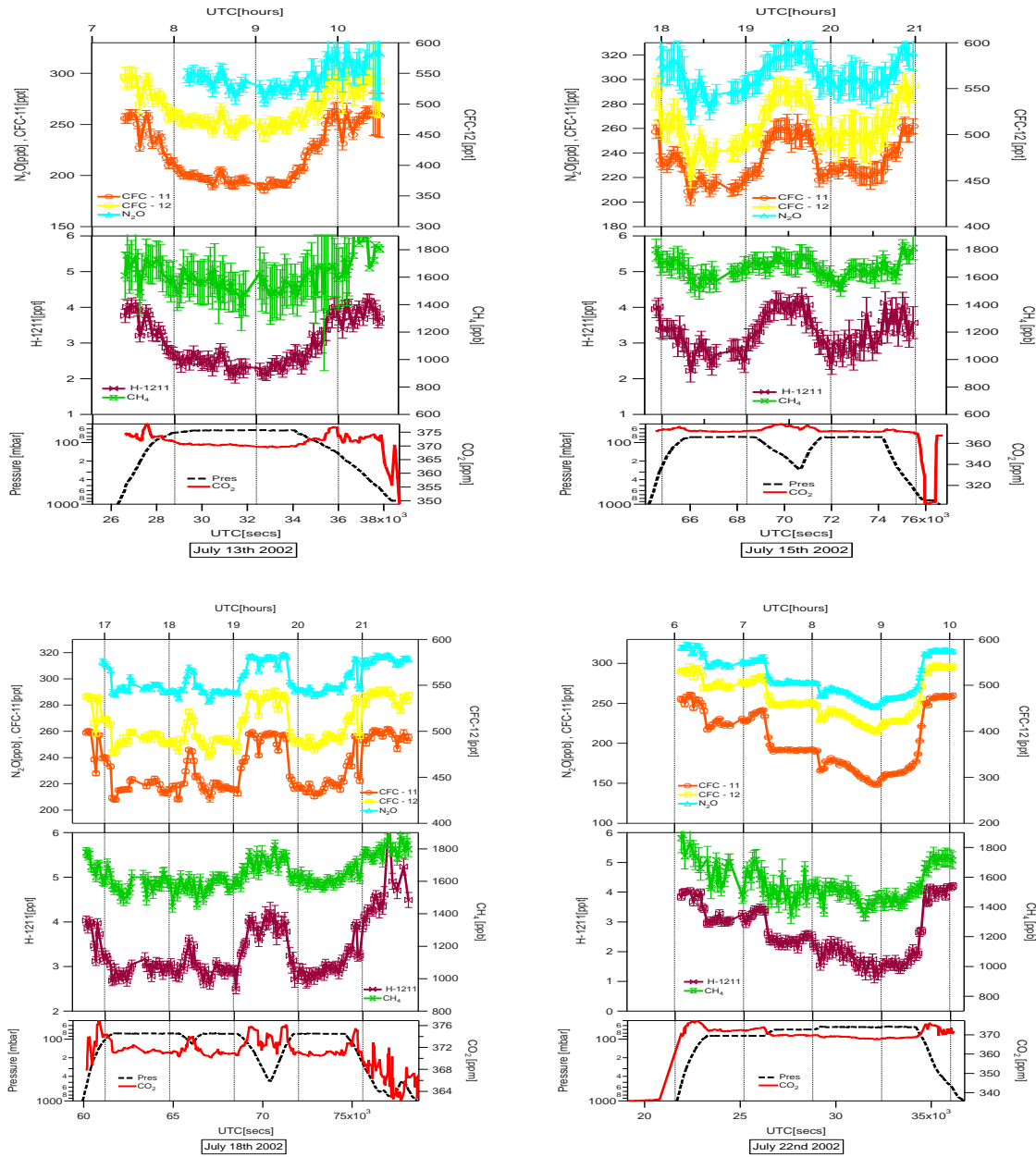


Figure D.1: Time series of HAGAR data from the flights on July 13, 15, 18 and 22, 2002.



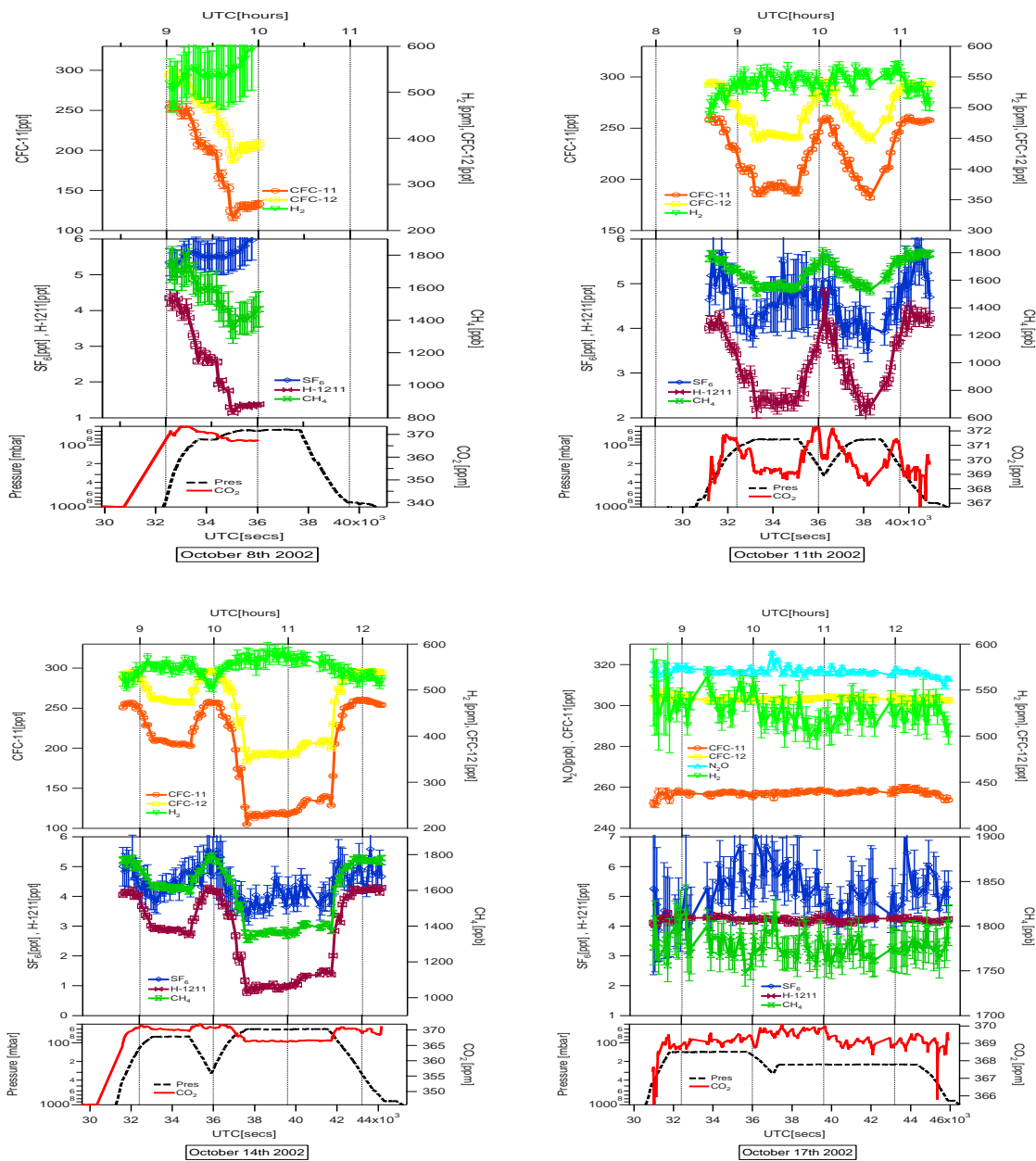


Figure D.2: Time series of HAGAR data from the flights on October 8, 11, 14 and 17, 2002.

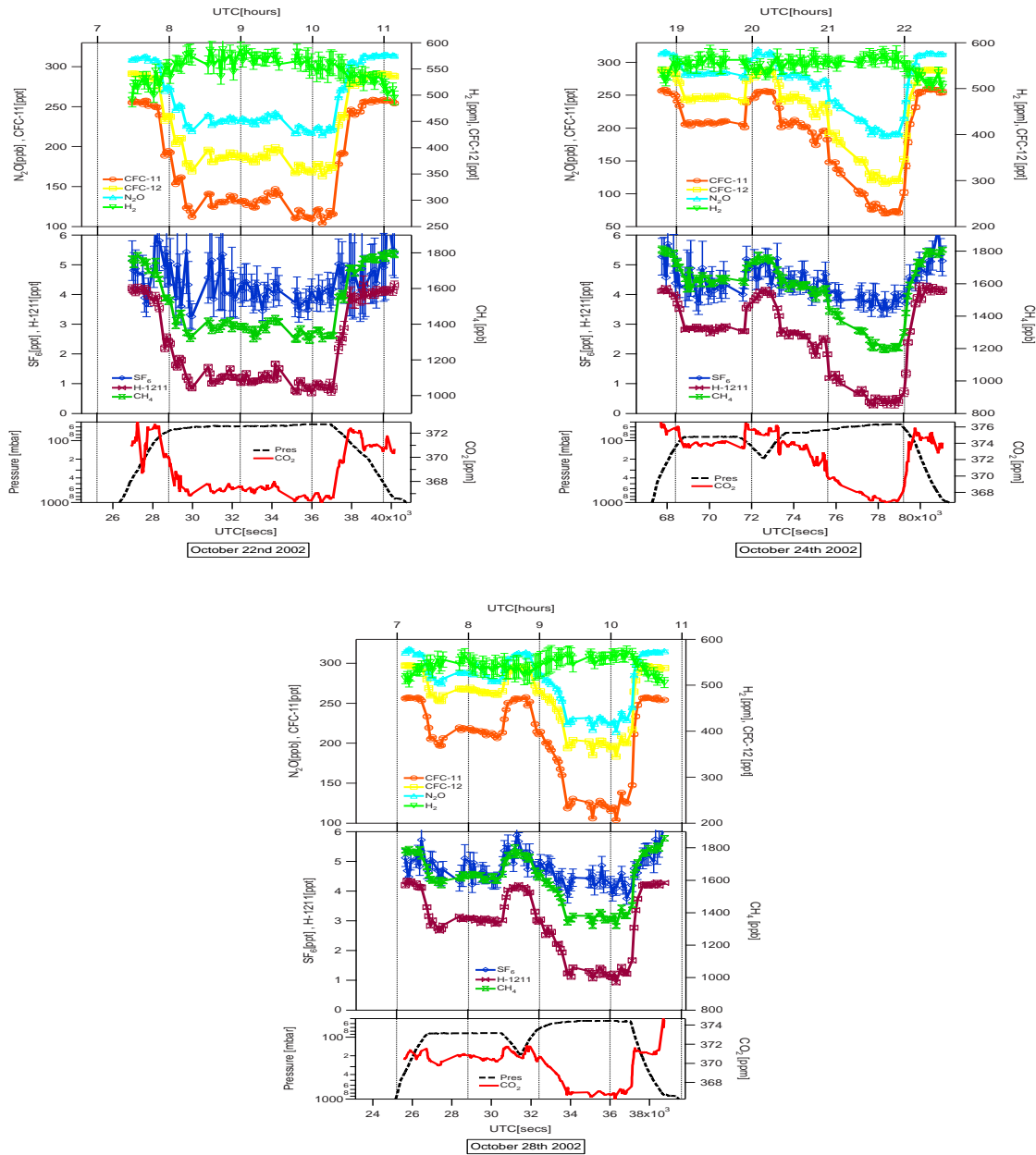


Figure D.3: Time series of HAGAR data from the flights on October 22, 24 and 28, 2002.

## D.2 Vintersol EuPLEX

All data were obtained during the EuPLEX campaign in Kiruna/Sweden in January/February 2003.

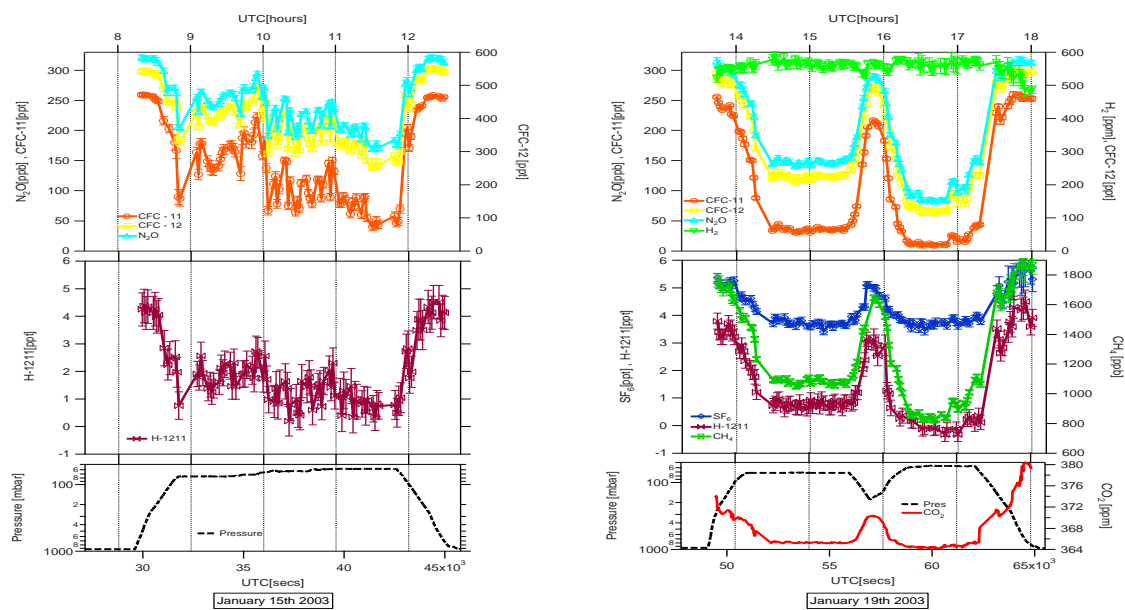


Figure D.4: Time series of HAGAR data from the flights on January 15 and 19, 2003.

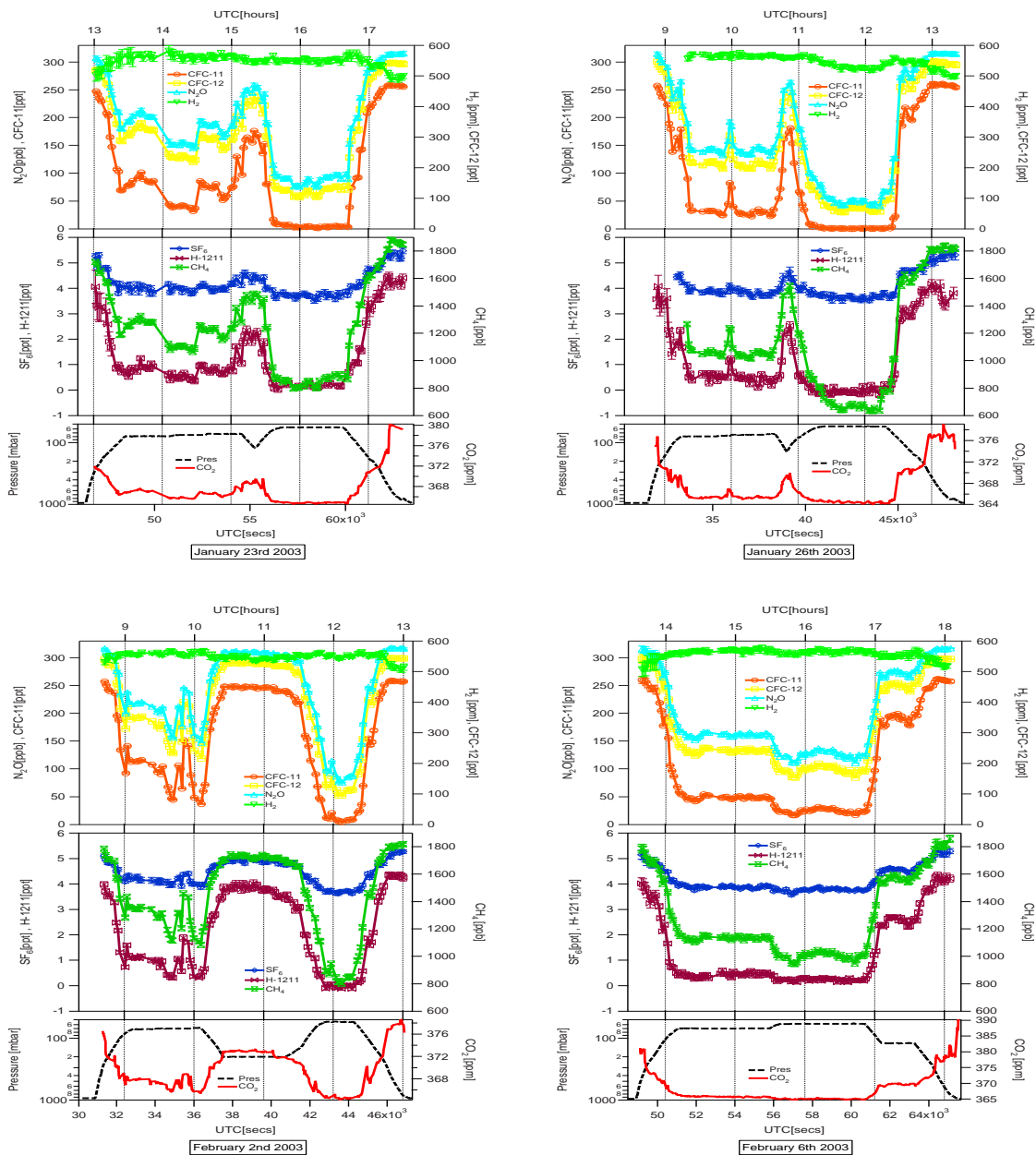


Figure D.5: Time series of HAGAR data from the flights on January 23 and 26 and on February 2 and 8, 2003.

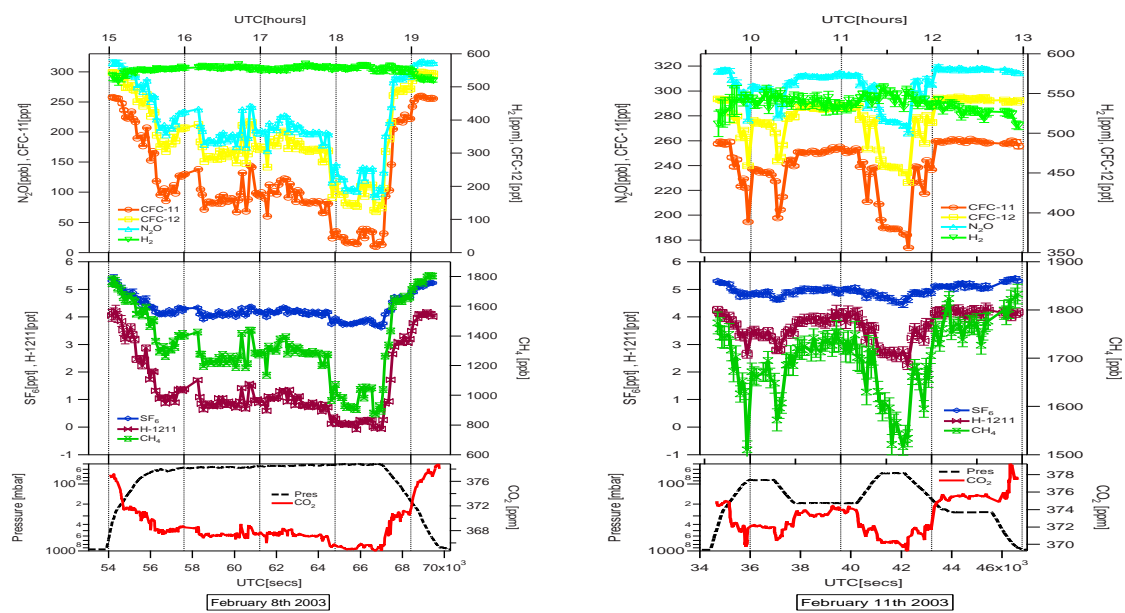


Figure D.6: Time series of HAGAR data from the flights on February 8 and 11, 2003.

### D.3 APE ENVISAT Arctic Validation Campaign

All data were obtained during the APE ENVISAT AVC campaign in Kiruna/Sweden in February/March 2003.

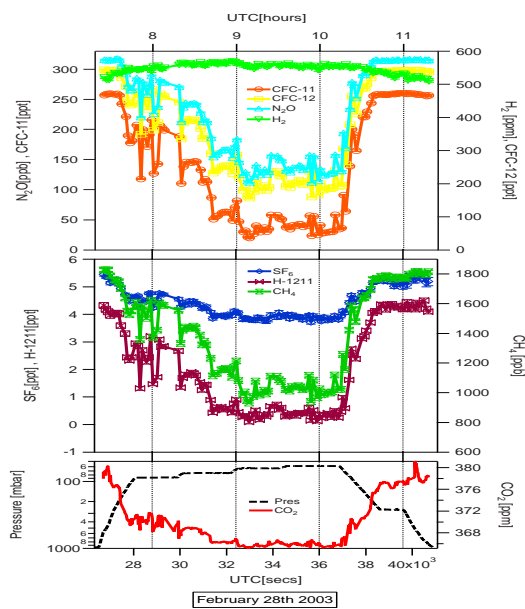


Figure D.7: Time series of HAGAR data from the flight on February 28, 2003

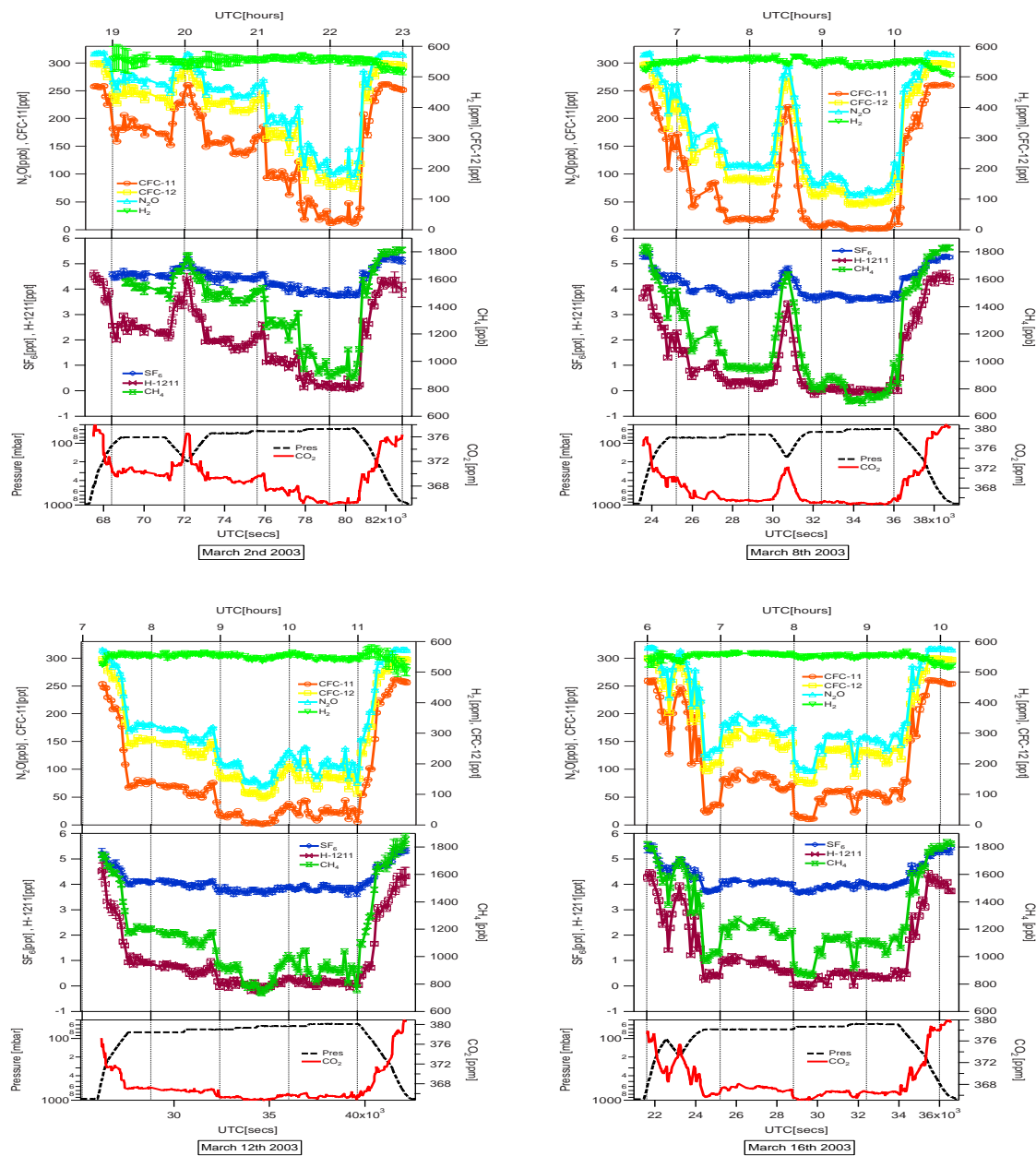


Figure D.8: Time series of HAGAR data from the flights on March 2, 8, 12 and 16, 2003.





# Appendix E

## Meteorological Analysis

These are the reanalysis data of the NCEP<sup>1</sup>. The data are valid for 0:00 UTC and include 500hPa geopotential, surface pressure at sealevel and the temperature at 850 hPa. The maps are taken from [Wetterzentrale, 2006].

### E.1 July 2002

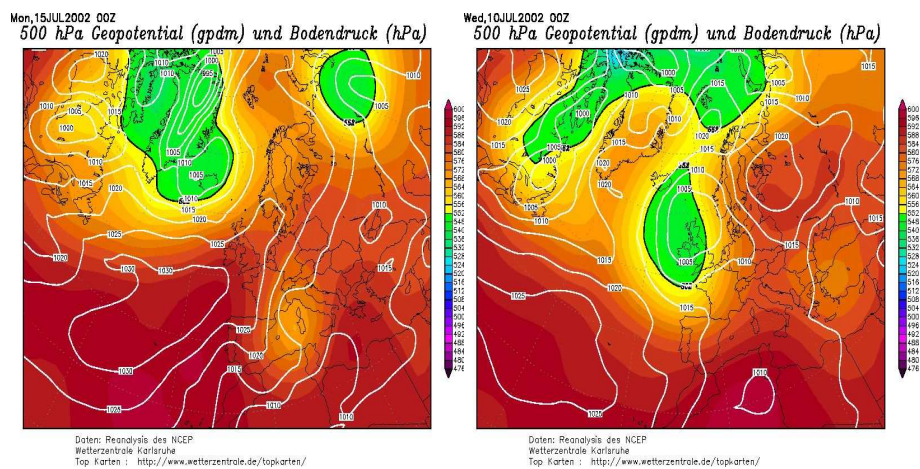


Figure E.1: NCEP reanalysis of the 500 hPa geopotential height [gpm] and the sealevel pressure [hPa] from July 10 and 11, 2002

<sup>1</sup>National Weather Service USA; National Centers for Environmental Prediction

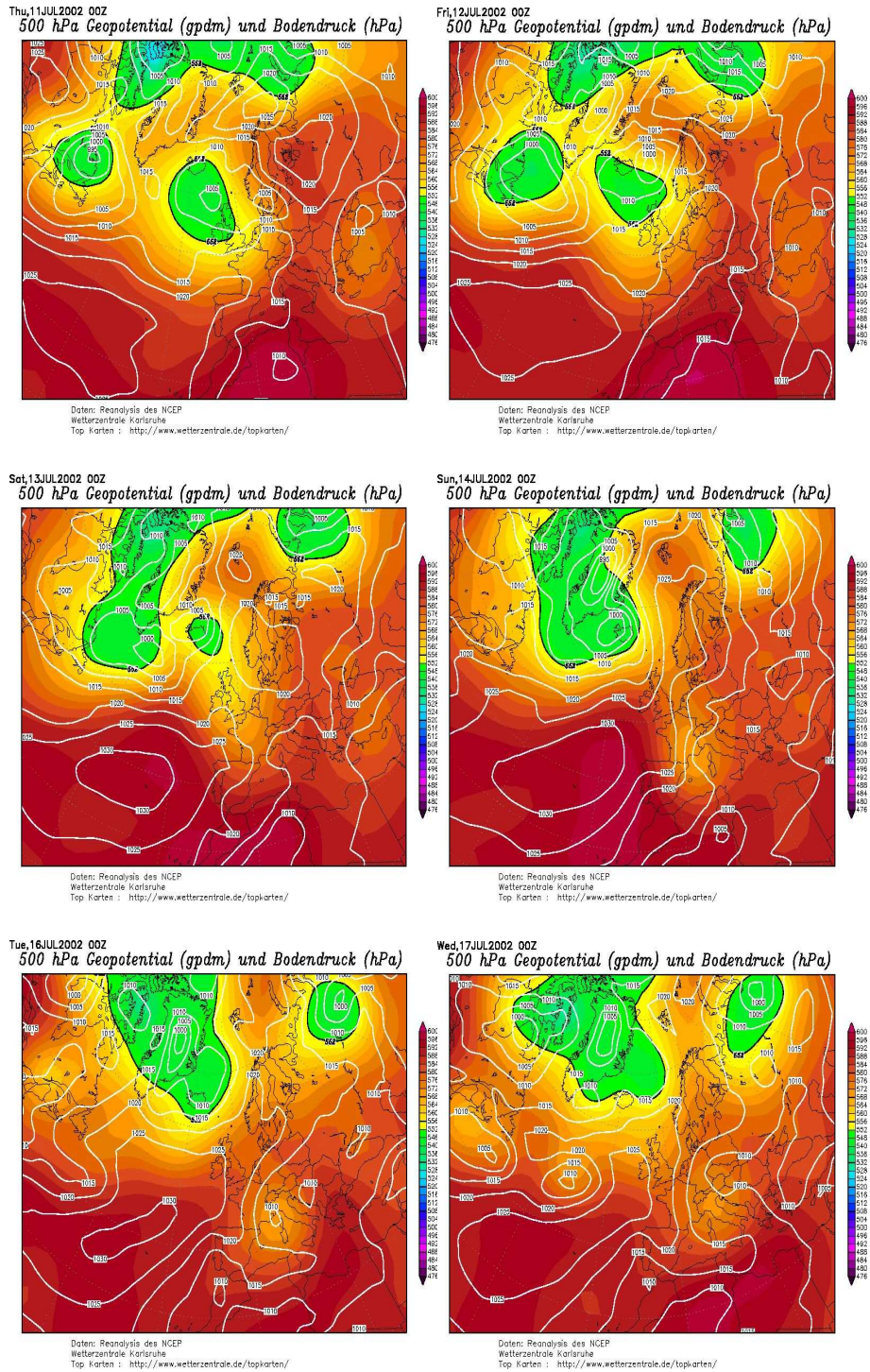


Figure E.2: NCEP reanalysis of the 500 hPa geopotential height [gpm] and the sealevel pressure [hPa] from the July 12 to 17, 2002

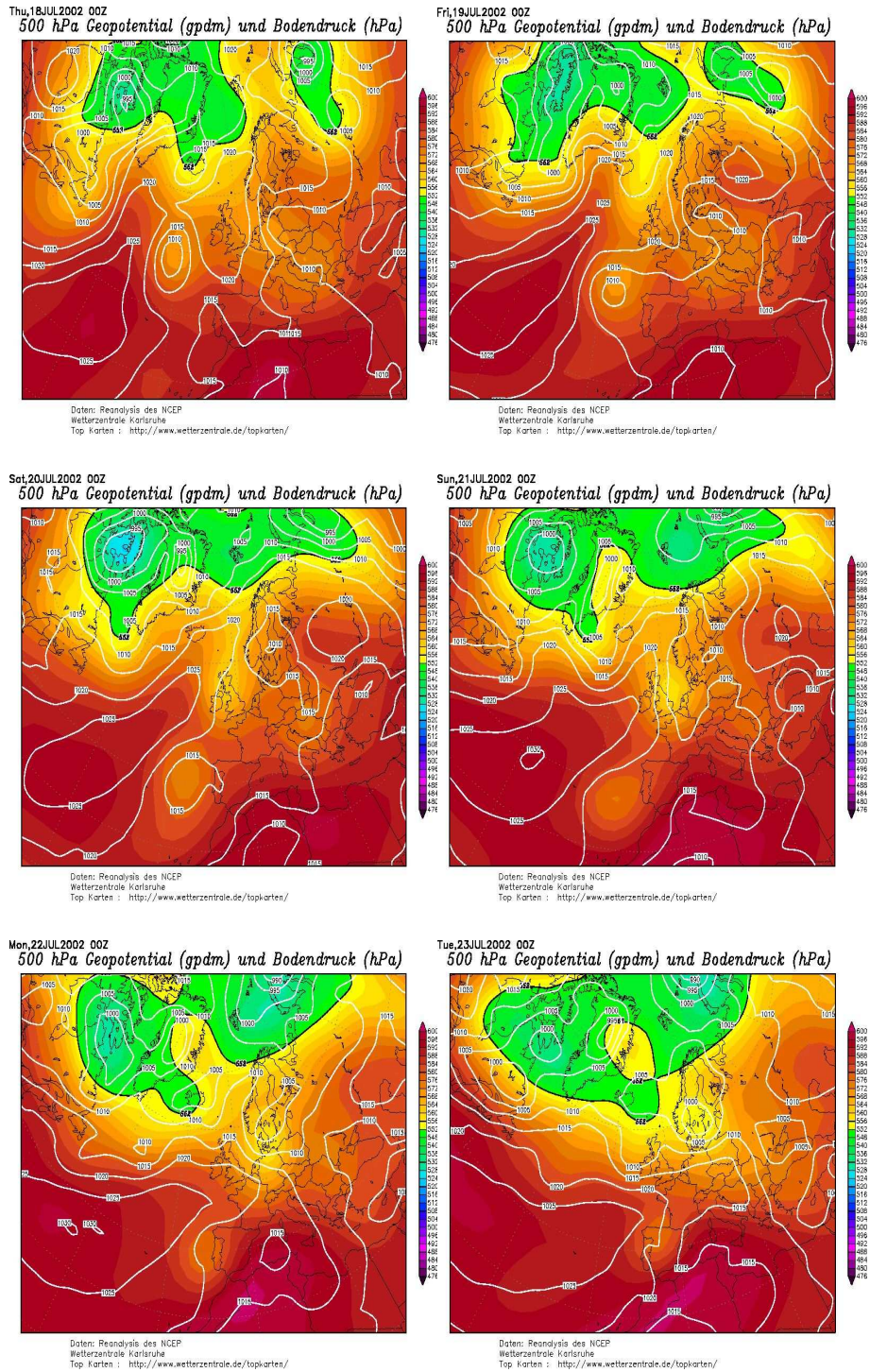


Figure E.3: NCEP reanalysis of the 500 hPa geopotential height [gpm] and the sealevel pressure [hPa] from July 18 to 23, 2002

## E.2 October 2002

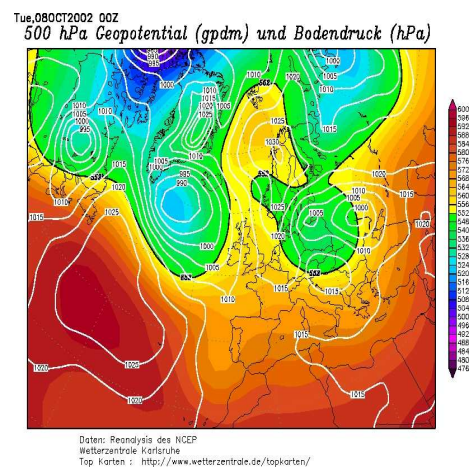


Figure E.4: NCEP reanalysis of the 500 hPa geopotential height [gpm] and the sealevel pressure [hPa] for the flight on October 8, 2000.

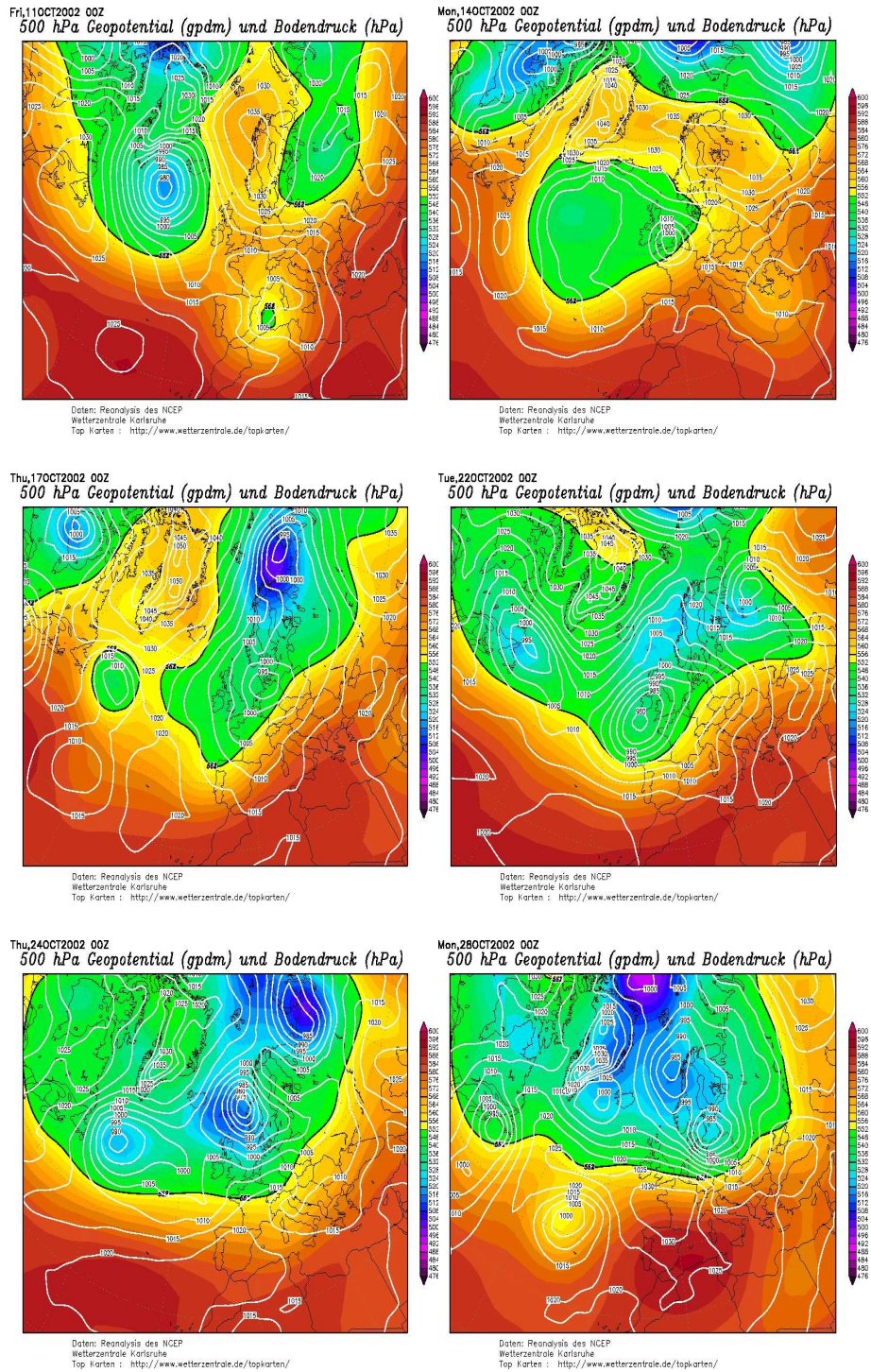


Figure E.5: NCEP reanalysis of the 500 hPa geopotential height [gpm] and the sealevel pressure [hPa] for the flights on October 11, 14, 17, 22, 24 and 28, 2002



# List of Figures

1.1	Scheme of the lowermost stratosphere . . . . .	4
1.2	The global stratospheric transport . . . . .	6
1.3	Scheme of a tropopause fold . . . . .	8
1.4	Scheme of a cut-off low formation . . . . .	9
1.5	Scheme of a warm conveyor belt . . . . .	10
1.6	Transport into the LMS, Ray et al. 1999 . . . . .	12
1.7	tracer correlation and mixing, Plumb et al. 2000 . . . . .	14
2.1	Principle scheme of HAGAR . . . . .	18
2.2	Plumbing diagram of HAGAR . . . . .	20
2.3	Chromatogram of channel I . . . . .	22
2.4	Chromatogram of channel II . . . . .	22
2.5	Fitting of a tangent baseline . . . . .	23
2.6	Gaussian peak fitting . . . . .	24
2.7	Detector response function . . . . .	25
2.8	Chromatogram channel I with Siemens ECD . . . . .	31
2.9	Chromatogram channel I with Siemens ECD and “heart cut” technique . . . . .	32
2.10	Chromatogram channel I with Shimadzu ECD during the test phase . . . . .	33
2.11	Chromatogram channel I, July 2002, Forlí . . . . .	35
2.12	M55 - Geophysica aircraft . . . . .	37
2.13	Flight routes Forlí, July 2002 . . . . .	40
2.14	Flight routes Forlí, October 2002 . . . . .	43
2.15	EuPLEX logo . . . . .	45
2.16	Flight routes during EuPLEX . . . . .	46
2.17	Flight routes during AVC . . . . .	49
3.1	Scheme of the lowermost stratosphere . . . . .	52
3.2	Tracer mixing ratios vs $\theta$ ; EuPLEX . . . . .	56
3.3	Tracer mixing ratios vs $\theta$ ; AVC . . . . .	57
3.4	Determining boundary conditions . . . . .	58
3.5	CFC-11 vs $\theta$ ; EuPLEX and AVC . . . . .	60
3.6	CFC-11 vs $\Delta\theta$ ; EuPLEX and AVC . . . . .	60
3.7	Definition of vortex data . . . . .	61

3.8	PV at 450 K on February 6, 2003 . . . . .	62
3.9	CFC-11 vs $\theta$ binned by $\Delta N_2O$ ; EuPLEx . . . . .	63
3.10	Vortex profiles of CFC-11; MKIV, EuPLEx and AVC . . . . .	65
3.11	Change of the vortex boundary with time . . . . .	66
3.12	Trajectories by the CLaMS model . . . . .	67
3.13	CFC-11 vs $\phi_{equiv}$ ; EuPLEx and AVC . . . . .	69
3.14	$H_2O$ entry function . . . . .	71
3.15	Water vapour vs $\theta$ ; FISH data . . . . .	71
3.16	Normalized profiles of CFC-11 and $O_3$ . . . . .	73
3.17	Histograms of the Monte Carlo simulation . . . . .	75
3.18	Cumulative histogram of the Monte Carlo simulation . . . . .	77
3.19	Vertical profile of CFC-11 with lower and upper envelope; EuPLEx and AVC . . . . .	80
3.20	$\theta/\Phi_{equiv}$ plot of CFC-11; EuPLEx and AVC . . . . .	81
3.21	Fraction vs $\theta$ ; EuPLEx . . . . .	82
3.22	Mass balance fractions in $\theta - \phi_{equiv}$ space; EuPLEx . . . . .	85
3.23	$H_2O$ and CFC-11 for the flight on January 19, 2003 . . . . .	86
3.24	Fraction vs $\theta$ ; AVC . . . . .	88
3.25	Mass balance fractions in $\theta - \phi_{equiv}$ space ; AVC . . . . .	89
3.26	$H_2O$ and CFC-11 for the flight on March 16, 2003 . . . . .	90
3.27	CLaMS vortex tracer . . . . .	91
4.1	PV at 350 K; July 2002 . . . . .	96
4.2	PV at 350 K and 370 K; July 2002 . . . . .	97
4.3	Sounding at San Pietro Capofiume . . . . .	98
4.4	PV cross section, July 2002 . . . . .	99
4.5	PV at 350 K; Forlí, October 2002 . . . . .	100
4.6	$O_3$ and CFC-11 vs $\theta$ , Forlí, 2002 . . . . .	101
4.7	CFC-11 vs $\theta$ , Forlí, 2002 . . . . .	102
4.8	CFC-11 vs $O_3$ for all flights during July 2002 . . . . .	103
4.9	Tropopause height vs $\theta$ and CFC-11 vs $\Delta\theta$ for all flights during July and October 2002 . . . . .	104
4.10	Flight on July 13, 2002; CFC-11 and backward trajectories during the ascent . . . . .	106
4.11	Flight on July 13, 2002; CFC-11 and backward trajectories during the descent . . . . .	107
4.12	Flight on July 15, 2002; CFC-11 and backward trajectories during the ascent . . . . .	108
4.13	Flight on July 15, 2002; CFC-11 during the dive and descent . . . . .	109
4.14	Flight on July 18, 2002; CFC-11 and backward trajectories during the ascent . . . . .	110
4.15	Flight on July 18, 2002; CFC-11 and backward trajectories during the first dive . . . . .	112



---

4.16	PV cross section, July 18, 2002 . . . . .	113
4.17	Flight on July 18, 2002; CFC-11 and backward trajectories during the second dive . . . . .	114
4.18	Flight on July 18, 2002; CFC-11 and backward trajectories during the descent . . . . .	115
4.19	Flight on July 22, 2002; CFC-11 and backward trajectories during the ascent . . . . .	116
4.20	Flight on July 22, 2002; CFC-11 and backward trajectories during the descent . . . . .	117
4.21	Flight on October 22, 2002; CFC-11 and backward trajectories during the ascent . . . . .	119
4.22	Flight on October 22, 2002; CFC-11 and backward trajectories during the descent . . . . .	120
4.23	Flight paths during SPURT . . . . .	122
4.24	Comparison with SPURT - CFC-12 data . . . . .	123
4.25	Determining initial profiles . . . . .	124
4.26	Tracer-theta-space plot for Forlí, July 2002 . . . . .	125
4.27	CFC-12 - O <sub>3</sub> correlation; APE ENVISAT, July 2002 and APE THE- SEO, 1999 . . . . .	126
4.28	Tracer-theta-space plot for SPURT, summer data . . . . .	127
4.29	Tracer-theta-space plot for Forlí, October 2002 . . . . .	128
4.30	CFC-12 - O <sub>3</sub> correlation; APE-ENVISAT, October 2002 and APE THESEO, 1999 . . . . .	129
4.31	Tracer-theta-space plot for SPURT, October 2002 . . . . .	129
B.1	Defining $\Delta N_2 O_{extra}$ . . . . .	144
C.1	Drift correction of CAL flight bottle . . . . .	150
C.2	LICOR: linearity . . . . .	156
D.1	HAGAR data July 2002. . . . .	160
D.2	HAGAR data on October 8, 11, 14 and 17, 2002 . . . . .	161
D.3	HAGAR data on October 22, 24 and 28, 2002 . . . . .	162
D.4	HAGAR data on January 15 and 19, 2003 . . . . .	163
D.5	HAGAR data on January 23 and 26 and February 2 and 6, 2003 . . . . .	164
D.6	HAGAR data on February 8 and 11, 2003 . . . . .	165
D.7	HAGAR data February 28, 2003. . . . .	166
D.8	HAGAR data on March 2, 8, 12 and 16, 2003 . . . . .	167
E.1	NCEP reanalysis July 10 and 11, 2002 . . . . .	169
E.2	NCEP reanalysis July 12 to 17, 2002 . . . . .	170
E.3	NCEP reanalysis July 18 to 23, 2002 . . . . .	171
E.4	NCEP reanalysis October 8, 2002 . . . . .	172
E.5	NCEP reanalysis October 11, 14, 17, 22, 24 and 28, 2002 . . . . .	173



# List of Tables

2.1	HAGAR columns . . . . .	21
2.2	Channel I set-up, December 2001 . . . . .	31
2.3	Channel I set-up, January and May 2002 . . . . .	33
2.4	Channel I set-up, May and early June 2002 . . . . .	34
2.5	Channel I set-up, July 2002 . . . . .	34
2.6	Channel I set-up, September to December 2002 . . . . .	35
2.7	Channel I set-up, January to March, 2003 . . . . .	36
2.8	Geophysica payload . . . . .	39
2.9	Data status during July 2002 . . . . .	42
2.10	Data status during October 2002 . . . . .	44
2.11	Data status during EuPLEx . . . . .	48
2.12	Data status during AVC . . . . .	50
3.1	Tracers used in the analysis . . . . .	54
3.2	Tropospheric boundary values . . . . .	64
3.3	Errors of the vortex boundary values . . . . .	68
3.4	Stratospheric boundary values . . . . .	70
3.5	Weighting factors of the mass balance calculation . . . . .	73
4.1	Tropospheric boundary values, SPURT and HAGAR . . . . .	124
C.1	HAGAR calibration gases, CAL . . . . .	151
C.2	HAGAR calibration gases, SPAN . . . . .	152
C.3	Precision of HAGAR during the Forlí campaigns . . . . .	157
C.4	Precision of HAGAR during EuPLEx . . . . .	158



# Bibliography

- Andrews, A. E., K. A. Boering, B. C. Daube, S. C. Wofsy, E. J. Hintsa, E. M. Weinstock & T. P. Bui. Empirical age spectra for the lower tropical stratosphere from in situ observations of CO<sub>2</sub>: Implications for stratospheric transport. *J. Geophys. Res.*, *104*, 26 581–26 595, 1999.
- Appenzeller, C. & H. Davies. Structure of stratospheric intrusions into the troposphere. *J. Geophys. Res.*, *101*, 1435–1456, 1996.
- Baray, J.-L., G. Ancellet, T. Randriambelo & S. Baldy. Tropical cyclone Marlene and stratosphere-troposphere exchange. *J. Geophys. Res.*, *104*, 13 953–13 970, 1999.
- Bevington, P. R. & K. R. Robinson. *Data Reduction and Error Analysis for the Physical Sciences*. McGraw-Hill, Inc., 2. Aufl., 1992.
- Bönisch, H. *Untersuchung des Transports in der untersten Stratosphäre anhand von in-situ Messungen langlebiger Spurengase*. Dissertation, Johann Wolfgang Goethe-Universität Frankfurt, 2006.
- Boering, K. A., B. C. Daube Jr., S. C. Wofsy, M. Loewenstein, J. R. Podolske & E. R. Keim. Tracer-tracer relationships and lower stratospheric dynamics: CO<sub>2</sub> and N<sub>2</sub>O correlations during SPADE. *Geophys. Res. Lett.*, *21*, 2567–2570, 1994.
- Bosch, K. *Elementare Einführung in die Wahrscheinlichkeitsrechnung*. Vieweg, 6. Aufl., 1995.
- Brewer, A. W. Evidence for a world circulation provided by the measurements of helium and water vapour distribution in the stratosphere. *Q. J. R. Meteorol. Soc.*, *75*, 351–363, 1949.
- Bronstein, I. N., K. A. Semendjajew, G. Musiol & H. Mühlig. *Taschenbuch der Mathematik*. Verlag Harry Deutsch, Frankfurt am Main, 1. Aufl., 1993.
- Bujok, O., V. Tan, E. Klein, R. Bauer, A. Engel & U. Schmidt. In-situ measurements of long-lived tracers in the tropopause region: a novel automated airborne gas chromatograph. *Proceedings of the 1996 Quadrennial Ozone Symposium L'Aquila, Italy*, 1996.

- Chen, P. Isentropic cross-tropopause mass exchange in the extratropics. *J. Geophys. Res.*, *100*, 16 661–16 673, 1995.
- Curtius, J., R. Weigel, H.-J. Vössing, H. Wernli, A. Werner, C. Volk, P. Konopka, M. Krebsbach, C. Schiller, A. Roiger, H. Schlager, V. Dreiling & S. Borrmann. Observations of meteoric material and implications for aerosol nucleation in the winter Arctic lower stratosphere derived from in situ particle measurements. *Atmos. Chem. Phys.*, *11*, 3053–3069, 2005.
- Delden, A. v. & R. Neggers. A case study of tropopause cyclogenesis. *Meteorol. Appl.*, *10*, 187–199, 2003. Doi:10.1017/S1350482703002081.
- Dessler, A. E., E. J. Hintsala, E. M. Weinstock, J. G. Anderson & K. Chan. Mechanisms controlling water vapor in the lower stratosphere: “A Tale of two stratospheres“. *J. Geophys. Res.*, *100*, 23 167–23 172, 1995.
- Dethof, A., A. O’Neill & J. Slingo. Quantification of Isentropic Mass Transport Across the Dynamical Tropopause. *J. Geophys. Res.*, *105*, 12 279–12 293, 2000.
- Dobson, G. M. B., D. Harrison & J. Lawrences. Measurements of the amount of ozone in the earth’s atmosphere and its relation to other geophysical conditions. *Proc. Roy. Soc. London, A*, 456–486, 1929.
- Elkins, J. W., D. W. Fahey, J. M. Gilligan, G. S. Dutton, T. J. Baring, C. M. Volk, R. E. Dunn, R. C. Myers, S. A. Montzka, P. R. Wamsley, A. H. Hayden, J. H. Butler, T. M. Thompson, T. H. Swanson, E. J. Dlugokencky, P. C. Novelli, D. F. Hurst, J. M. Lobert, S. J. Ciciora, R. J. McLaughlin, T. L. Thompson, R. H. Winkler, P. J. Fraser, L. P. Steele & M. P. Lucarelli. Airborne gas chromatograph for in-situ measurements of long-lived species in the upper troposphere and lower stratosphere. *Geophys. Res. Lett.*, *23*, 347–350, 1996.
- Engel, A., H. Bönisch, D. Brunner, H. Fischer, H. Franke, G. Günther, C. Gruk, M. Hegglin, P. Hoor, R. Königstedt, M. Krebsbach, R. Maser, U. Parchatka, T. Peter, D. Schell, C. Schiller, U. Schmidt, N. Spelten, T. Szabo, U. Weers, H. Wernli, T. Wetter & V. Wirth. Highly resolved observations of trace gases in the lowermost stratosphere und upper troposphere from the Spurt project: an overview. *Atmospheric Chemistry and Physics*, *S*, 283–301, 2006.
- Esler, J., D. Tan, P. Haynes, M. Evans, K. Law, P. Plantevin & J. Pyle. Stratosphere-troposphere exchange: Chemical sensitivity to mixing. *J. Geophys. Res.*, *106*, 4717–4731, 2001.
- EuPLEx. Description of Work. Report, EuPLEx, Forschungszentrum Jülich, 2001. Coordinator: F. Stroh.
- EuPLEx. Final Report. Summary report, EuPLEx, Forschungszentrum Jülich, 2004. Coordinator: F. Stroh.

- Exxact. *ADC3: Universelles Prozessinterface für die Verarbeitung von Spannungs- und Stromsignalen*. Exxact, Gesellschaft für elektronische Präzisionsmesstechnik mbH, 1998.
- Farman, J., B. G. Gardiner & J. D. Shankin. Large losses of total ozone in Antarctica reveal seasonal  $\text{ClO}_x/\text{NO}_x$  interaction. *Nature*, 315, 207–210, 1985.
- Fischer, H., P. Hoor & J. Lelieveld. Seasonal Variation of Extratropical Cross-tropopause Transport Inferred from Chemical Tracer Measurements. *Stratospheric Processes and their Role in Climate, SPARC-Newsletter*, 2001.
- Fujiwara, M., K. Kita & T. Ogawa. Stratosphere-troposphere exchange of ozone associated with equatorial Kelvin waves as observed with ozonesondes and raw-insondes. *J. Geophys. Res.*, S. 19 173–19 182, 1998.
- Geist, K., U. Parlitz & W. Lauterborn. Comparison of different methods for computing Lyapunov exponents. *Prog. Theor. Phys.*, S. 875–893, 1990.
- Gouget, H., G. Vaughan, A. Marenco & H. Smit. Decay of a cut-off low and contribution to stratosphere troposphere exchange. *Q.J.R. Meteorol. Soc.*, 126, 1117–1141, 2000.
- Greenblatt, J. B., H.-J. Jost, M. Loewenstein, J. R. Podolske, P. T. Bui, D. F. Hurst, J. W. Elkins, R. L. Herman, C. R. Webster, S. M. Schauffler, E. L. Atlas, P. A. Newmann, L. R. Lait, M. Müller, A. Engel & U. Schmidt. Defining the polar vortex edge from an  $\text{N}_2\text{O}$ :potential temperature correlation. *J. Geophys. Res.*, 107, 2002. Doi:10.1029/2001JD000575.
- Hall, T. M. & R. A. Plumb. Age as a diagnostic of stratospheric transport. *J. Geophys. Res.*, 99, 1059–1070, 1994.
- HALO. <http://www.halo.dlr.de>. 2006.
- Harnisch, J., R. Borchers, P. Fabian & M. Maiss.  $\text{CF}_4$  and the age of mesospheric and polar vortex air. *Geophys. Res. Lett.*, 26, 295–298, 1999.
- Haynes, P., C. Marks, M. E. McIntyre, T. G. Shepard & K. P. Shine. On the “downward control” of extratropical diabatic circulations by eddy induced mean zonal forces. *J. Aerosol. Sci.*, 48, 651–678, 1991.
- Haynes, P. & T. Shepard. Report on the SPARC Tropopause Workshop. SPARC Newsletter 17, Stratospheric Processes And Their Role In Climate, World Climate Research Programme, Verrierres-le-Buisson, France, 2001.
- Haynes, P. & E. Shuckburgh. Effective diffusivity as a diagnostic of atmospheric transport 1. Stratosphere. *J. Geophys. Res.*, 105, 22 777–22 794, 2000a.

- Haynes, P. & E. Shuckburgh. Effective diffusivity as a diagnostic of atmospheric transport 2. Troposphere and lower stratosphere. *J. Geophys. Res.*, *105*, 22 795–22 810, 2000b.
- Hegglin, M., D. Brunner, T. Peter, P. Hoor, H. Fischer, J. Steahelin, M. Krebsbach, C. Schiller, U. Parchatka & U. Weers. Measurements of NO, NO<sub>y</sub>, N<sub>2</sub>O and O<sub>3</sub> during Spurt: implications for transport and chemistry in the lowermost stratosphere. *Atmos. Chem. Phys.*, *5*, 1680–7324, 2006.
- Hints, E. J., K. Boering, E. M. Weinstock, J. G. Anderson, B. L. Gary, L. Pfister, B. C. Daube, S. C. Wofsy, M. Loewenstein, J. R. Podolske, J. J. Margitan & T. P. Bui. Troposphere-to-stratosphere transport in the lowermost stratosphere from measurements of H<sub>2</sub>O, CO<sub>2</sub>, N<sub>2</sub>O and O<sub>3</sub>. *Geophys. Res. Lett.*, *25*, 2655–2658, 1998.
- Hoerling, M., T. Schaak & A. Lenzen. Global objective tropopause analysis. *Monthly Weather Review*, *119*, 1991.
- Holton, J. R. *An Introduction to Dynamic Meteorology*. Academic Press, London, 1992. 3. edition.
- Holton, J. R., P. H. Haynes, M. E. McIntyre, A. R. Douglass, R. B. Rood & L. Pfister. Stratosphere-Troposphere Exchange. *Reviews of Geophysics*, *33*, 403–439, 1995.
- Hoor, P., H. Fischer, L. Lange, J. Lelieveld & D. Brunner. Seasonal Variations of a mixing layer in the lowermost stratosphere as identified by the CO-O<sub>3</sub> correlation from in-situ measurements. *J. Geophys. Res.*, *107*, 2002.
- Hoor, P., C. Gurk, D. Brunner, M. Hegglin, H. Wernli & H. Fischer. Seasonality and extent of extratropical TST derived from in-situ CO measurements during Spurt. *Atmos. Chem. Phys.*, *4*, 1427–1442, 2004.
- Hoskins, B. Towards a PV- $\Theta$  view of the general circulation. *Tellus*, *43AB*, 27–35, 1991.
- IPCC. *Climate Change 2001: The scientific basis. Contribution of working group I to the third assessment report of the intergovernmental panel on climate change*. Cambridge University Press, Cambridge and New York, 2001. Edited by J. T. Houghton, Y. Ding, D. J. Griggs, M. Noguer, P. J. van der Linden, X. Dai, K. Maskell, and C. A. Johnson.
- Jost, H., K. Drdla, A. Stohl, L. Pfister, J. P. Loewenstein, M. Lopez, P. K. Hudson, D. M. Murphy, D. J. Cziczo, M. Fromm, T. P. Bui, J. Dean-Day, C. Gerbig, M. J. Mahoney, E. C. Richard, N. Spichtinger, J. V. Pittman, E. M. Weinstock, J. C. Wilson & I. Xueref. In-situ observations of mid-latitude forest fire plumes deep in the stratosphere. *Geophys. Res. Lett.*, *31*, doi:10.1029/2003GL019 253, 2004.



- Kida, H. General Circulation of Air Parcels and Transport Characteristics Derived from a Hemispheric GCM, Part 2, Very Long-Term Motions of Air Parcels in the Troposphere and Stratosphere. *J. Meteorol. Soc. Jpn.*, *61*, 510–522, 1983.
- Krebsbach, M. *Trace gas transport in the UT/LS. Seasonality, stratosphere - troposphere exchange and implications for the extra-tropical mixing layer derived from airborne O<sub>3</sub> and H<sub>2</sub>O measurements*. Dissertation, Universität Wuppertal, 2005.
- Kritz, M., S. Rosner, E. Danielsen & H. Selkirk. Air mass origins and troposphere-to-stratosphere exchange associated with mid-latitude cyclogenesis and tropopause folding inferred from <sup>7</sup>Be measurements. *J. Geophys. Res.*, *96*, 17405–17414, 1991.
- Lacis, A. A., D. J. Wuebbles & A. J. Logan. Radiative forcing by changes in the vertical distribution of ozone. *J. Geophys. Res.*, *95*, 9971–9981, 1990.
- Lange, L. *Aircraft-borne trace gas measurements during the STREAM 98 campaign*. Dissertation, Universität Utrecht, Niederlande, 2001.
- LI-COR. *LI-6251 CO<sub>2</sub> Analyzer, Instruction Manual*. LI-COR, Inc., Lincoln, Nebraska USA, 1992.
- McIntyre, M. E. & T. N. Palmer. Breaking planetary waves in the stratosphere. *Nature*, *305*, 593–600, 1983.
- McIntyre, M. E. & T. N. Palmer. The 'surf zone' in the stratosphere. *J. Atmos. Terr. Phys.*, *46*, 825–849, 1984.
- McKenna, D., J.-U. Groöß, G. Günther, P. Konopka, R. Müller, G. Carver & Y. Sasano. A new Chemical Lagrangian Model of the Stratosphere (CLaMS) 2. Formulation of chemistry scheme and initialization. *J. Geophys. Res.*, *107*, 2002a.
- McKenna, D., P. Konopka, J.-U. Groöß, G. Günther, R. Müller, R. Spang, D. Offermann & Y. Orsolini. A new Chemical Lagrangian Model of the Stratosphere (CLaMS) 1. Formulation of advection and mixing. *J. Geophys. Res.*, *107*, 2002b.
- Moore, F. L., J. W. Elkins, E. A. Ray, R. E. Dunn, G. S. Dutton, C. M. Volk & Fahey. First in-situ gas chromatographic balloon measurements of the trace gases in the middle stratosphere. *EOS Trans. AGU*, *78*, 1997. Fall Meeting Suppl.
- Moore, F. L., J. W. Elkins, E. A. Ray, G. S. Dutton, R. E. Dunn, D. W. Fahey, R. J. McLaughlin, T. L. Thompson, P. A. Romashkin, H. D. F. & P. R. Wamsley. Balloonborne in situ gas chromatograph for measurements in the troposphere and stratosphere. *J. Geophys. Res.*, *108*, 8330, 2003. Doi:10.1029/2001JD000891.
- Müller, R. personal communication. 2004.

- Nash, E., P. Newman, J. Rosenfield & M. Schoeverl. An objective determination of the polar vortex using Ertel's potential vorticity. *J. Geophys. Res.*, *101*, 9471–9478, 1996.
- NOAA-CMDL. [www.cmdl.noaa.gov](http://www.cmdl.noaa.gov). 2006.
- Pan, L., S. Solomon, W. Randel, J.-F. Lamarque, P. Hess, J. Gille, E.-W. Chiou & M. P. McCormick. Hemispheric asymmetries and seasonal variations of the lowermost stratospheric water vapor and ozone derived from SAGE II data. *J. Geophys. Res.*, *102*, 28 177 – 28 184, 1997.
- Pawson, S., K. Labitzke & S. Leder. Stepwise changes in stratospheric temperature. *Geophys. Res. Lett.*, *25*, 2157–2160, 1998.
- Phillips, M. P., R. E. Sievers, P. D. Goldan, W. C. Kuster & F. C. Fehsenfeld. Enhancement of Electron Capture Detector Sensitivity to Nonelectron Attaching Compounds by Addition of Nitrous Oxide to the Carrier Gas. *Anal. Chem.*, *51*, 1819–1825, 1979.
- Plumb, R. A. A "tropical pipe" model of stratospheric transport. *J. Geophys. Res.*, *101*, 3957–3972, 1996.
- Plumb, R. A. Stratospheric Transport. *Journal of the Meteorological Society of Japan*, *80*, 793–809, 2002.
- Plumb, R. A. & M. K. W. Ko. Interrelations between Mixing Ratios of Long-Lived Stratospheric Constituents. *J. Geophys. Res.*, *97*, 10 145–10 156, 1992.
- Plumb, R. A., D. W. Waugh & M. P. Chipperfield. The effect of mixing on tracer relationships in the polar vortices. *J. Geophys. Res.*, *105*, 10 047–10 062, 2000.
- Poulida, O., R. Dickerson & A. Heymsfiel. Stratosphere-troposphere exchange in a midlatitude mesoscale convective complex. *J. Geophys. Res.*, *101*, 6823–6836, 1996.
- Press, W. H., S. A. Teukolsky, W. T. Vetterling & B. P. Flannery. *Numerical Recipes in C*. Cambridge University Press, Cambridge, 2. Aufl., 1992.
- Ramaswamy, V., M. D. Schwarzkopf & K. P. Shine. Radiative forcing of climate from halocarbon-induced global stratospheric ozone loss. *Nature*, *355*, 810–812, 1992.
- Ray, E. A., F. L. Moore, J. W. Elkins, G. S. Dutton, D. W. Fahey, H. Vömel, S. J. Oltmans & K. H. Rosenlof. Transport into the Northern Hemisphere lowermost stratosphere revealed by in situ tracer measurements. *J. Geophys. Res.*, *104*, 26 565–26 580, 1999.

- Riediger, O. *Entwicklung und Einsatz eines flugzeuggetragenen Instrumentes zur in-situ-Messung langlebiger Spurengase in der Stratosphäre*. Dissertation, Johann Wolfgang Goethe-Universität Frankfurt, 2000.
- Rohs, S. personal communication. 2006.
- Rosenlof, K. & J. Holton. Estimates of the stratospheric residual circulation using the downward control principle. *J. Geophys. Res.*, *98*, 10 465–10 479, 1993.
- Rosenlof, K., A. F. Tuck, K. K. Kelly, J. M. Russell III & P. McCormick. Hemispheric asymmetries in water vapor and inferences about transport in the lowermost stratosphere. *J. Geophys. Res.*, *102*, 13 213–13 234, 1997.
- Rosenlof, K. H. Transport changes inferred from HALOE water and methane measurements. *Journal of the Meteorological Society of Japan*, *80*, 831–848, 2002.
- Rossberg, R. personal communication. 2003.
- Schiller, C. & N. Spelten. personal communication. 2006.
- Schmidt, U., A. Engel & C. M. Volk. Ist der Ozonabbau gestoppt ? *Forschung Frankfurt*, S. 11–19, 2001.
- Schmidt, U. & A. Khedim. In Situ Measurements of Carbon Dioxide in the Winter Arctic Vortex and at Midlatitudes: An Indicator of the 'Age' of Stratospheric Air. *Geophys. Res. Lett.*, *18*, 763–766, 1991.
- Schmidt, U., G. Kulesa, E. Klein, E.-P. Röth, P. Fabian & R. Borchers. Intercomparison of balloon borne cryogenic whole air samplers during MAP/GLOBUS 1983 campaign. *Planet. Space Sci.*, *35*, 647–656, 1987.
- Schönwiese, C. D. *Praktische Statistik für Meteorologen und Geowissenschaftler*. Gebrüder Borntraeger, Berlin, Stuttgart, 2. Aufl., 1992.
- Shapiro, M. Turbulent mixing within tropopause folds as a mechanism for the exchange of chemical constituents between the stratosphere and troposphere. *J. Atmos. Sci.*, *37*, 994–1004, 1980.
- Stohl, A. A 1-year Lagrangian climatology of airstreams in the Northern Hemisphere troposphere and lowermost stratosphere. *J. Geophys. Res.*, *106*, 7263–7279, 2001.
- Stohl, A., P. Bonasoni, P. Cristofanelli, W. Collins, J. Feichter, A. Frank, C. Forster, E. Gerasopoulos, H. Gäggeler, P. James, T. Kentarchos, H. Kromb-Kolb, B. Krüger, C. Land, J. Meloan, A. Papayannis, A. Priller, P. Seibert, M. Sprenger, G. J. Poelofs, H. E. Scheel, C. Chnabel, P. Siegmund, L. Tobler, T. Trickl, H. Wernli, V. Wirth, P. Zanis & C. Zerefos. Stratosphere-troposphere exchange: a review, and what we have learned from STACCATO. *J. Geophys. Res.*, *108*, 2003a. Doi:10.1029/2002JD002490.

- Stohl, A., H. Wernli, P. James, M. Bourqui, C. Forster, M. Liniger, P. Seibert & M. Sprenger. A new perspective of stratosphere-troposphere exchange. *Bull. Am. Met. Soc.*, 2003b.
- Strunk, M. *An Experimental Study on the Mean Age of Stratospheric Air*. Dissertation, Johann Wolfgang Goethe-Universität Frankfurt, 1999.
- Ulanovsky, A. personal communication. 2006.
- UNEP. Montreal Protocol on substances that deplete the ozone layer. Techn. Ber., United Environmental Programme, Nairobi, 1987.
- Vaughan, G. & C. Timmis. Transport of near tropopause air into the lower mid latitude stratosphere. *Q.J.R. Meteorol. Soc.*, 124, 1559–1578, 1998.
- Volk, C. M. *Stratospheric transport and tracer lifetimes from airborne in-situ observations*. Ph.D. Thesis, University of Colorado, Boulder, USA, 1996.
- Volk, C. M. & J. Baehr. laboratory measurements; personal communication. 2004.
- Volk, C. M., J. W. Elkins, D. W. Fahey, G. S. Dutton, J. M. Gilligan, M. Loewenstein, J. R. Podolske, K. R. Chan & M. R. Gunson. Evaluation of source gas lifetimes from stratospheric observations. *J. Geophys. Res.*, 102, 25 543–25 564, 1997.
- Volk, C. M., J. W. Elkins, D. W. Fahey, R. J. Salawitch, G. S. Dutton, J. M. Gilligan, M. H. Proffitt, M. Loewenstein, J. R. Podolske, K. Minschwaner & K. R. Margitan, J. J. Chan. Quantifying Transport Between the Tropical and Mid-Latitude Lower Stratosphere. *Science*, 272, 17631 768, 1996.
- Wave Metric, I. *IGOR Pro Version 4.0*, 2000. Revision 10/00 Version 4.01.
- Wernli, H. & M. Bourqui. A Lagrangian „one-year climatology“ of (deep) cross-tropopause exchange in the extratropical Northern Hemisphere. *J. Geophys. Res.*, 107, 2002.
- Wernli, H. & H. C. Davies. A Lagrangian-based analysis of extratropical cyclones,I; The method and some applications. *Q.J.R. Meteorol. Soc.*, 123, 467–489, 1997.
- Wetterzentrale. <http://www.wetterzentrale.de/topkarten/>. 2006.
- Wirth, V. Static stability in the extratropical tropopause region. *J. Atmos. Sci.*, 60, 1395–1409, 2003.
- WMO. WMO-Bulletin. Volume 6, 136, World Meteorological Organization, Geneva, Switzerland, 1957.

- 
- WMO. Atmospheric Ozone: 1985. Global Ozone Research and Monitoring Project – Report No 16, World Meteorological Organization, Geneva, Switzerland, 1986.
- WMO. Scientific assessment of ozone depletion: 1998. Global Ozone Research and Monitoring Project – Report No 44, World Meteorological Organization, Geneva, Switzerland, 1999.
- Zachariasse, M., H. Smit, P. van Velthoven & H. Kelder. Cross tropopause and interhemispheric transports into the tropical free troposphere over the Indian Ocean. *J. Geophys. Res.*, 106, 28 441–28 452, 2001.



# Zusammenfassung

Die unterste Stratosphäre („lowermost stratosphere“, kurz LMS) ist der Teil der Stratosphäre zwischen der Tropopause und der 380 K Isentrope, der in direktem Austausch mit der Troposphäre steht [Holton *et al.*, 1995]. Der Eintrag von Luftmassen in die unterste Stratosphäre erfolgt in den mittleren Breiten im wesentlichen auf zwei Wegen: Zum einen durch Absinken stratosphärischer Luft von oberhalb der 380 K Isentrope im Rahmen der Brewer-Dobson Zirkulation [Brewer, 1949] und zum anderen durch quasi-isentropen Transport von troposphärischer Luft durch die Tropopause.

Austauschprozesse zwischen der Troposphäre und der LMS (stratosphere-troposphere-exchange, kurz STE) bestimmen in signifikantem Ausmaß die chemische Zusammensetzung [Pan *et al.*, 1997] und die Strahlungsbilanz der LMS und der Tropopausenregion [Holton *et al.*, 1995]. Änderungen der Strahlungsbilanz der Tropopausenregion durch Änderungen der Treibhausgaskonzentrationen sind in höchstem Maße relevant für das Klima der Atmosphäre [Haynes & Shepard, 2001]. So führt der Anstieg der Treibhausgaskonzentrationen zur Abkühlung der Stratosphäre und Erwärmung der Troposphäre [Pawson *et al.*, 1998]. Im Zusammenhang mit tieferen Temperaturen in der mittleren und oberen Stratosphäre wird die Abnahme der Stabilität in der Stratosphäre [Stohl *et al.*, 2003a] und damit Änderungen der globalen Zirkulation diskutiert. Zusammenfassend lässt sich sagen, dass das Wissen über Transportprozesse in der Tropopausenregion und der LMS elementar ist für das Verständnis von Spurengasbudgets (z.B. Ozon) und dem Klimawandel in der Atmosphäre.

Diese Studie liefert einen Beitrag zur Untersuchung der Dynamik im Bereich der LMS. Anhand von flugzeuggetragenen in-situ Messungen der langlebigen Spurengase N<sub>2</sub>O, CFC-12, CFC-11, H-1211, CH<sub>4</sub>, SF<sub>6</sub>, H<sub>2</sub> und CO<sub>2</sub> wurde der Transport in der und in die LMS untersucht.

## Instrumentierung und Datenbasis

Datenbasis dieser Arbeit sind Messungen mit dem High Altitude Gas Analyser (HAGAR) der Universität Frankfurt, einem in-situ Gaschromatographen, der die langlebigen Spurengase N<sub>2</sub>O, CH<sub>4</sub>, H<sub>2</sub>, CFC-12, CFC-11, H-1211 und SF<sub>6</sub> misst. Zusätzlich ist HAGAR mit einem auf Infrarotabsorption basierenden CO<sub>2</sub>-

Messgerät ausgestattet. Ozon wurde mit dem Fast Ozone Analyzer (FOZAN<sup>2</sup>) und FOX<sup>3</sup> gemessen und H<sub>2</sub>O mit dem FISH<sup>4</sup>. Plattform für die Messungen ist die M55-Geophysica, ein russisches Höhenforschungsflugzeug, das Gipfelhöhen bis zu 21 km erreicht. Auf Messkampagnen in Forlì/Italien im Juli und Oktober 2002 (APE ENVISAT Mid Latitude Test and Validation Campaigns) und in Kiruna/Schweden von Januar bis März 2003 (EuPLEX<sup>5</sup> und APE ENVISAT AVC<sup>6</sup>) ist ein umfangreicher Datensatz entstanden, der die mittleren bis hohen Breiten der Nordhemisphäre abdeckt.

Eine der wesentlichen Arbeiten am Instrument in der Vorbereitung der Messkampagnen war die Modifikation eines der zwei gaschromatographischen Kanäle des HAGARs zur Messung von Methan, CH<sub>4</sub>. Dies war notwendig, um zum einen einer der Aufgabenstellungen der Messkampagnen nachzukommen, der Validierung von Satellitenmessungen mit dem ENVISAT Forschungssatelliten, zum anderen zur Erweiterung des HAGAR-Datensatzes um weitere Spurengase. So ist CH<sub>4</sub> eines der Spurengase, die eine wichtige Rolle bei der Untersuchung der nordhemisphärischen LMS einnehmen.

Die instrumentellen Änderungen sowie theoretische Grundlagen zur CH<sub>4</sub>-Chromatographie sind in Kapitel 2.2 beschrieben. Die Detektion des Messsignals erfolgt mit Elektroneneinfang-Detektoren (electron capture detector; kurz ECD). Da organische Substanzen, wie CH<sub>4</sub>, keine Elektronen einfangen, können diese Moleküle nicht direkt von ECDs detektiert werden. Durch die Zugabe einer geringen Menge einer weiteren Substanz, in diesem Falle N<sub>2</sub>O, kann jedoch die Sensitivität der Detektoren bezüglich organischer Substanzen verstärkt werden. CH<sub>4</sub> wird messbar (Gleiches gilt im Übrigen für H<sub>2</sub>). Diese Sensitivitätserhöhung unter Zuhilfenahme einer weiteren Substanz nennt man Doping [Phillips *et al.*, 1979]. In Testreihen im Labor wurde diese Technik für den Einsatz im HAGAR optimiert und schließlich wurden notwendige mechanische Modifikationen am Instrument umgesetzt. Im Rahmen dieser Arbeit konnten somit erstmals CH<sub>4</sub> und H<sub>2</sub> mit HAGAR gemessen werden.

## Quantifizierung des Transports in die arktische LMS

Transport in die arktische LMS erfolgt im wesentlichen entlang dreier Transportwege: (i) isentroper Transport von der Troposphäre durch die Tropopause und von der untersten tropischen Stratosphäre, (ii) Absinken stratosphärischer Luft durch die 400 K Isentrope außerhalb des arktischen Wirbels und (iii) Absinken von Luftmassen durch die 400 K Isentrope aus dem Polarwirbel. Mittels einer einfachen Massenbilanz, inspiriert durch die Arbeit von Ray *et al.* [1999], lässt sich Transport von Luft aus diesen Quellregionen in die LMS quantifizieren.

<sup>2</sup>Dye Chemiluminescence; CAO, Russland und ISAC-CNR, Italien

<sup>3</sup>UV-Absorption, DLR, Deutschland

<sup>4</sup>Lyman- $\alpha$  photo-fragment fluorescence; Forschungszentrum Jülich

<sup>5</sup>European Polar stratospheric cloud and Lee wave Experiment

<sup>6</sup>Arctic Validation Campaign



Die Anteile der Luftmassen in der LMS, die ihren Ursprung in der Troposphäre sowie der unteren Stratosphäre außerhalb und innerhalb des Polarwirbels hatten, werden durch Lösung eines überbestimmten linearen Gleichungssystems bestimmt. Grundlage hierzu sind Beobachtungen von Spurengasen, die eine nicht-lineare Korrelation zueinander aufweisen und daher hinreichend verschiedene Randbedingungen zur Lösung des linearen Gleichungssystems liefern. Als geeignete Spurengase werden  $N_2O$ , F11, H-1211,  $CH_4$  (HAGAR-Tracer),  $O_3$  (FOX; DLR) und  $H_2O$  (FISH, FZ Jülich) verwendet.

Der troposphärische Randwert wird als Mittelwert der troposphärischen Messungen bestimmt und der stratosphärische Randwert außerhalb des Polarwirbels als Mittelwert der Spurengasmessungen zwischen 395 K und 405 K in mittleren bis hohen Breiten, die nicht durch Luft aus dem Polarwirbel beeinflusst sind. Bei der Bestimmung des Randwertes entlang der 400 K Isentrope im Polarwirbel wird die zeitliche Änderung der Mischungsverhältnisse durch verstärktes Absinken der Luftmassen im Polarwirbel berücksichtigt. Ein zeitlich variabler Randwert wird mit Hilfe von Spurengasmessungen (HAGAR und MKIV<sup>7</sup>) und Trajektorien des CLaMS Modells [McKenna *et al.*, 2002a,b] berechnet, die das Absinken der Luftmassen im Winter 2002/2003 beschreiben. Eine Ausnahme bildet hier  $H_2O$ , gemessen durch FISH, dessen Verteilung sich grundlegend von den restlichen Spurengasen unterscheidet. Die Randwerte an der 400 K Isentrope innerhalb und außerhalb des Polarwirbels wurden als Mittelwert zwischen 395 K und 405 K berechnet. Der Eintrag aus der Troposphäre jedoch ist abhängig von der Temperatur an der Tropopause und damit abhängig von der potentiellen Temperatur. Daher wurde der troposphärische Randwert aus einer Klimatologie des  $H_2O$  Eintrags aus SPURT<sup>8</sup> und POLSTAR<sup>9</sup> Daten [Krebsbach, 2005] bestimmt.

Die Lösung des linearen Gleichungssystems reagiert äußerst sensibel auf Änderungen in den Randbedingungen. Eine Sensitivitätsstudie wurde deshalb mit Hilfe einer Monte Carlo Simulation durchgeführt. Das lineare Gleichungssystem wurde für simultan variierende Eingangsgrößen gelöst. Die Variationsbreite der Eingangsgrößen wurde dabei entsprechend dem Fehler der jeweiligen Randbedingung gewählt. Es zeigt sich, dass die Ergebnisse zum Teil großen Unsicherheiten unterliegen, dennoch aber sinnvolle, qualitative wie quantitative Aussagen über den Transport in die LMS getroffen werden können.

## Ergebnisse und Schlussfolgerungen

Zur Analyse der Ergebnisse wurden die Daten in zwei Datensätze unterteilt, die den Extrema der Messwerte entsprechen: Zum einen Daten, die bei niedrigen  $N_2O$  Mischungsverhältnissen gemessen wurden und am stärksten durch den Polarwirbel beeinflusst sind (genannt “low  $N_2O$ ” Datensatz), zum anderen Daten, die bei hohen

<sup>7</sup>Ein Fourier Transform InfraRed (FTIR) Interferometer

<sup>8</sup>SPURstofftransport in der Tropopausenregion [Engel *et al.*, 2006]

<sup>9</sup>Polar Stratospheric Aerosol Experiment; 1997/98

$N_2O$ -Mischungsverhältnissen gemessen wurden und den geringsten Einfluss durch Luft aus dem Polarwirbel zeigen (genannt "high  $N_2O$ " Datensatz).

Im wesentlichen zeigen die Ergebnisse, dass ein verstärkter troposphärischer Einfluss in der LMS nur in den unteren 20 K der LMS zu finden ist. Dieser Einfluss ist größer als 50% während der EuPLEX Kampagne und größer als 30% während der AVC Kampagne. Dies ist vergleichbar mit Ergebnissen von *Hoor et al.* [2004], die eine dünne Mischungsschicht mit erhöhtem troposphärischen Einfluss in den untersten 20 bis 30 K der LMS finden.

Oberhalb dieser Schicht finden sich mit einem Anteil von etwa 75% vorwiegend Luftmassen, die aus der Stratosphäre außerhalb des Polarwirbels abgesunken sind.

Nur in der oberen Hälfte der LMS des "low  $N_2O$ " Datensatzes lässt sich ein wesentlicher Einfluss des Polarwirbels finden. Der Anteil von Vortex-Luft nimmt von rund 50% bei 370 K bis auf 100% bei 400 K zu. Die Unterschiede sind hierbei zwischen den Kampagnen sehr gering, da im Winter 2002/2003 der Großteil des Absinkens innerhalb des Polarwirbels bereits vor Januar (EuPLEX) stattgefunden hatte. So findet sich in den Daten der AVC Kampagne nur ein leicht erhöhter Vortex Einfluss verglichen zu EuPLEX.

Ein moderater Einfluss durch Luftmassen aus dem Polarwirbel ( $f_{vortex} \approx 30\%$ ) in den obersten Schichten der LMS im "high  $N_2O$ " Datensatz der AVC Kampagne lässt auf Mischung zwischen Luftmassen des Polarwirbels und der mittleren Breiten schließen. In der Tat zeigt ein Vergleich des mit der Massenbilanz bestimmten Anteils der Wirbelluft mit einem künstlichen Tracer für Wirbelluft (CLaMS) für potentielle Temperaturen oberhalb 400 K Mischung zwischen Wirbelluft und Luft mittlerer Breiten.

## Ein „cut-off low“ über Europa — Abschätzung der Mischung in der LMS

Während der ENVISAT Test- und Validierungskampagnen in den mittleren Breiten in Forlì im Juli und Oktober 2002 wurden insgesamt 11 Flüge in der LMS zwischen 30° and 45° N durchgeführt. In Verbindung mit dem Durchzug eines „cut-off low“ wurden im Juli 2002 in der LMS über Italien stark variierende Spurengasmischungsverhältnisse gemessen. Eine Trajektorienanalyse (5-Tage Rückwärtstrajektorien) zeigt, dass in Verbindung mit dem „cut-off low“ Luftmassen aus verschiedenen Quellgebieten heran transportiert wurden: Luft aus hohen Breiten, verbunden mit niedrigen Mischungsverhältnissen der Spurengase (hohe Mischungsverhältnisse für  $O_3$ ) und Luft mit Mischungsverhältnissen troposphärischen Charakters aus der Tropopausenregion, sowie den Subtropen. Eine vergleichbare meteorologische Situation im Oktober zeigte jedoch minimale Auswirkung auf die Mischungsverhältnisse der gemessenen Spurengase.

Ein Vergleich dieser Messungen mit Spurengasverteilungen, wie sie im Frühling

in der LMS zu finden sind, gibt Aufschluss darüber, in welchem Ausmaß Mischungsprozesse in der LMS stattgefunden haben. Im Frühling, kurz nach Auflösung des Polarwirbels findet sich ein relativ starker meridionaler Gradienten in der Spurengasverteilung der LMS, der erst mit zunehmendem Einfluss von Mischungsprozessen abgeschwächt wird. Typische Spurengasverteilungen für den Frühling wurden anhand von ENVISAT AVC und SPURT Daten erstellt.

## Ergebnisse und Schlussfolgerungen

Es zeigt sich, dass die im Juli während des Durchzugs des „cut-off low“ gemessenen Mischungsverhältnisse einen den Spurengasverteilungen des Frühlings vergleichbaren meridionalen Gradienten aufweisen. Gleiches gilt auch für die im Sommer gemessenen SPURT Daten. Gleichermaßen werden aber auch Mischungsverhältnisse nahe dem troposphärischen Hintergrund in der LMS gemessen, ein Hinweis auf erst kürzlich erfolgte Einmischung von troposphärischen Luftmassen. Durch starken isentropen Transport im Zusammenhang mit dem „cut-off low“ werden also Luftmassen verschiedener Quellregionen über Forlí zusammengeführt. Da aber zu diesem Zeitpunkt noch die ursprünglichen Charakteristika (typische Mischungsverhältnisse am Ende des Winters) der Quellregionen vorhanden sind, kann man davon ausgehen, dass nur wenig Mischung stattgefunden hat. Grundsätzlich wurden Mischungsverhältnisse nahe dem troposphärischen Hintergrund nur in den untersten 25 K der LMS gefunden. Eine „Mischungsschicht“ in den unteren 20 bis 30 K der LMS mit verstärktem troposphärischen Einfluss konnte auch in den SPURT Daten identifiziert werden [Hoor *et al.*, 2004]. Darüber ist der troposphärische Einfluss wesentlich geringer, wie auch in Luftmassen aus hohen Breiten.

Ein etwas andere Situation findet sich in der Schicht zwischen 380 K und 400 K, in der vorwiegend Luftmassen mit tropischem Charakter gefunden werden. In diesem Höhenbereich befindet sich die „tropically controlled transition region“ [Rosenlof *et al.*, 1997], eine Region, die durch regen meridionalen Transport aus den Tropen beeinflusst wird. So zeigen die in Forlí gemessenen Mischungsverhältnisse von O<sub>3</sub> Werte (FOZAN) größer 100 ppb, während die übrigen gemessenen Spurengas Mischungsverhältnisse im Bereich des troposphärischen Hintergrundes aufweisen. Dies ist ein Hinweis auf Transport aus der tropischen Stratosphäre. Absinken von Luftmassen aus diesem Höhenbereich führt dann zum Eintrag von tropischer Luft in die LMS. Hinweise auf den Eintrag tropischer Luftmassen in die LMS finden sich auch im SPURT Datensatz [Bönisch, 2006; Hegglin *et al.*, 2006; Hoor *et al.*, 2004]. Je nach Saison kann dieser Eintrag bis zu 50% betragen.

Im Herbst lässt sich eine andere Situation in der LMS beobachten. Obwohl während der Oktober-Kampagne Luftmassen über Forlí gemessen wurden, die ihren Ursprung in unterschiedlichen Quellregionen hatten, zeigt sich nur eine geringe Streubreite in den Daten. Durch starken STE und Mischungsprozesse im Verlauf des Sommers hat sich der Gradient in der Spurengasverteilung zwischen hohen und niederen Breiten offensichtlich

abgeschwächt. Die Variabilität der Spurengasmessungen nimmt folglich ab und es zeigt sich ein insgesamt höherer troposphärischer Einfluss. Dies konnte auch in den Messungen der SPURT Kampagne, die im Herbst 2001 und 2002 durchgeführt wurden, festgestellt werden: Die in verschiedenen Breiten gemessenen Spurengastverteilungen weisen ein sehr kompaktes Bild auf mit deutlich geringerer Streuung als im Sommer.

Insgesamt zeigt sich, dass die Daten der ENVISAT- und SPURT-Kampagnen zu vergleichbaren Ergebnissen führen. Unterhalb von 380 K finden sich frische Einträge von troposphärischer Luft nur in den untersten 25 K der LMS. Zwischen Frühling und Sommer konnte in den hohen Breiten ( $> 60^\circ\text{N}$ ) kaum Einmischung von troposphärischer Luft beobachtet werden. Es bestehen signifikante Unterschiede zwischen Luftmassen der niederen und hohen Breiten; in der Spurengasverteilung zeigt sich ein deutlicher meridionaler Gradient. Erst im Verlauf des Sommers wird dieser Gradient durch Mischungsprozesse abgebaut und im Herbst kann eine gut durchmischte LMS bis zu einer potentiellen Temperatur von 380 K beobachtet werden. Diese Schlussfolgerungen sind in Übereinstimmung mit Ergebnissen von *Hoor et al.* [2004], die eine 20 bis 30 K dicke Mischungsschicht oberhalb der Tropopause identifizierten, in der Mischung zwischen troposphärischen und stratosphärischen Luftmassen auf kurzen Zeitskalen stattfindet. In den höheren Regionen der LMS findet Mischung auf längeren Zeitskalen und mit einem Zeitversatz von etwa 2,5 Monaten statt.

In direktem Zusammenhang mit dem „cut-off low“ können keine Aussagen bezüglich der Mischung getroffen werden, da keine Messungen in einer „ungestörten“ LMS direkt vor dem Eintreffen des „cut-off low“ existieren. Messungen nach dessen Durchzug zeigen jedoch eine Spurengasverteilung mit relativ großem troposphärischen Einfluss in der LMS, vergleichbar zu Messungen im Herbst. Obwohl keine Aussage darüber getroffen werden kann, ob dies tatsächlich ein lokaler Effekt des „cut-off low“ ist, zeigt sich, dass dieses meteorologische Phänomen mit großräumigen Transportprozessen verbunden ist. Großräumiger isentroper Transport führt troposphärische Luft in die LMS und Luftmassen stratosphärischen Charakters in die Tropopausenregion und schafft damit die Voraussetzung für die kleinskalige Vermischung zwischen troposphärischer und stratosphärischer Luft in der LMS.

## Ausblick

Die Ergebnisse dieser Arbeit zeigen, dass anhand von hochpräzisen Messungen langlebiger Spurengase wertvolle Information über Transportprozesse in der UT/LS Region gewonnen werden. So konnte Transport aus dem Polarwirbel, der unteren Stratosphäre und der Troposphäre in die arktische LMS quantifiziert werden. Während des Sommers konnten großskalige Transportprozesse in Verbindung mit einem „cut-off“ low beobachtet werden, die photochemisch gealterte Luftmassen aus den hohen Breiten und Luft troposphärischen Ursprungs in die mittleren Breiten der

LMS zusammenführen. In der Folge findet die Vermischung dieser Luftmassen durch kleinskalige Prozesse statt, und im Herbst kann ein abgeschwächter meridionaler Gradienten in den Spurengasverteilungen beobachtet werden. In Übereinstimmung mit Ergebnissen der SPURT-Kampagnen konnte nur in den unteren 20 K bis 30 K der LMS ein signifikanter Einfluss durch troposphärische Luftmassen festgestellt werden. In den darüberliegenden Schichten findet STE auf längeren Zeitskalen statt. In den obersten Schichten der LMS lässt sich auch ein signifikanter Einfluss Luft aus der untersten tropischen Stratosphäre beobachten.

Der HAGAR-Datensatz wurde kürzlich um Daten weiterer Messkampagnen erweitert (TroCCiNOx, Brasilien, Januar/Februar 2005; SCOUT-O3, Australien, November/Dezember 2005; und in Kürze auch AMMA, Burkina Faso, August 2006). Dieser erweiterte Datensatz erstreckt sich auf die Antarktis (Frühling), die Tropen und Subtropen beider Hemisphären in verschiedenen Jahreszeiten und geographischen Längen, die mittleren Breiten der Nordhemisphäre im Sommer, Herbst und Winter, sowie auf die winterliche Arktis. In diesen Daten steckt ein großes Potential für weitere Untersuchungen der UT/LS Region anhand von hochpräzisen Messungen langlebiger Spurengase, wie sie in dieser Arbeit vorgestellt wurden.

Ab 2009 steht mit dem Start von HALO<sup>10</sup> [HALO, 2006] eine neue Plattform zur Erforschung der Tropopausenregion und LMS zur Verfügung. Dank der Gipfelhöhe von nahezu 16 km, sowie großer Reichweite und Nutzlast, bietet sich zukünftig die Möglichkeit, die räumliche und zeitliche Abdeckung der Messungen in der Atmosphäre zu verbessern. Dies ist ein weiterer, wichtiger Schritt um zu neuen Erkenntnissen über die Dynamik, sowie den Chemie- und Strahlungshaushalt der UT/LS Region zu gelangen und somit zu verbesserten Vorhersagen der Zusammensetzung und des Klimas unserer Atmosphäre beitragen zu können.

---

<sup>10</sup>High Altitude and Long Range Research Aircraft



# Acknowledgements

The EuPLEX campaign was funded by the European Union through its 5th Framework Programme. The APE ENVISAT campaigns in Forlì and the Arctic validation campaign (AVC) were funded by the Bundesministerium für Bildung und Forschung (BMBF), the European Space Agency (ESA) and the Italian Space Agency. The development of HAGAR was funded by the European Community (EC) and the BMBF.

For the years 2001 to 2003, my work on this thesis was financed by the Scholarship “Promotionsstipendium für Ingenieur- und Naturwissenschaftlerinnen” funded by the Hessisches Ministerium für Wissenschaft und Kunst.

Very special thanks to the pilots and the crew of the M-55 Geophysica aircraft and our many colleagues who made all Geophysica campaigns a success. It has been a great pleasure and fun to work with you all! Thank you, Grazie, Merci, Dank u well, spa'si:ba!

Please forgive me that I will switch back to my mother language for further acknowledgments!

## Ein Dankeschön...

...an alle, die zum Gelingen dieser Arbeit beigetragen haben!

Allen voran möchte ich Herrn Prof. Dr. Ulrich Schmidt für die Betreuung meiner Arbeit und die Möglichkeit danken, im Fach der Atmosphärenwissenschaften promovieren zu dürfen. Lieber Herr Schmidt, nicht nur ihre fachliche Expertise, sondern auch ihre freundliche und menschliche Art unsere Arbeitsgruppe zu leiten, hat es zu einem nicht nur wissenschaftlichen Vergnügen gemacht hier zu arbeiten.

Dr. C. Michael Volk danke ich für die Betreuung der Arbeit, die aufopfernde Korrektur meines Englisch, sowie ausgiebige wissenschaftliche Diskussionen zum Thema der Arbeit und darüber hinaus, wann immer ich Fragen hatte.

Ein herzliches Dankeschön geht an Dr. Andreas Engel für das Interesse an meiner

Arbeit und diverse Gespräche auch nicht wissenschaftlicher Art von „A“ wie Atmosphäre bis „Z“ wie Zeitfahren der Tour de France. Ich freue mich auf die zukünftige Zusammenarbeit!

Für die vielen Tage und Nächte im Labor und Hangar, die ich nicht alleine verbringen musste, danke ich natürlich allen aktiven und ehemaligen Hagaristi: Carine Homann, das jüngste Mitglied unseres HAGAR-Teams. Ich hoffe, dass sie die ersten Kampagnenschocks gut überstanden hat und ein bisschen Freude dem Klackern unseres HAGARs abgewinnen kann! Anna Christina Kuhn wünsche ich alles Gute für die Datenauswertung und die Fertigstellung ihrer Doktorarbeit! Dr. Janine Baehr wünsche ich alles Gute für die Zukunft, Glück und Gesundheit für die Geburt ihres Kindes.

Dr. Oliver Riediger und Dr. Martin Strunk, Ex-Hagaristi und quasi die Ziehväter von HAGAR, Euch danke ich für die fantastische Arbeit, die ihr geleistet habt und das immer anhaltende Interesse und die Freude an der tickenden Bombe! Ohne unseren „Kampagnen-Touristen“ Oli hätten wir wohl manches mal geschraubt „bis der Arzt kommt“!

Liebe Katja, Dir danke ich von ganzem Herzen für 6 wunderbare Jahre! Ich hätte mir keine bessere Zimmerkollegin und inzwischen Freundin wünschen können! Danke für Deine Versuche mir ein paar Brocken Russisch beizubringen, das Blumengießen, russische Schokolade und dafür, immer ein offenes Ohr für mich zu haben. Ich bewundere Dich dafür, mit welcher Liebe, Kraft und Energie Du Dein Leben, Familie und Promotion (und, und, und) meisterst! Nochmals, Danke!

Für die Bereitstellung der Ozondaten und gute Zusammenarbeit bei den Messkampagnen danke ich den Mitarbeitern des DLR Anke-Elisabeth Roiger, Paul Stock und Hans Schlager(FOX-Ozon), sowie Alexey Ulanovsky (CAO) und Fabrizio Ravegnani (ISAO-CNR)(FOZAN-Ozon).

Den (Ex-) Jülichern Armin Afchine, Markus Boremski, Jens Uwe Groß, Gebhart Günther, Marc von Hobe, Paul Konopka, Marc Krebsbach, Rolf Müller, Susanne Rohs, Cornelius Schiller, Nicole Spelten, Hildegart Steinhorst, Fred Stroh und Vicheith Tan (und und und) danke ich für Diskussionen rund um das Thema meiner Arbeit, CLaMS Daten, FISH-H<sub>2</sub>O Daten, Hilfe bei Problemen mit HAGAR und immer eine tolle Zusammenarbeit.

Ich danke den Kollegen aus Mainz, Thomas Böttger, Joachim Curtius, Wilhelm Schneider, und Ralf Weigel neben der wissenschaftlichen Zusammenarbeit auch für „Geduld und Spucke“ beim Ein- und Ausbau des HAGARs und das auch mitten in der Nacht. Mit Eurem Humor habt ihr Kampagendurchhänger um einiges erträglicher gemacht.

Natürlich danke ich auch allen anderen Kollegen der Arbeitsgruppe „Physik der Atmosphäre“ des Instituts für Atmosphäre und Umwelt, die immer eine Hilfe waren und eine sehr nette Zusammenarbeit und Arbeitsatmosphäre ermöglicht haben:



---

Ich danke dem ehemaligen Hagaristi, Thomas Wetter, der bei Wind und Wetter in Forlí und Kiruna nicht nur wissenschaftliche, sondern auch kulinarische Beiträge leisten konnte! Ulrich Bundke sei Dank für seine Kompetenz in Sachen Atmosphäre und Netz und darüber hinaus für tausende von Ohrwürmern! Den weiteren Mitgliedern der SFB - Gruppe, Heinz Bingemer, Holger Klein, Björn Nillius danke ich für eine sehr nette Zusammenarbeit, Hilfe bei Problemen und die schnelle Erstellung von PV-Plots (Danke Holger!).

Für Unmengen geliehener Fittinge, Werkzeuge, Informationen, wissenschaftliche Diskussionen und Tipps der Woche danke ich Tanja Möbius, Harald Bönisch und Johannes Laube - letzterem insbesondere für die TdWs! Was wissenschaftliche Diskussionen aber auch Gespräche allgemeiner Natur angeht, danke ich ganz besonders Harald, der mich durch sein schier unendliches Wissen in Wissenschaft und Sport immer wieder beeindruckt hat. Ich freue mich auf die Zusammenarbeit mit Euch!

An dieser Stelle darf keinesfalls der Dank an Christine Lidzba fehlen, die das Sekretariat fest in der Hand hat und immer ein paar gut Tipps für Wohlbefinden und Gesundheit auf Lager hat - es macht Spaß mit Dir zu arbeiten! Bei dieser Gelegenheit bedanke ich mich auch bei unserer AG-Managerin im wohlverdienten Ruhestand, Frau Cecilia Stickler-Schmidt, für eine tolle Zusammenarbeit, exzellente Betreuung bei Reisen nach Schweden und für den Sprachkurs, den wir bei Ihnen machen durften: Tack så mycket!

Ohne die feinmechanische Werkstatt unter Leitung von Herrn Robert Röder wäre HAGAR sicherlich schon in seine Einzelteile zerfallen. Herzlichen Dank für die schnelle und geschickte Umsetzung diverser vager, zölliger (!) Ideen. Gleichmaßen Dank auch an das E-Labor, Dr. Rainer Rossberg und Vera Fischer, die sich trotz diverser nicht dokumentierter Modifikationen und abenteuerlicher Verkabelungen im HAGAR immer durch den „Kabelsalat“ durchgekämpft haben.

Meinen Kommilitonen und Freunden, Dr. Silke Trömel und Dr. Hans-Peter Haase, danke ich für jahrelangen Beistand während der Promotion, dem Diplom, im Hörsaal, in Übungen, Seminaren, Tagungen und bei den nicht-meteorologischen Dingen des Lebens. Ihr habt den Weg bis zu diesem Punkt um einiges leichter gemacht! Obwohl sich mittlerweile unsere Wege getrennt haben, hoffe ich doch, dass wir hin und wieder bei Bier und Äppler zusammenkommen.

Ich danke allen meinen Freunden, die mich auch während stressigen Zeiten ertragen und wieder aufgebaut haben. Ein Abend mit Euch und mir geht es meistens viel, viel besser! Danke! Ein extra Dankeschön an Christine Peter, die einen Großteil dieser Arbeit Korrektur gelesen hat.

Der größte Dank geht an meine Familie für die bedingungslose Unterstützung und Liebe, die mich immer begleitet. Ihr habt es sicherlich nicht immer leicht mit

mir!

Danke an meine Eltern Inge und Rudolf Werner, die sich von begeisterten Kampagnenberichten bis hin zu missmutigem Schweigen alles anhören mussten. Für Hilfe bei kleinen mathematischen Fragen, Computerkaufberatung, blöde Sprüche und für die Tatsache, dass er so ist wie er ist danke ich meinem „kleinen“ Bruder Christian - mach weiter so, ich bin stolz auf Dich! Eine herzliche Umarmung und riesiges Dankeschön geht an meine Oma, Helene Hartmann. Schön das es Dich gibt!

Vielen, vielen Dank!

Frankfurt am Main  
Juli, 2006

Anja Werner

# Curriculum Vitae

**Name:**Anja Sabine Werner

**Date of birth:** 7. Mai 1974

**Place of birth:** Gelnhausen, Germany

**Nationality:** German

**1980 - 1984** Philipp Reis Schule Gelnhausen, elementary school.

**1984 - 1993** Grimmelshausen Gymnasium Gelnhausen

**1993** Abitur (school-leaving examinations)

**1993 - 2000** Meteorological studies at the Johann Wolfgang Goethe-University of Frankfurt am Main, Germany

**1995** intermediate examination (Vordiplom)

**2000** Diploma (Degree: Diplom Meteorologe)

Diploma thesis: „The North Atlantic Oscillation and its impact on europe“. Supervisor: Prof. C.D. Schönwiese; Department of Meteorological Environmental Research. Johann Wolfgang Goethe-University of Frankfurt am Main, Germany

**2002** The Global Atmosphere and Ocean System, Vol.8,No.4, pp. 293 - 306: „A statistical analysis of the North Atlantic Oscillation and its impact on european temperature.“

**since Juli 2000** PhD student at the Institute for Atmosphere and Environment (former Institute for Meteorology and Geophysics) in the department of Atmospheric Physics (Supervisor: Prof. Dr. Ulrich Schmidt).

**since February 2002** Treasurer in the Frankfurt group of the German Meteorological Society.

